DEVELOPMENT OF A METHODOLOGY TO MEASURE AERODYNAMIC FORCES ON PIN FINS IN CHANNEL FLOW

Scott J. Brumbaugh

Thesis submitted to the Faculty
of the Virginia Polytechnic Institute and State University
in partial fulfillment of the requirements for the degree of

Master of Science
in
Mechanical Engineering

Dr. K.A. Thole, Chair
Dr. M.R. Paul
Dr. P.P. Vlachos

January 5, 2006
Blacksburg, VA

Keywords: pin fin, cylinder drag, lift, force measurement, internal cooling, pressure drop

Development of a Methodology to Measure Aerodynamic Forces on Pin Fins in Channel Flow

Scott J. Brumbaugh

Abstract

The desire for smaller, faster, and more efficient products places a strain on thermal management in components ranging from gas turbine blades to computers. Heat exchangers that utilize internal cooling flows have shown promise in both of these industries. Although pin fins are often placed in the cooling channels to augment heat transfer, their addition comes at the expense of increased pressure drop. Consequently, the pin fin geometry must be judiciously chosen to achieve the desired heat transfer rate while minimizing the pressure drop and accompanying pumping requirements.

This project culminates in the construction of a new test facility and the development of a unique force measurement methodology. Direct force measurement is achieved with a cantilever beam force sensor that uses sensitive piezoresistive strain gauges to simultaneously measure aerodynamic lift and drag forces on a pin fin. After eliminating the detrimental environmental influences, forces as small as one-tenth the weight of a paper clip are successfully measured.

Although the drag of an infinitely long cylinder in uniform cross flow is well documented, the literature does not discuss the aerodynamic forces on a cylinder with an aspect ratio of unity in channel flow. Measured results indicate that the drag coefficient of a cylindrical pin in a single row array is greater than the drag coefficient of an infinite cylinder in cross flow. This phenomenon is believed to be caused by an augmentation of viscous drag on the pin fin induced by the increased viscous effects inherent in channel flow.

Acknowledgements

I would like to express my sincere gratitude to Dr. Karen Thole for providing me the opportunity to work as part of her research lab. The dedication and concern that Dr. Thole exhibits towards her students is truly rare. As evidence, one need only consider the countless nights and weekends she spends addressing her students' research concerns or listening to their latest personal crisis.

To each one of my labmates, I would like to say thank you for your comradery. Mike B., Steve, Nick, Joe, Will, Sundar, Cam, Alan, Eric, Mike L., Seth, Paul, Scott W, and Erin have all made my stay in Blacksburg enjoyable. I need to especially thank Alan Thrift for his assistance in taking some of the data presented in this thesis, and Eric Lyall for the conversation during those long nights in the lab. Becca Lynch also deserves special recognition for her fine culinary skills.

I must also express my gratitude to Pratt and Whitney for the research opportunity they provided. I would like to especially thank Atul Kohli for his support of my work.

From Sandia National Laboratories, I would like to recognize Jim Harrison, Pat Sena, Tana Lucy, and Steve Rottler. These four individuals made it possible for me to attend graduate school.

From Behrend, I would like to thank Dr. Jack Young, Dr. Jim Sonnenmeier, Dr. Amir Khalilollahi, and Dr. Bill Lasher. These gentlemen inspired my desire to learn and provided a professional model by which I strive to conduct myself.

My family has made me who I am today. Both of my parents sacrificed selflessly to afford me the opportunity to succeed in life. I can only hope to be as good a parent someday. I am grateful for my grandparents who have provided, and continue to provide, friendship and memories that I will always cherish. Grandma deserves a special thank you for rooming me for my first three years at Behrend. I am blessed to have my brother Justin, who provides inspiration to me through his admirable work ethic, principled character, and angling ability.

Most importantly, I must thank my fiancée, Allison, whose love and support adds a dimension to my life that no one else can. Thank you for the good times we have shared and I look forward to the good times we have yet to share.

Contents

Nomenclature

A	= Area
b	= Distance from the base of the pin fin to the top of the threads
B	= Bias error
$B_{95\%}$	= 95% confidence interval error bound
c	= Radius from beam neutral axis to edge of beam
C	= Orifice / venturi discharge coefficient
C_D	= Drag coefficient (no subscript indicates based on mass averaged channel velocity (U))
C_L	= Lift coefficient based on mass averaged channel velocity
d	= DSC-6 calibration constant (V/V-kg-cm), orifice / venturi bore diameter
D	= Diameter, without subscript indicates pin diameter
D_h	= Channel hydraulic diameter
$\mathscr{D}$	= Aerodynamic drag force
dp	= Pressure drop across venture / orifice flow meter
E	= Elastic modulus
F	= Force
F_i	= Mechanical spring preload force
f	= Darcy friction factor
f_F	= Fanning friction factor
g	= Acceleration due to gravity, 9.81 m/s²
G	= Gauge factor of strain gauge
H	= Channel height (pin height within the channel)
h	= Total length of pin fin
I	= Area moment of inertia
K	= Orifice / venture flow coefficient
L	= Total cantilever beam length, length of the mechanical spring
L_C	= Characteristic length
L_i	= Initial length of the mechanical spring

$\mathscr{L}$ = Aerodynamic lift force

m = Distance between the bottom of the pin in and the apparent channel floor

M = Moment

n = Distance from the base of the cantilever beam to the bottom surface of the channel floor

p = Wetted perimeter

P = Pressure

P_1 = Static pressure at pressure tap #1

P_i = Static pressure at the i^{th} static pressure tap

Q = Volumetric flow rate

R = Resultant calculated value

Re = Reynolds number (no subscript indicates based on channel hydraulic diameter, D_h, and mass averaged open channel bulk velocity, U)

S = Transverse pin spacing, Precision error

SG = Specific gravity (defined to be one for air)

T = Temperature

t = Time, total ceiling /floor channel thickness

u = Uncertainty

U = Velocity (no subscript denotes mass averaged velocity based on channel open area)

V_{cross} = Output voltage from a sensor axis aligned 90° to the applied force

V_e = Generic Wheatstone bridge excitation

V_{ex} = X-axis excitation voltage

V_{ey} = Y-axis excitation voltage

V_{Ix} = Voltage induced in the x-axis by a force applied solely in the y-direction

V_{Iy} = Voltage induced in the y-axis by a force applied solely in the x-direction

V_o = Output voltage from a sensor axis parallel with the applied force

V_{ox} = Displayed x-axis output voltage

V_{ox_corr} = X output voltage corrected for zero voltage plane

V_{oy} = Displayed y-axis output voltage

V_{oy_corr} = Y output voltage corrected for zero voltage plane

V_X = True x-axis output voltage (corrected for ξ and/or zero voltage plane)

V_Y = True y-axis output voltage (corrected for ψ and/or zero voltage plane)

V_{zero_x} = Sensor output voltage in x-axis with no applied load

V_{zero_y} = Sensor output voltage in y-axis with no applied load

V = Characteristic velocity

W = Channel width

w = Apparent channel ceiling / floor material thickness

X = Stream wise pin spacing

x = Linear distance in the channel axial direction

Y = Expansion coefficient

Greek:

β = Linear least squares regression slope, orifice / venturi beta ratio

Δ = Difference in the subsequent quantity

ΔF_X = X-component of applied force in a mechanical spring

ΔF_Y = X-component of applied force in a mechanical spring

$\overline{\Delta P}$ = Average static pressure difference in the stream wise direction

ΔP_i = Static pressure difference at the i^{th} pressure tap

δ = Distance of applied force from DSC-6 beam tip; defined to be positive towards the base of the sensor, negative away from the base of the sensor, mechanical spring deflection, linearly translated deflection of cantilever beam

ε = Strain

ϕ = Angle of applied force

λ = Distance from channel midline to outside surface of apparent ledge

μ = Dynamic viscosity, average

θ = Cantilever beam / sensor deflection angle

ρ = Density

ξ = X cross axis correction factor

ψ	= Y cross axis correction factor

Subscripts:

1	= Time before lift and drag forces are applied
2	= Time after lift and drag forces are applied
Actual	= Value at actual test conditions
b	= beam diameter
CH	= Channel open area
D	= Length scale based on pin fin diameter, velocity based on open channel area
Dh	= Length scale based on channel hydraulic diameter, velocity based on open channel area
FR	= Projected frontal area of pin fin
L	= Line absolute pressure or temperature
max	= Maximum velocity of a fully developed turbulent velocity profile
min	= Mass averaged velocity through the minimum channel area
S	= Static
STD	= Density at standard atmospheric conditions
T	= Total
x	= Streamwise, drag
y	= Spanwise, lift

List of Tables

List of Figures

Chapter 1
Introduction

Today's cooling needs, whether it is for electronic components or for gas turbine airfoils, are more demanding than ever. The continuous demand for increased efficiency, performance, and part life has placed severe thermal requirements on a wide range of products. Additionally, the recent trend to miniaturize electronic components has further complicated the task of thermal management.

Gas turbines are an example of an industry where the cooling demands are especially stringent. Gas turbines operate in a Brayton thermodynamic cycle. The efficiency of an ideal Brayton cycle is given by Equation 1.1

$$\eta = 1 - \frac{T_4 - T_1}{T_3 - T_2} \tag{1.1}$$

In Equation 1.1, T_1 represents the temperature of the ambient air entering the engine, T_2 is the compressor discharge temperature, T_3 is the turbine inlet temperature, and T_4 represents the temperature of the exhaust gas exiting the turbine. Inspection of Equation 1.1 shows that increasing the turbine inlet temperature (T_3) increases the efficiency of the gas turbine engine. This increase in efficiency can be realized as in increase in engine thrust or fuel economy. However, the turbine inlet temperature cannot be arbitrarily increased without considering the turbine blade metal temperature. Although today's modern engines have gas temperatures around 1650°C at the turbine inlet, the material in a typical turbine blade will melt at approximately 1315°C. Even if the blade is cooled to a temperature below the melting temperature, the blade temperature still affects the life of the blade. Blade temperatures that deviate above the design temperature by just 15°C can half the blade service life [Han et al., 2000]. Obviously, an effective cooling scheme is needed to maintain blade temperatures at an acceptable level. Today's modern, high performance turbine blades use a combination of internal channel flow cooling and external film cooling to protect the blade. The coolant air provided to the internal cooling

channels and film cooling holes is bled from the engine compressor. Consequently, the required mass of coolant flow and pumping power needed to push the flow through the internal channels directly affect the efficiency of the engine.

The electronics industry is another area where thermal management is crucial. As with turbine blades, the life of electronic components increases with decreasing temperature. In fact, service life is an exponential function of component temperature reduction [Seri, 1995]. Heat generation from microprocessors grows at an unbounded rate as the number of transistors placed on a single silicone chip continues to escalate. The increase in heat generation must be offset by an increase in heat rejection to assure the reliability of the processor. This task is further complicated by the trend to produce ever smaller components. The decreased component size coupled with increased heat generation results in a higher power density. The smaller components provide less surface area from which to reject heat. Additionally, the compact size of the product package limits the available volume for the heat sink or heat exchanger. In the past, electronics manufacturers commonly used heat sinks with large externally cooled fins to maintain component temperatures. However, the need for increased heat rejection in limited space has forced the manufacturers to turn to smaller, more effective heat sinks cooled by internal channel flows. Internally cooled heat sinks provide the potential for higher heat flux capability, more compact design, lower weight, and less acoustic noise than the traditional externally cooled heat sinks [www.thermacore.com].

Both of the industries mentioned above use internal cooling channel flows to meet their thermal management needs. The channels used to transport the cooling fluid are rarely simple, open channels. Often, devices are added to the channel to promote turbulence and heat transfer. Pin fins that span the entire height of the channel are a common device in heat exchanger channels. The pin fins increase heat transfer in two ways; they promote turbulence and increase the surface area. However, a price is paid for the increased heat transfer in the form of pressure loss. The pressure loss through an array of pin fins places increased demand on the pumping or fan requirements of the device. This study aims to provide data that will aid in the fluid dynamic design of heat exchangers that use internal cooling channels with pin fins.

1.1 Motivation

Designing the optimal heat exchanger involves a tradeoff between heat transfer performance and fluid dynamic performance. The best heat exchanger design is not necessarily the one that rejects the most heat. The pressure drop of the flow through the heat exchanger, and the accompanying pumping requirements, must be considered. Certainly, any energy that must be allocated to the heat exchanger pump or fan detracts from the overall efficiency of the product. Pumping requirements are especially important for products that are power or energy limited. Products such as launch vehicles and unmanned military aircraft have a limited power source from which they can draw. Efficiency is paramount so that the entire energy source is not wasted on thermal management. The permissible size and mass of the heat exchanger pump or fan is another key factor. Again, this is especially important to launch vehicle and unmanned aircraft where weight and space are at a premium. Minimizing the pressure drop through the heat exchanger, while meeting thermal requirements, is essential to optimizing the overall efficiency and performance of the product.

Presently, most pin fin arrays are designed with correlations developed for an array with uniform pin fin geometry. The interested reader may consult Armstrong and Winstanley [1988] for a concise summary of available correlations. However, a uniform array of pins may not be optimal for every cooling situation. This is especially true where the product is subject to an intense, localized heat flux. Using an array of uniform pins, the entire array must be designed to accommodate the intense heat flux that is only applied in a local area. This results in an over designed heat exchanger that suffers from an unnecessarily large pressure drop. The design method could be improved by using a customized pin fin geometry within the array. As such, the heat exchanger could be designed to remove a large heat flux in the localized area while providing a sparser pin fin distribution where the heat flux is not as strong. This would minimize the pressure drop through the heat exchanger while meeting the thermal requirements.

This project strives to provide the fluid dynamic information necessary to design such a custom heat exchanger. Specifically, this project develops a method capable of measuring the aerodynamic lift and drag forces on a pin fin in channel flow. These forces may be used in a momentum balance to determine the pressure drop through a

custom pin fin array. The work of Lyall [2006] is a compliment to this project, providing localized heat transfer data for specific pin fin geometries. Combined, the two studies will enable future designers to create custom pin fin arrays and more efficient heat exchangers.

1.2 Research Objectives

The main goal of this study was to develop a capability to measure two-axis aerodynamic forces on pin fins in channel flow. To achieve the main goal, two objectives were met. The first objective required the design, construction, and benchmarking of an entirely new test facility in the Virginia Tech Experimental and Computational Convection Laboratory (VTExCCL). The second objective was to develop a new force measurement methodology. The measurement methodology required the cultivation of an effective force sensor and the definition of an experimental procedure capable of achieving valid results.

This thesis summarizes how the above stated objectives were met. Chapter 2 provides a review of currently published information on cylinder drag and skin friction measurement. Chapter 3 discusses the development of the DSC-6 force sensor and experimental procedure. The design and construction of the test facility is discussed in Chapter 4, while Chapter 5 summarizes the experimental results obtained for a single row of pin fins. Finally, Chapter 6 comments on the viability of the measurement method, summarizes the experimental results, and makes recommendations for future efforts.

Chapter 2
Review of Relevant Literature

The drag of an infinitely long cylindrical body in external cross flow is a well understood phenomenon. Drag coefficient curves for cylinders, and an explanation of the fluid dynamics that shape the drag curve, can be found in nearly every undergraduate fluid dynamics textbook. However, the drag of a cylindrical pin fin in channel flow is, to date, undocumented. It is unclear how the effects of a non-uniform velocity profile, bounding channel walls, and neighboring pin fins affect the drag coefficient.

This project used a direct force measurement technique to quantify the drag on a channel pin fin. The method was adapted from the measurement technique used by DeTurris et al. [1990] to quantify skin friction on a combustor wall in supersonic flow. DeTurris et al. [1990] provided the inspiration for the selection of the DSC-6 force sensor and the pin fin / channel wall decoupling method.

Section 4.1 presents a summary of pertinent information currently available regarding the drag of cylinders. Section 4.2 provides an overview of DeTurris et al.'s [1990] work, and the direct force measurement method. Finally, Section 4.3 evaluates the merit of this research thesis with regard to uniqueness and applicability to cooling design.

2.1 Cylinder Drag Studies

The drag of an infinitely long cylinder in external cross flow has been studied since the beginning of the 20th century. The interest in cylinder drag spawned out of a desire to quantify the drag on airfoil support wires used on World War I military aircraft. Both British and German engineers worked to provide their country with a technological edge in the battle for air supremacy. Figure 2.1 provides the culmination of both nations' efforts in the form of a curve relating infinite cylinder drag to Reynolds number. The NPL (National Physical Laboratory) curve represents the British effort, as tested by E.F. Relf [Goldstein, 1938]. The Gottingen curve summarizes the German results measured by Wieselsberger and Prandtl [Goldstein, 1938]. Both drag curves match each other

exactly until approximately Re = 8.0 X 10^4, where the NPL drag curve precipitously decreases in magnitude. The Gottingen curve does not drop off until approximately Re = 2.0 X 10^5. The sudden decrease in drag coefficient is known as drag crisis. Drag crisis occurs when the boundary layer on the cylinder surface transitions from a laminar boundary layer to a turbulent boundary layer [Munson et al., 1998]. The increased fluid momentum inherent in the turbulent boundary layer retards the boundary layer separation point on the cylinder surface. Typically, boundary layer separation from the cylinder surface occurs at approximately 90° from the stagnation point for sub-critical flows [Munson et al., 1998]. Once the boundary layer becomes turbulent, the separation point is delayed to approximately 110° (or beyond) from the stagnation point [Munson et al., 1998]. The net result is a significant decrease in pressure drag on the cylinder.

The discrepancy in the onset of drag crisis between the NPL and Gottingen curves was a result of experimental setup. Cylinder surface roughness and free stream turbulence affect when the boundary layer transitions to a turbulent profile [Munson et al., 1998]. Drag crisis in the Gottingen curve was delayed because the tests at Gottingen were conducted with a smoother cylinder or less free stream turbulence (or both) than the NPL tests. Most modern fluid dynamic texts cite the Gottingen curve as the standard for cylinder drag.

Goldstein [1938] provides a breakdown between viscous drag and pressure drag on a cylinder as a function of Reynolds number. Figure 2.2 illustrates the contribution of the viscous drag and pressure drag to the total cylinder drag. As expected, the contribution of viscous drag to the total drag decreases with increasing Reynolds number. Figure 2.2 shows that the viscous drag can be neglected for flows greater than approximately Re = 9.0 X 10^3. It is unclear how the distribution of viscous drag and pressure drag will change for a cylinder in channel flow. Recall that a fully developed velocity profile represents the merging of two boundary layers in the channel. Since viscous effects are significant in boundary layers, and generally negligible in external flows, it stands to reason that viscous drag could be augmented on pin fins in a fully developed profile.

Limited information is available regarding the drag of finite length cylinders in free stream flow. Oldenbourg [1921] reports drag coefficient values for cylinders

ranging from H/D = 1 to H/D = ∞ for a Re = 8.8 x 10^4 flow. The results of Oldenbourg [1921] are summarized in Figure 2.3 for reference. It is interesting to note that the drag coefficient of a finite length cylinder is less than an infinite cylinder. In fact, the drag coefficient is significantly effected at aspect ratios as large as H/D = 40. The cylinder drag coefficient decreases with aspect ratio (H/D), such that the H/D = 1 cylinder drag coefficient is almost 50% the magnitude of the infinite length cylinder. This phenomenon might be expected after comparing the drag of a cylinder and a sphere. For a given Reynolds number, the spherical drag coefficient is always less than a cylindrical drag coefficient. Because the sphere is three dimensional, the flow has an extra dimension to move around the object. Alternately stated, the third dimension provides an additional route for the flow to escape and get out of its own way. The net result is a decrease in drag coefficient. As the cylinder decreases in aspect ratio, the cylinder becomes more three-dimensional. Similar to the sphere, the three-dimensional cylinder may experience less drag due to the third "escape" dimension. The extra escape dimension argument does not apply to a finite length pin fin in channel flow. The bounding channel floor and ceiling prevent flow from escaping over the top and bottom of the pin fin. With the third escape dimension removed, the finite length pin fin may seem more like a two-dimensional cylinder than a finite length cylinder to the flow.

Ames et al. [2005] and Ames and Dvorak [2006] studied localized fluid dynamic phenomena and heat transfer within a pin fin array. Specifically, the two studies strove to correlate local turbulence levels to local heat transfer rates. The experiment used an eight row array of staggered pin fins with H/D = 2 and S/D = X/D = 2.5. Both studies considered three flow rates, Re_D = 3.0 X 10^3, 1.0 X 10^4, and 3.0 X 10^4 [Ames et al, 2005], where Re_D is based on the mass averaged velocity through the minimum metering area (U_{min}). Hot wire anemometry was used to obtain near pin velocity distributions and turbulence levels. Additionally, the static pressure distribution at the pin fin midline was obtained with static pressure ports molded at 6° increments in the pin fin.

Although Ames et al. [2005] and Ames and Dvorak [2006] consider turbulence levels, velocity distributions, and pressure distributions for pin fins throughout the array, the data from the first row of pins is most applicable to this research thesis. The data presented in these studies is the closest information available regarding the drag of a

channel pin fin in a single row. For this discussion, the effect of the downstream pin rows on the first pin row will be neglected.

The pressure distribution about a first row pin fin, as measured and documented by Ames et al. [2005], is shown in Figure 2.4 for $Re_D = 3.0 \text{ X } 10^3$, $1.0 \text{ X } 10^4$, and $3.0 \text{ X } 10^4$. In Figure 2.4, the pressure distribution is quantified by the pressure coefficient defined in Equation 2.1.

$$C_P = \frac{P_S(0) - P_S(\theta)}{\frac{1}{2}\rho U_{min}^2} \text{ [Ames et al., 2005]} \qquad (2.1)$$

The pressure distributions indicate that boundary layer separation occurs between 80° and 100° for each flow, as is typical for sub-critical flows on infinite cylinders. This observation is supported by the hotwire measurements obtained by Ames and Dvorak [2006]. The hotwire data show inflections in the velocity profile near the cylinder surface as well as high levels of streamwise velocity fluctuations (u') at the 90° station [Ames and Dvorak, 2006]. Both measurements suggest the boundary layer is separated at that location (90°).

The pressure coefficient distribution published by Ames et al. [2005], and shown in Figure 2.4, can be integrated to find the pressure drag coefficient at the pin fin midline. This analysis was not the focus of Ames et al. [2005], but I have taken the liberty to numerically integrate the data for this thesis. The integrated pressure drag coefficients for $Re_D = 3.0 \text{ X } 10^3$, $1.0 \text{ X } 10^4$, and $3.0 \text{ X } 10^4$ are respectively 0.74, 0.73, and 0.85. One should keep in mind that these coefficients represent only the pressure drag at the midspan of the pin fin. They do not consider pressure variations in the axial direction nor do they consider the viscous drag. For an infinite cylinder, Figure 2.2 shows that the respective $Re_D = 3.0 \text{ X } 10^3$, $1.0 \text{ X } 10^4$, and $3.0 \text{ X } 10^4$ pressure drag coefficients are 0.9, 1.1, and 1.2.

The numerical difference between the channel pin fin and infinite cylinder drag coefficients may only be a matter of selecting the correct scaling velocity. The drag coefficients integrated above use U_{min} as the scaling velocity (implicit by the definition of the pressure coefficient, C_P). A different velocity, such as the channel centerline velocity

(U_{max}) may be more appropriate. More research is needed to evaluate the correct scaling velocity. Additionally, it is unclear how the pin fin pressure drag will change at different heights on the pin fin, what effect the viscous drag will contribute to the total drag, and how these parameters are effected by varying H/D, X/D, and S/D within the array.

2.2 Direct Force Measurement Techniques

Two-component (and higher) aerodynamic force measurements are commonly made on bodies in external flow. Usually, the object of interest is attached to a multi-axis force balance via an aerodynamic sting. The sting is shaped with a symmetric airfoil so that the aerodynamic effect of the sting can often be neglected (or removed with a tare) from the measurement.

Aerodynamic force measurements on bodies in channel flow require a more complex measurement technique. The force measurement must be made on an object that is normally rigidly connected to at least one channel wall. The body of interest cannot be mounted to a sting and placed in a free stream, because the fluid dynamic interaction between the body and the channel walls is significant. To directly measure the force on the object of interest, it must be detached from the surrounding wall while maintaining the fluid dynamic interaction that is realized in real life. The detachment, or decoupling, of the object from the channel walls must also be achieved in such a manner as to not attenuate or augment the force apparent to the measuring device.

As discussed above, a review of the literature did not yield any experimental work that measured aerodynamic forces on channel pin fins. However, a concept for pin fin force measurement was found by studying the experimental efforts to quantify skin friction. Skin friction measurement was found to be remarkably similar to pin fin drag measurement, in that the skin friction acted on a section of wall rigidly attached to the surrounding substrate. In order to measure the force acting on the wall section of interest, the section must be detached from the surrounding wall.

Schetz [2004] provides an overview of how direct skin friction measurements are quantified. Figure 2.5 provides a generic illustration of a typical experimental setup for skin friction measurement. The measurement is made on a floating or movable element that is attached to an elastic measurement device. A thin gap surrounds the force element

to permit deflection of the measurement device. Some experiments fill the gap with a viscous fluid to minimize the fluid dynamic effects of the gap. More discussion regarding the gap and viscous filler fluid will be provided later in this section.

A summary of past, present, and future skin friction measurement devices is also provided by Schetz [2004]. Past skin friction measuring devices generally use mechanically complex flexures or springs and pulleys to measure skin friction. The mechanical complexity of the devices makes them difficult to use, and introduce inaccuracies in the measurements. Future skin friction devices may utilize innovations such as MEMS technology and fiber optics. However, Schetz [2004] states that these devices and methods are not developed enough for current use.

Currently, skin friction measurements are being made with good accuracy using a cantilever beam method [Schetz 2004]. The method involves relating the measured strain at the base of the cantilever beam to the applied aerodynamic force on the element. The sensitivity of the measurement can be adjusted by changing the length of the cantilever beam. Schetz [2004] suggests the use of a Kistler Morse DSC-6, shown in Figure 2.6, as a cantilever beam style measuring device capable of two-axis resolution. The DSC-6 is a commercially available force sensor that measures the strain at the base of the cantilever beam via four piezoresistive strain gauges [Schetz, 2004]. These strain gauges are very sensitive to strain, with a gauge factor of approximately 150 (traditional metal foil strain gauges only have a gauge factor of 2) [Schetz, 2004]. However, the strain gauges are also very temperature sensitive. As such, the temperature of the DSC-6 must be carefully controlled.

DeTurris et al. [1990] used the DSC-6 to measure two-component skin friction forces in a supersonic combustion flow. The forces of interest to DeTurris et al. [1990] ranged from 2.0×10^{-3} N to 1.0×10^{-2} N. Figure 2.7 provides a diagram of the experimental setup used by DeTurris et al [1990]. The DSC-6 was press fit into a housing that could be bolted to the bottom of the wind tunnel floor. The floating element was bolted to the DSC-6 sensor and aligned flush with the top surface of the wind tunnel floor. A gap of 0.01 cm [DeTurris et al., 1990] surrounded the floating element, allowing the DSC-6 to deflect. Dow Corning 1.0×10^{3} cSt oil was poured into the sensor housing such that it filled the housing and surrounded the floating element in the wind tunnel floor [DeTurris

et al., 1990]. The 1.0 X 10^3 cSt viscosity oil was chosen so that it did not blow out of the gap at test conditions. The silicone oil served a multitude of purposes. Primarily, the oil was used to fill the gap between the element head and the wind tunnel floor to provide a continuous impermeable surface for the flow. The oil also provided mechanical damping against ambient vibrations, minimized pressure gradients in the gap, aided in maintaining a constant sensor temperature, and prevented foreign matter from becoming lodged between the sensor head and the wind tunnel floor [Schetz, 2004]. DeTurris et al. [1990] note that it was necessary to remove all air bubbles in the oil before the test could begin.

Because DeTurris et al. [1990] dealt with super sonic combustion flows, sensor heating was a significant concern. Figure 2.7 shows that cooling fins were added to cool the sensor. Cold water was passed through copper tubing for the same purposes. For some extreme heating environments, liquid mercury was poured into the base of the sensor housing to promote heat transfer.

Calibration of the DSC-6 sensor was achieved by hanging known masses from the sensor. DeTurris et al. [1990] noted that the presence of the silicone oil in the sensor housing did not affect the calibration of the sensor. Both sensor axes were recorded during calibration. DeTurris et al. [1990] documented that the horizontally aligned axis (perpendicular to gravity) displayed an output force even though no force was applied to that axis. DeTurris et al. [1990] explained that the DSC-6 sensor outputs a voltage up to 5% of the gravity aligned axis in the perpendicular axis. This percentage of induced output was simply subtracted from the sensor output during testing [DeTurris et al, 1990]. However, DeTurris et al. [1990] imply that this correction was only made to the test data recorded in the cross stream axis. No corrections were made to the streamwise axis.

DeTurris [1992] discusses potential error sources in the measurement technique used by DeTurris et al. [1990]. Figure 2.8 graphically illustrates the three sources of error identified by DeTurris [1992]: misalignment, normal force moment, and lip force. Misalignment and normal force moment are of no concern to this project, as the geometry of the pin fin precludes the problem. The lip force, however, may affect the results of this project. Figure 2.8 shows that the lip force is generated by a pressure gradient in the gap between the pin fin and channel wall. Consequently, a resultant force is created by the net pressure imbalance acting on the element below the wind tunnel floor. The

pressure gradient can be decreased in severity, thus minimizing the lip force, by filling the gap with a viscous fluid [Schetz, 2004]. This is in part the reason why DeTurris et al. [1990] used silicone oil to fill the gap around the force sensing element. A close look at Figure 2.7 will show that DeTurris et al. [1990] used a fillet or taper on the force sensing element. This taper reduces the effective element surface area exposed to the pressure gradient, and minimizes the lip force.

DeTurris [1992] lists the overall uncertainty in the skin friction measurement to be 7%. Despite the inherent errors in the measurement technique listed above, DeTurris [1992] states that the severe temperature changes induced by the supersonic combustion flow account for 5% of the total error. Clearly, temperature considerations account for the majority of the experimental error. It stands to reason that an application of the DSC-6 in less thermally severe environments could achieve better results. DeTurris et al.'s [1990] experimental approach is attractive for application in this project, given its ability to resolve small forces with acceptable measurement uncertainty.

2.3 Uniqueness of Research

This research is unique, in that it will fill a void left by the cylinder studies discussed above. The literature review did not yield any studies that quantified drag on a cylindrical pin fin in channel flow. The work of Ames et al. [2005] and Ames and Dvorak [2006] can only be interpreted to provide limited insight into the drag of a pin fin in channel flow. This project will develop an experimental methodology capable of quantifying pin fin drag in channel flow.

Although the measurement method is based off the work of DeTurris et al. [1990], the methodology requires modification for application to this project. Because the pin fin extends across the entire height of the channel, it must be decoupled from both the channel floor and channel ceiling. Previous skin friction measurements only required that the force element be decoupled from the channel floor. This seemingly simple modification actually results in an order of magnitude increase in assembly difficulty (as discussed in Chapter 4). Additionally, the silicone oil must now be retained in a pin fin gap where gravity pulls the oil out of the gap. DeTurris et al. [1990] explicitly identify this "upside-down" configuration as difficult to work with, due to leakage out of the gap.

This project develops a novel methodology for quantifying the drag on cylindrical pin fins. However, this technique could be applied to any cross sectional shape and is capable of resolving two-component forces. The experimental facility and methodology developed here can be used by future researchers to explore the aerodynamic forces on an infinite test matrix of geometries. Test data from those experiments can be used by engineers to custom design heat exchangers to eliminate local hot spots or solve other extreme cooling needs. Specifically, the aerodynamic force data provided by this technique can be used in a momentum balance to determine the pressure drop through a custom pin fin array. Combined with the localized thermal data obtained from Lyall [2006], this method may radically change how heat exchangers are designed.

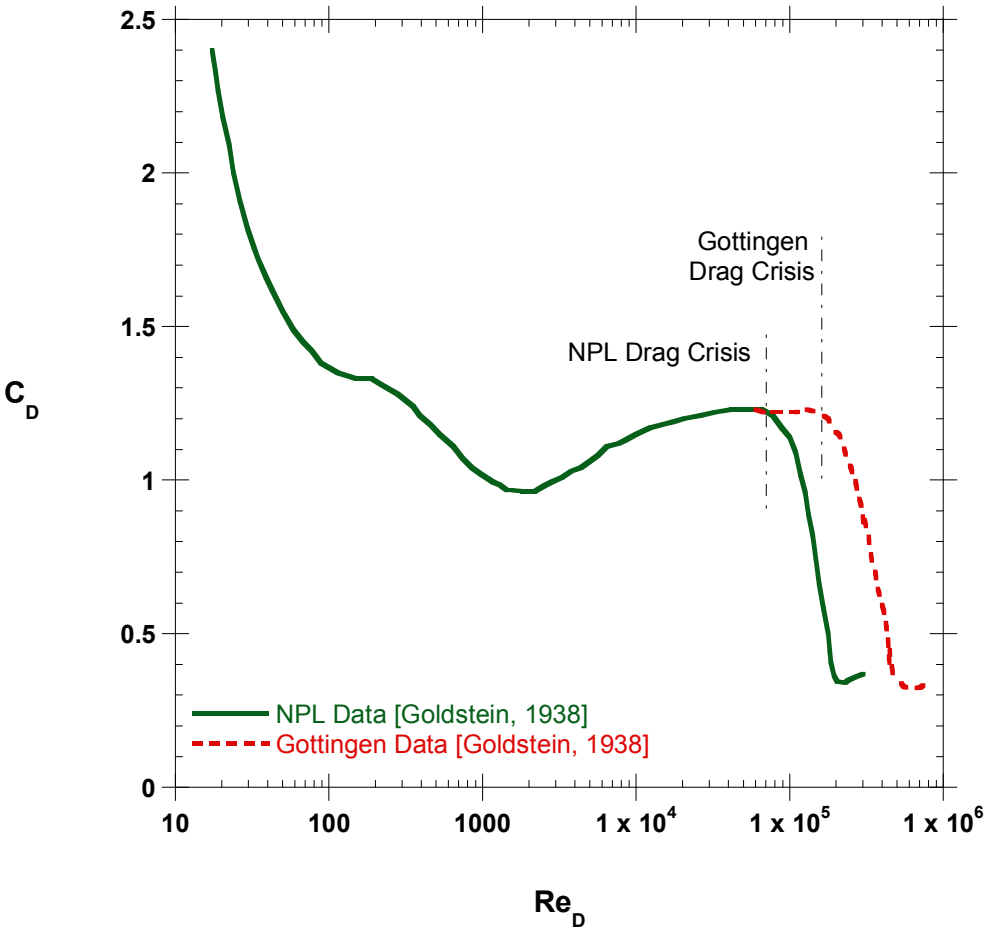

Figure 2.1 Drag coefficient curve for an infinite cylinder. Note that drag crisis occurs at two different Reynolds numbers depending on the free stream turbulence or cylinder surface roughness at each facility. The Gottingen facility had either less free stream turbulence or a smoother cylinder, resulting in a delayed drag crisis.

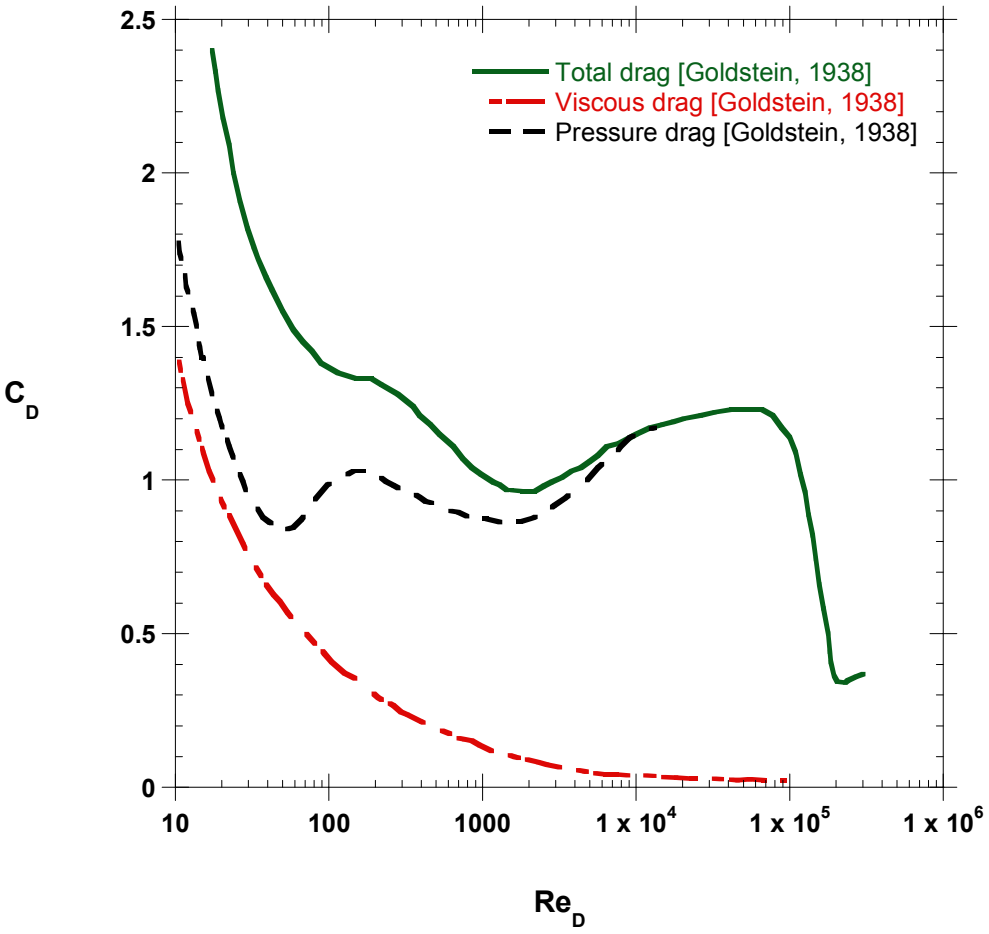

Figure 2.2 Drag coefficient curve showing the relative contribution of viscous drag and pressure drag to the overall drag of an infinite cylinder. Note that the pressure drag becomes indistinguishable from the total drag at approximately Re = 9.0 X 10^3.

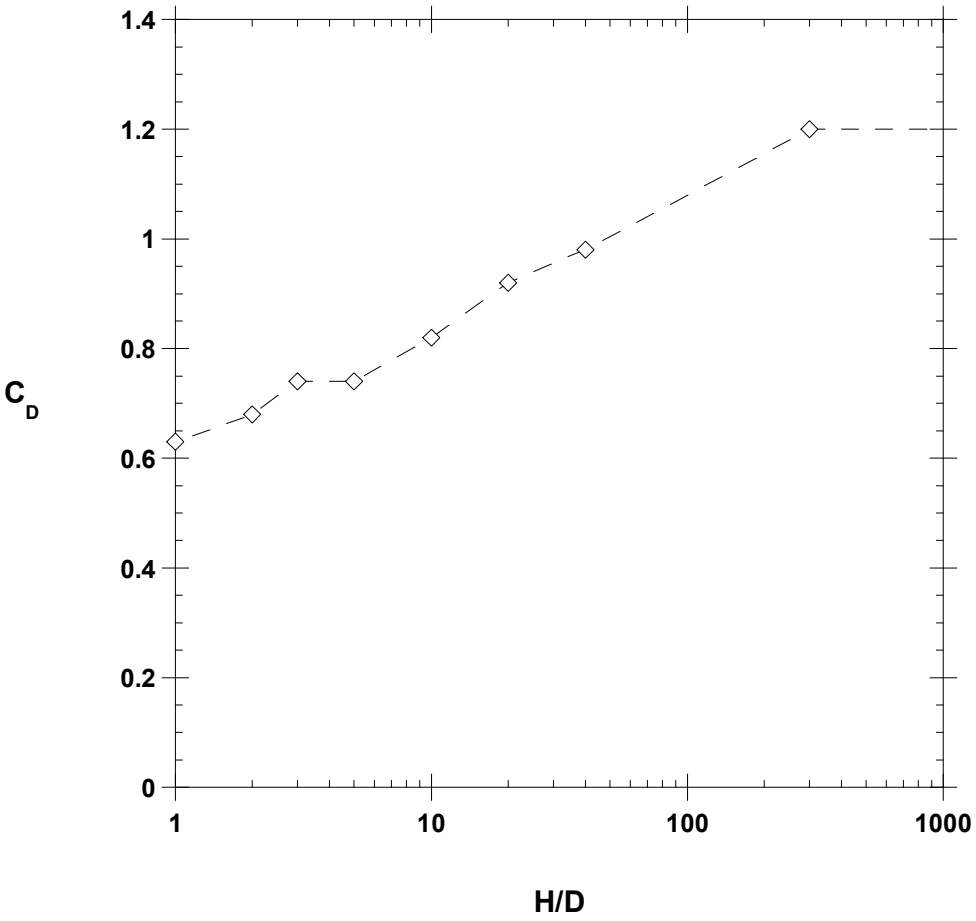

Figure 2.3 Effect of aspect ratio on drag coefficient for a finite length cylinder in external cross flow at $Re_D = 8.8 \times 10^4$, as reported by Oldenbourg [1921].

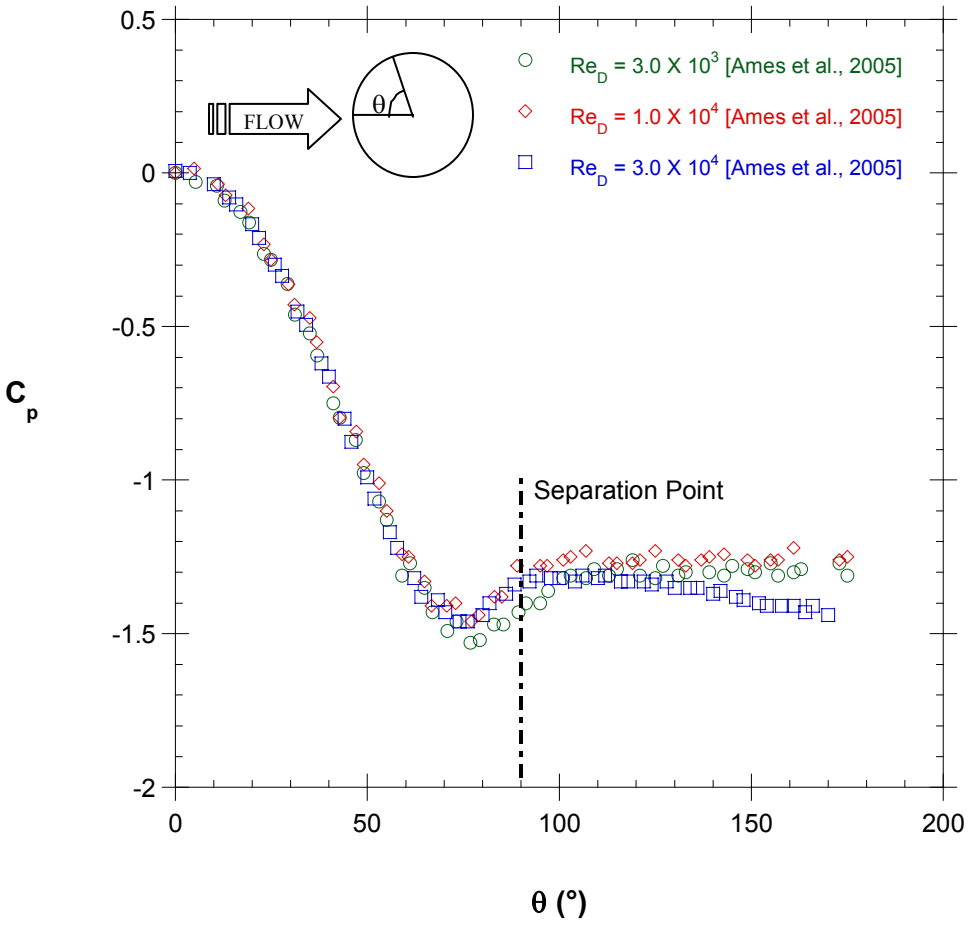

Figure 2.4 Pressure coefficient distribution at the centerline of a first row pin fin (H/D = 2) as measured by Ames et al. [2005]. Note that separation occurs between θ = 80 and θ = 100 for all three flows. This separation location is typical of a sub-critical flow around a cylinder, indicating that the boundary layer has not transitioned to a turbulent profile.

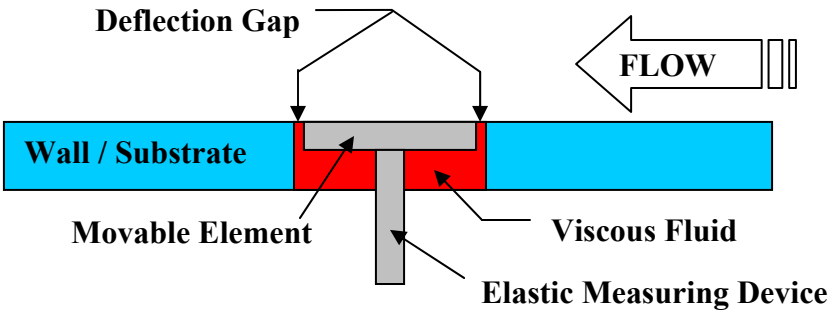

Figure 2.5 Generic experimental setup for skin friction measurements. The elastic measuring device is not illustrated in its entirety. Several different elastic measurement devices exist for use.

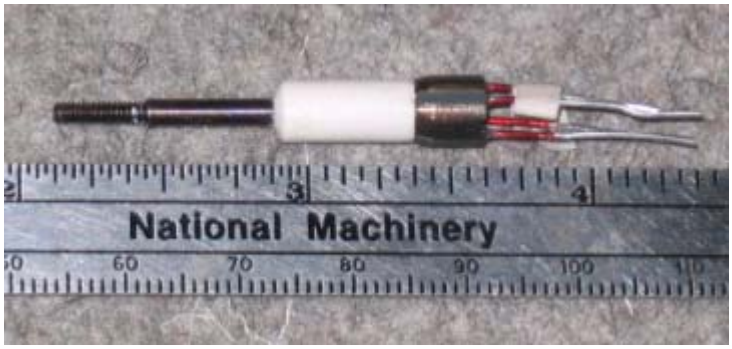

Figure 2.6 Photograph of the DSC-6 force sensor. The piezoresistive strain gauges are located beneath the white rubber encapsulant.

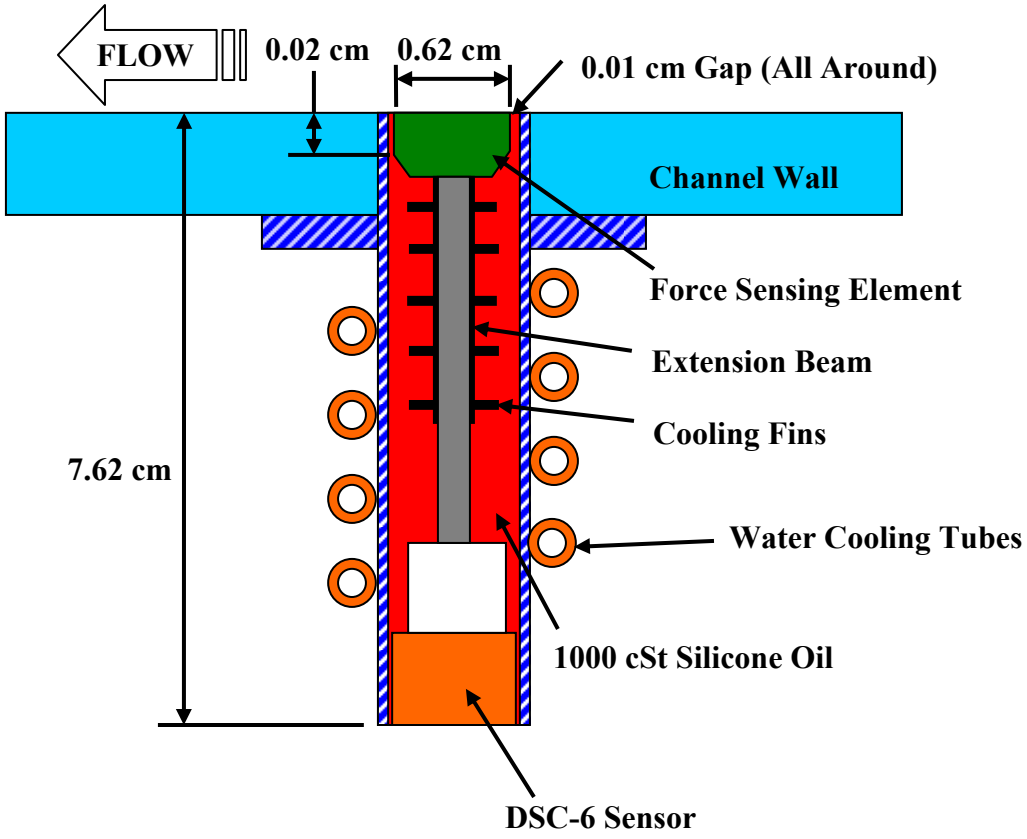

Figure 2.7 Schematic of experimental setup used by DeTurris et al. [1990] to measure skin friction.

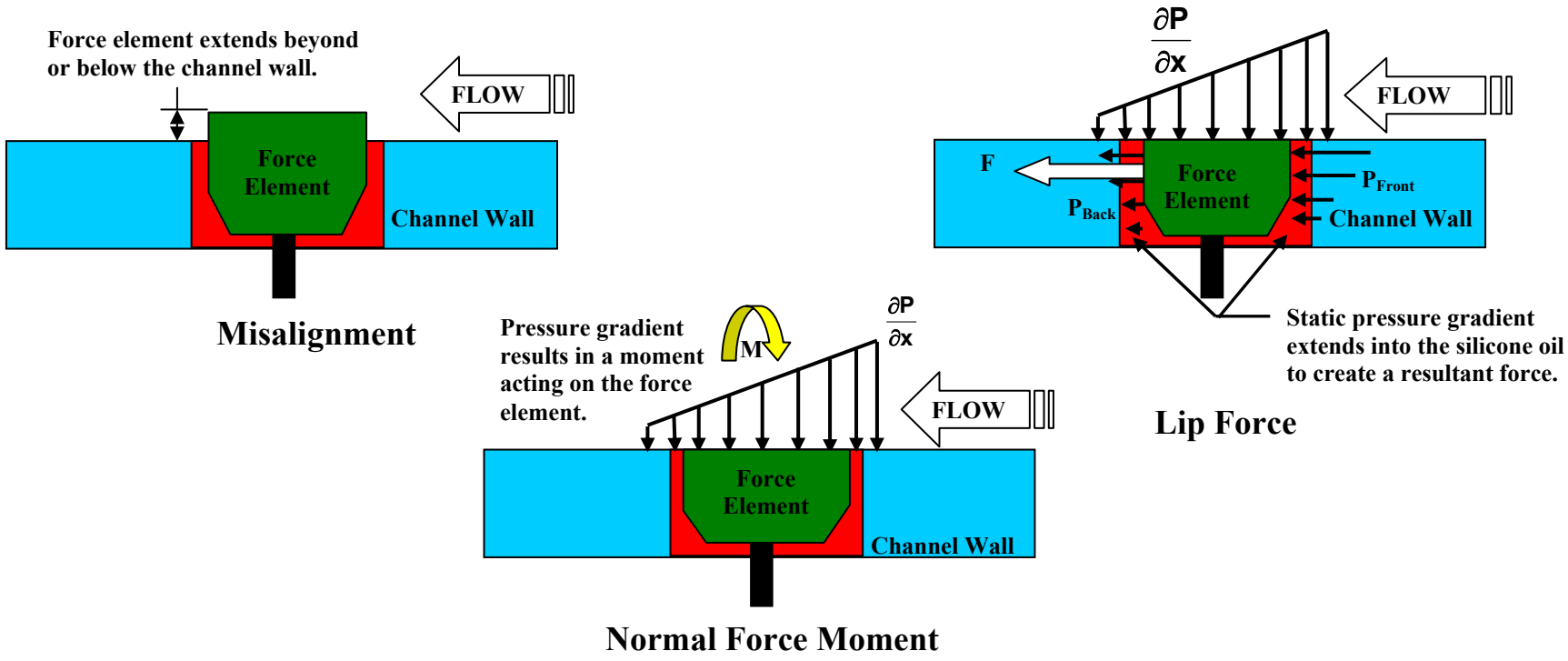

Figure 2.8 Illustration of misalignment, normal force moment, and lip force errors.

Chapter 3
Summary of Force Measurement Methodology

Measuring the aerodynamic forces on pin fins in a channel array presented many unique challenges. First, the pin fin had to be decoupled from the channel wall so that the forces could be measured. This decoupling was difficult, as the pin had to be separated from the channel wall without adversely affecting the flow dynamics. Additionally, as we will see, the magnitude of the forces to be measured was quite small. The measurement difficulty was further compounded by the intricate sensitivities of the DSC-6 force sensor.

This chapter describes the methodology used to measure the aerodynamic forces and the lessons learned along the way. Section 3.1 outlines the work that went into selecting an appropriate force measurement methodology. Section 3.2 provides a detailed description of the DSC-6 sensor, how it works, and the important environmental sensitivities. Details regarding the data collection equipment used by this project are provided in Section 3.3. A detailed description of sensor calibration methodology is provided in Section 3.4, while Section 3.5 discusses testing methodology. Finally, Section 3.6 provides a discussion of the experimental uncertainty.

3.1 Predictions and Measurement Alternatives Considered

Before a measurement methodology could be selected and developed, a prediction of the magnitude of the forces was estimated based on known correlations. As discussed in the literature review section, drag data for short aspect ratio pin fins in channel flow was not readily available. Thus, the estimates of the drag force on the pin fins were made by assuming an infinitely long, two-dimensional cross section in an external cross flow.

Two different cross sectional shapes were used to estimate the bounding minimum and maximum drag forces. An infinite cylinder, with a drag coefficient of 1.1 [Munson et al., 1998] was used to estimate the minimum drag force on a cylindrical pin fin. The maximum drag force was estimated using a rectangular cross section with a drag coefficient of three [Munson et al., 1998]. Although a rectangular shape was not

specifically requested by the sponsor, the high drag coefficient was meant to bound any odd-geometry, bluff shape that might be specified in the future. The cross sectional area was found by assuming an aspect ratio of H/D = 1/7.

Figure 3.1 plots the drag force estimates as a function of channel Reynolds number for both the H/D = 1 cylindrical pin fin and the H/D = 1/7 rectangle. The graph shows the exceptionally small forces associated with the cylindrical pin fin. At the lowest flow of interest, Re = 7500, the drag force was only 2.1 X 10^{-3} N. Indeed, a very sensitive force measurement device with high resolution was required to accurately quantify a force this small. The maximum predicted drag force for the rectangle was 1.8 N. This force did not pose any significant problems, other than to present a full scale force requirement for the chosen measurement device and methodology.

A short discussion is in order regarding the difference between the channel Reynolds number (Re) and pin fin Reynolds number (Re_D). The generic Reynolds number is defined by Equation 3.1.

$$Re = \frac{\rho v L_c}{\mu} \tag{3.1}$$

The Reynolds number may be defined in a variety of ways, depending on the definition of the characteristic velocity (v) and the characteristic length, L_C.

For the channel Reynolds number (Re), the characteristic velocity is defined to be the mass averaged velocity (U) and the characteristic length is defined to be the hydraulic diameter (D_h). The hydraulic diameter is defined by Equation 3.2.

$$D_h = \frac{4WH}{2(W+H)} \tag{3.2}$$

For channels with large width to height aspect ratios, the hydraulic diameter reduces to Equation 3.3.

$$D_h \approx 2H \tag{3.3}$$

The channel used in this project has a very large width to height aspect ratio (64), and thus Equation 3.3 applies. Consequently, the relationship between the hydraulic diameter and pin diameter is given by Equation 3.4.

$$D \approx \frac{1}{2}\left(\frac{D}{H}\right)D_h \tag{3.4}$$

The characteristic velocity for the pin fin Reynolds number is again the mass averaged velocity (U), but the characteristic length is the pin diameter, D.

$$Re_D = \frac{\rho U D}{\mu} \tag{3.5}$$

It follows that the relationship between channel and pin fin Reynolds number is given by Equation 3.6.

$$Re_D \approx \frac{1}{2}\left(\frac{D}{H}\right)Re \tag{3.6}$$

All cylindrical pin fins tested in this thesis have an aspect ratio of H/D = 1. Thus, the pin Reynolds number is approximately half the channel Reynolds number.

As stated in Chapter 1, this project strove to achieve two-component force measurement capabilities. Although not necessary to measure cylinder drag, the lift force component will be necessary to describe the aerodynamic forces acting on future pin fin geometries. A rigorous attempt to estimate the lift forces was not made. It was assumed that any lift force on a pin fin would be at least as large as the minimum drag force on a cylindrical pin fin. Similarly, the maximum lift force was assumed to be less than the maximum rectangular drag force. Thus, the drag estimates listed above provided the bounding estimates used in selecting the force measurement methodology.

As a side note, the magnitude of the forces could not be increased by changing the scale of the pin fins. Because the range of aspect ratios and channel Reynolds numbers were fixed by the project sponsor (regardless of experimental scale), any change in

geometric size (frontal area) was countered by an equal and opposite change in the square of the velocity. This point is confirmed by substituting Equation 3.3 into Equation 3.1 to obtain:

$$\mathrm{Re} \approx \frac{2\rho \mathrm{UH}}{\mu} \tag{3.7}$$

For the sake of discussion, assume the pin diameter, D, is increased to provide a larger frontal area. If the pin diameter (D) is increased, then the pin height (H) must also increase to maintain the specified H/D ratio. Equation 3.7 shows the velocity necessarily decreases inversely proportional to the channel height such as to maintain the same Reynolds number.

Now, recall the definition of the drag and lift:

$$\begin{aligned} \mathscr{D} &= \tfrac{1}{2}\rho v^2 A_{FR} C_D \\ \mathscr{L} &= \tfrac{1}{2}\rho v^2 A_{FR} C_L \end{aligned} \tag{3.8}$$

and substitute in for the definition of the pin fin frontal projected area to obtain:

$$\begin{aligned} \mathscr{D} &= \tfrac{1}{2}\rho v^2 (HD) C_D \\ \mathscr{L} &= \tfrac{1}{2}\rho v^2 (HD) C_L \end{aligned} \tag{3.9}$$

Referring to the discussion above, the velocity (v) decreases inversely proportional to the increase in height (H). The lift and drag coefficients are only a function of Reynolds number, and remain unaltered by a change in scale. Equation 3.9 shows that the increase in the product of H*D (frontal area) is exactly cancelled by a decrease in v^2, resulting in a zero net sum gain on the lift and drag forces.

Two different force measurement techniques were considered for this project. The first measurement technique involved optically measuring the deflection of a mechanical spring. Figure 3.2 provides a simplified schematic of the concept in the flow channel. The pin fin protruded through a tight clearance hole in the channel floor and

ceiling. A viscous, Newtonian silicone oil was used to fill the gap between the pin fin and channel wall. Ideally, the Newtonian oil would prevent air from blowing out of the channel without biasing the force measurement. The concept of using silicone oil to decouple the pin fin from the channel wall was taken from DeTurris et al. [1990], who used it to measure skin friction in a supersonic combustion flow.

This optical measurement technique was founded on the ability to relate spring deflection to applied force, as in Equation 3.10.

$$F = k\delta \tag{3.10}$$

The concept used high resolution cameras and imaging software to measure the deflection of the mechanical spring. Initial estimates for the method predicted a resolution of 3.7 X 10^{-6} N, or 0.2% of the minimum expected drag force [Vlachos, 2004]. Certainly, this level of accuracy made the method an appealing alternative.

Although this methodology was never tested in actual flow conditions, bench top testing was conducted to evaluate its merit. Figure 3.3 shows the physical setup of the camera and mechanical spring bench top test. The mechanical spring was deflected by placing calibrated masses on a basket hung from the end of the spring. A Phantom V4.0 camera was used to measure the deflection of the optical target. Specifically, the camera focused in on graphite flakes glued to the optical target and photographed their location from one mass application to the next. An image was taken for every mass application, such as to create a sequence of deflection images. Each image was 512 X 512 pixels, with a physical pixel size of 7 μm. The graphite particles sprinkled on the optical target ranged in size from 100 μm to 350 μm.

The deflection of the graphite flakes was analyzed with a PIV software code, FlowIQ. The code broke each photograph into an array of windows, and used a cross correlation technique to find each window in the image of the next deflection. In this manner, the motion of the window was tracked from image to image, and the deflection of the optical target calculated [Vlachos, 2004].

Figure 3.4 provides a summary of results from four deflection tests analyzed with the FlowIQ software. Figure 3.4 shows that the method actually achieved higher

accuracy with smaller applied loads. The large experimental error realized at an applied force of 9.8×10^{-3} N was the result of too much deflection by the optical target. As shown in Figure 3.5, a significant portion of the graphite flakes moved out of the picture at this relatively high force. This had the effect of depriving the FlowIQ software of the data (in the form of graphite particles) it needed to track the target. As such, the accuracy of the calculated deflection suffered when too many of the particles moved out of the image. The accuracy at the 9.8×10^{-3} N applied force could be improved by using less camera zoom to achieve a larger physical size in the photograph [Vlachos, 2004]. This would prevent the graphite flakes from moving out of the photograph. At the lower force ranges (5×10^{-4} N to 2×10^{-3} N), the error ranged from 1% to 30%. In this range, the accuracy of the method could likely be improved by replacing the graphite flakes with a more densely spaced pattern of smaller particles [Vlachos, 2004]. The exploratory test provided encouraging results that suggested accurate measurements could be made, as long as the correct photograph and target particle size were used.

Ultimately, however, this technique was abandoned for a multitude of reasons. The first reason was the prohibitive cost of a high resolution camera. The camera used in the experiment described above cost nearly $30,000. Additionally, the optical spring method was difficult to adapt to two-dimensional force measurements. As shown in Appendix A, the measured lift and drag on the pin fin were a function of the mechanical spring pretension. A finite force was required to overcome the pretension before the spring was deflected. Quantification of this force was difficult, because it required the experimental measurement of zero deflection. As such, a better and more direct force measurement alternative was sought.

Direct force measurement using an elastic measuring device was the second technique explored. This technique made use of a sensor whose output voltage was proportional to the applied force. Figure 3.6 illustrates the basic design implemented by this project to measure the pin fin aerodynamic forces. Again, the silicone oil filled clearance hole design used by DeTurris et al. [1990] allowed the pin fin to deflect while preventing air from blowing out of the channel.

Using the force estimates obtained above, an extensive search was conducted to locate a suitable force sensor. Although several one-axis force sensors were available for

measuring forces in the range of interest, incredibly few sensors were available for measuring two-component forces. After considering the list of alternatives, the Kistler Morse DSC-6 was selected. With a full scale force limit of 2.45 N, this sensor provided two-axis measurement capability with the highest level of sensitivity and a reasonable price. Additionally, some knowledge of the sensor could be obtained by studying the work of DeTurris et al. [1990], as their work used the exact same DSC-6 sensor.

A total of ten DSC-6 sensors were ordered in support of this project. Two single axis sensors were ordered for the purpose of exploring the behavior of the DSC-6. The single axis sensors were immediately available from stock, while the two-axis sensors were approximately a ten week lead item. The eight dual axis sensors are listed by serial number in Appendix B. Appendix B provides the wiring configuration, resistor values, and current working status of each DSC-6 sensor.

3.2 General Description and Operation of Force Sensor

The sensor, which is a Kistler Morse DSC-6, makes use of a cantilever beam. A dimensioned schematic of the sensor is provided in Figure 3.7. The sensor cantilever beam, 3.18 cm long, is constructed of 17-4 precipitation hardened stainless steel. The pin fin is threaded onto the sensor using 2-56 UNC-2A threads tapped in the end of the cantilever beam. A counterbore thru hole at the base of the sensor allows the sensor to be rigidly secured to a stationary mount. Figure 3.8 illustrates the naming convention used to identify the DSC-6 sensor axes. Note that the sensor is sensitive in the x-axis and y-axis direction, but insensitive to forces applied in the z-axis.

In principle, the DSC-6 senses the applied force by measuring the induced strain at the base of the cantilever beam. Strain (ε) at the base of the beam may be related to the applied force according to Equation 3.11:

$$\varepsilon = \frac{(F * L)c}{EI} \tag{3.11}$$

The effective length of the beam, L, is the distance from the applied force to the base of the beam. The variable c represents the radius of the beam cross section, while E and I

respectively represent the material modulus of elasticity and area moment of inertia of the beam.

Strain at the base of the sensor is measured by two pairs of semi-conductor strain gauges fused to the cantilever beam. The strain gauge pairs, each pair corresponding to one axis of sensitivity, are encapsulated in silicone rubber for protection. Figure 3.9 provides a dimensioned photograph of the DSC-6 with the rubber encapsulant partially removed to expose one of the strain gauges. Note that the strain gauge is not located exactly at the base of the beam. The center of the strain gauge is approximately 2.54 cm from the tip of the sensor beam. As such, the effective beam length used in relating applied force to strain (Equation 3.11) should be 2.54 cm rather than the total distance of 3.18 cm.

Each strain gauge pair consists of two gauges located 180° apart from each other. The pair of gauges forms what is commonly known as a half bridge, type II Wheatstone Bridge. In this configuration, bending places one strain gauge in compression while the other gauge is symmetrically loaded in tension. For a cantilever beam in bending, the type II Wheatstone Bridge provides maximum sensitivity.

Figure 3.10 depicts the electrical configuration for a half bridge, type II Wheatstone Bridge. For the DSC-6 sensor, each strain gauge resistor has a resistance of $1000 \pm 100\ \Omega$. A bending stress results in an equal and opposite resistance change within a pair of strain gauges. This resistance change imbalances the bridge, resulting in a voltage potential across the circuit bridge. Equation 3.12 provides the relation between measured strain and output voltage for a half bridge, type II Wheatstone Bridge.

$$\frac{V_o}{V_e} = \frac{G\varepsilon}{2} \tag{3.12}$$

In Equation 3.12, V_e represents the excitation voltage applied to the Wheatstone Bridge, while V_o represents the output voltage across the bridge. The measured ratio of these voltages is proportional to the mechanical strain. Equation 3.4 shows that the gauge factor, G, is also directly proportional to the output voltage. Increasing the strain gauge factor increases the sensitivity of the sensor. The DSC-6 takes advantage of this principle

by using semiconductor strain gauges that have a gauge factor approximately two orders of magnitude greater than traditional metal foil strain gauges.

The sensitivity of the DSC-6 can also be increased by lengthening the cantilever beam, as shown by combining Equations 3.11 and 3.12 to obtain Equation 3.13.

$$\frac{V_o}{V_e} = \frac{GLc}{2EI}F \tag{3.13}$$

Equation 3.13 may be simplified to the form provided in Equation 3.14

$$\frac{V_o}{V_e} = d(2.54 - \delta)F \tag{3.14}$$

Here, the strain gauge factor and beam mechanical properties are described by a single constant of proportionality, d. The beam length, L, is replaced by inserting the term (2.54-δ). This quantity represents the distance from the applied force to the center of the semiconductor strain gauges. The distance from the end of the beam, δ, is defined to be positive towards and negative away from the base of the beam. Finally, Equation 3.14 can be rearranged to solve for the applied force in terms of excitation voltage and beam length.

$$F = \frac{V_o}{V_e}\frac{1}{d(2.54 - \delta)} \tag{3.15}$$

Equation 3.15 provides the relationship that is published by Kistler Morse [1998] to relate the DSC-6 sensor output voltage to the applied force.

Although Equation 3.15 can be used to ideally describe the output of the DSC-6 sensor, the voltage ratio (V_o/V_e) must be corrected for cross axis effects. The output voltage of one axis is dependent on the loading of the perpendicular axis. The cross-axis effects are unexpected, as they theoretically should not exist and are not documented by Kistler Morse.

The cross axis-phenomenon was identified by studying the output voltage from both sensor axes during calibration testing. As will be described in Section 3.4, the sensor was calibrated with one axis aligned parallel with gravity and the other axis perpendicular to gravity. The perpendicular axis should have theoretically had zero voltage output, as there was no loading in that direction. The results of Figure 3.11, however, show that a voltage was produced in the perpendicular axis. Figure 3.11 plots the output voltage ratio of the perpendicular axis to the gravity aligned axis for four different sensor axes (on two different DSC-6 sensors).

Two key observations can be made from Figure 3.11. First, the cross axis sensitivity is not consistent between sensors, or even between axes on the same sensor. Second, the ratio of the output voltage in the perpendicular axis to the gravity aligned axis is very nearly constant for a given sensor axis. This is true except at low force applications. It is believed that the ratios at the low forces deviate from the constant value due to insufficient measurement resolution. Inspection of Figure 3.11 shows that the voltage ratio begins to deviate below an applied force of approximately 5×10^{-3} N for all four curves. This force corresponds to a voltage output on the order of 1×10^{-6} V in the perpendicular axis. A voltage this small is difficult to accurately measure, and likely leads to the apparent ratio change at the low forces.

The fact that the ratio of outputs between the perpendicular and parallel axes is constant suggests that cross-axis effects can be nulled by subtracting a fraction of the aligned axis' output. Equation 3.16 provides an equation for the linear correction of cross axis effects in the sensor x and y axes.

$$\mathrm{X-axis}: \frac{V_x}{V_{ex}} = \frac{V_{ox}}{V_{ex}} - \xi \frac{V_{oy}}{V_{ey}}$$
$$\mathrm{Y-axis}: \frac{V_y}{V_{ey}} = \frac{V_{oy}}{V_{ey}} - \psi \frac{V_{ox}}{V_{ex}} \qquad \text{(Equation 3.16)}$$

The cross-axis correction coefficients, ξ and ψ, can be experimentally determined from calibration testing (as described in Section 3.4). Equation 3.17 provides the definition of ξ and ψ.

$$\xi = \frac{V_{Ix} / V_{ex}}{V_{oy} / V_{ey}}$$

$$\psi = \frac{V_{Iy} / V_{ey}}{V_{ox} / V_{ex}} \qquad \text{(Equation 3.17)}$$

V_{IX} represents the voltage induced in the x-axis when a load is applied solely to the y-axis. Conversely, V_{IY} represents the voltage induced in the y-axis when a load is applied solely to the x-axis. Simply put, the ξ and ψ coefficients represent the voltage induced in the unloaded respective sensor axis as a percentage of the voltage in the loaded perpendicular axis. The corrected voltage ratios provided by Equation 3.16 are the values that should be substituted into Equation 3.15 to calculate the applied force.

The cross-axis phenomenon is not believed to be caused by electrical cross talk between the two sensor axes. To prove this theory, the sensor can be "electrically forced" by unbalancing the Wheatstone Bridge with the potentiometer. This induces a bridge voltage in one axis of the sensor without applying a physical force to the sensor. The results of the test show that a large induced voltage in one axis of the sensor has a negligible effect on the other axis. Thus, electrical cross talk is not the reason for the induced voltage in the perpendicular axis.

Angular misalignment by the user was ruled out as the cause of the cross talk by uninstalling and re-installing the DSC-6 sensor multiple times. Each installation resulted in approximately the same cross talk phenomenon, suggesting that the user installation of the DSC-6 sensor was not the cause for the induced voltage.

Thus, it is believed that the cross axis sensitivity is a mechanical, strain induced phenomenon. It is likely that the induced cross axis output is caused by strain gauges that are not installed exactly parallel to the axis of the DSC-6 beam. Because the cross talk cannot be eliminated from the sensor output, the effects are analytically negated by Equation 3.16.

The DSC-6 sensor is sensitive to several environmental factors. First, the semi-conductor strain gauges used on the DSC-6 are extremely temperature sensitive. Kistler

Morse reports that the temperature sensitivity of the DSC-6 is approximately 0.054%/°C/full scale loading [Kistler, 1998]. With respect to the estimated minimum drag force, this translates into an 86% change in sensor output for a 1°C change in temperature. Fortunately, the sensor temperature can be controlled to variations much less than 1°C. Temperature effects also indirectly limit the sensitivity of the DSC-6 sensor. Although Equation 3.15 shows that increasing the bridge excitation voltage increases the sensitivity of the sensor, increased excitation voltages result in increased power dissipation within the sensor strain gauge resistors. This power dissipation manifests itself as heat generation, leading to temperature increases.

Figure 3.12 summarizes a series of calibration tests conducted with a one-axis DSC-6 sensor at three different excitation voltages (2V, 5V, and 10V). The test results showed that the 2V excitation performed slightly better than the other excitation voltages. This option generated the least amount of heat among the tested voltages, approximately 0.004 W for a two axis sensor. Because of its superior performance, the sensor was powered with 2V of excitation (each axis) throughout this project.

A second environmental effect on sensor output is light exposure. Although this sensitivity is currently neither documented nor understood, the DSC-6 sensor output is a function of the incident light intensity. Changing intensities in light level result in changing output voltages from the sensor. This phenomenon is highly dependent on the magnitude of the light level change, and the individual strain gauge pair. Conversely, the degree of light sensitivity appears to be independent of the bridge excitation voltage and applied force. This is indeed fortunate, because it means the sensor need not be calibrated and tested at the same light intensity. As long as the light level is constant during use, the light presents only a bias error that can be nulled before conducting the test or calibration. Kistler Morse engineers are unable to explain this unexpected sensor behavior.

To illustrate the effect of light on sensor output, Figure 3.13 graphs sensor output vs. time for a sensor drift test. The test is conducted by covering the calibration stand with a sheet, turning off the lights, and allowing the sensor to drift over night. The next morning, the lights are turned on and the cover sheet is removed. Figure 3.13 shows that the sensor output jumps by 7.0×10^{-4} N and 9.1×10^{-4} N, respectively, when the

calibration stand is covered and uncovered with the sheet. Referring to Figure 3.1, removing the cover sheet changes the output by 43% of the expected minimum drag. Smaller output changes are realized when the lights are turned off and on with the sheet still covering the calibration stand. It is believed that the cover sheet does not block 100% of the light from reaching the sensor. Thus, when the lights are turned off, the light level under the sheet changes. This test also proves that the change in sensor output is not due to electrical noise. The cover sheet is made of cloth, which is a dielectric. Because dielectric materials are transparent to electromagnetic waves (electrical noise), the sheet cannot shield the DSC-6 sensor from the electrical noise in the room. Thus, the output voltage change is not induced by electrical noise.

Further proof is offered by shining a battery operated flashlight on the DSC-6. Because the flash light is a DC circuit, it cannot impose electrical noise on the DSC-6 sensor. Passing the flashlight beam over the sensor results in an output voltage change. Switching which side of the sensor that the light beam is incident upon switches the polarity of the voltage change. This phenomenon is observed to occur with the flash light greater than 5 m away from the sensor, eliminating the possibility that the heat generated from the flash light causes the voltage change.

Another parameter affecting sensor performance is the sensor's forcing history. Kistler Morse suggests "exercising" the DSC-6 sensor to full scale range ten times in each axis prior to conducting a test. This pre-test exercise is intended to minimize hysteresis effects in the sensor. However, this exercise activity results in significant changes in sensor heat generation. The change in heat generation results from the resistance change in the strain gauges under the varying load. Consequently, significant drift in the sensor output is experienced for up to 1.5 hrs after completion of the anti-hysteresis exercise. Figure 3.14 provides a representative sensor output immediately following a full scale deflection of the sensor. Note that the drift rate is relatively high (1×10^{-4} N/min) immediately after the load is released from the sensor. The rate then steadies to a value of 4.4×10^{-6} N/min after the heat flux has reached steady state. The sensor output must be carefully scrutinized before beginning a test. The user should study the voltage output for at least 5 minutes prior to testing, and ensure the sensor drift is insignificant compared to the expected sensor output.

Drift testing of the sensor output was conducted on several sensors. Once the above listed environmental factors were eliminated, no sensor was found to drift at steady state by more than 7.0 X 10^{-6} N per minute. Equivalently, the drift rate was less than 0.3% per minute of the minimum expected drag force. Thus, the steady state drift rate was deemed acceptable.

Because the sensor output voltage is as small as 12 μV at low flow rates, noise reduction and electrical shielding are important considerations. The DSC-6 sensor is connected to the SCXI signal conditioning equipment via Alpha 6010C SL005 cable. Figure 3.15, Figure 3.16, and Figure 3.17 illustrate how the DSC-6, Alpha cable, and SCXI signal conditioning equipment are connected. Figure 3.15 provides an illustration of the DSC-6 and Alpha cable to define the electrical connection naming convention. The naming convention for the SCXI 1314 terminal block used in this thesis is printed on the SCXI 1314 circuit board, and is not provided here. Figure 3.16 is an electrical schematic showing how the Alpha cable is wired to the DSC-6 sensor. Figure 3.17 provides an electrical schematic showing the connection between the Alpha cable and the SCXI 1314 terminal block. Although it is possible to determine which sensor leads correspond to a single axis (pair of strain gauges), it is not possible to determine which side of the cantilever beam that pair of strain gauges is fused to. As such, Figure 3.17 provides two different configurations for connecting the Alpha wire to the SCXI 1314. The DSC-6 should be connected in whichever configuration (nominal or inverse) yields a positive voltage when the sensor is deflected in the positive axis direction (as defined in Figure 3.8). If the nominal wiring configuration yields a negative voltage for a positive deflection, the leads can be switched to the inverse configuration to yield a positive output.

Each sensor axis requires its own individual cable. (Although Figure 3-16 only provides a diagram for connection to one axis of the DSC-6 sensor, the other axis may be connected to the second Alpha cable in exactly the same manner.) Within a single cable are three individually shielded, twisted pairs of 22 AWG wires. By using twisted pair wires, electromagnetic noise is minimized. Electrostatic noise reduction is achieved by twisting the shielding from all three wire pairs together, and draining them to ground on the signal conditioner end of the cable. As a means of further noise reduction, a drain

wire is attached to the aluminum sensor mount. The other end of the drain wire is grounded to the SCXI 1000 chassis, thereby grounding the mount and lead wire shielding to the same voltage plane.

3.3 Data Collection Equipment and Methodology

Selection of an adequate data acquisition system is another important aspect of developing the force measurement methodology. The key parameter for selecting signal conditioning equipment is Wheatstone Bridge completion. The signal conditioning equipment must provide: a stable excitation voltage to power the Wheatstone Bridge, precision resistors to complete the static arm of the Wheatstone Bridge, and a potentiometer to balance the Wheatstone Bridge. The bridge balance requirement is particularly difficult for the DSC-6 sensor, as the strain gauge resistors are only matched to within ±10%. This means that the Wheatstone Bridge may be unbalanced by up to ±5% of the input voltage due to sensor gauge mismatch.

Two different signal conditioning systems were considered for this project. The first system, the Vishay Model 2310 signal conditioner, was suggested by Dr. Schetz [2004]. Dr. Schetz had considerable experience working with the DSC-6 sensor through his skin friction studies with DeTurris et al. [1990] and several subsequent projects. Dr. Schetz [2004] suggested that the Model 2310 worked well with the DSC-6 sensor in his more recent skin friction studies.

The Vishay Model 2310 is a full feature signal conditioner commonly used in strain gauge experiments. The signal conditioner is capable of providing up to 10V of excitation voltage (more than enough for our application), but only capable of balancing the Wheatstone bridge to within ± 1.25% of the excitation voltage. For a single DSC-6 sensor, the cost of the Vishay Model 2310 was approximately on par with the competing National Instruments SXCI system (described below). However, expansion of the signal conditioning equipment to allow for more than one sensor is prohibitively expensive at a price of $3000 per sensor.

The National Instruments SCXI 1520 is the second signal conditioning system that was considered. The SCXI 1520 can provide a Wheatstone Bridge balance range of ±4% of the input voltage. Additionally, a SCXI 1314 terminal block bolted to the front

of the SCXI 1520 provides an economical means of connecting up to eight channels (four DSC-6 sensors). These features, coupled with the ability to seamlessly integrate the signal conditioner with the National Instruments DAQ hardware and software, make the SCXI signal conditioner an obvious choice. The SCXI 1520 signal conditioner and SCXI 1314 terminal block are housed in a SCXI 1000 chassis. Two additional SCXI 1102 signal conditioners with attached SCXI 1303 terminal blocks are adjacently housed in the SCXI 1000 chassis. These signal conditioners are used to obtain temperature and pressure data, as described in Chapter 4.

The National Instruments PCI-6280M DAQ card provides 18-bit resolution for analog to digital conversion. The 6280M is a new product offered by National Instruments that takes advantage of new chip architecture to provide increased resolution at a lower cost. The 6280M DAQ card is housed in a Dell 4550 Dimension computer with a 2.4 GHz Pentium 4 processor and 1.5 GB of RAM.

Virtual instrument modules, created and controlled by Labview 7.1 software, provide explicit control over nearly every aspect of the test. Excitation voltage, bridge completion, signal filtering, and data collection parameters are easily constrained by using the software. All data is sampled at a rate of 1.0×10^3 samples per second. The 1.0×10^3 samples are then averaged to provide a single data point for one second. For example, a 60 second sampling period yields 60 data points, each data point representing the average of 1.0×10^3 samples over the duration of that second.

3.4 Sensor Calibration Methodology and Data Reduction

In order to obtain the d_x, d_y, ξ, and ψ coefficients for each sensor, the sensors have to be individually calibrated. This section describes how sensor calibration is conducted and the data reduction methodology used to obtain the desired coefficients.

To eliminate the detrimental environmental effects discussed in Section 3.2, calibration tests are conducted inside the wooden calibration shelter shown in Figure 3.18. The calibration shelter is constructed of a wooden two by four frame with a 0.476 cm thick plywood skin. Perhaps the most important function of the calibration shelter is to prevent air currents from swaying the mass basket while suspended from the DSC-6 sensor. Any attempt to calibrate the DSC-6 sensor without eliminating the air currents

will result in transient outputs that contaminate the calibration. The calibration shelter is also effective at maintaining a constant light level, mechanically damping ground-borne and acoustical vibrations, and thermally damping small fluctuations in the ambient air temperature.

Figure 3.19 shows the calibration setup inside the shelter. The DSC-6 sensor and surrounding silicone well are mounted to a Lexan plate in exactly the same manner as they mount to the test section floor. The Lexan plate is suspended from a Unistrut frame to provide vertical clearance for the hanging masses. An aluminum calibration beam, with multiple grooves cut in it, is threaded onto the DSC-6. A mesh basket, constructed of fish netting and nylon string, is then hung from the calibration beam. The effective length of the sensor cantilever beam can be varied by hanging the mesh basket in the different grooves. The weight of the aluminum calibration beam (0.83 g) and the mesh basket (0.52 g) are nulled from the sensor output by re-balancing the Wheatstone bridge (via potentiometer adjustment). Figure 3.19 also shows a sheet metal trough attached to the bottom of the Lexan plate. The purpose of the trough is to prevent silicone oil that leaks out from around the DSC-6 beam from dripping onto the mesh basket. A drop of silicone on the basket would increase the mass of the basket and invalidate the calibration test.

Although not clearly visible in Figure 3.19, the Unistrut calibration frame is suspended on a vibration isolation system. Figure 3.20 shows the isolation system, constructed of a series of layers of felt and foam pads. This isolation system is designed to damp the ground borne vibrations present in the VTExCCL laboratory. Disturbances such as tables being slide across the room or moving the drain covers is clearly visible in the DSC-6 sensor output without the isolation system in place. These disturbances are not apparent in the output when the calibration frame is suspended on the isolation system.

Figure 3.21 provides a flow chart detailing the steps used to conduct a calibration test. The DSC-6 sensor is calibrated by hanging ANSI/ASTM E617 Class 6 masses from the sensor beam. The Class 6 masses provide an acceptable level of accuracy at an affordable cost. At a 95% confidence interval, the uncertainty in a Class 6 200 mg mass (equivalent cylinder drag force at $Re = 7.5 \times 10^3$) is 0.05%. The uncertainty in the

calibration mass will contribute negligibly to the overall uncertainty in the force measurement when compared to other sources.

A variety of different sensor angles are used to calibrate the DSC-6 sensor. To sample d_x and ψ (reference Equation 3.16 and Equation 3.17), the masses are hung from the sensor with the x-axis aligned with vertical gravity. Conversely, d_y and ξ are obtained by aligning the sensor y-axis with gravity. Tests conducted with both axes rotated askew to gravity, or with different beam lengths, are used to gain confidence in the calibrated quantities.

The masses hung from the DSC-6 sensor are selected and applied per the guidelines of ASTM E74 [2002]. The document recommends calibrating over a range of forces above and below the expected force range to be measured. The applied masses should be spaced such that a calibration mass is applied for every 10% of the chosen force range. No less than 30 force applications, at least ten of which are different, should be applied [ASTM, 2002]. Accordingly, Table 3.1 provides the sequence of masses applied to the DSC-6 sensor to calibrate for the expected cylindrical pin fin force range. A sequence of 17 masses is applied to the DSC-6 sensor during one calibration test. The test is conducted at least twice, in order to exceed the 30 application minimum.

It is worth noting that the calibration masses are only applied in ascending order (from lower mass to higher mass). Experience with the DSC-6 sensor has shown that this calibration method leads to the most accurate results. The reason for which is related to the zero load bridge balance and sensor drift. The zero load bridge balance refers to the output voltage from the sensor when no load is applied (V_{zero}). This voltage is subtracted from the output voltage (V_o) to achieve the corrected voltage (V_{o_corr}). In this manner, the bias error associated with the finite sensor output at zero load can be removed. As shown in Figure 3.21, the sensor zero load reading is taken prior to conducting the calibration test. Because the forces are applied in increasing order, the smallest forces are applied temporally closest to the zero load measurement. As such, the sensor output does not have much time to drift.

As discussed in Section 3.2, the DSC-6 sensor steady state drift rate is less than 7.0×10^{-6} N/min. By the end of the calibration test, which takes approximately 2 hrs to complete, the sensor output could drift in output by up to 9×10^{-4} N. This drift, although

insignificant to the higher forces applied in the calibration sequence (1.96×10^{-1} N), is actually greater than the lowest applied force (4.9×10^{-4} N). Thus, the lowest forces must be measured as soon as possible after the zero load voltage is recorded.

The order of the calibration test should not be switched to apply the masses in descending order with the zero-load voltage then read upon test completion. Recall the discussion from Section 3.2 regarding the increased sensor drift rate after exercising the sensor to full scale (to remove hysteresis effects). The changing load on the sensor increases the drift rate by increasing the amount of heat generated in the strain gauge resistors. This same effect would apply to a calibration test, where the forces change as different masses are hung and removed from the DSC-6 beam. If the zero-load voltage is recorded upon completion of the calibration test, the data will be subject to high drift rates. Consequently, the post test zero load voltage reading will contain more error (due to increased drift) than the pre-test zero load voltage. This error propagates through all of the measurements, leading to decreased calibration accuracy.

ASTM E74 validates calibration by ascending mass application only if the sensor is to measure forces that are applied in an increasing manner. In actual testing, this requirement is satisfied because the drag force increases as the blower accelerates from zero velocity to steady state.

Calibration of the DSC-6 is conducted in such a way as to replicate test conditions as much as possible. For this reason, all calibration tests are completed with the DSC-6 sensor submerged in silicone oil. Figure 3.22 compares the relative accuracy between sensor output and applied force for calibration tests conducted with silicone oil ("wet") and without silicone oil ("dry"). Calibration with the sensor submerged in silicone oil appears to slightly improve the accuracy of the sensor for forces below 4×10^{-3}N, but has no apparent effect on accuracy above that value. Although not proven, the logical hypothesis for the improved accuracy at the lower forces is that the silicone oil provides additional damping of ambient vibrations above the protection afforded by the calibration shelter.

Note that the flowchart in Figure 3.21 specifies that 360 seconds are allowed to elapse between placing the calibration mass on the sensor beam and the start of data collection. Experimentally, it was found that up to 360 seconds are required to allow the

sensor output to come to steady state during an actual flow / force test (the reasons for which are discussed in Section 3.4). This dwell time is duplicated in calibration testing for the sole purpose of matching test conditions.

Figure 3.23 provides a flowchart for the data reduction methodology used to calculate d_x, while Figure 3.24 depicts the methodology for calculating ψ. (In the interest of brevity, flowcharts for d_y and ξ are not provided. The calculation of d_y and ξ can be surmised by simply switching the x and y variables in Figures 3.23 and 3.24.) In short, the sensor proportionality constant (d_x) is obtained by performing a linear regression of the x-axis sensor output with respect to the applied mass sequence. The cross axis sensitivity, ψ, is calculated at each mass application according to Equation 3.17. The median ψ value of the test sequence is selected as the representative test value. The median is a better indicator of central tendency than the mean, as the calculated values of ψ at low forces are generally skewed due to measurement resolution issues (refer to the discussion in Section 3.2 and Figure 3.11). These outlying values at the low end of the range distort the mean but do not affect the median. The "post test zero" reading is not used in the data reduction method for the reasons discussed earlier regarding increased sensor drift rates after dynamically loading the sensor.

A summary of calibration results for sensor serial number 5117 is now presented. Although the performance of several sensors was studied over the course of the project, this sensor represents the culmination of the knowledge gained about the sensor's behavior. Appendix B lists the current status of sensor 5117 as damaged. The x-axis of the sensor was damaged during a disassembly process to remove the sensor from the test channel.

Table 3.2 summarizes the 14 calibration tests that were performed over a one week period on sensor 5117. As shown by Table 3.2, the sensor calibration was conducted at a variety of angles and beam lengths. Table 3.3 summarizes the values obtained for ξ and ψ from tests 3-6 and 1-2 (respectively). Averaging the results from all tests, ξ was measured to be -0.0938, and ψ was measured to be 0.1135. Note that cross axis effects decrease the magnitude of the x-axis output while they increase the magnitude of the y-axis output.

Calibration tests 7 – 12 were conducted with both sensor axes rotated askew to gravity. For these calibration tests, the values of ξ and ψ obtained in tests 1 – 6 were used to correct for cross axis effects. Tests 7-10 were performed at a 45° angle with beam lengths that ranged from 2.45 cm to 3.40 cm. Tests 11 and 12 were conducted with the x-axis rotated 25° from vertical (y-axis 65° from vertical) at beam lengths of 2.79 cm and 3.25 cm respectively. Table 3.4 summarizes the d_x coefficients obtained from all calibration tests. Similarly, Table 3.5 lists all d_y coefficients obtained from testing. Averaging the sum of all values, d_x was calculated to be 0.1036 (V/V-kg-cm) ± 0.4% while d_y was found to be 0.0995 (V/V-kg-cm) ± 0.4%. Both values are reported at a 95% confidence level. The relatively small confidence interval (± 0.4% for both coefficients) provides assurance that calibration tests are repeatable. Additionally, an R^2 value of 1.000 was achieved for each calibration test. This provides concrete support that the linear curve produced for each calibration test is appropriate.

Plots of relative error between the DSC-6 sensor displayed force and the calibration force are provided in Figures 3.25 – 3.28. Figure 3.25 plots the absolute relative error as a function of applied force for the sensor x-axis. The plot shows that the relative error between the measured force and the actual force is never more than 4% for forces above the minimum expected cylinder drag force. The measurement error decreases monotonically towards zero as the calibration forces are increased. Figure 3.26 provides exactly the same relative error data as Figure 3.25, but the x-axis is changed to an equivalent Reynolds number. The equivalent Reynolds number is the channel Reynolds number at which an infinite cylinder would produce the same drag force as the applied calibration force. This x-axis scale is particularly useful for determining the lowest flow rate for which the DSC-6 can be used to measure drag.

Figure 3.27 plots the relative error results for the y-axis calibration tests as a function of applied force. Reference to Figure 3.27 shows that Test 13 and Test 14 produced excessively large errors (up to 45%) in the low force ranges. Table 3.2 shows that both these calibration tests were conducted with the y-axis rotated 65° from vertical. As such, the effective sensitivity of the y-axis was reduced. This reduction in sensitivity lead to the larger measurement error that is shown in Figure 3.27 for tests 13 and 14. Note,

however, that the measurement error of tests 13 and 14 fall back in line with the other tests for forces larger than 1 X 10^{-3}N.

Figure 3.28 plots the relative error for the y-axis calibration tests again, with the outlying data points from Test 13 and Test 14 removed. Figure 3.28 shows that measurement errors larger than 4% were not experienced in the force ranges above the minimum expected drag value. As with the x-axis, the measurement error decreases towards zero as the applied calibration forces increase.

The discussion above is intended to provide the reader with a sense of the quality of calibration that can be achieved with the DSC-6 sensor when the environmental factors are properly controlled. A formal uncertainty analysis is provided in Section 3.6

3.5 Testing Methodology and Data Reduction

Attention to detail is required to achieve accurate lift and drag measurements. The flow tests, as of yet, are not automatic. The user cannot simply turn the flow on, record measurements, and then analyze the data. Special consideration must be given to the conditioning of the sensor and the silicone oil before the test begins. User interaction is required during the test to maintain a constant flow temperature. Additionally, careful inspection after the test is required to ensure the validity of the measurements. This section will discuss the key points in conducting a successful force measurement test.

Before conducting a test, the silicone oil in both the top and bottom reservoirs is inspected. The height of the silicone oil in the top reservoir must be even across the entire reservoir. If a height imbalance exists from one side of the reservoir to the other, the resultant hydro-static pressure imbalance will yield a net force on the pin fin. This problem is easily corrected by allowing the viscous silicone oil enough time to flow and settle to an even level. Both silicone reservoirs must be free of air bubbles. Bubbles rising through the silicone fluid apply a dynamic force to the pin fin that can be observed in the sensor output. Additionally, static bubbles in contact with the pin fin (usually found at the top of the floor silicone reservoir) present a bias error.

The effect of a static bubble in the floor silicone reservoir can be seen in Figure 3.29. Figure 3.29 plots the DSC-6 sensor output for a Re = 1.8 x 10^4 test. A sudden change in the sensor output occurred at approximately 135 seconds. The drag force

decreased by approximately 2.4 X 10^{-3}N, while the lift force decreased by approximately 8.5 X 10^{-4} N. The formation of a bubble at the leading edge of the cylinder in the floor silicone reservoir was observed to appear at approximately the same time as the step change in sensor output. The correspondence between a step change in sensor output and the formation of a static bubble in the floor reservoir was observed several times over the course of testing. In every instance, a bubble at the front of the cylinder was found to decrease the drag measurement, while a bubble at the rear of the cylinder increased the drag measurement. Thus, it was determined that a bubble in the floor reservoir induced a bias error in the measurement.

Any static bubbles in the floor reservoir are removed by squeezing excess silicone oil from the modified soda bottle (discussed in Chapter 4) into the reservoir. However, this process invariably results in excess silicone oil flowing through the pin fin gap into the channel. Excess silicone oil must be removed from the channel before the test begins. If the oil is not removed, the airflow sweeps the oil behind the pin fin, where it collects. Figure 3.30 shows how the puddle of oil collects behind the pin fin, and is drawn upwards into a bulb like shape. Figure 3.31 shows how the silicone bulb can affect sensor output. In Figure 3.31, the silicone bulb begins to form at approximately 100 seconds into the test. As the bulb grows in size, both the measured lift and drag decrease. It is believed that the silicone bulb actually makes the cylindrical pin fin more aerodynamic. The silicone bulb merges with the cylinder to approximate an airfoil shape, retarding the separation point on the cylinder and reducing the drag. The bulb continues to grow until approximately 550 seconds, when the bulb begins to oscillate in the flow. Note that the oscillation of the silicone bulb affects both the drag and lift measurements.

Removing excess silicone oil from the channel is an iterative process. Capillary forces tend to draw the oil up from the bottom reservoir into the channel. Given enough time (8 – 10 hours), the silicone oil level will come to equilibrium with the level of the channel floor. However, if too much oil is wiped away while waiting for the fluid to equilibrate, a bubble will form in the reservoir. Consequently, a delicate balance exists between cleaning the silicone oil away from the pin fin and waiting for the level of the oil to equilibrate. It is recommended that the silicone fluid be wiped away from the pin fin at

a rate of once every two hours. This cleaning schedule effectively removes excess silicone oil without producing a bubble in the reservoir.

Once the silicone oil is level with the channel floor, the sheet metal diffuser is bolted to the test section. Then, as shown in Figure 3.32, three cloth sheets are placed over the test section to shield the sensor from light. With the sheets in place, the sensor output is monitored to ensure an acceptable drift rate. Although the definition of an acceptable drift rate depends on the magnitude of forces to be measured, 1×10^{-6} V/min is a good rule of thumb to use as an acceptable drift rate. The silicone oil temperature is also monitored to ensure that the sensor is not subject to thermal transients. No general rule for an acceptable temperature drift exists, as temperature effects on the sensor are captured by studying the sensor voltage drift.

Once the sensor and silicone oil are properly conditioned, the experiment is conducted. Figure 3.33 provides a flow chart detailing the execution of the flow test. The correct blower frequency and pressure relief valve settings are always set prior to conducting the force test. Due to the sensitivity of the DSC-6 sensor and the silicone oil to the flow conditions, it is not possible to tune the flow while running the test. If the user attempts to tune the flow and static pressure in the test section while conducting the test, there is a high likelihood that the results will be ruined by bubble formation, silicone oil leakage, or poor sensor conditioning. Thus, separate runs are made to establish the correct blower and relief valve settings ahead of time.

Frictional air heating in the blower necessitates the use of a heat exchanger to cool the flow. Initially, the flow test is started with water flow to the heat exchanger turned off. (Turning the heat exchanger flow on before the air flow is detrimental, as this will make the air flow too cold to start the test.) The air flow temperature and silicone oil temperature are monitored continuously throughout the flow test. As the temperature of the flow rises, the cold water flow to the heat exchanger is adjusted. It is often necessary to increase or decrease the cold water flow to the heat exchanger several times during the course of a single experiment in order to maintain an acceptable flow temperature.

After recording 15 minutes of data from the flow test, the blower is turned off. Another six minutes are allowed to elapse before recording a second DSC-6 sensor "zero" reading. This data is recorded for reference only, and is not used in any data

reduction calculations (due to increased sensor drift). Additionally, the test section is inspected at the conclusion of the test. Specifically, the channel is examined for excess silicone oil. Any sign of a silicone puddle behind the pin fin indicates that silicone oil leaked out of the pin fin gap during the test. As discussed above, excess silicone oil in the test section channel adversely affects the test results. A check for bubbles in the silicone reservoir is also conducted. Although bubble formation is usually apparent in the sensor output, a visual check is warranted. Tests that show excessive silicone oil in the test channel, or a bubble in the reservoir, are discarded and rerun.

Figure 3.34 provides a flow chart for the data reduction methodology of the drag force component. (Again, a flowchart for the lift component is omitted in the interest of brevity. The lift force can be found by simply substituting y for x, and ψ for ξ.) In short, the applied aerodynamic forces are calculated according to Equation 3.15 after applying the cross axis correction defined by Equation 3.16. Because the ultimate goal of the test is to provide lift and drag coefficients, the measured aerodynamic forces are normalized by the product of the dynamic head and projected frontal area (refer again to Equation 3.8).

A final note regarding data analysis is in order. The entire 15 minutes of data is not analyzed. Instead, a 60 second analysis window is chosen, and the data within those 60 seconds is analyzed. The 60 second analysis window is chosen to begin as soon as the sensor output has stabilized. The amount of time required for the sensor output is not hard and fast, and appears to be dependent upon the flow rate. To help keep the data analysis consistent from test to test, 2 different guidelines for analyzing the sensor output were created.

The first guideline applies to flows of less than $Re = 1.8 \times 10^4$. Figure 3.35 shows representative sensor output data for a $Re = 1.5 \times 10^4$ flow. Figure 3.36 provides a zoomed-in-view of the data analysis window shown in Figure 3.35. Figure 3.35 shows how the sensor output first ramps up, and then drifts off for the first 360 seconds. After about 360 seconds, the output stabilizes and reaches a steady value (in the mean). This behavior in the sensor output is common for flows less than $Re = 1.8 \times 10^4$. Consistent with analyzing the data as soon as the sensor output stabilizes, the data recorded between 360 and 420 seconds is used in the data analysis for flows less than $Re = 1.8 \times 10^4$.

Flows greater than Re = 1.8 X 10^4 require a different data analysis window. Thus far, it has not been possible to stop silicone leakage out of the pin fin gap at these higher flow rates. Consequently, it is necessary to analyze the force data recorded before the effects of silicone leakage become significant. Figure 3.37 provides a typical sensor output for a Re = 3.5 X 10^4 flow. Figure 3.38 provides a zoomed-in-view of the data analysis window shown in Figure 3.37. In Figure 3.37, the sensor output ramps up and briefly stabilizes before drifting away. The increased drift rate shown in Figure 3.37 is due to silicone leakage and collection behind the pin fin, as discussed above. The data analysis window should be taken where the output is stable, approximately from 90 to 150 seconds. This behavior is common for flows greater than Re = 1.8 X 10^4. Thus, for flows greater than Re = 1.8 X 10^4, the data analysis window spans the sensor output from 90 to 150 seconds.

Originally, the data analysis window was chosen to be 60 seconds long by estimating how many data points needed to be averaged to obtain a representative measurement. Admittedly, this was an educated guess, but it was not possible to perform a statistical analysis ahead of time to determine how long of a sampling window was needed. After several tests were conducted, an analysis was performed to prove that the 60 second analysis window was sufficient. For each Reynolds number in the test sequence, a single test was chosen to analyze. Five different sampling durations were considered for every test: 60 sec, 120 sec, 180 sec, 240 sec, and 300 sec. For each sample duration, the average drag coefficient was calculated, along with a 95% confidence interval. The confidence intervals were normalized by the averaged drag coefficients, and plotted in Figure 3.39. Figure 3.39 shows that the normalized confidence interval is less than 1% for all Reynolds numbers. As the sample size (duration) is increased, the confidence intervals decrease, but not enough to warrant increasing the sample duration from 60 seconds. Increasing the sample duration would only serve to subject the data to more sensor drift or possible effects from silicone leakage out of the pin fin gap.

3.6 Experimental Uncertainty

Uncertainty analyses were conducted on the drag coefficient (C_D), lift coefficient C_L), and channel Reynolds number (Re) according to the methodology of Moffat [1988]. This technique entails reducing the desired calculation down to a function of only directly measurable quantities. The partial derivative of the reduced equation is then calculated with respect to each measured quantity, and multiplied by the uncertainty in that single variable. The root sum square of all terms is the overall uncertainty of the calculated result, as shown in Equation 3.18.

$$u_R = \sqrt{\left\{\sqrt{\sum_{i=1}^{N}\left(\frac{\partial R}{\partial X_i}B_i\right)^2}\right\}^2 + \left\{\sqrt{\sum_{i=1}^{N}\left(\frac{\partial R}{\partial X_i}S_i\right)^2}\right\}^2} \qquad (3.18)$$

The uncertainty analysis was conducted on representative tests at the lowest (Re = 7.5 X 10^3) and highest flow rates (Re = 3.5 X 10^4), providing bounding uncertainty estimates. Table 3.6 summarizes the results of the uncertainty analyses at a 95% confidence level. Details regarding the uncertainty estimates are provided in Appendix C.

Studying Table 3.6, one immediately notices that the lift coefficient uncertainty is tremendously high for both the 7.5 X 10^3 flow (± 48%) and the Re = 3.5 X 10^4 flow (± 38%). However, the high uncertainty must be taken in context with the small magnitude of the lift coefficient. Theoretically, the lift coefficient is zero for a cylinder. It is difficult, experimentally, to accurately measure a zero magnitude force.

The estimated uncertainty in the drag coefficient at Re = 7.5 X 10^3 is ± 6.5%. Reference to Appendix C shows that the majority of the uncertainty is due to an analytical uncertainty in the linear regression analysis and dimensional uncertainty in the channel height.

The estimated uncertainty in the drag coefficient at the Re = 3.5 X 10^4 is ± 4.8%. Appendix C shows that the uncertainty at Re = 7.5 X 10^3 is driven by uncertainty in the channel height and sensor rotation angle.

Initially, the uncertainty in the drag coefficient for both flows seems unrealistically low. However, three other data sources provide points of reference to compare with the calculated estimate. The first data source is provided by DeTurris [1992], who uses the same DSC-6 sensor and a similar silicone oil configuration as this project. DeTurris [1992] quotes the uncertainty in her supersonic friction factor measurements to be ±7.1%. The majority of this uncertainty stems from the temperature change resulting from the heated supersonic flow. DeTurris [1992] estimates the uncertainty due to temperature changes to be ±3% during calibration, and ±5% during actual testing. Clearly, the root sum square of the total uncertainty is dominated by these thermal effects.

This project does not suffer from the extreme thermal environments found in a supersonic combustion flow. The air temperature of the $Re = 7.5 \times 10^3$ flow only changed by 0.01°C during the entire test, while temperature of the $Re = 3.5 \times 10^4$ changed 0.2°C during the test. The uncertainty in the temperature output due to these temperature changes was estimated to be less than 0.4% for both tests. The flow temperate was an insignificant effect on measurement uncertainty for both experiments. Because the current experiment was not subject to the severe thermal differentials experienced by DeTurris, it stands to reason that uncertainty in this project was less than in the DeTurris experiment.

The second point of comparison is provided by studying the results from multiple sensor calibration tests. For each sensor calibration test, the resultant linear regression can be compared to the actual applied mass (as in Figure 3.15). A summary study of sensor calibration results shows that at an equivalent $Re = 7.5 \times 10^3$ drag force ($\mathcal{D} = 3.5 \times 10^{-3}$ N), the linear regression estimate never produces an error larger than 4% compared to the actual applied mass. For the $Re = 3.5 \times 10^4$ case ($\mathcal{D} = 0.1$ N), the calibration never errs by more than 1%. Obviously, this uncertainty is much lower than the estimated uncertainty with the pin in the flow, but the conditions in the calibration rig are ideal. The calibration test is not subject to the complications inherent to the flow test (uncertainty in air flow, uncertainty in the channel height, etc.). Thus, the flow test

uncertainty should be expected to be higher than the idealized calibration uncertainty, and the point of reference adds credibility to the flow test estimate.

The final point of reference is provided by the scatter in the actual flow test results. Table 3.7 tabulates the resultant drag coefficients from four flow tests conducted at $Re = 7.5 \times 10^3$. Table 3.7 shows that the four tests produce a spread of approximately ± 8.6% about the mean of the tests. Admittedly, this number is approximately 30% higher than the estimated uncertainty value. However, the uncertainty estimate does not account for affects due to the silicone oil / air flow / pin fin interaction. Such effects include the lip force discussed in Chapter 2 and the gap leakage of the silicone oil discussed in Section 3.2. At this time, the magnitude of those effects is unknown, and cannot be modeled in the uncertainty estimate. Because the scatter in the data is larger than the estimated uncertainty, one can conclude that the $Re = 7.5 \times 10^3$ uncertainty estimate is incomplete (lacking the affects of the silicone oil / air flow / pin fin interaction), but not unreasonable.

Table 3.8 tabulates the calculated drag coefficients from three $Re = 3.5 \times 10^4$ flow tests. Table 3.8 shows that none of the three tests exceeds 1% deviation from the mean. Thus, the scatter in the experimental results is less than the estimated uncertainty. The fact that there is less scatter in experimental results at the higher flow rates is likely due to sensor resolution. Simply put, the DSC-6 sensor can more accurately measure the higher forces produced at the higher flow rates.

Although the three reference points do not explicitly confirm the uncertainty estimate, they all add credibility. Each reference, in its own way, shows that the estimate is at least reasonable. Additional accuracy can be added to the analysis by including the effects of the silicone oil / air flow / pin fin interaction, which needs future development.

Table 3.1 Sensor Calibration Mass Application Sequence

Sequence	Nominal Applied Mass (g)	Nominal Applied Force (N)
1	0.05	4.90E-04
2	0.1	9.81E-04
3	0.2	1.96E-03
4	0.5	4.90E-03
5	0.7	6.86E-03
6	1	9.81E-03
7	2	1.96E-02
8	4	3.92E-02
9	5	4.90E-02
10	6	5.88E-02
11	8	7.85E-02
12	10	9.81E-02
13	12	1.18E-01
14	14	1.37E-01
15	16	1.57E-01
16	18	1.77E-01
17	20	1.96E-01

Table 3.2 Summary of Calibration Tests Performed on Sensor 5117

Index	Date	Angle from Vertical (°)		Beam Length (cm)	Notes / Objectives
		x	y		
1	9/24/2005	0	90	2.79	Sample d_x and ψ
2	9/24/2005	0	90	2.79	Sample d_x and ψ
3	9/27/2005	90	0	2.79	Sample d_y and ξ
4	9/27/2005	90	0	2.79	Sample d_y and ξ
5	9/27/2005	90	0	2.79	Sample d_y and ξ
6	9/27/2005	90	0	2.79	Sample d_y and ξ
7	9/22/2005	45	45	2.79	Sample d_x and d_y with known ξ and ψ
8	9/23/2005	45	45	2.79	Sample d_x and d_y with known ξ and ψ
9	9/23/2005	45	45	3.25	Sample d_x and d_y with known ξ and ψ
10	9/23/2005	45	45	2.45	Sample d_x and d_y with known ξ and ψ
11	9/23/2005	45	45	2.96	Sample d_x and d_y with known ξ and ψ
12	9/23/2005	45	45	3.40	Sample d_x and d_y with known ξ and ψ
13	9/28/2005	25	65	2.79	Sample d_x and d_y with known ξ and ψ
14	9/29/2005	25	65	3.25	Sample d_x and d_y with known ξ and ψ

Table 3.3 Summary of ξ and ψ Results for Sensor 5117

ξ				ψ		
Index	**ξ_{median}**	**$\%\Delta\xi_{avg}$**		**Index**	**ψ_{median}**	**$\%\Delta\psi_{avg}$**
3	-0.0930	-0.84%		1	0.1139	0.39%
4	-0.0957	1.98%		2	0.1130	-0.39%
5	-0.0936	-0.28%		-		
6	-0.0930	-0.86%		-		
ξ_{avg}:	**-0.0938**			**ψ_{avg}:**	**0.1135**	

Table 3.4 Summary of d_x Calibration Results for Sensor 5117

Index	Angle from Vertical (°)	Beam Length (cm)	d_x (V/V-kg-cm)	$\%\Delta d_{x\_avg}$	R^2
1	0	2.79	0.1038	0.19%	1.000
2	0	2.79	0.1037	0.08%	1.000
7	45	2.79	0.1035	-0.15%	1.000
8	45	2.79	0.1037	0.02%	1.000
9	45	3.25	0.1028	-0.78%	1.000
10	45	2.45	0.1042	0.57%	1.000
11	45	2.96	0.1033	-0.37%	1.000
12	45	3.40	0.1027	-0.86%	1.000
13	25	2.79	0.1045	0.84%	1.000
14	25	3.25	0.1041	0.45%	1.000
		d_{x_avg} (V/V-kg-cm)	**0.1036**		
		95 % Confidence Interval (±%)	**0.39%**		

Table 3.5 Summary of d_y Calibration Results for Sensor 5117

Index	Angle from Vertical (°)	Beam Length (cm)	d_y (V/V-kg-cm)	$\%\Delta d_{y\_avg}$	R^2
3	0	2.79	0.0989	-0.59%	1.000
4	0	2.79	0.0988	-0.74%	1.000
5	0	2.79	0.0988	-0.71%	1.000
6	0	2.79	0.0987	-0.76%	1.000
7	45	2.79	0.0996	0.13%	1.000
8	45	2.79	0.1001	0.58%	1.000
9	45	3.25	0.0997	0.26%	1.000
10	45	2.45	0.1004	0.91%	1.000
11	45	2.96	0.1000	0.48%	1.000
12	45	3.40	0.0995	0.04%	1.000
13	65	2.79	0.0998	0.26%	1.000
14	65	3.25	0.0996	0.15%	1.000
		d_{y_avg} (V/V-kg-cm)	**0.0995**		
		95 % Confidence Interval (±%)	**0.36%**		

Table 3.6 Summary of Bounding Uncertainty Estimates

	Calculation	Value	Uncertainty	% Uncertainty
Re = 7568	C_D	1.56	± 0.10	± 6.51%
	C_L	0.09	± 0.04	± 48%
	Re	7568	± 74	± 1.0%
	Calculation	**Value**	**Uncertainty**	**% Uncertainty**
Re = 35192	C_D	1.85	± 0.09	± 4.8%
	C_L	-0.02	± 0.008	± 38%
	Re	35192	± 317	± 0.9%

Table 3.7 Summary of Drag Coefficient Results for Re = 7500 Tests

Test Date	C_D	%Δ from Mean
11/9/2005	1.46	-3.9%
11/9/2005	1.65	8.6%
11/10/2005	1.41	-7.2%
11/13/2005	1.56	2.5%
Mean =	**1.52**	

Table 3.8 Summary of Drag Coefficient Results for Re = 35000 Tests

Test Date	C_D	%Δ from Mean
11/29/2005	1.88	0.89%
12/2/2005	1.85	-0.46%
12/13/2005	1.86	-0.43%
Mean =	**1.86**	

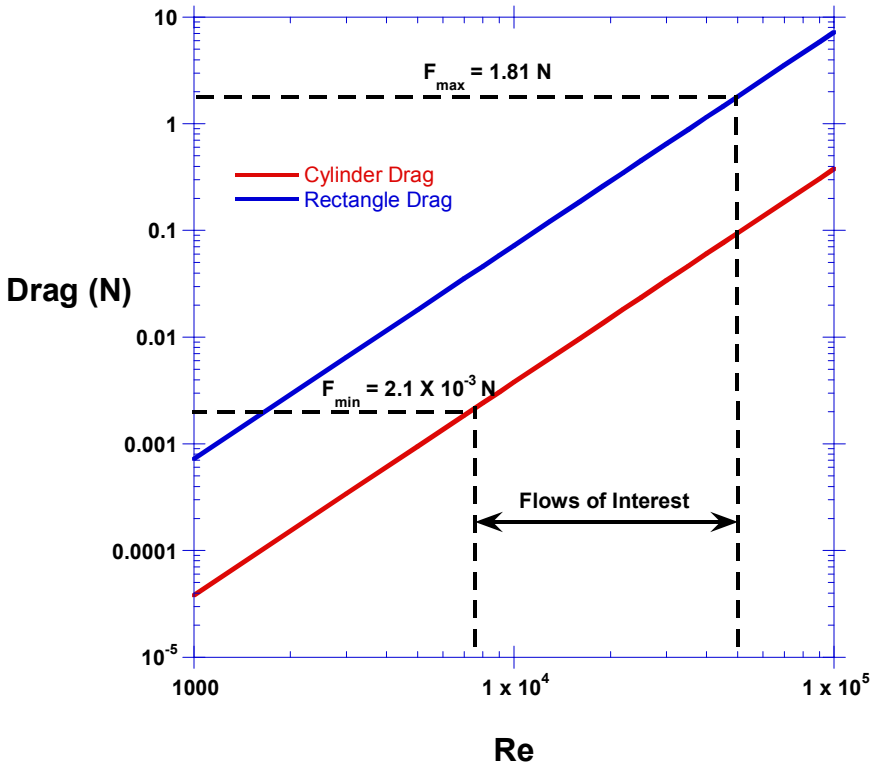

Figure 3.1 Plot of predicted drag forces on a pin fin based on an infinite cylinder and an infinite rectangle in cross flow. The flow range of interest, 7.5 X 10^3 < Re < 5.0 X 10^4, is also indicated on the graph.

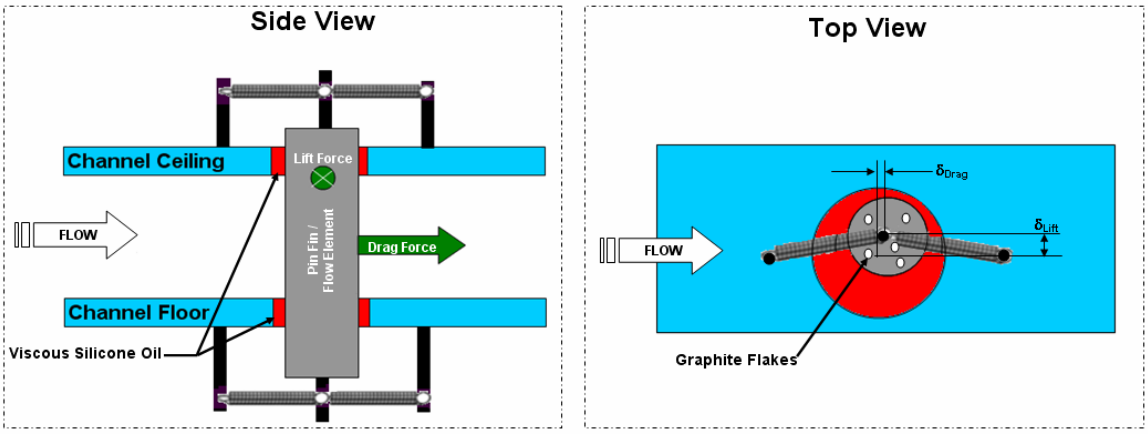

Figure 3.2 Simplified schematic showing the mechanical spring and pin fin force measurement concept. The lift and drag forces deflect the mechanical spring, as shown in the top view. The graphite flakes were used to track the motion of the pin fin.

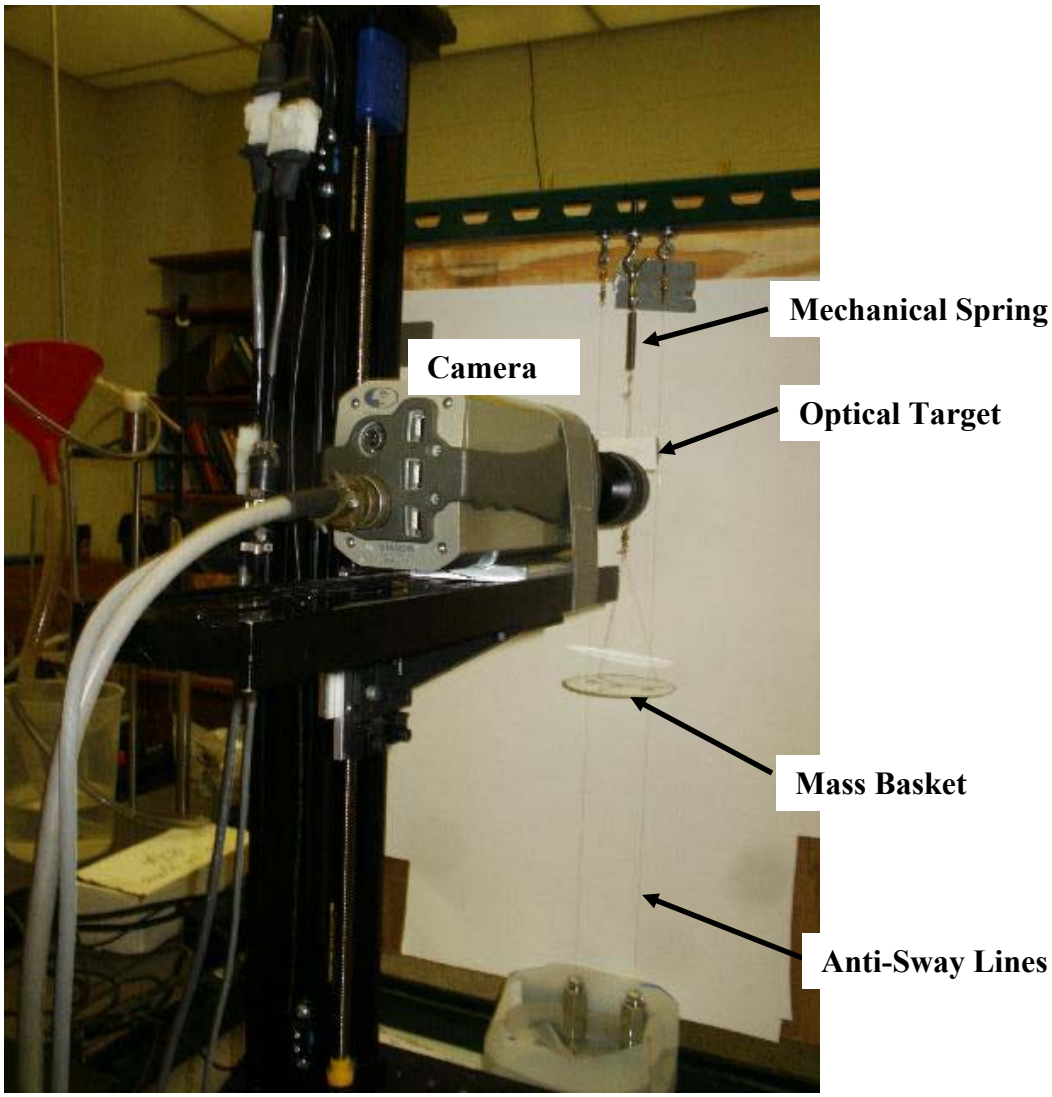

Figure 3.3 Photograph of test setup for evaluation of the mechanical spring force measurement methodology. Masses were placed on the mass basket, deflecting the spring downwards. The camera tracked the optical target, which had graphite flakes adhered to it. Anti-sway lines were added to eliminate the side to side and rotational motion of the optical target.

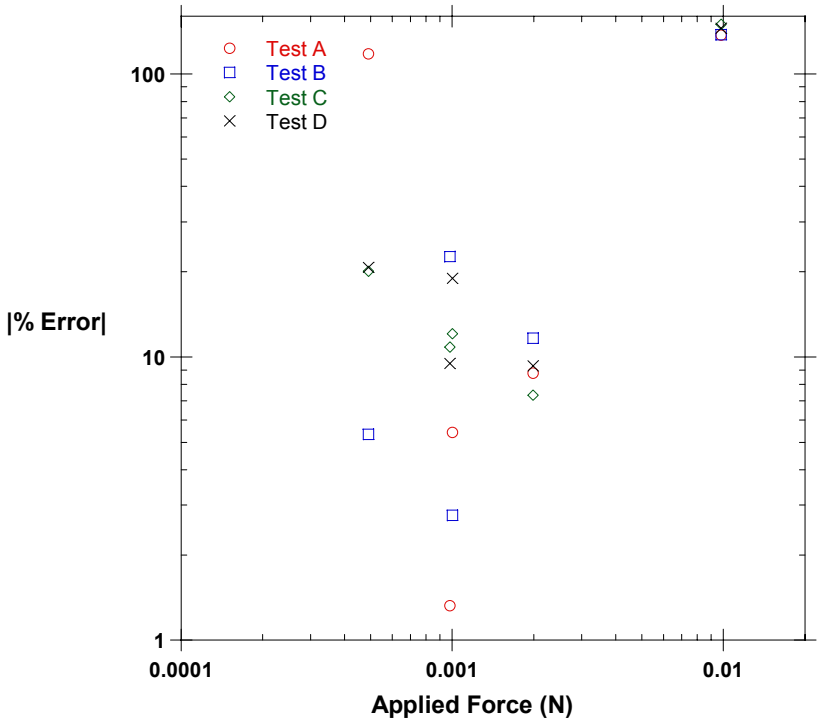

Figure 3.4 Plot of relative error (with respect to applied force) vs. applied force for the mechanical spring and camera bench top test. Results from four different tests are displayed.

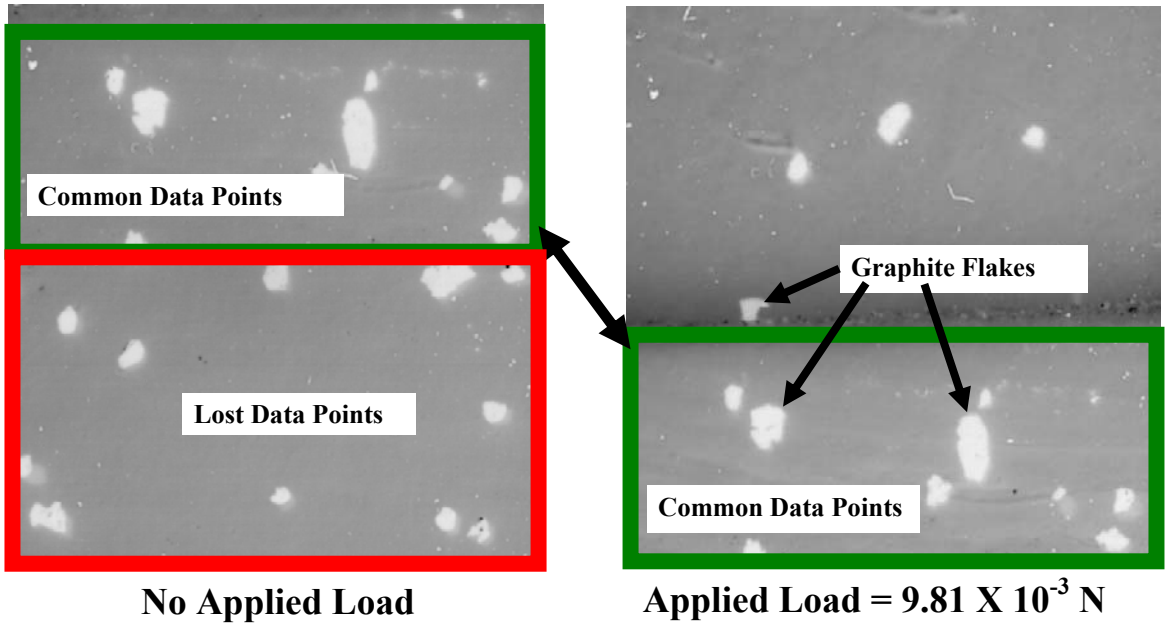

Figure 3.5 Illustration demonstrates the effect of applying too large a force for a given image size. The image on the left shows the no load photograph, with all graphite flake data points. The image on the right shows the optical target after it deflected under a 9.8 X 10^{-3} N force. This deflection is too large for the physical size of the photograph. More than 50% of the graphite flakes used to track the target were lost when they moved out of the image.

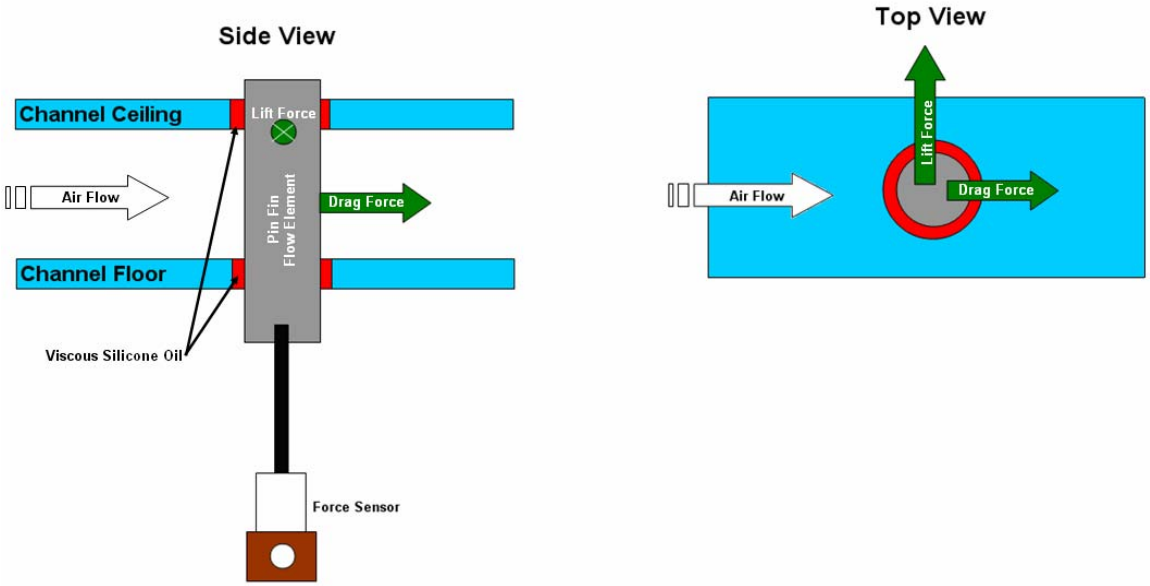

Figure 3.6 Simplified schematic of elastic force measuring device and pin fin configuration in the channel.

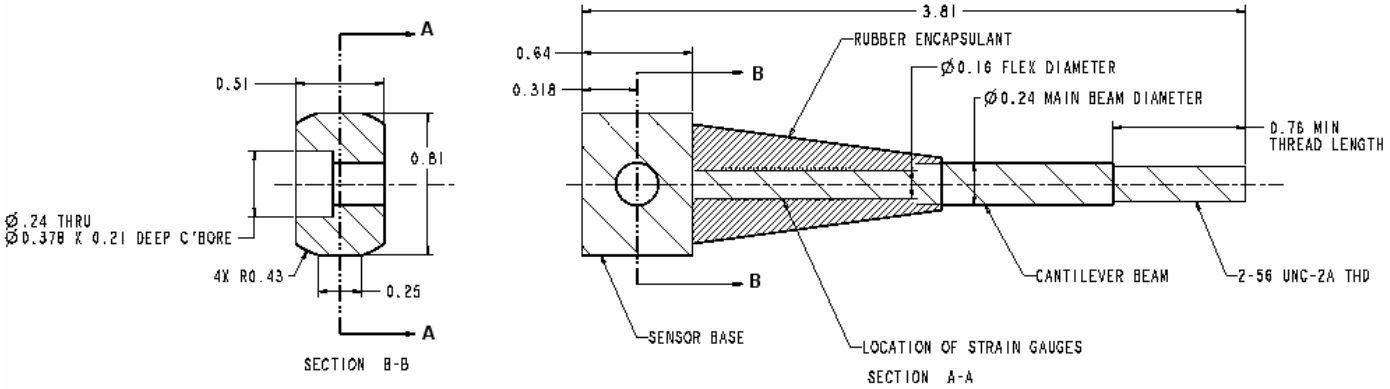

Figure 3.7 Diagram of pertinent DSC-6 sensor dimensions. All dimensions are in cm.

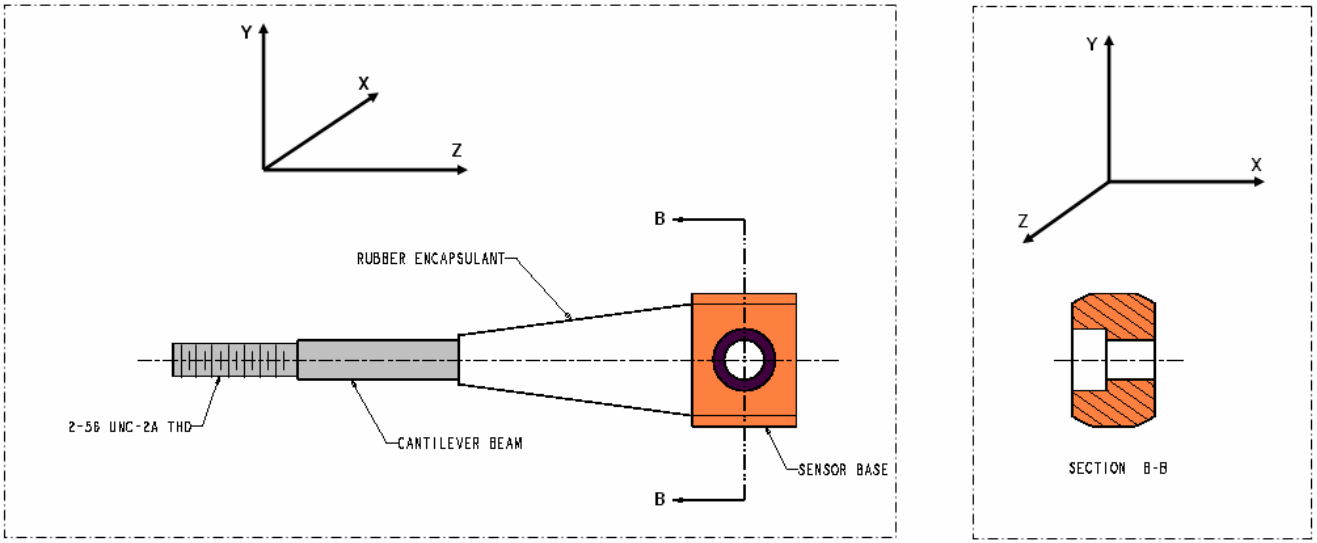

Figure 3.8 Schematic illustrating the assigned sensor axis naming convention. The diagram to the left shows the x-axis pointing into the plane of the page. On the right, the z-axis is shown pointing out of the page of the plane.

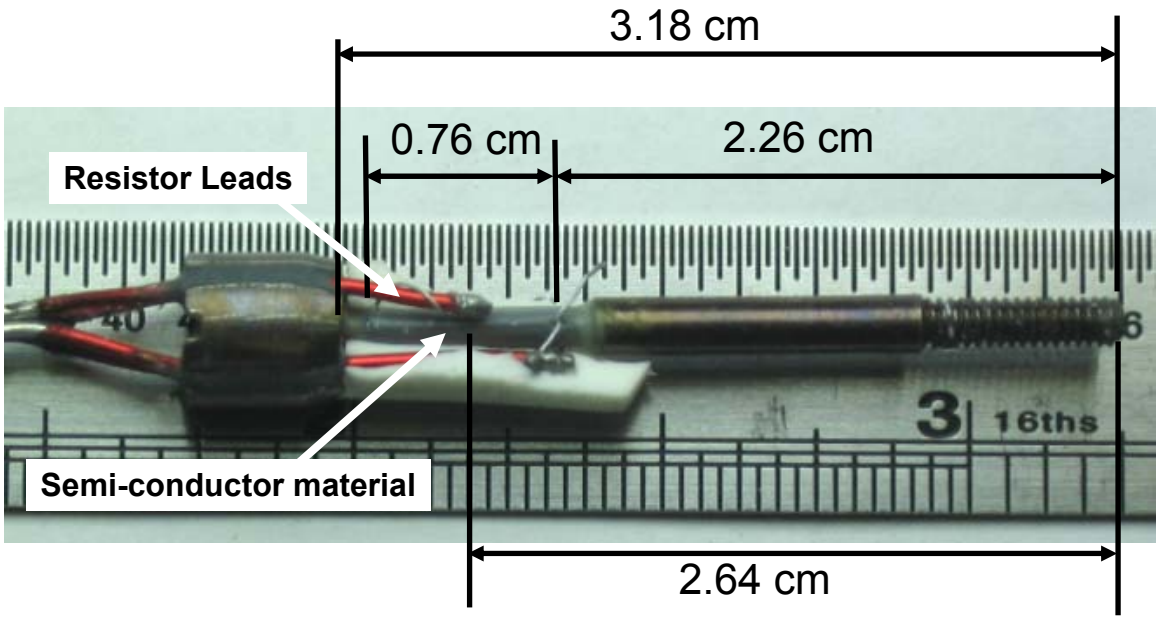

Figure 3.9 Cut-away view of DSC-6 sensor. The semi-conductor strain gauges are faintly visible at the base of the beam. Each strain gauge is approximately 0.76 cm long. The distance from the end of the DSC-6 beam to the middle of the semi-conductor strain gauge is approximately 2.64 cm.

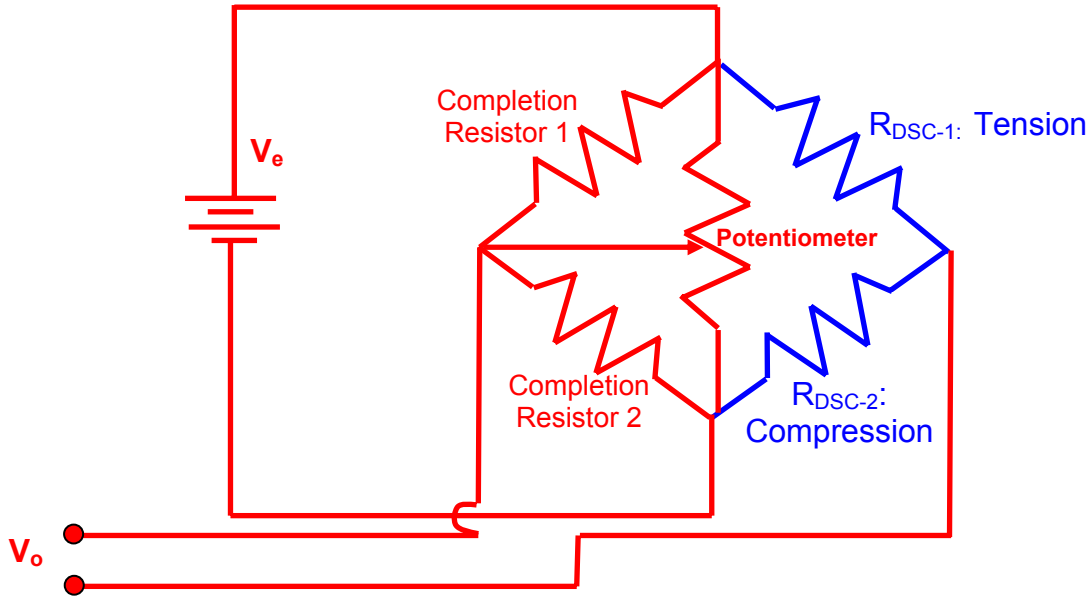

Figure 3.10 Electrical schematic of half Wheatstone Bridge, type II. Blue indicates components internal to the DSC-6 sensor. Red indicates components internal to the signal conditioning equipment.

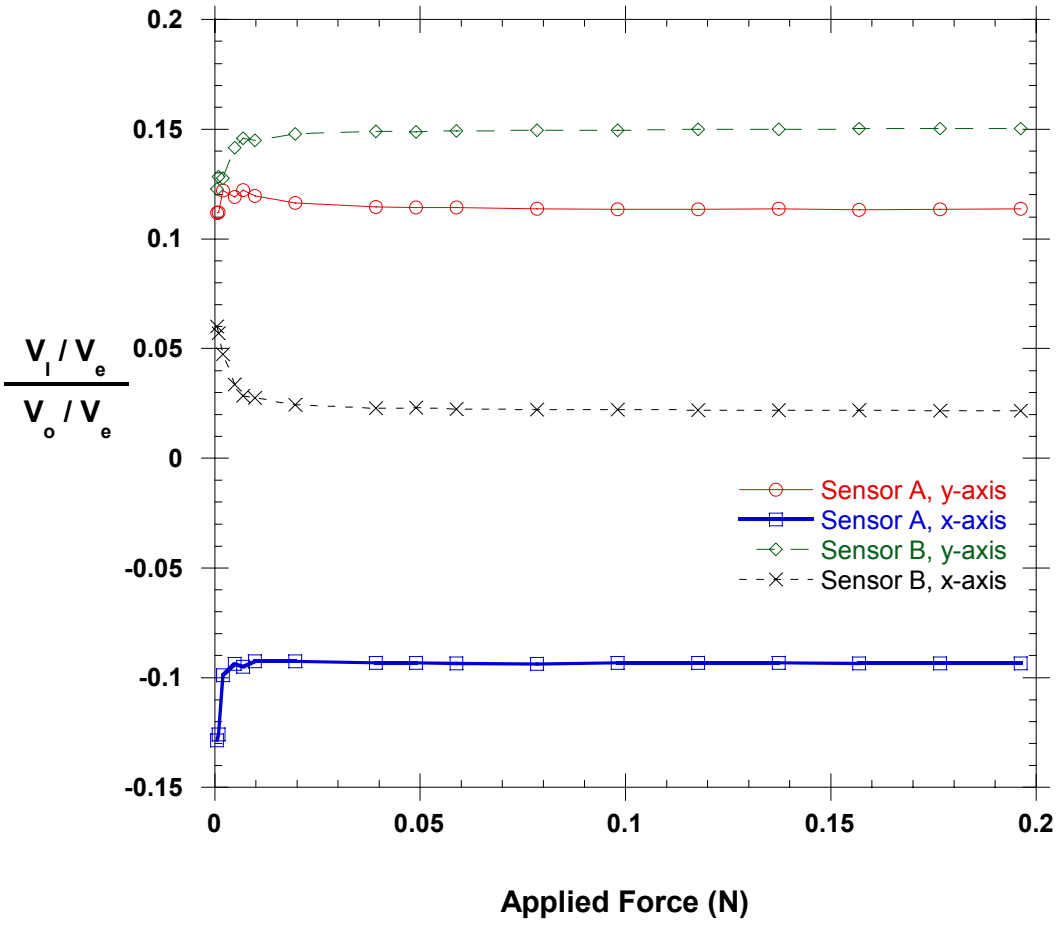

Figure 3.11 The plot demonstrates the cross axis sensitivity of four different sensor axes. Note that the ratio of the perpendicular axis output to the aligned axis is approximately constant for each sensor axis. The deviation at the lower forces is likely due to poor measurement resolution of the small output voltages.

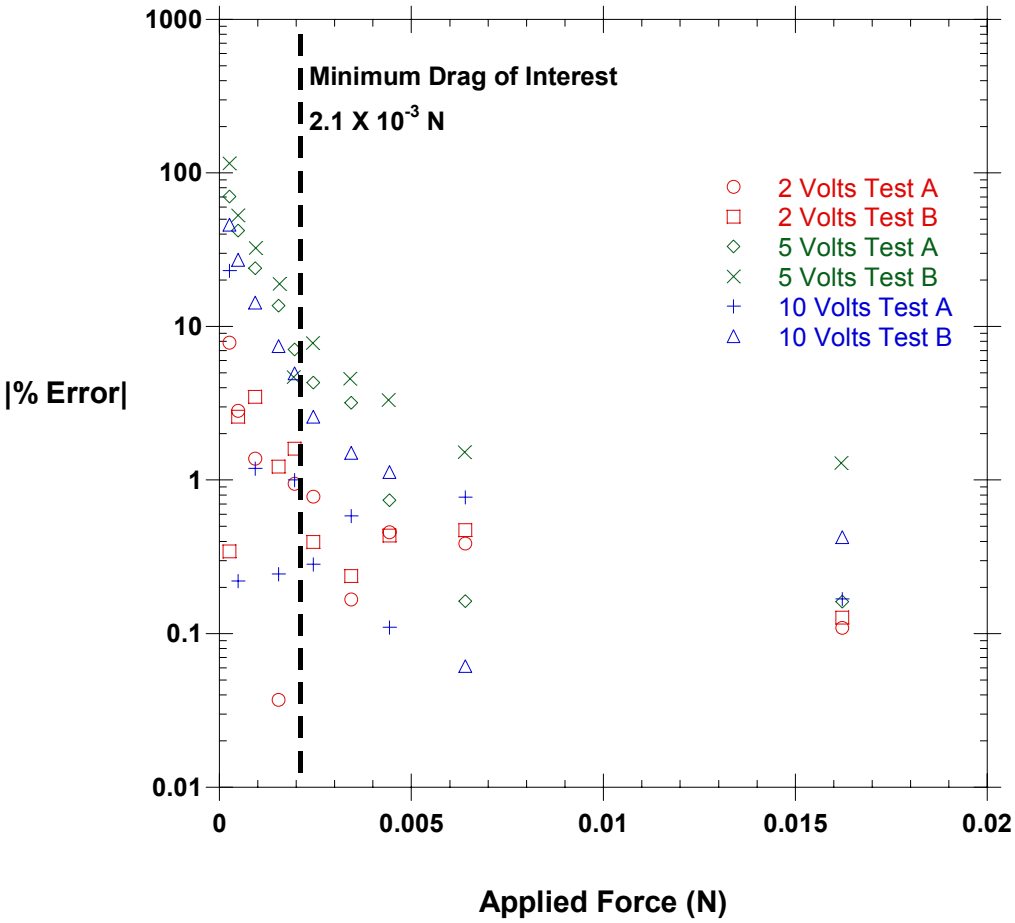

Figure 3.12 The scatter plot summarizes the results of one-axis DSC-6 calibration testing with a variety of excitation voltages. Generally speaking, 2 Volts of excitation provided the most accurate sensor results.

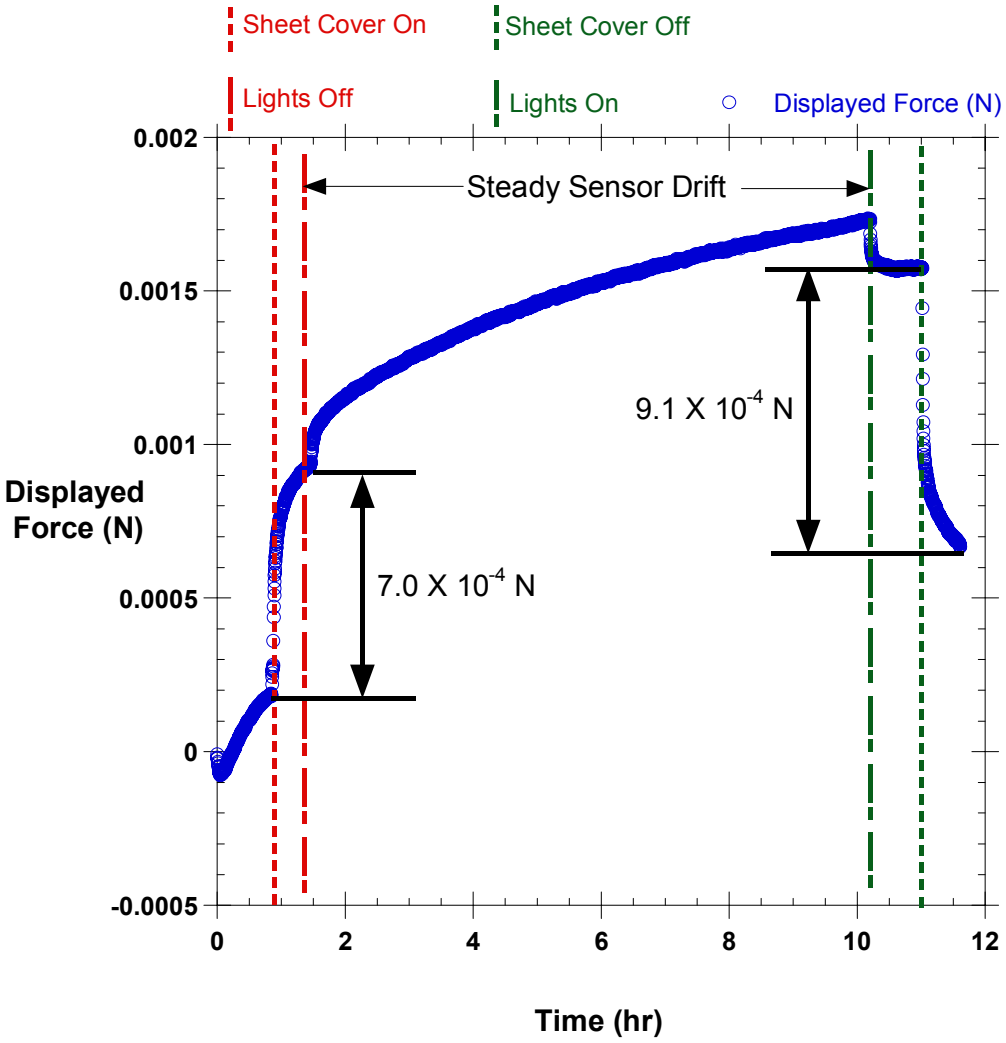

Figure 3.13 Sensor output from an overnight drift test. The figure shows the effect of changing light intensity on the sensor output.

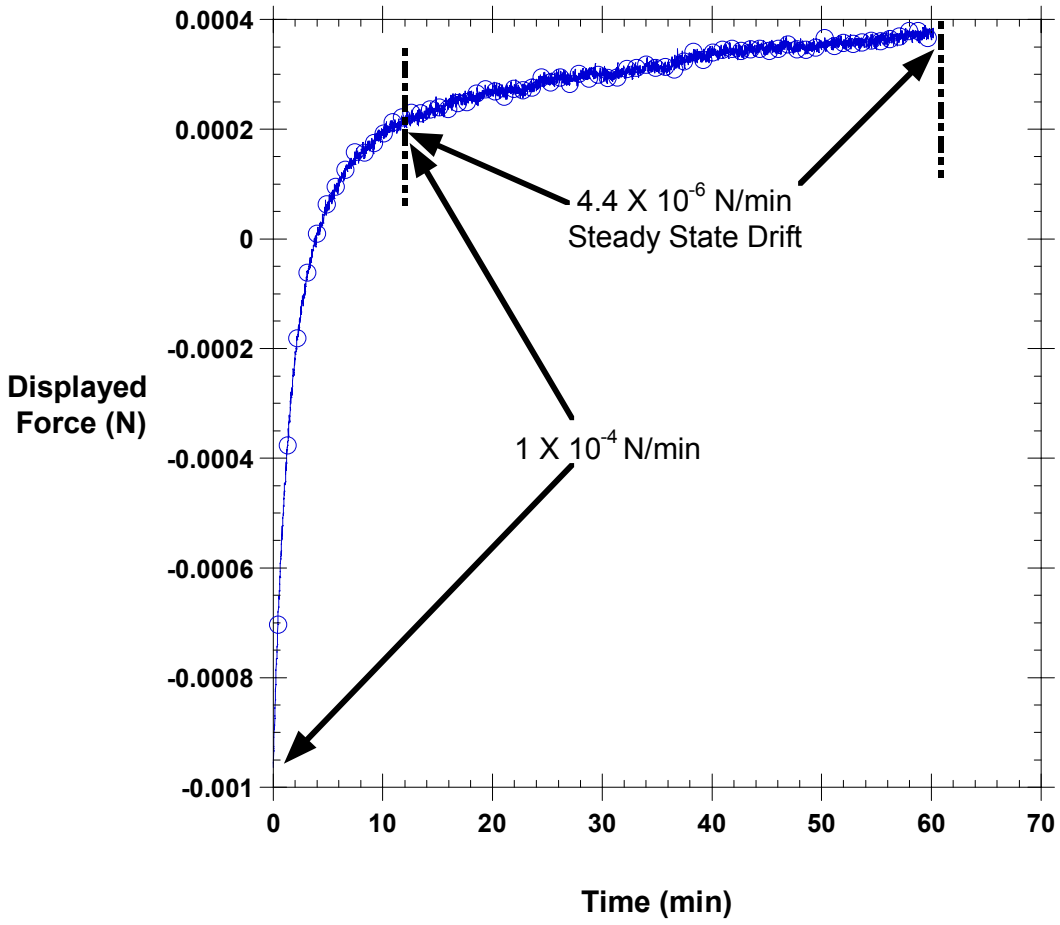

Figure 3.14 Plot illustrating increased sensor drift rates after exercising the sensor to full scale. Data collection starts approximately ten seconds after releasing the DSC-6 sensor from a full scale deflection. The drift rate is significantly increased for the first 15 minutes, before leveling to a steady state drift rate.

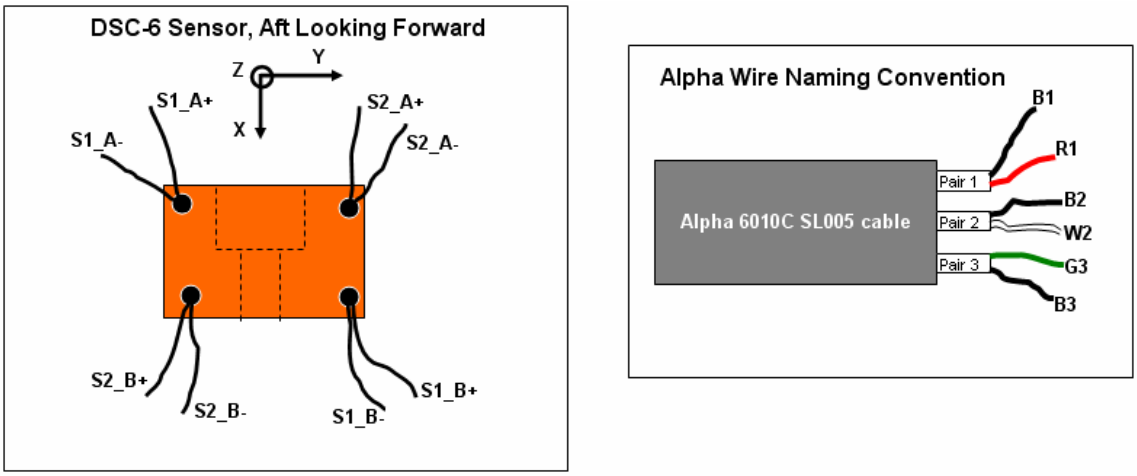

Figure 3.15 Diagram defining the DSC-6 lead wire and Alpha cable electrical naming convention.

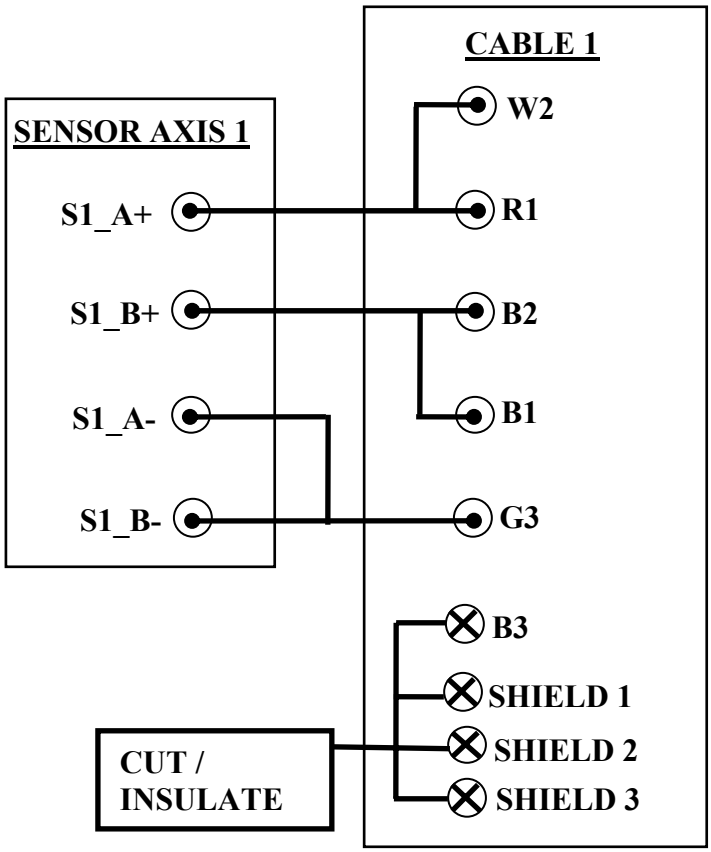

Figure 3.16 Electrical schematic defining the connection between the DSC-6 sensor and the Alpha cable. Although not illustrated here, connection of Sensor Axis 2 to Cable 2 is accomplished in exactly the same manner.

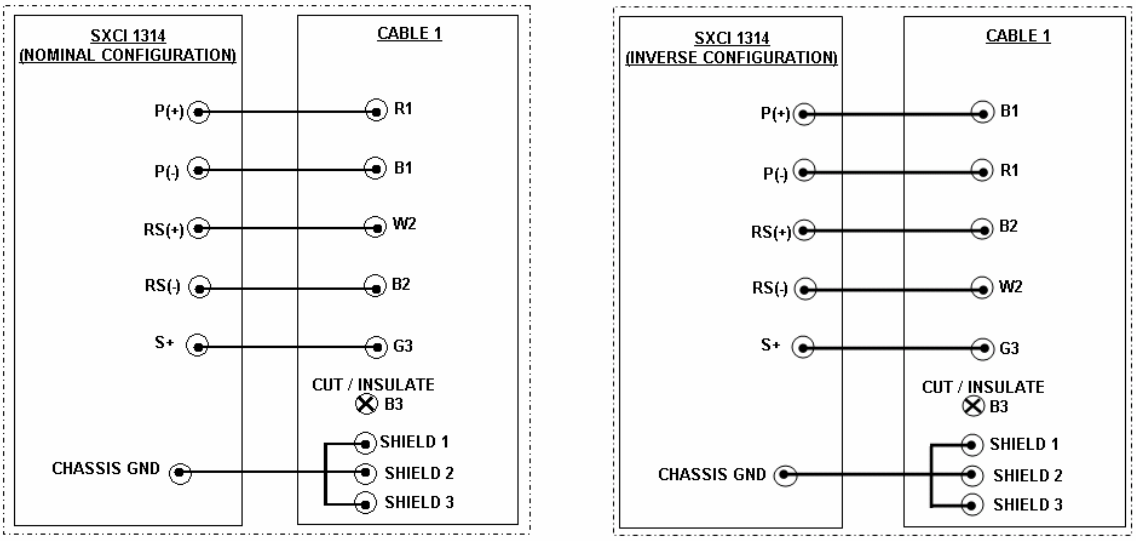

Figure 3.17 Electrical schematic defining the connection between the Alpha cable and the SCXI 1314 terminal block. The correct wiring configuration (nominal or inverse) should be used to achieve a positive output voltage for a deflection in the positive axis direction (reference Figure 3.8).

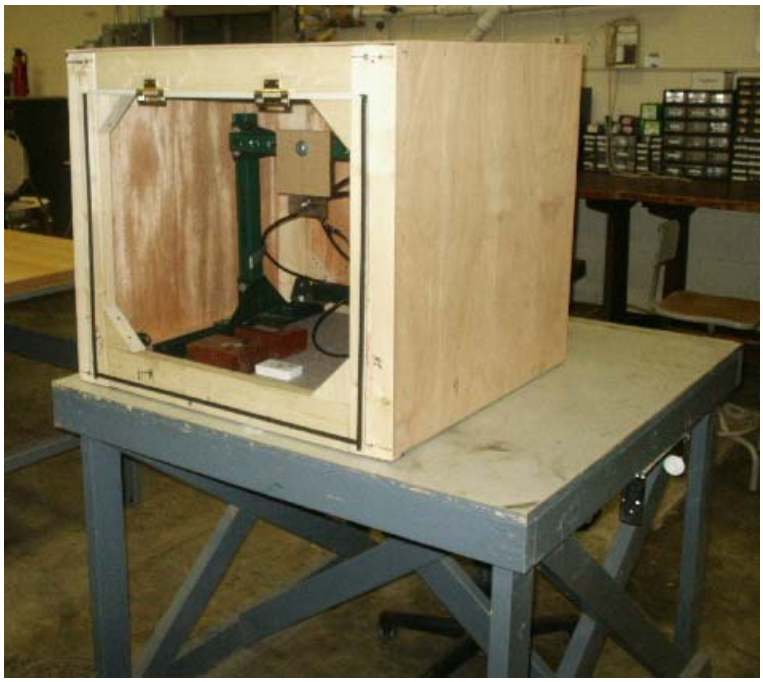

Figure 3.18 Photograph of the calibration shelter used for calibration testing.

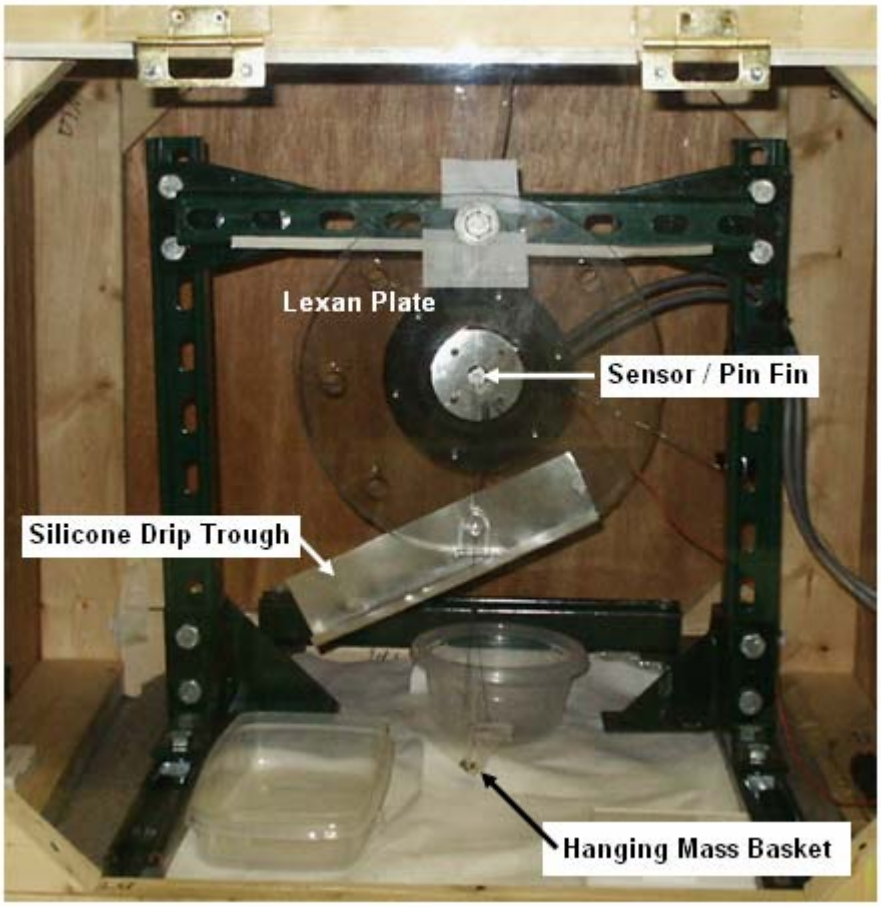

Figure 3.19 DSC-6 sensor mounted into the calibration frame inside the calibration shelter.

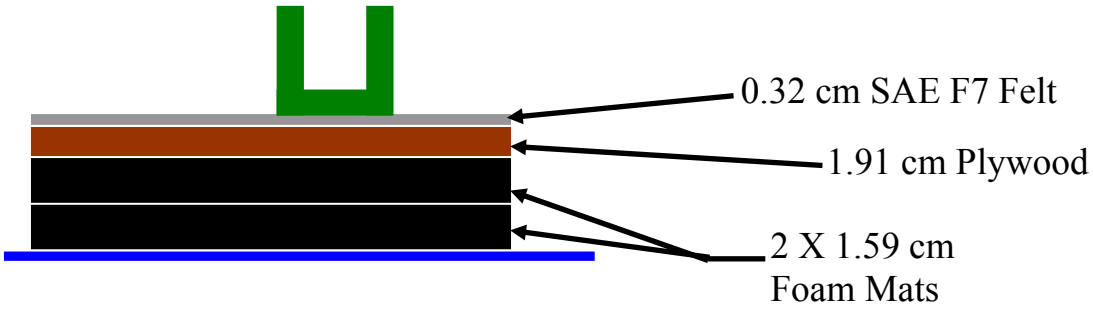

Figure 3.20 Schematic of the vibration isolation system used under the sensor calibration frame.

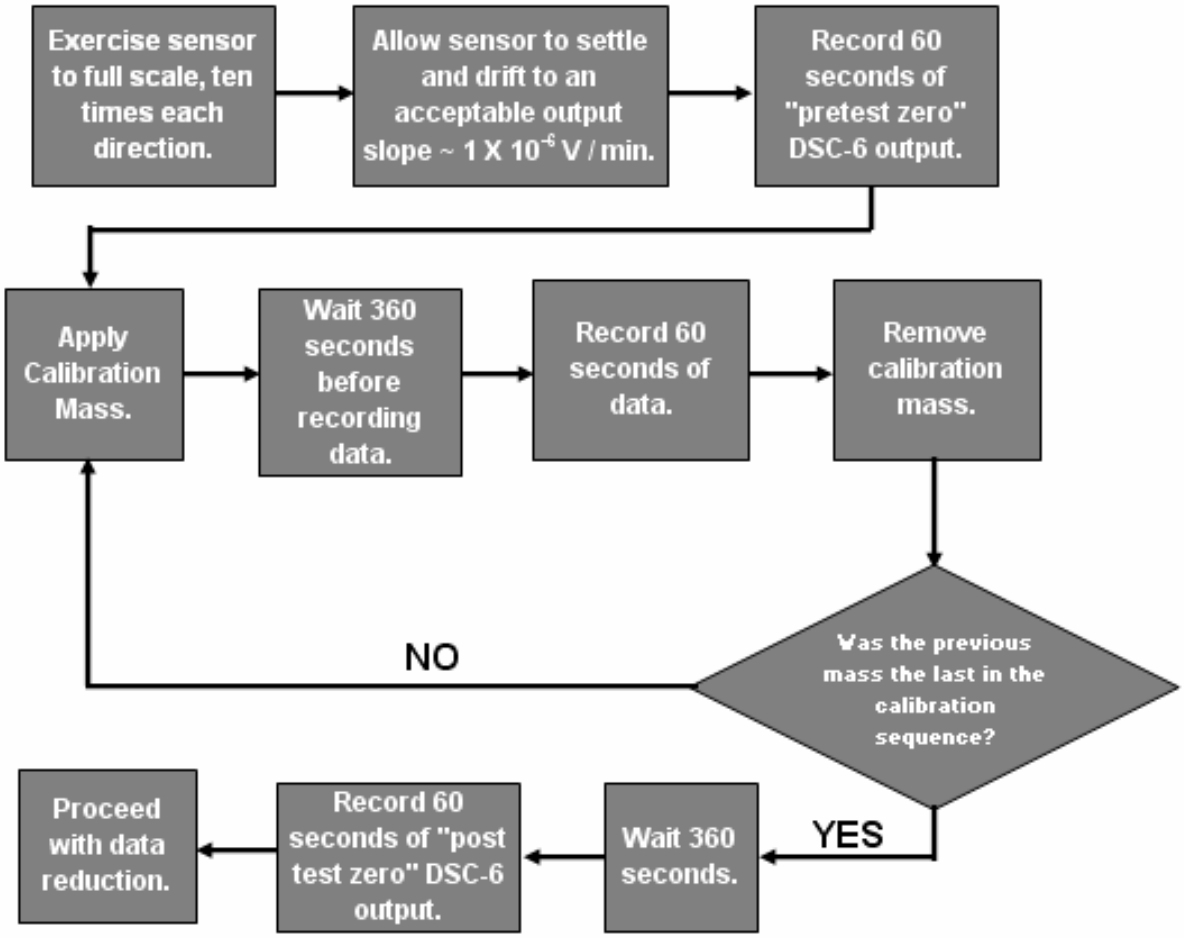

Figure 3.21 Flowchart describing execution of calibration testing.

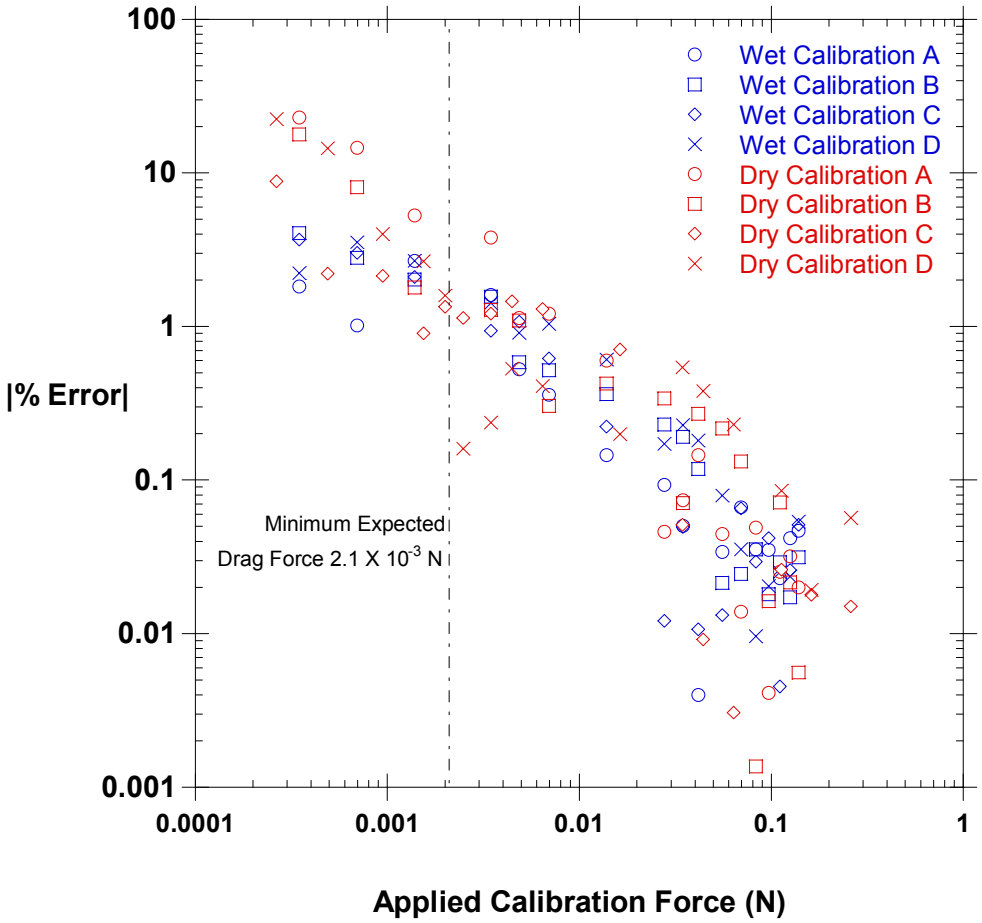

Figure 3.22 Plot of relative error between sensor output and applied calibration force. The "dry" data points refer to tests conducted with silicone oil. "Wet" data points refer to tests conducted with the sensor submerged in silicone oil. The plot shows that tests performed with the sensor submerged in oil have improved accuracy at the low force range.

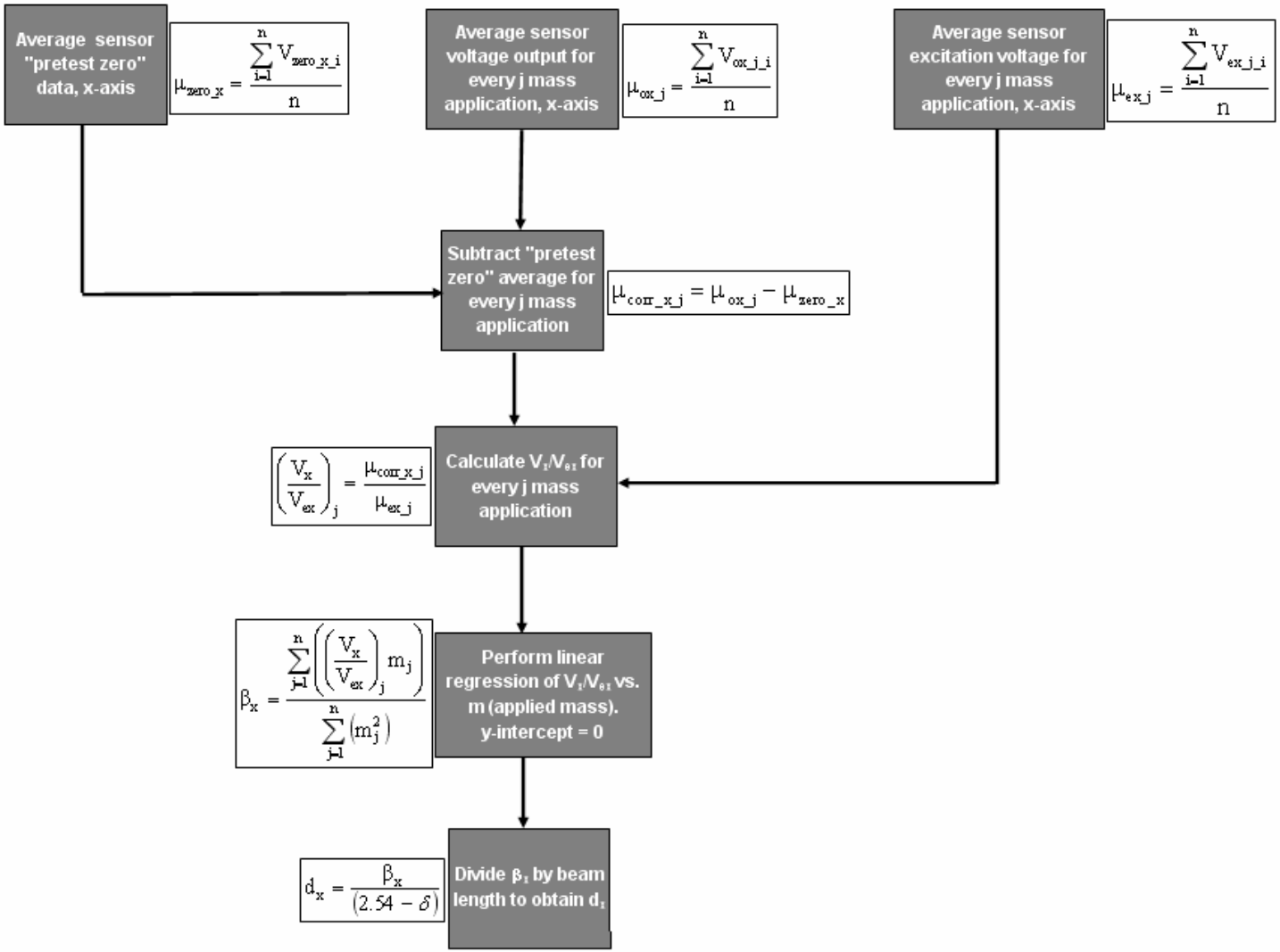

Figure 3.23 Flowchart describing the calibration data reduction methodology for d_x.

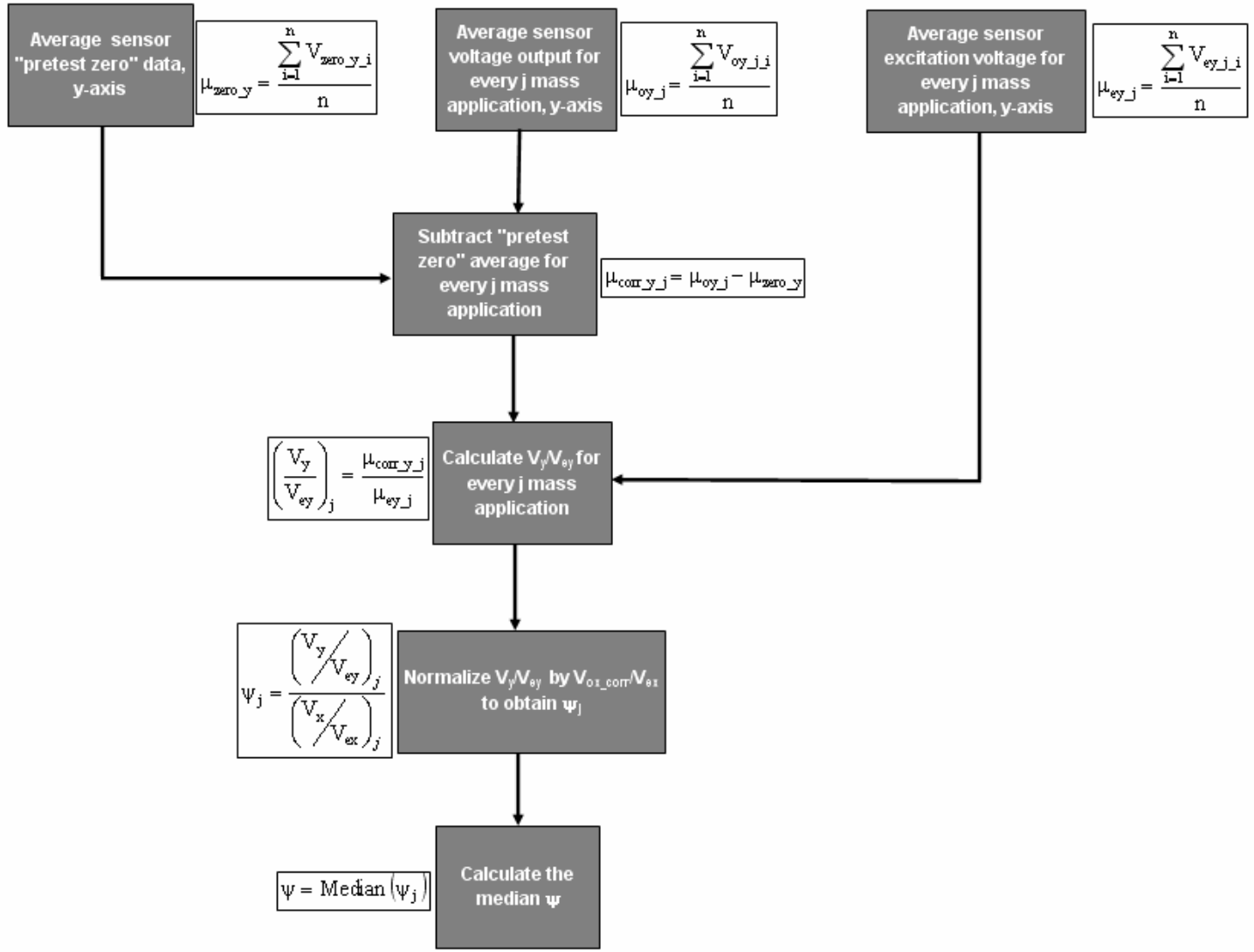

Figure 3.24 Flowchart describing the calibration data reduction methodology for ψ.

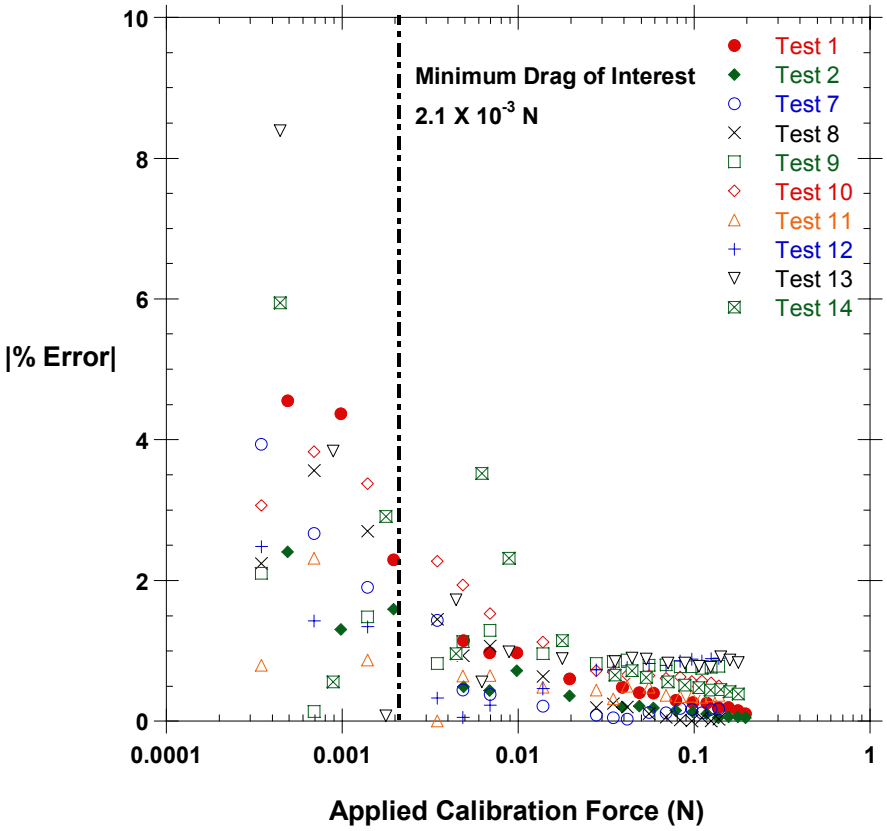

Figure 3.25 Summary of relative error between the x-axis sensor output and the applied calibration force. For all calibration tests, the relative error in the force measurement never exceeds 4% for forces greater than the estimated minimum cylinder drag.

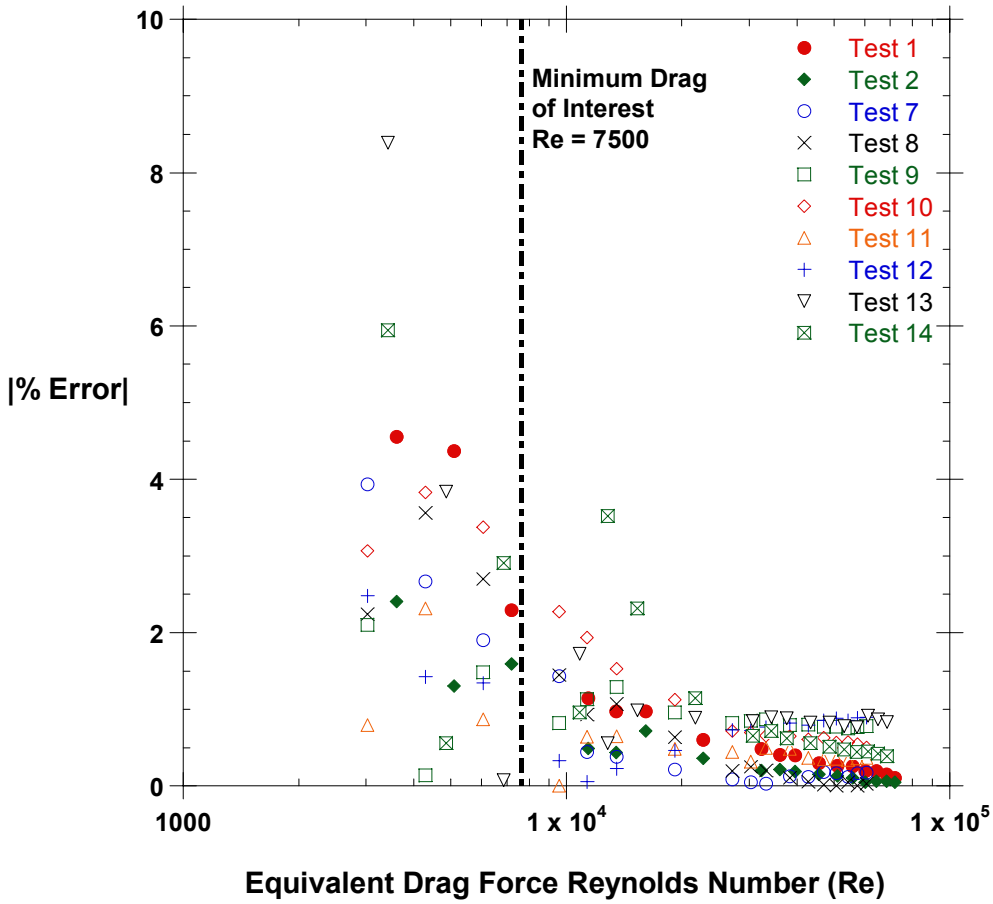

Figure 3.26 Summary of relative error between the x-axis sensor output and the applied calibration force. The x-axis scale is the channel Reynolds number that would produce an equivalent cylinder drag force equal to the applied calibration force.

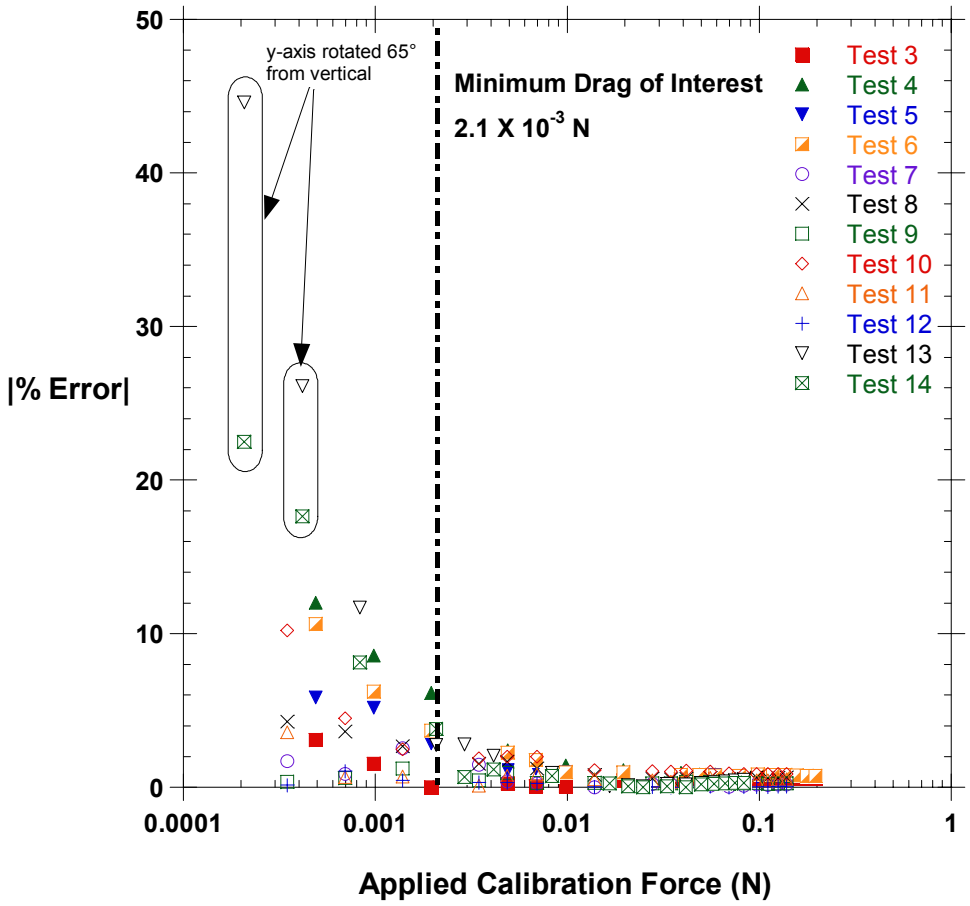

Figure 3.27 Summary of relative error between the y-axis sensor output and the applied calibration force. The excessively large error points circled for Test 13 and Test 14 were taken with the y-axis rotated 65° away from vertical. The sensitivity of the sensor is greatly reduced for such a large angle, resulting in larger measurement errors.

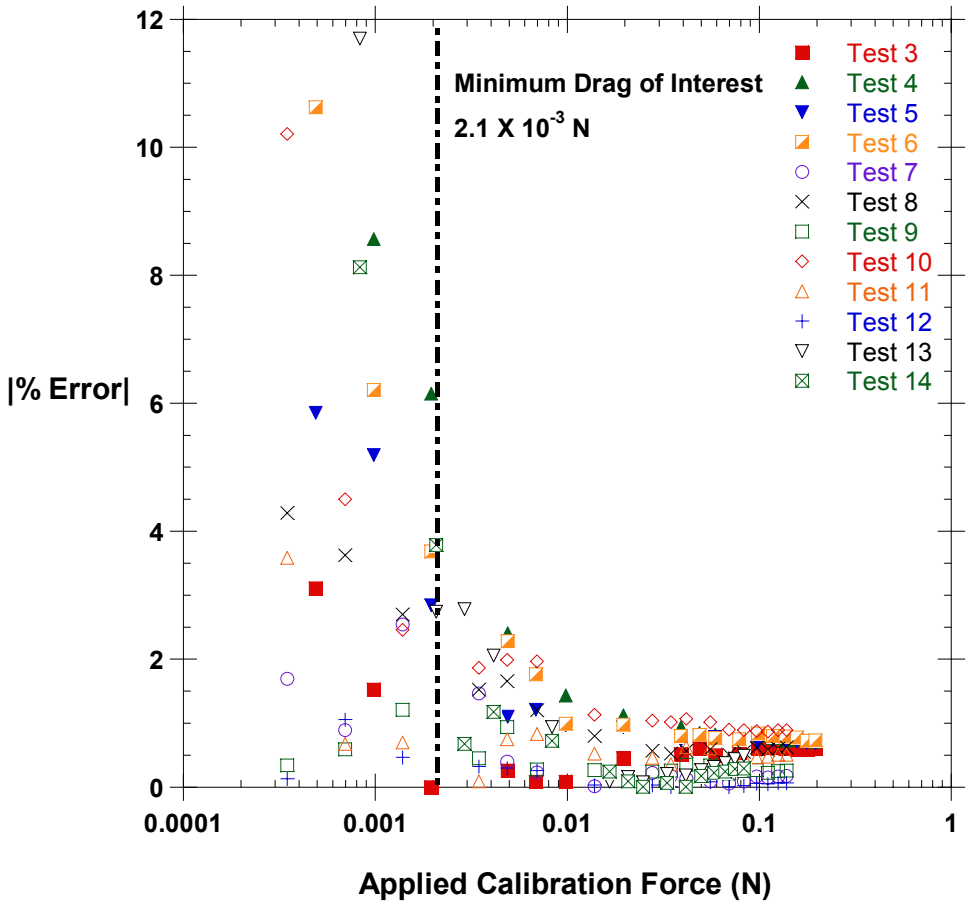

Figure 3.28 Summary of relative error between the y-axis sensor output and the applied calibration force after removing the outlier results from Test 13 and Test 14. For all calibration tests, the measurement error for forces greater than the minimum expected drag value is no greater than 4%.

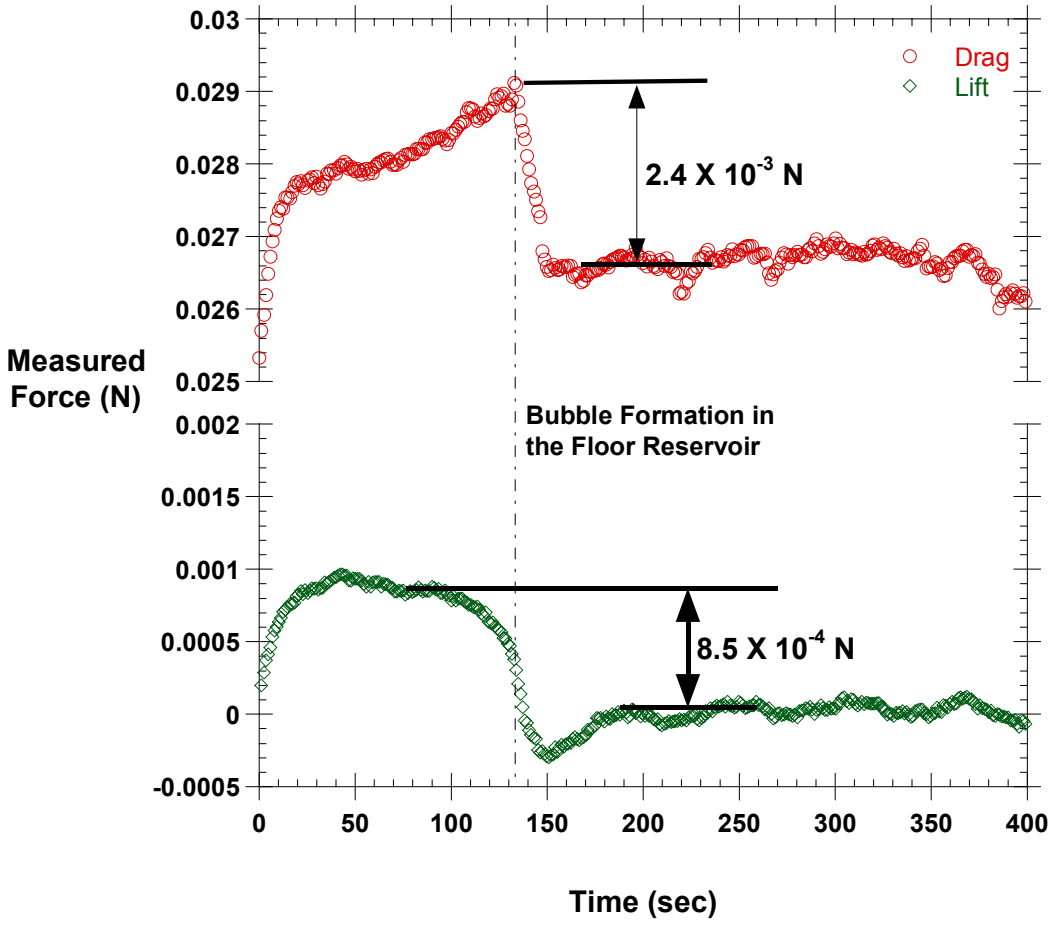

Figure 3.29 Plot of sensor output showing the effect of a bubble in the floor silicone reservoir at the leading edge of the cylinder. The bubble was visually observed to occur at approximately 130 seconds, causing the step change in sensor output.

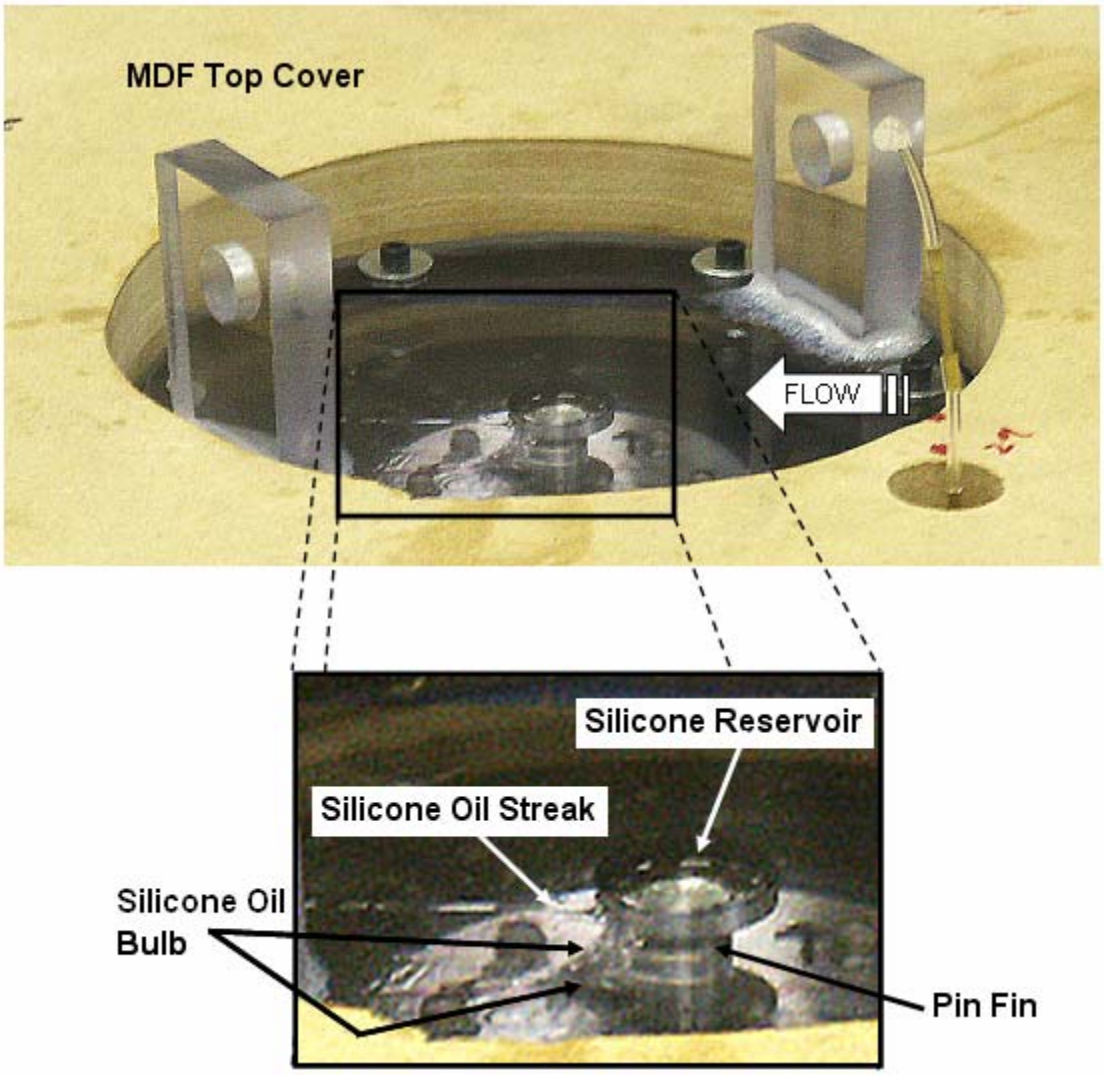

Figure 3.30 Annotated photograph showing how excess silicone oil is drawn upwards into a bulb when the flow is turned on.

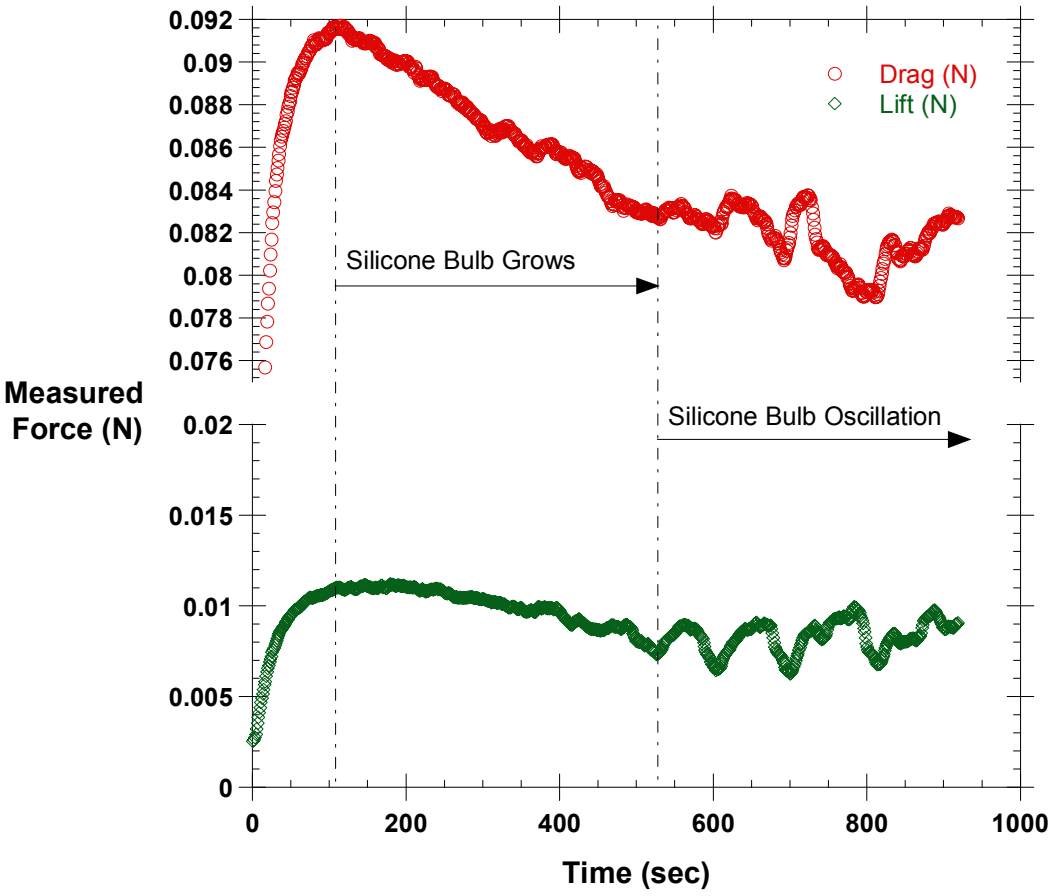

Figure 3.31 Plot showing the effect of silicone oil collecting behind the sensor pin. The silicone bulb grows in size behind the pin from approximately 100 seconds to 550 seconds. At 550 seconds, the silicone bulb begins to oscillate in the flow. The oscillations of the silicone bulb can be seen in both the lift and drag output.

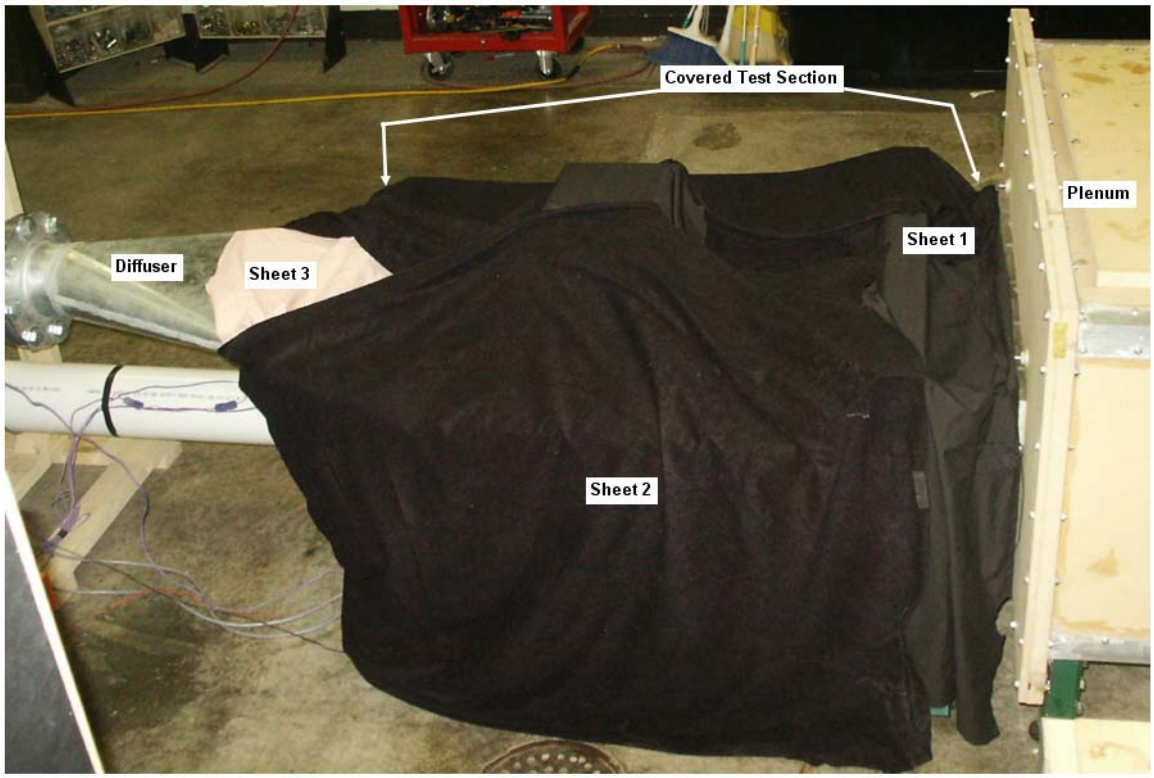

Figure 3.32 Photograph of covered test section, ready to conduct a force test. Three sheets are used to cover the entire test section and shield the sensor from ambient light.

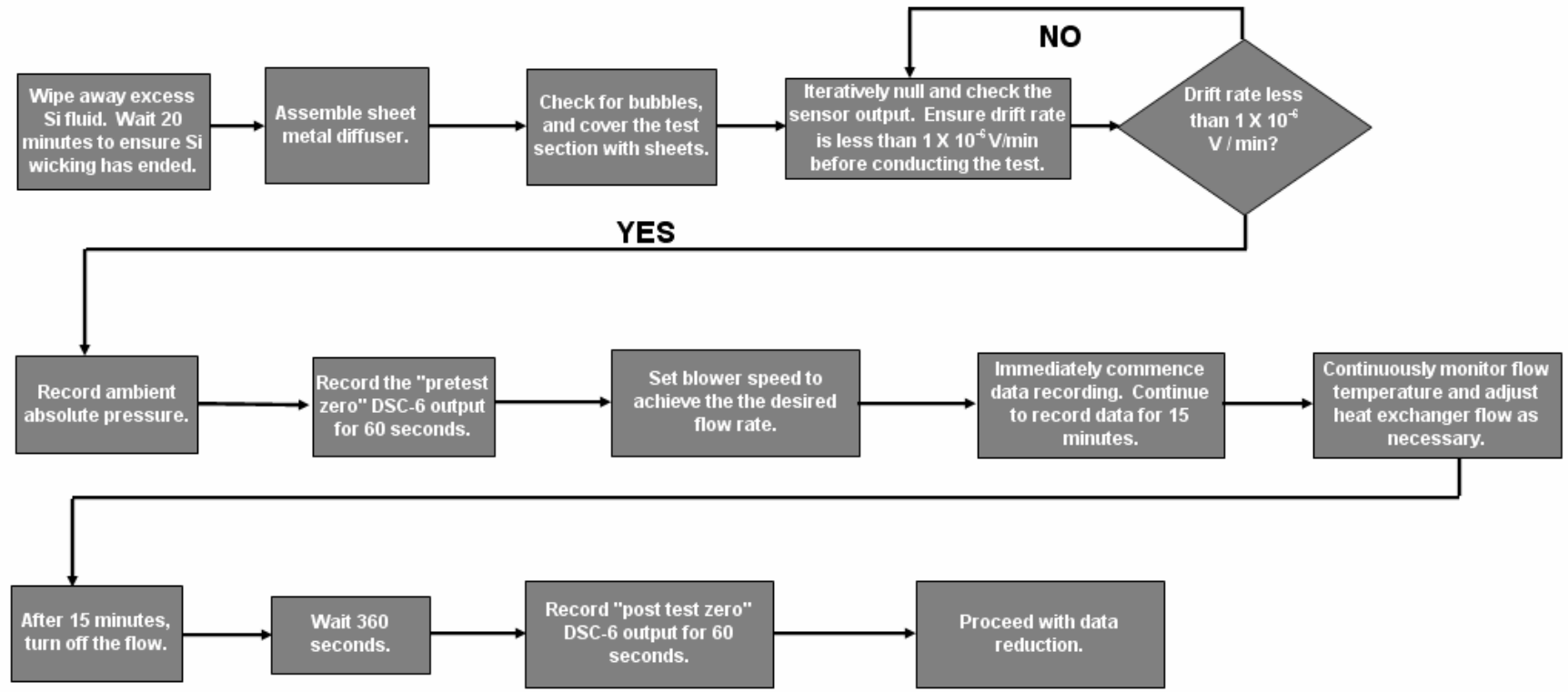

Figure 3.33 Flow chart detailing execution of flow testing.

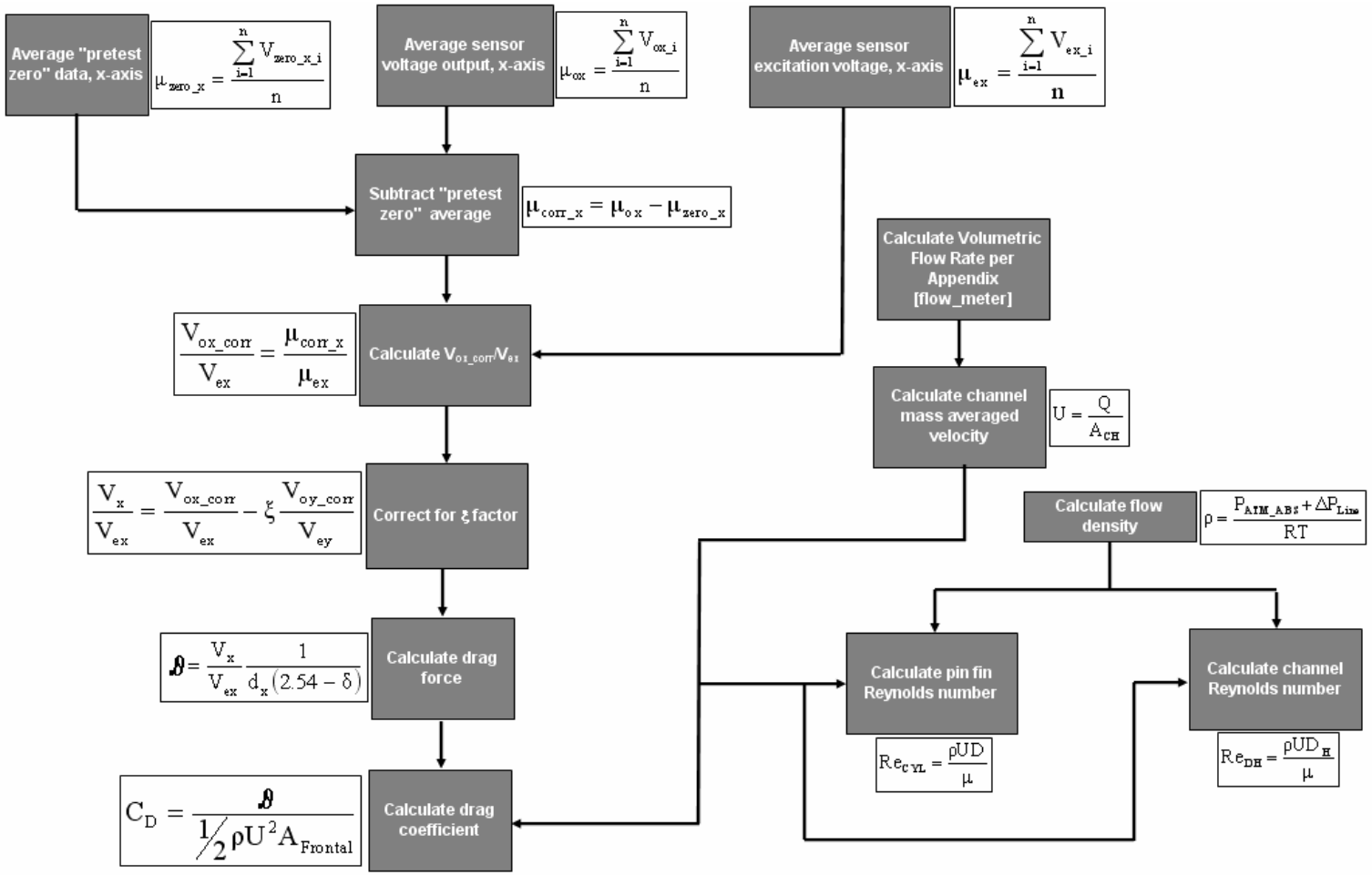

Figure 3.34 Flow chart detailing the drag coefficient data reduction methodology. Calculation of the lift coefficient follows an identical process by inverting the axes.

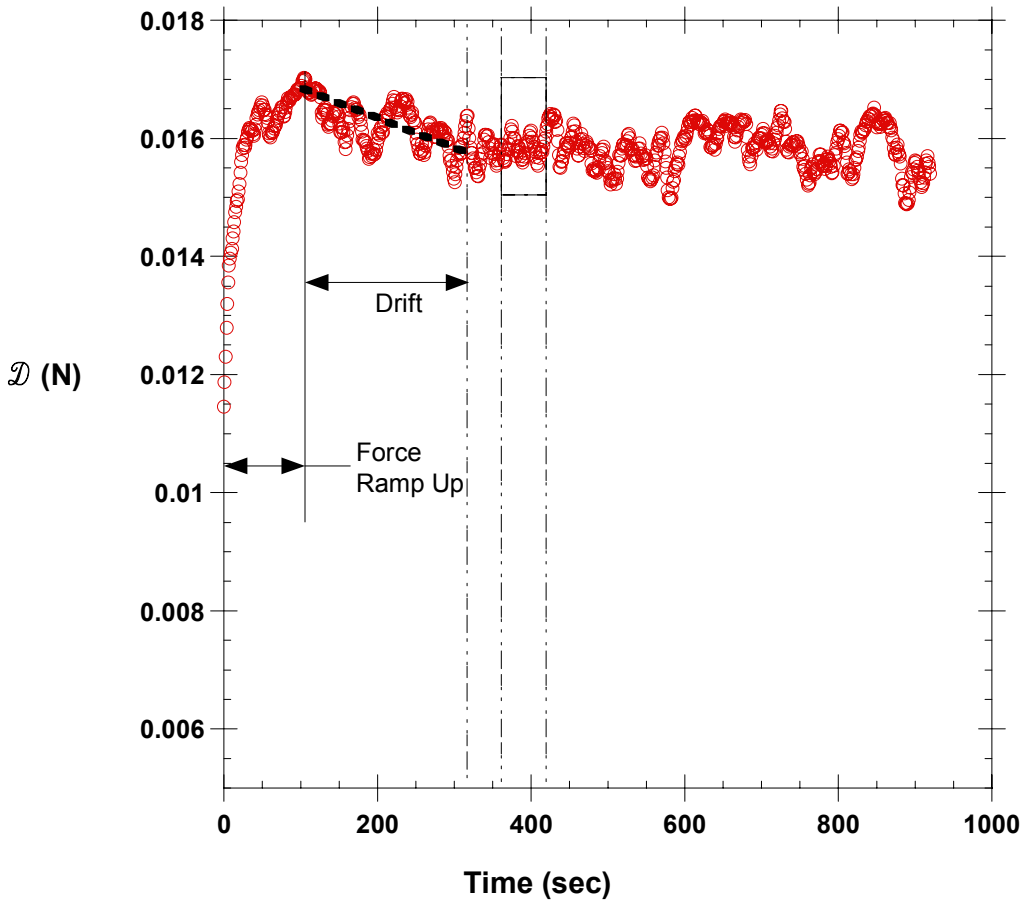

Figure 3.35 Plot of typical output from a Re = 1.5 X 10^4 test. The plot shows that the data analysis window occurs after 360 seconds of testing, where the output is steady.

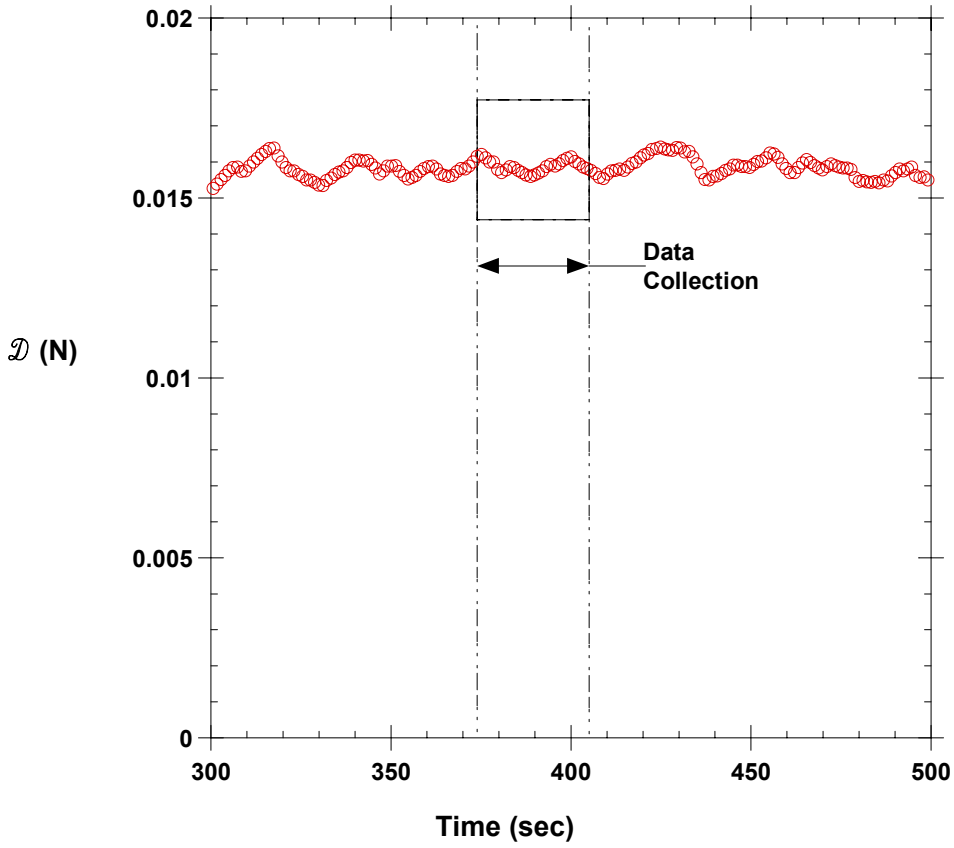

Figure 3.36 Zoomed-in plot of the data analysis window shown in Figure 3.35. In terms of the mean, the signal is approximately steady.

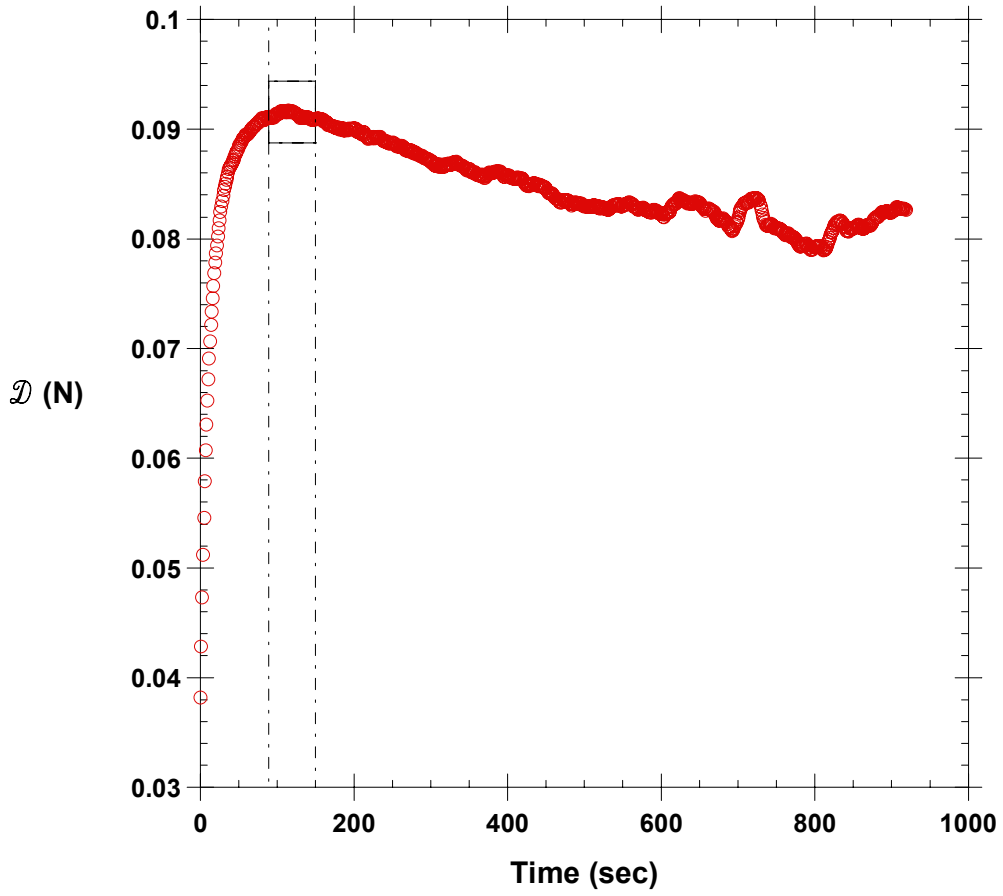

Figure 3.37 Plot of typical output from a Re = 3.5 X 10^4 test. The plot shows that the data analysis window occurs after 90 seconds of testing, where the output is steady. The data analysis window occurs sooner than for tests less than Re = 1.8 X 10^4 to avoid the effects of the silicone bulb forming behind the cylinder.

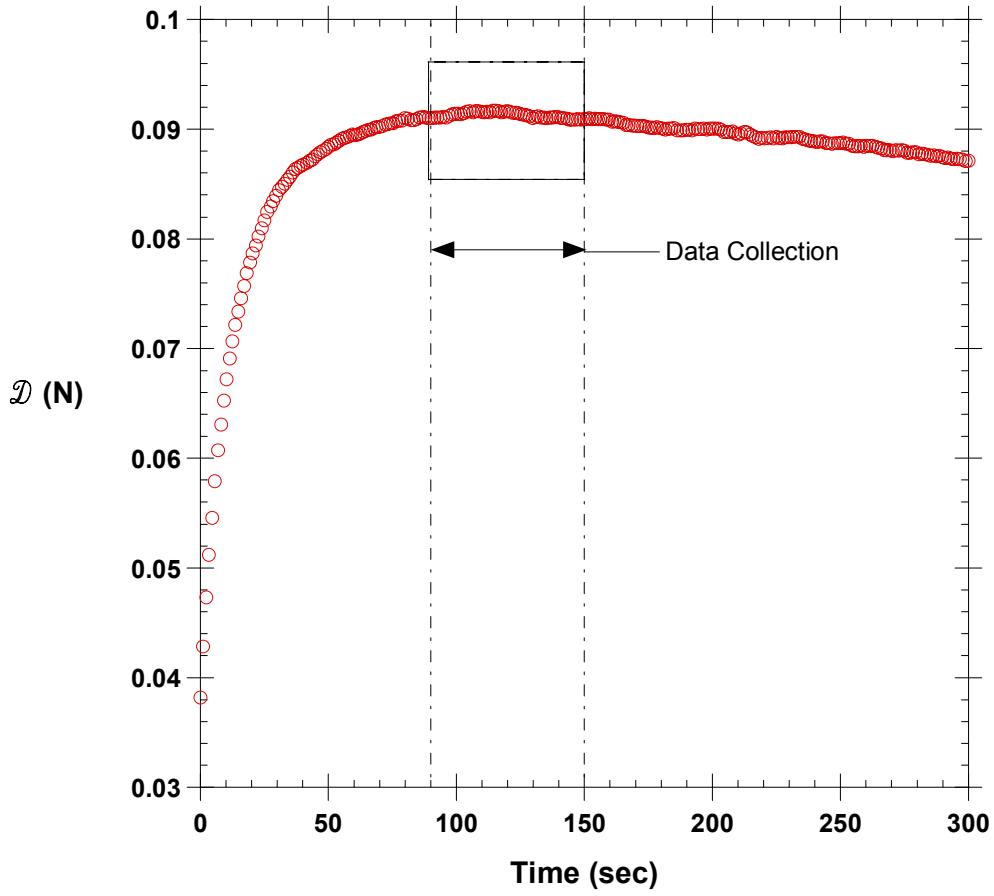

Figure 3.38 Zoomed-in plot of the data analysis window shown in Figure 3.37. The data collection window occurs at the apex of the force signal, where it is approximately steady.

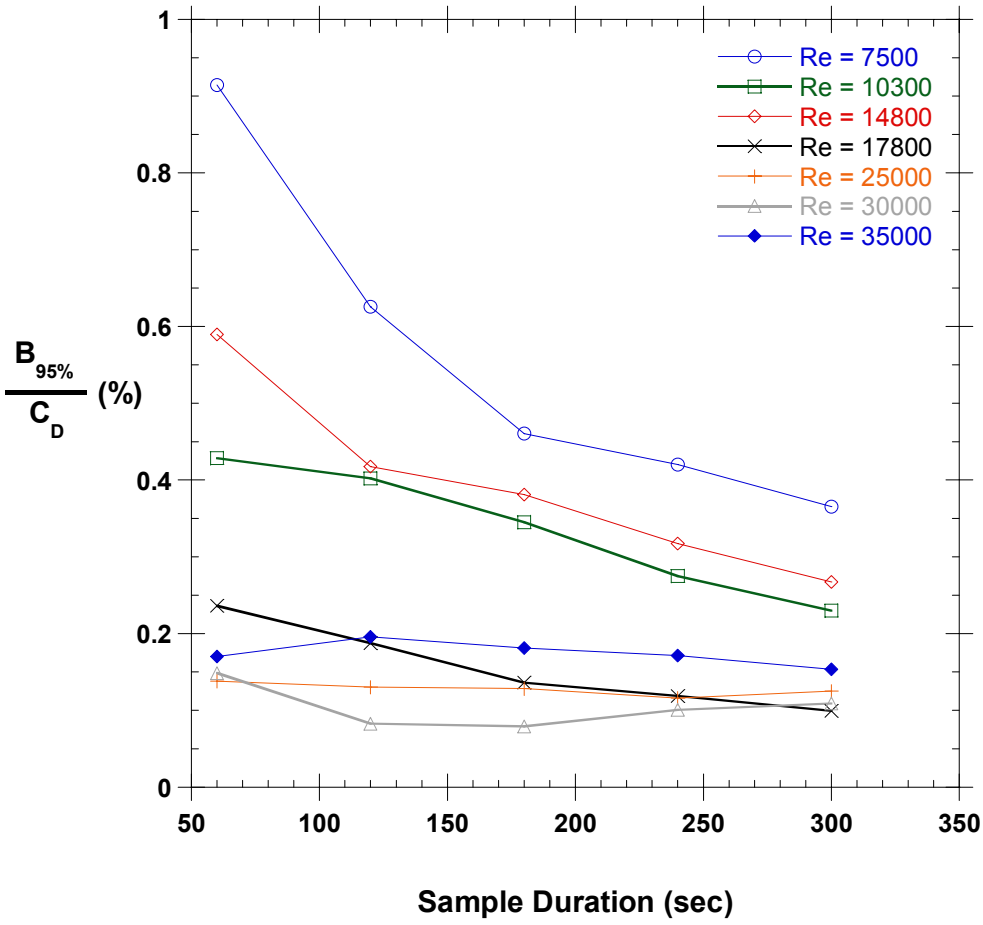

Figure 3.39 Representative plot of the 95% confidence interval normalized by the sample mean for six different flow conditions. The plot shows that the 95% confidence interval is less than 1% for all sample durations and flows. Marginal gains are achieved by increasing the sample size beyond 60 seconds.

Chapter 4

Design and Construction of Experimental Facility

The goals of this study required the design, development, and construction of a new facility within the VTExCCL laboratory. Due to the multi-faceted goals of this project, two different test facilities were constructed. One facility, the focus of this thesis, was designed and constructed to obtain aerodynamic force measurements. An identical facility, with a slightly different test section, was developed to obtain heat transfer measurements [Lyall, 2006].

The test facility was designed to operate in a closed loop, recirculating flow configuration. Figure 4.1 provides a three-dimensional, rotated view of the entire test facility. The test facility was approximately 9 meters long, consisting of four major components: plenum, test section, flow measurement section, and flow recirculation section. From the perspective of Figure 4.1, the flow circulated in a clockwise direction. For simplicity, air was chosen to be the working fluid in the test rig. The flows of interest ranged from $Re = 7.5 \times 10^3$ to $Re = 5.0 \times 10^4$.

To ensure acceptable resolution in the heat transfer and aerodynamic force measurements, a large geometric scale was desired. However, limited laboratory floor space provided an opposing design constraint. Ultimately, the scale chosen for the pin fin geometries to be tested was 25 times larger than engine scale. The resultant test channel cross section was 0.96 cm high by 61 cm wide, achieving a width to height aspect ratio of 64.

This chapter will describe the individual sections that comprise the aerodynamic test facility. Section 4.1 describes the plenum, flow measurement section, and flow recirculation section of the test facility. These components, however, were not the primary focus of the research project. The purpose of these components was to provide conditioned, metered flow to the test section. The design and construction of the test section is described in Section 4.2, while Section 4.3 provides specific information regarding sensor installation into the test section. The information contained in Sections 4.2 and 4.3 are the most pertinent for making accurate force measurements.

4.1 Overall Test Facility

This section of the thesis will provide a description of the entire facility, except for the test section. Specifically, the plenum, flow measurement section, and flow recirculation section will be discussed. Although not directly involved with quantifying the aerodynamic forces on the pin, each section served an important role in the test facility.

Plenum. The plenum, shown in the top right corner of Figure 4.1, was located at the front of the channel to condition the flow before it entered the test section. The function of the plenum was to ensure a constant air temperature for the entering air and provide a means to achieve dynamic flow uniformity. The plenum was the most logical location to cool the air, as the total pressure drop through the heat exchanger was proportional to the square of the flow velocity. Because the flow was slowest in the plenum, the heat exchanger produced the smallest pressure penalty there. Additionally, the large cross sectional area provided ample room to place several rows of heat exchanger fins.

The plenum was constructed of 2.5 cm thick medium density fiberboard (MDF) with aluminum angles and silicone caulking used to seal the joints. The internal, open area dimensions of the plenum volume were 1.24 m long by 1.17 m wide by 0.55 m tall. The cross sectional flow area was approximately 0.64 m², achieving a plenum to test channel cross sectional area ratio of 110:1. Generally, a ratio of at least 10:1 is considered requisite for an acceptable plenum box. Due to the large area ratio, the velocity in the plenum was assumed to be approximately zero.

Figure 4.2 provides a cut-away view of the plenum, exposing the box's internal components. Air discharged into the plenum from the recirculation pipe, shown to the far right of Figure 4.2, and immediately encountered a two plate baffle. The purpose of the baffle was to evenly distribute the entering jet of air over the entire plenum cross sectional area. The first baffle was a splash plate that the entering jet impinged upon. The second baffle was a hollow rectangle, through which the air passed through the center. Previous experiences in the VTExCCL lab have shown that the first splash plate should have an open flow area equal to twice the PVC inlet pipe area. The second baffle

should have an open area in the center equal to four times the PVC pipe inlet area [Prausa, 2004]. Accordingly, the splash plate was cut to 1.1 m wide by 0.53 m tall, while the second baffle was fabricated with an inner open area of 0.42 m wide by 0.19 m tall. In both cases, the open flow area maintained the height to width aspect ratio of the plenum cross sectional area. The first splash plate was located 18 cm downstream of the PVC inlet, with the second baffle 11 cm downstream of the splash plate.

The flow next encountered the heat exchanger, 31 cm downstream of the second baffle. Although the flow through the test section was not intentionally heated, the blower heated the air through frictional effects. To maintain a constant velocity through the test section, it was necessary to cool the flow via a heat exchanger. The heat exchanger used in the plenum was graciously donated to VTExCCL by Super Radiator Coils of Richmond, Virginia. Operating in a multi-pass, cross-flow configuration, the tube and fin heat exchanger measured approximately 1.1 m wide by 0.5 m tall. Appendix D provides detailed information regarding the design of the heat exchanger. Cold tap water was used as the cooling fluid in the heat exchanger. The temperature of the entering tap water varied from 17°C to 23°C, depending on the outside temperature. Details regarding the operation of the heat exchanger during testing are discussed in Chapter 3.

Perhaps the most important design features in the plenum were the inlet guides, shown to the far left of Figure 4.2. Figure 4.3 provides a photograph of the installed inlet guides. The inlet guides served to provide a smooth contraction for flow into the test section. The plenum was originally designed without the inlet guides, as they were not thought to be necessary. However, static pressure distributions in the flow channel indicated that severe flow deformations occurred without the inlet guides at the front of the test section. Once the inlet guides were added, the test section static pressure distribution yielded friction factors that agreed well with published correlations. This will be discussed further in Chapter 5.

Each inlet guide was a 180° section of an ASTM D-1785, 15.2 cm schedule 40 PVC pipe. The inlet guides were assembled to the test section by placing one edge of the PVC guide tangent to the inner surface of the test section, and bolting the guide to the plenum wall. It was crucial that the inlet guides met flush with the test section surface

across the entire channel width. If the inlet guides were installed slightly crooked, significant variations in flow velocity developed across the width of the test section. The ends of the PVC inlets were closed by adding a 0.32 cm thick piece of particle board to each side, and sealed with AT-200Y tape. AT-200Y tape, advertised as a vacuum bag sealant, was purchased from General Sealants Inc.

Flow Measurement Section. The purpose of the flow measurement section, shown immediately downstream of the test section in Figure 4.1, was to quantify the volumetric flow rate through the test rig. Figure 4.4 provides a detailed view of the flow measurement section, along with pertinent dimensions. As seen in Figure 4.4, a sheet metal diffuser transitions the flow from the rectangular test section to the circular PVC pipe. The sheet metal diffuser was fabricated by the Virginia Tech Physical Plant Sheet Metal Shop. Mechanical drawings of the transition piece are provided in Appendix E. Note that the cross sectional flow area of the diffuser increased three-fold in transitioning from the test section flow area to the PVC pipe flow area. ASTM D-1785, 15.2 cm schedule 40 PVC pipe was used to feed one of two interchangeable flow meters. An orifice meter was used to measure volumetric flow rates for $Re < 1.8 \times 10^4$, while a venturi was used for $1.8 \times 10^4 < Re < 5.0 \times 10^4$. This combination of flow meters provided maximum resolution in flow measurement while minimizing total pressure loss at high flow rates. The orifice meter, the Oripac Model 4150-P-06-2.500-150, and the venturi, Model 2300-06-3.58, were both manufactured by Lambda Square of Babylon, New York. The meters were selected such that the interface thickness of both pieces was the same. Thus, the flow meters were completely interchangeable and used the same PVC piping and ASME 150# flanges.

Pressure drop vs. flow rate curves for both the venturi and the orifice can be found in Appendix D. Appendix D also provides the physical parameters of the flow meters with an equation sheet that can be used to calculate the flow rate through the device. The equations given in Appendix D provide a slightly more accurate flow rate estimate than the published curves, because the equations consider local ambient conditions. The advertised accuracy for the venturi and orifice meters was ± 0.75% and ± 0.6% respectively [Lambda Square, 2005]. To achieve this level of accuracy, a sufficient

length of smooth, straight pipe must be placed upstream and downstream of the flow meters. In general, orifice meters require longer pipe lengths than venturi meters. Lambda Square recommended the smooth pipe extend at least ten hydraulic diameters upstream and five hydraulic diameters downstream of the orifice [Lambda Square, 1996]. Referring to Figure 4.4, one can see that the test facility was constructed with uninterrupted PVC pipe extending 15 hydraulic diameters upstream and nine hydraulic diameters downstream of the flow meter. Thus, the manufacturer's specifications were met with margin to spare.

The pressure difference across the flow meters was measured using a Setra Model 264 differential pressure transducer. The scale of the pressure transducer was 0 – 1.24 kPa, with an accuracy of ±0.4% of full scale [Setra Systems, 2001]. Temperature data, used to correct flow density in the volumetric flow correlations, was collected with E-type thermocouples. Two separate National Instruments SCXI 1102 signal conditioners, with SCXI 1303 terminal blocks, were used to collect the voltage output from the pressure transducers and thermocouples. The pressure and temperature signal conditioning equipment was plugged into the same SCXI-1000 chassis, and digitized by the same PCI-6280 DAQ used to collect the DSC-6 sensor output voltage. See Chapter 3 for more detailed information regarding the signal conditioning and DAQ equipment.

Flow Recirculation. As shown in Figure 4.1, the facility was designed to operate in a closed-loop configuration, which ensured that the flow was not subject to the changes in room temperature. To circulate the air through the test facility, a Chicago blower (model D53-J4) was used. The blower was driven by an 11.2 kW, Frame 254T Baldor electric motor powered by 3-phase 460 V AC power. The rotational speed of the electric motor was controlled via a Baldor (model ID15H415-E) inverter control.

The blower was selected after calculating the pressure drop through the facility for a range of flow rates and pin fin geometries. Although this thesis only deals with one row of circular pin fins, future studies will involve multiple rows and shapes. Consequently, multiple rows and pin fin shapes were considered when selecting the blower. A model of the test facility was created in spreadsheet form to predict the requisite static pressure head as a function of volumetric flow rate. System curves were generated to show how

the facility would respond to different flow rates and pin fin geometries. For example, a volumetric flow rate of 0.24 m³/sec with a static pressure head of 6 kPa was required to push air through a 5 row-deep circular pin fin array at $Re = 5.0 \times 10^4$.

The calculations indicated that the static pressure head requirement was excessively large for some pin fin geometries. In one instance, the model predicted a static pressure head of 41 kPa would be necessary to push the air through the test section at $Re = 5.0 \times 10^4$. In contrast, the required volumetric flow rates were relatively low, ranging from 3.6×10^{-2} m³/sec to 2.42×10^{-1} m³/sec. Thus, the static pressure head requirement drove the selection of a high-pressure blower. Appendix D provides blower performance data and geometric interface information for the Chicago D53-J4 blower.

Air flowed from the blower outlet back to the plenum via return ducting constructed of ASTM D-1785, 15.2 cm schedule 40 PVC pipe, as shown in Figure 4.1. Although this section was relatively simple, one design feature should be noted. Figure 4.1 shows that two ball valves, each open to atmosphere on one side, were added to the PVC piping. One ball valve penetrated the PVC pipe upstream of the blower, while the other ball valve was placed downstream of the blower. Additionally, a butterfly valve (also shown in Figure 4.1) was positioned between the downstream ball valve and the plenum. The goal of this series of valves was to allow the user to adjust the flow such that the absolute pressure in the test section was balanced with atmospheric pressure. Experience with the test section demonstrated that differences between the test section static pressure and ambient pressure promoted bubble formation in the silicone oil that surrounded the DSC-6 sensor. By adjusting the valves in the return duct, the pressure imbalance between the test section and the room was alleviated. Specifically, opening the ball valve downstream of the blower and/or closing the butterfly valve reduced the absolute pressure in the test section. Conversely, opening the ball valve upstream of the blower acted to increase the static pressure in the test section.

4.2 Test Section

The test section, where all pin fin force measurements were made, was the heart of the test facility. This section was located immediately downstream of the plenum, as shown in Figure 4.1. Figure 4.5 provides a three-dimensional rotated view of the test

section portion of the wind tunnel. The test section penetrated through the 1.3 cm thick rear plenum wall, and extended 5.1 cm upstream into the plenum. AT-200Y sealant tape was used to seal the gap in the rear plenum wall around the test section. The sealant tape was placed inside the plenum, where the positive pressure in the plenum helped push the AT-200Y into the gap.

The test section was 1.33 m long, with an open flow area of 61 cm wide by 0.96 cm high. Figure 4.6 provides a dimensioned schematic of the test section, and shows the location of the pin fin row studied in this thesis. The height and width of the test channel were constrained by the requirements discussed at the opening of this chapter. The test section length was constrained by a combination of pin fin geometry and flow requirements. Although Figure 4.6 shows that only one pin fin row was studied in this thesis, future studies will include multiple pin rows. As such, approximately 25 cm of channel length was reserved to accommodate up to five streamwise rows of pin fins.

The upstream channel length was dictated by the need to achieve a fully developed turbulent velocity profile before reaching the pin fin array. Equation 4.1 provides a correlation for the hydrodynamic entrance length of a turbulent channel flow [Munson, et al, 1998].

$$L_e = 4.4 D_H (Re)^{1/6} \tag{4.1}$$

Equation 4.1 was used to calculate a maximum required entrance length of 27 hydraulic diameters at the highest flow condition of Re = 5.0 X 10^4. For conservatism, this entrance length was rounded up to 37 hydraulic diameters (70 cm) to account for uncertainty in the correlation's applicability to rectangular channels. Downstream of the pin fin array, 20 hydraulic diameters (51 cm) were included to eliminate any propagation of dynamic effects from the diffuser into the pin fin array. Summing these three lengths, the entire test section achieved a length of 70 D_h (1.33 m).

The test section channel floor was constructed from a single Lexan plate, 1.33 m long by 76 cm wide by 1.3 cm thick. The test section ceiling was constructed of two separate Lexan plates to allow for installation of the force sensor and assembly to the plenum. The upstream ceiling protruded into the plenum box, and measured 42 cm long by 76 cm

wide by 1.3 cm thick. The downstream ceiling measured 91 cm long by 76 cm wide by 1.3 cm thick. The two ceilings were joined by Plexiglas flanges glued to each plate. Through holes were machined into the floor plate and the downstream ceiling to provide clearance for the sensor and pin fin to penetrate the channel walls. The DSC-6 sensor assembled to the test section floor via an adjustable mount. A Lexan cup, painted black to shield the sensor from light, was bolted to the bottom of the test section such that the DSC-6 sensor may be submerged in a silicone oil bath. Silicone oil was fed into the cup by squeezing a modified soda bottle. Figure 4.7 shows the silicone well and modified soda bottle. The silicone reservoir on top of the ceiling was achieved via a counterbore in the Lexan ceiling. Gravity fed the silicone from the counterbore down into the pin fin gap. Further discussion of the sensor mount and silicone wells is provided in Section 4.3.

All three Lexan sheets (two acting as the test section ceiling and one as the test section floor) were machined by an external machine shop, Mountain Precision Tool. The adjustable sensor mount was manufactured by the Virginia Tech Mechanical Engineering Machine Shop. Mechanical drawings of the Lexan pieces and ancillary sensor mounting equipment are provided in Appendix E.

The ceiling and floor were separated by a MDF spacer on each side. The MDF spacers were cut from 0.98 cm thick sheet (advertised as 0.95 cm thick) to a size of 1.33 m long by 7.6 cm wide. The spacers were then sanded down to the desired thickness of 0.96 cm. Over time, however, the MDF spacers were compressed to be thinner by the applied clamping force. To alleviate this problem, 0.01 cm thick masking tape was added in layers at appropriate locations to increase the thickness back to 0.96 cm. Figure 4.8 provides a cross-sectional view of a taped MDF spacer sandwiched between the Lexan floor and ceiling.

Due to the large aspect ratio of the channel, the test section velocity was very sensitive to the channel height. A variation in channel height of just 0.048 cm resulted in a velocity change of approximately 5%. However, the elasticity of the Lexan ceiling and the wide aspect ratio of the test channel made it difficult to maintain an appropriate tolerance in the channel height. To minimize deformation of the test section, a combination of internal supports, an external aluminum I-beam, and an external MDF ceiling cover were used. Figure 4.9 presents a dimensioned diagram of how the internal

ceiling supports were placed in the channel. The internal supports consisted of cylindrical pins and symmetric airfoils strategically placed to support the ceiling without adversely affecting the flow through the pin fin array. Figure 4.10 shows a photograph of the test section, illustrating how the aluminum I-beam and MDF cover were installed. The aluminum I-beam was bolted over top of the upstream ceiling, and measured 10 cm tall by 7 cm wide. The MDF ceiling cover was bolted down over top of the downstream ceiling. The purpose of both the aluminum I-beam and the MDF cover was to evenly distribute the clamping force over the ceiling area.

To obtain accurate mass flow measurements, it was essential that the test section be well sealed. Poron foam strips, 1.27 cm wide by 0.64 cm thick, were used to seal the test section between the MDF spacers and Lexan plates. Gasket glands were machined into the Lexan plate floor and ceilings to control foam compression to 70%. Figure 4.8 provides a cross sectional view of the test section wall, illustrating how the Poron gasket fits into the machined gland. Poron foam was chosen as the gasketing material because it would not deteriorate in the presence of silicone oil and had excellent compression set resistance. Poron gasketing strips may be purchased by the roll from McMaster Carr.

Pressure taps were placed in the ceiling to obtain static pressure measurements throughout the channel. Figure 4.11 illustrates an installed pressure tap in the channel ceiling. The pressure taps were constructed of brass tubing with an outer diameter of 0.16 cm and an inner diameter of 0.08 cm. The flow end of the pressure tap was beveled and mounted flush with the inner surface of the channel ceiling. Care was taken to ensure that the pressure tap did not protrude into the flow, as this would adversely affect the accuracy of the pressure measurement. A quantity of 15 pressure taps was spaced in the streamwise direction to permit calculation of the friction factor used in channel benchmarking. Additionally, two rows of seven pressure taps spanning the entire width of the test section were placed 8.67 D_h upstream and 6.67 D_h downstream of the pin fin row. The purpose of the two rows of pressure taps was to measure the pressure difference across the pin fin row. The upstream pressure tap row was located farther away from the pin fins to ensure the static pressure measurement was not affected by the downstream pin fins. The static pressure taps were also used to confirm flow uniformity and ensure the internal ceiling supports (reference Figure 4.9) had no effect on the flow at

the pin fin array. Table 4.1 details the locations of all static pressure taps. Reference Figure 4.9 for definition of the X and Y test section axes cited in Table 4.1.

The entire test section was supported by a Unistrut frame with a 2.5 cm thick MDF table top. The MDF table top was sanded and taped (much in the same way as the MDF spacers) to achieve a perfectly flat surface. This was necessary to achieve a uniform cross sectional flow area. SAE F-3 felt, 0.32 cm thick, was sandwiched between the MDF table and Unistrut frame to provide mechanical vibration damping. To isolate the test section from ambient vibrations, one piece of 0.32 cm thick SAE F-3 felt and one piece of 0.32 cm thick rubber were placed underneath each leg of the frame. In hindsight, the test section frame would have been better framed by wooden two-by-fours to take advantage of the inherent damping properties of wood.

4.3 Force Measurement and Sensor Mounting Considerations

Certainly, the key design consideration for the test section was how to achieve accurate force measurements. Chapter 3 briefly discusses how the DSC-6 sensor was configured to measure the aerodynamic forces on the pin fins. Recall that this design made use of the work done by DeTurris [1992]. This section provides specific details regarding the sensor mounting in the test section.

Figure 4.12 provides a cut-away CAD view depicting how the DSC-6 sensor mounted to the test section. Additionally, Figure 4.13 provides a photograph of the mounted sensor and pin fin in the test channel. Figure 4.12 shows that the sensor was bolted to an adjustable sensor mount, which was in turn bolted to the bottom of the test section floor. The DSC-6 sensor was completely submerged in silicone oil. The oil also filled the pin fin gap in the channel floor. The silicone well on top of the channel served to fill the pin fin gap in the ceiling with oil. Although the basic concept of the design was simple, four important points were given special attention during the design process.

The first point was the selection of a viscous, Newtonian fluid to fill the gap between the flow element and the hole. The fluid used in the gap must not exhibit any elastic or shear memory properties, as this would distort the force sensor output. Dow Corning 200 silicone oil, used by DeTurris [1992], was a Newtonian fluid that exhibited many advantageous properties. Two different viscosity grades could be blended together, on a

percent by weight basis, to form an intermediate viscosity fluid. This provided a nearly infinite range of possible viscosities. The 200 silicone oil was available in viscosities up to $1.0 \text{ X } 10^5$ cSt. Although the oil viscosity had no direct effect on force measurement (as discussed in Chapter 3), a high viscosity oil was desirable to prevent fluid from being sheared out of the sensor gap at the higher flow rates. Several different viscosity blends were used in the pin fin/hole gap on a trial-and-error basis. In the floor gap, silicone oils with viscosities greater than $5.0 \text{ x } 10^4$ cSt could be used for $Re < 1.5 \text{ X } 10^4$. For $Re > 1.5 \text{ X } 10^4$, it was necessary to use an oil with a viscosity greater than $1.0 \text{ X } 10^5$ cSt to keep the oil from blowing out of the pin fin gap. In general, it was preferred to use the least viscous oil possible in the bottom silicone well. The less viscous oils were easier to work with because they took less time to fill the relatively large bottom silicone well and did not wick up the cylinder as much as the more viscous oils. The ceiling silicone well required silicone oils with a viscosity greater than $1.0 \text{ X } 10^5$ cSt for all flow rates. The larger viscosity was required to prevent the oil from flowing down through the pin fin gap. Because the ceiling silicone well was only a counterbore in the downstream ceiling plate, the filling problems experienced in the bottom silicone well were not a problem.

The silicone oil also acted as a thermal sink for maintaining the sensor at a constant temperature. Because the fluid was static, conduction was the dominant heat transfer mode. Thus, thermal conductivity was considered for evaluating the ability of the silicone oil to maintain an isothermal sensor. The thermal conductivity of Dow Corning 200 silicone oil was approximately $1.59 \text{ X } 10^{-1}$ W/mK [Dow Corning, 2000]. Thus, the silicone oil was more thermally conductive than air ($k = 2.63 \text{ X } 10^{-2}$ W/mK), but less conductive than water ($k = 6.13 \text{ X } 10^{-1}$ W/mK) [Incropera and DeWitt, 1996].

Although silicone oil is not a great thermal conductor, this requirement must be balanced against the requirement for an electrically insulating fluid. Generally speaking, materials that conduct heat well are also excellent electrical conductors. Dow Corning 200 silicone oil is an exceptional electrical isolator, commonly used as a dielectric fluid in high voltage transformers. Consequently, Dow Corning 200 silicone oil provides a nice balance of thermal conductivity and electrical insulation.

Another favorable quality of the oil is a relatively low surface tension. Dow Corning [2000] states that the surface tension of the 200 silicone oil is $2.15 \text{ X } 10^{-2}$ N/m, compared

to 7.17 X 10^{-2} N/m for water [Incropera and DeWitt, 1996]. Surface tension can affect sensor output if the level of the silicone oil is not exactly the same around the entire circumference of the cylinder. Varying heights of silicone oil will pull the cylinder in the direction of the tallest fluid height. Additionally, surface tension will tend to pull the fluid up through the gap and into flow channel via capillary action. Choosing a low surface tension fluid can minimize these 2 effects. Appendix F provides the physical properties of silicone oil, as specified by Dow Corning.

The second point considered for the sensor installation was selection of a hole diameter for the sensor / pin fin to protrude through the floor and ceiling. The hole diameter had to provide enough room for the sensor to deflect under loading, yet be small enough to prevent silicone oil from flowing out of the gap. To this end, calculations were developed to predict the amount of sensor deflection under a given loading. Although Kistler Morse (manufacturer of the force measurement sensor) provided a deflection equation for their DSC-6 sensor, the equation did not appear to be grounded in any physical phenomena. As such, I developed my own deflection model rooted in classical mechanics of materials theory. The details of the model, along with applicable deflection equations, are described in Appendix G.

The forces applied to the DSC-6 sensor beam are reaction forces from the pin fin. The aerodynamic force acting on the pin fin is reacted (by the DSC-6 beam) in the form of an equal and opposite force, and an applied moment. The moment results from the linear distance between the aerodynamic center of pressure and the DSC-6 reaction force. Once the pin fin is deflected, the weight of the pin fin will further contribute to the deflection of the sensor. Because the pin fin is nearly 4 times the diameter of the DSC-6 beam, the pin fin is considered rigid and does not bend. The developed model uses linear superposition to combine beam deflections due to all three factors. The result of the superimposed deflections represents the net deflection of the DSC-6 beam.

Appendix G also provides output for the deflection of a ϕ 0.95 cm cylinder in a Re = 5.0 X 10^4 flow. For the current sensor mount, the beam tip extended approximately 0.29 cm above the channel floor. This meant the DSC-6 had an effective beam length of 3.46 cm. Using these inputs, the deflection model recommended a hole size of ϕ 0.98 ± 0.003 cm for the ϕ 0.95 ± 0.0013 cm cylinder after taking manufacturing tolerances into

account. This left a gap size of approximately 0.014 ± 0.002 cm between the hole and cylinder. Aside from determining the pin fin hole size, material selection was also carefully considered. The need for an orthogonal, tight tolerance hole drove the material selection for the test section. Although Plexiglas would have been stiffer and cheaper, Lexan was chosen because of its machineability.

Sensor alignment in the pin fin hole was the third point considered. Ideally, the sensor / pin fin assembly would be placed coaxially in the hole and orthogonal to the channel floor. Figure 4.14 provides a photograph of the sensor mount designed to meet the above requirements (mechanical drawings are provided in Appendix E). The mount was designed to accommodate the stack-up of manufacturing tolerances in both the channel floor and the mount itself. A geometric tolerance study was conducted to properly size clearance holes that allowed translation in the plane of the channel floor. Additionally, rotation of the sensor about all three axes was possible. A cylindrical gauge block was used to align the sensor orthogonal to the channel floor, while a concentric ring of set screws was used to adjust the location of the sensor in fine increments. A photograph of the installed ring is provided in Figure 4.15. The position of the sensor / pin fin in the hole was checked by deflecting the sensor in two perpendicular directions and checking the sensor output. In this manner, the sensor could be iteratively moved and checked until it was sufficiently centered in the hole. Appendix H provides detailed instructions on how to install the sensor using the aforementioned tooling.

The fourth, and perhaps most difficult point considered, was the alignment of the ceiling hole over the pin fin. The ceiling had to be carefully slid over the protruding pin fin and bolted to the MDF spacers while achieving the same gap tolerance found in the hole placed in the test section floor. Locating holes and dowel rods were included in the test section design in an attempt to achieve an efficient ceiling assembly process. The ceiling and floor Lexan plates were manufactured with four matched holes drilled to 0.635 ± 0.0025 cm in diameter. The holes were to be match drilled after aligning the ceiling and floor pin fin holes with a gauge pin. During assembly, a MS-51576 shoulder screw (ϕ 0.635 ± .0012 cm) could then be inserted into each match drilled hole in the floor. The ceiling could then be slid down over the shoulder bolts, ideally yielding a ceiling hole aligned perfectly above the floor hole. In practice however, this gauging

technique failed due to a combination of poor manufacturing tolerances and excessive deflection by the Lexan ceiling. Consequently, it became necessary to manually install the downstream ceiling over the pin fin, and iteratively tap the ceiling into place while tightening the bolts. Although laborious and time consuming, a satisfactory tooling method capable of improving the process was not found.

One can easily surmise that assembly of the test section is a difficult task. The need to span large, unsupported lengths with relatively flexible Lexan plates does not readily lend itself to the dimensionally exacting requirements of the test section. The dimensional accuracy of the test section is very sensitive to the assembly process. A detailed, step-by-step account of the assembly process is provided in Appendix H. It is imperative that this assembly process is carefully followed while assembling the test section.

4.4 Test Facility Summary

Without a doubt, a major part of this research project is the design and construction of the test facility. After significant testing and benchmarking efforts, I believe that the constructed facility meets the requirements and objectives of the project. However, due to the tight tolerances required to make accurate measurements, care must be exercised while assembling and running the test rig. Enough emphasis cannot be placed on following the assembly guidelines set forth in Appendix H, and vigilant attention to the sensor output. The environmental conditions discussed in this chapter that affect the DSC-6 sensor must be controlled. Accurate measurements can only be achieved with a correctly assembled test section and a properly conditioned force sensor.

Table 4.1 Test Section Pressure Tap Locations

Pressure Tap	X - Streamwise (cm)	Y - Spanwise (cm)
1	14.0	0.00
2	19.1	0.00
3	21.6	0.00
4	30.4	0.00
5	30.4	-3.81
6	35.6	0.00
7	38.1	0.00
8	45.7	0.00
9	53.3	0.00
10	62.2	0.00
11	66.0	0.00
12	66.0	-7.62
13	66.0	-14.0
14	66.0	-22.9
15	66.0	6.35
16	66.0	15.2
17	66.0	22.9
18	95.3	-1.27
19	95.3	-7.62
20	95.3	-15.2
21	95.3	-22.9
22	95.3	22.9
23	95.3	7.62
24	95.3	15.2
25	95.3	1.27
26	49.5	0.00
27	57.7	0.00
28	71.1	0.00
29	76.1	1.27

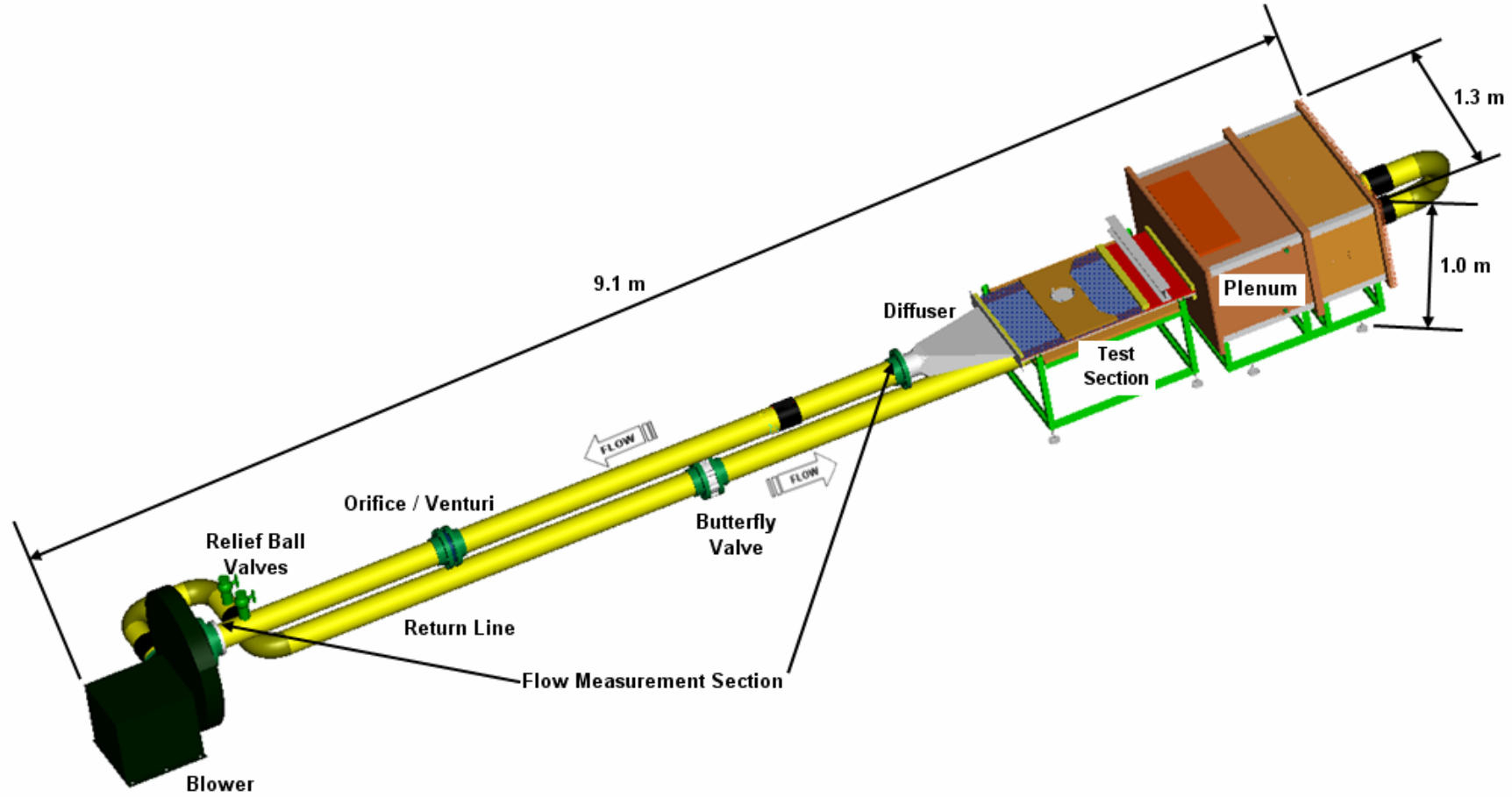

Figure 4.1 Annotated, three-dimensional CAD rendering of complete test facility. Each of the major facility components is noted.

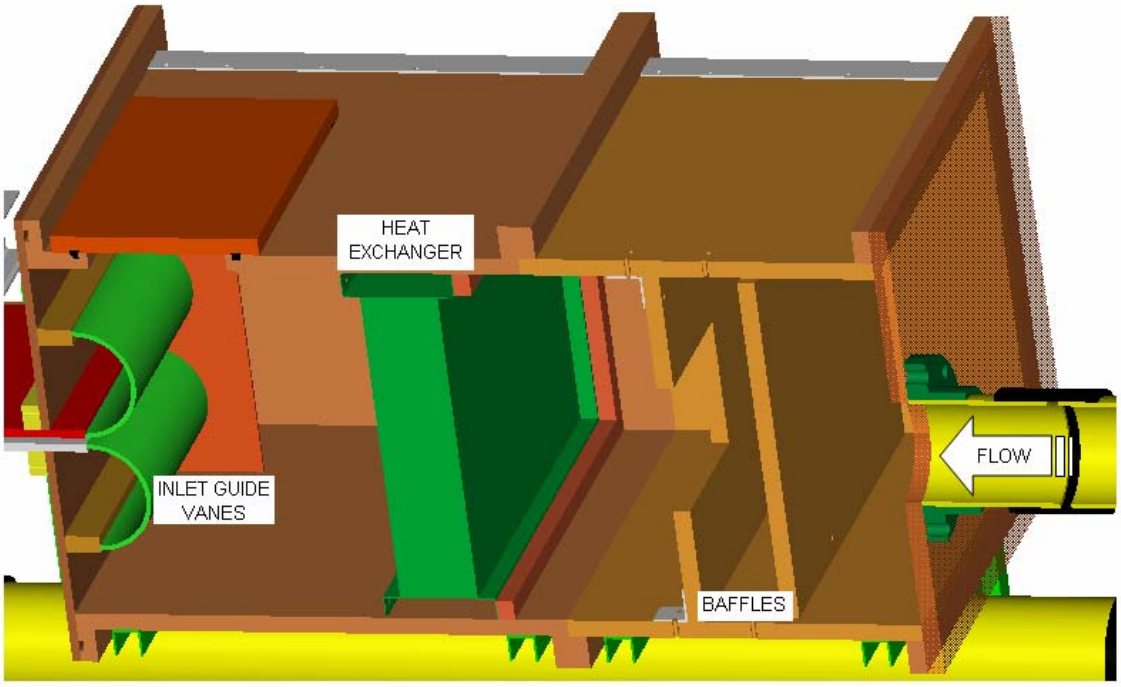

Figure 4.2 Three-dimensional cut-away view of the plenum. Key components are labeled in the figure. The test section can be seen protruding through the left wall.

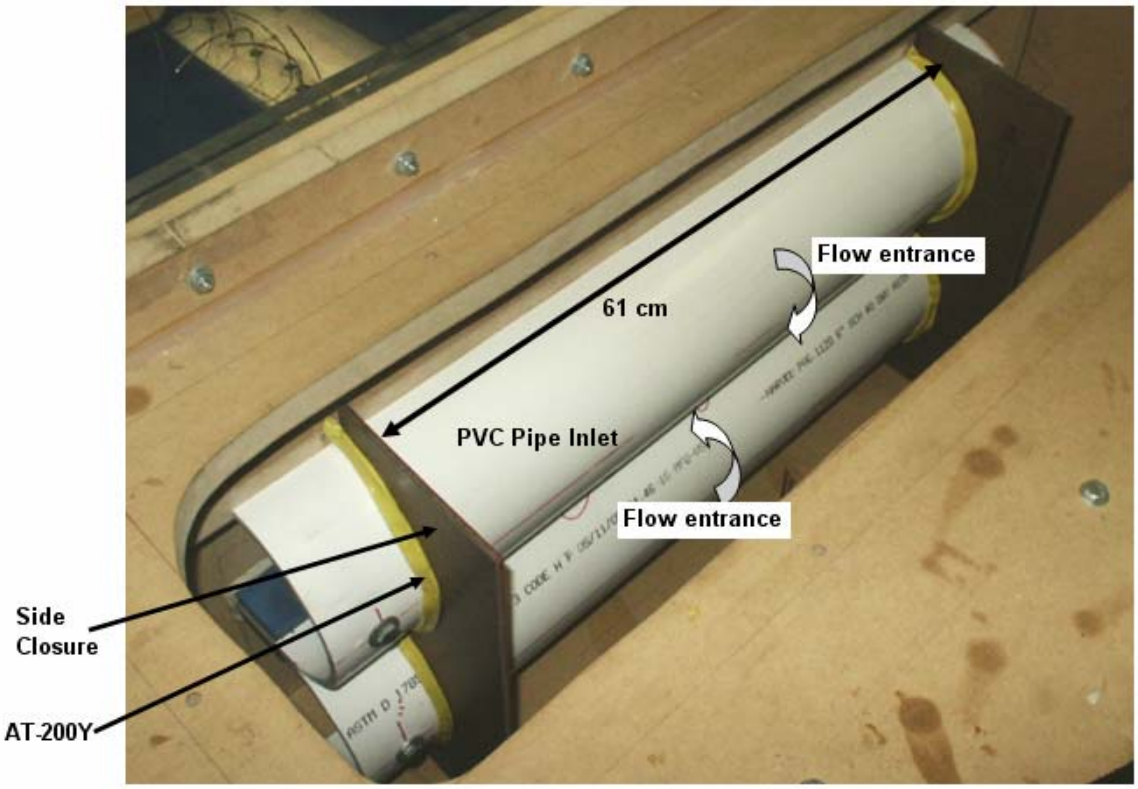

Figure 4.3 Photograph of inlet guides mated to the test channel in the plenum. The guides provide a smooth flow contraction into the test section.

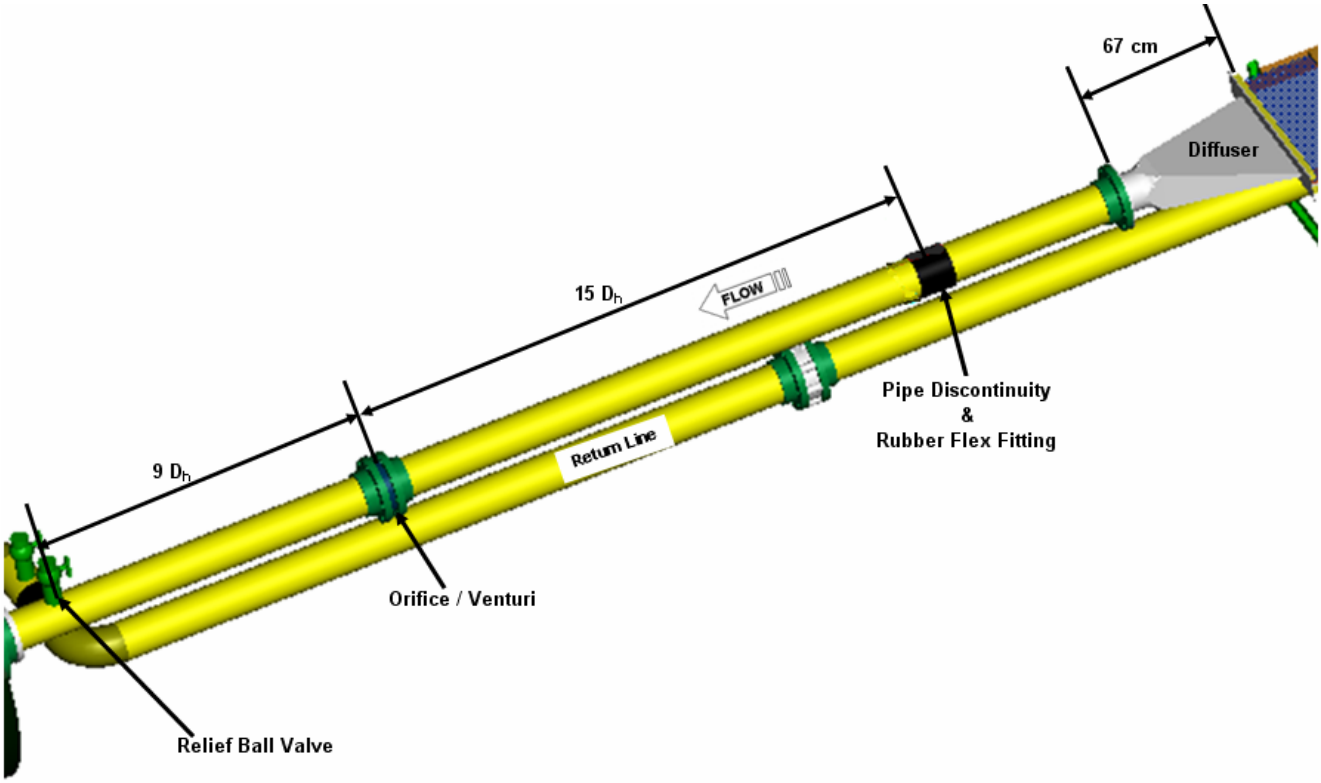

Figure 4.4 Three-dimensional view of the flow measurement section of the test facility. Uninterrupted pipe lengths upstream and downstream of the flow meter are dimensioned.

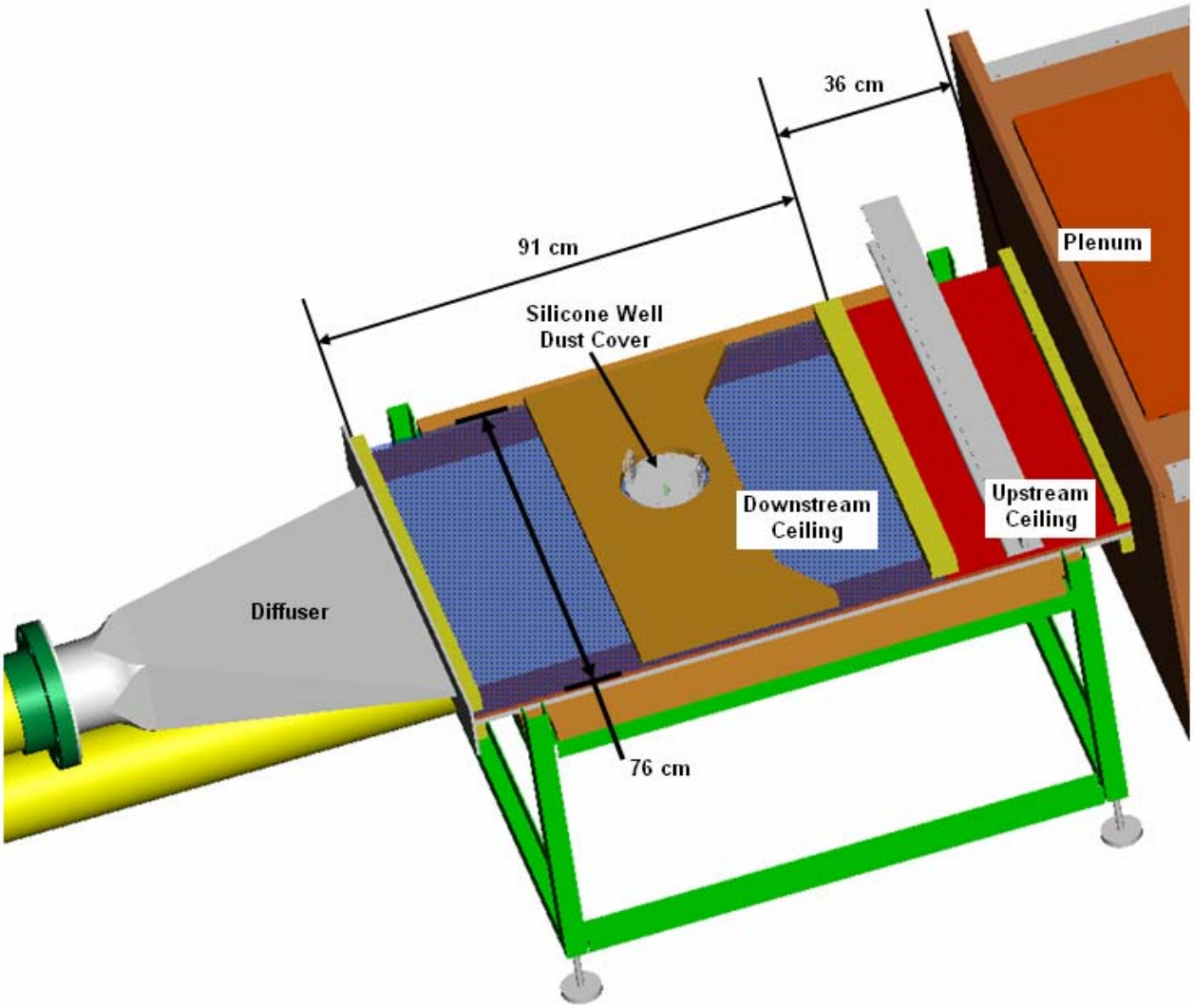

Figure 4.5 Three-dimensional CAD rendering of the test section. The upstream and downstream ceiling pieces are illustrated in red and purple, respectively.

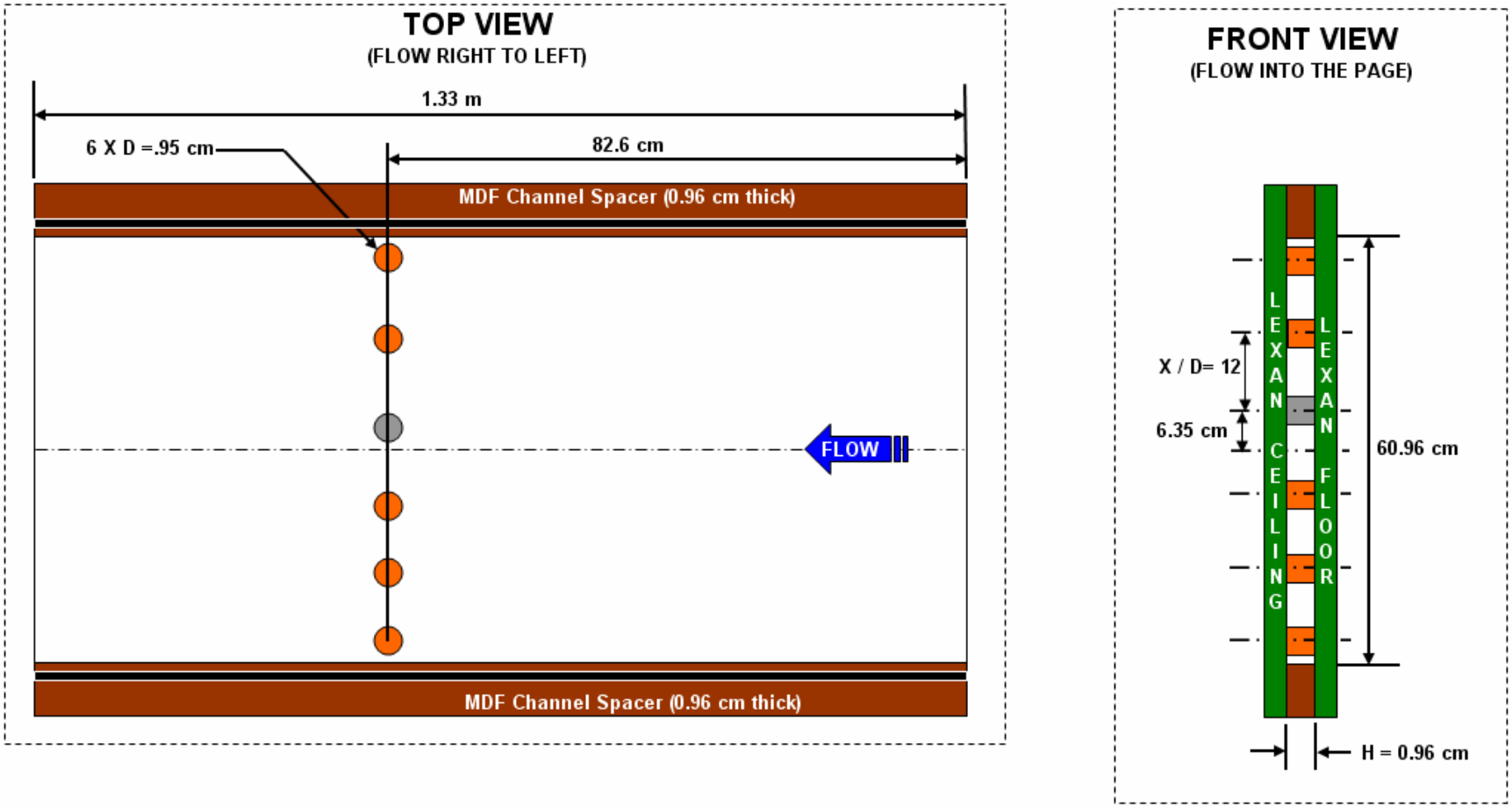

Figure 4.6 Schematic showing dimensions of test channel size and pin placement. The gray pin represents the pin on which force measurements were made. Orange pins are static "dummy" pins rigidly attached to the channel floor and ceiling.

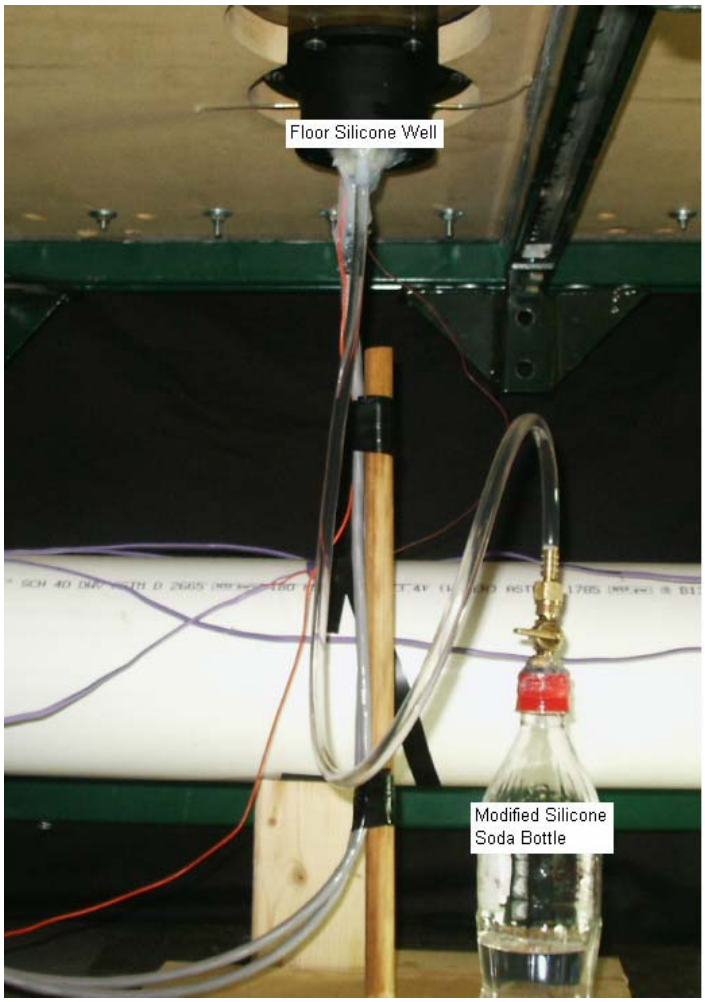

Figure 4.7 Annotated photograph of installed floor silicone well and modified soda bottle.

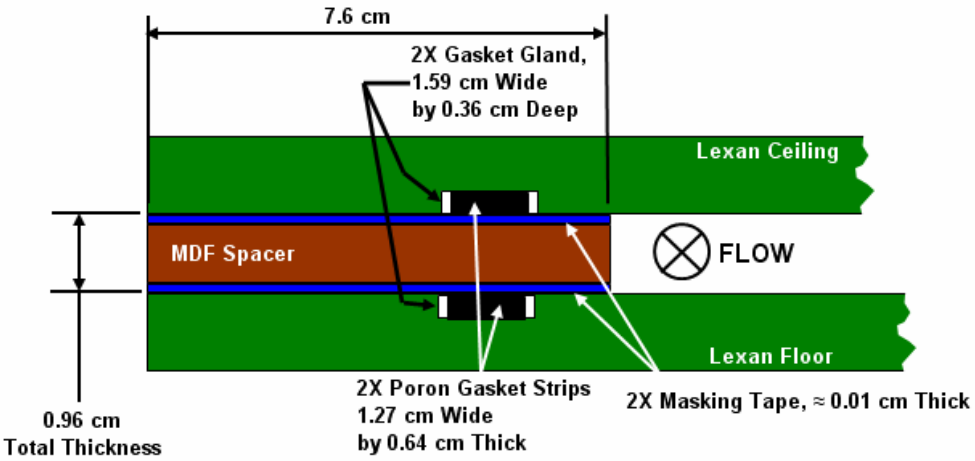

Figure 4.8 Cross sectional view of MDF spacer taped with blue masking tape to correct the spacer thickness. The correct channel height is 0.96 cm.

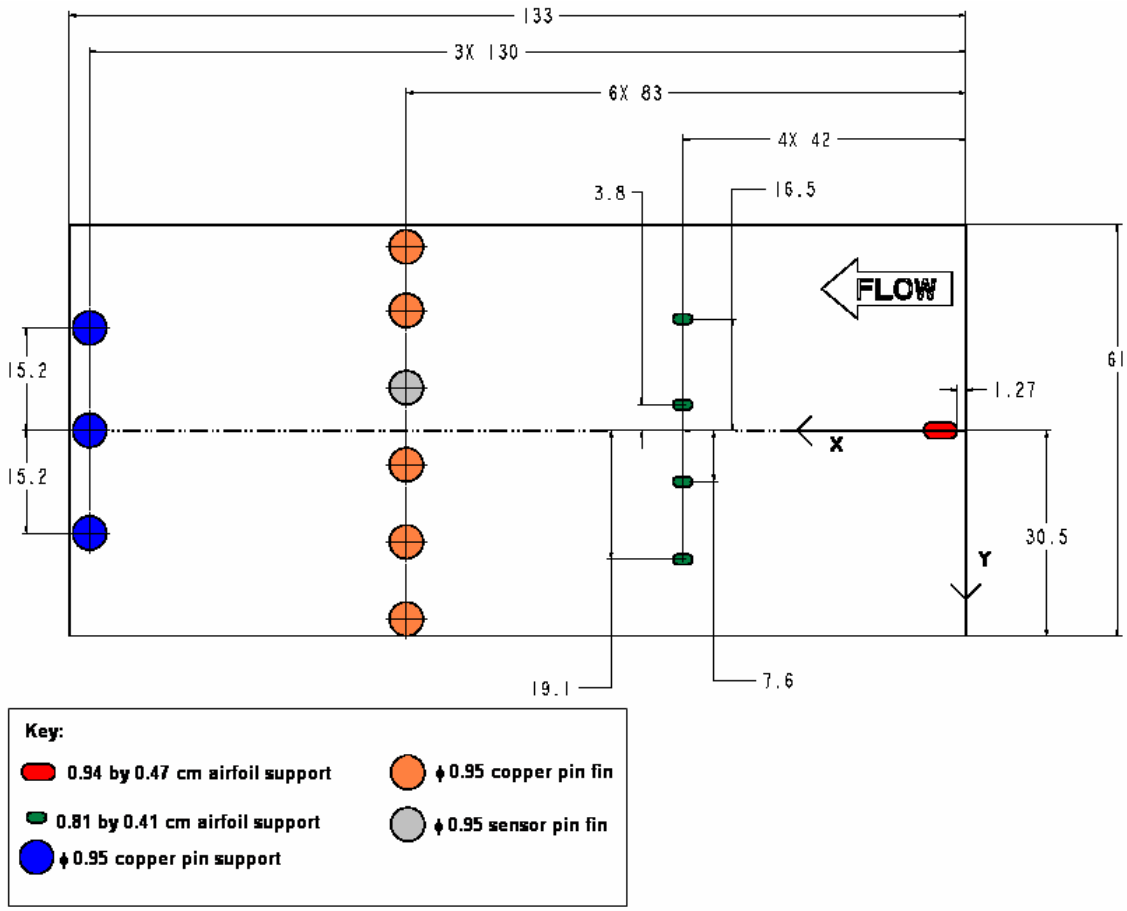

Figure 4.9 Diagram of internal ceiling support locations (all dimensions in cm). Symmetric airfoils are placed upstream of the pin fin array to minimize the effect on the flow dynamics. The copper pin fins used in the array provide additional support, along with the 3 copper pin supports at the rear of the test section.

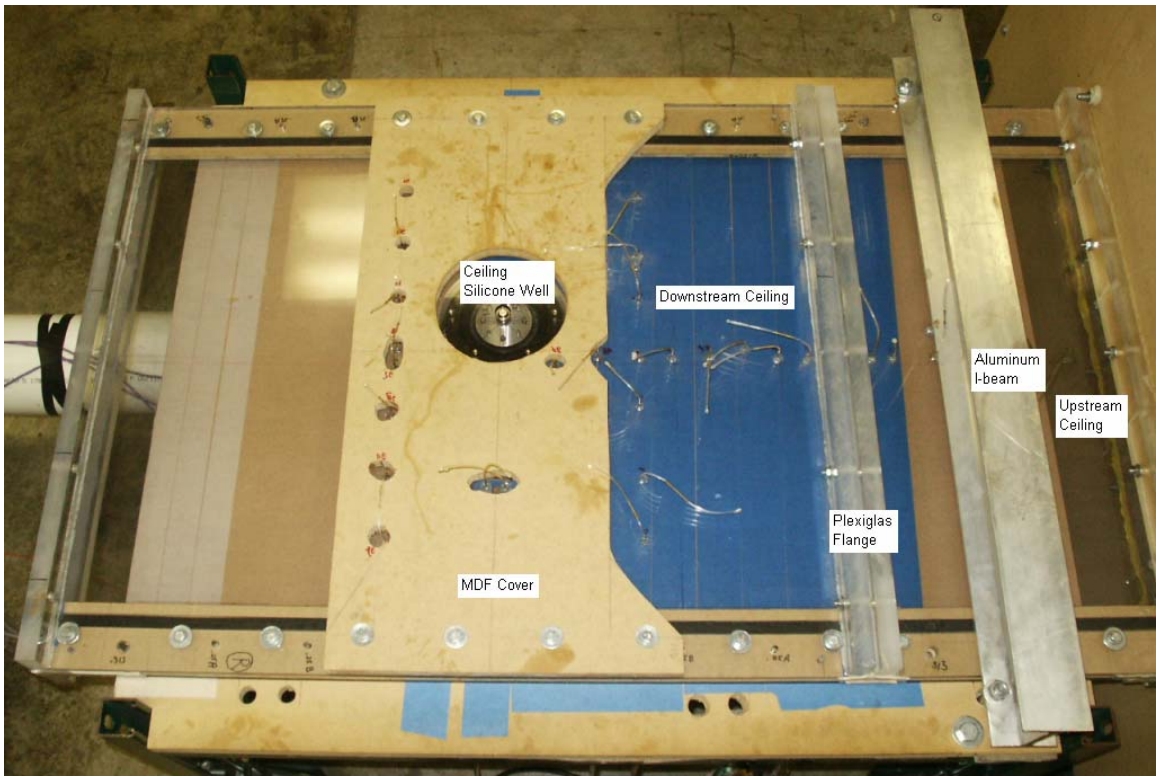

Figure 4.10 Annotated photograph of the test section, top looking down. The external ceiling support pieces are explicitly labeled.

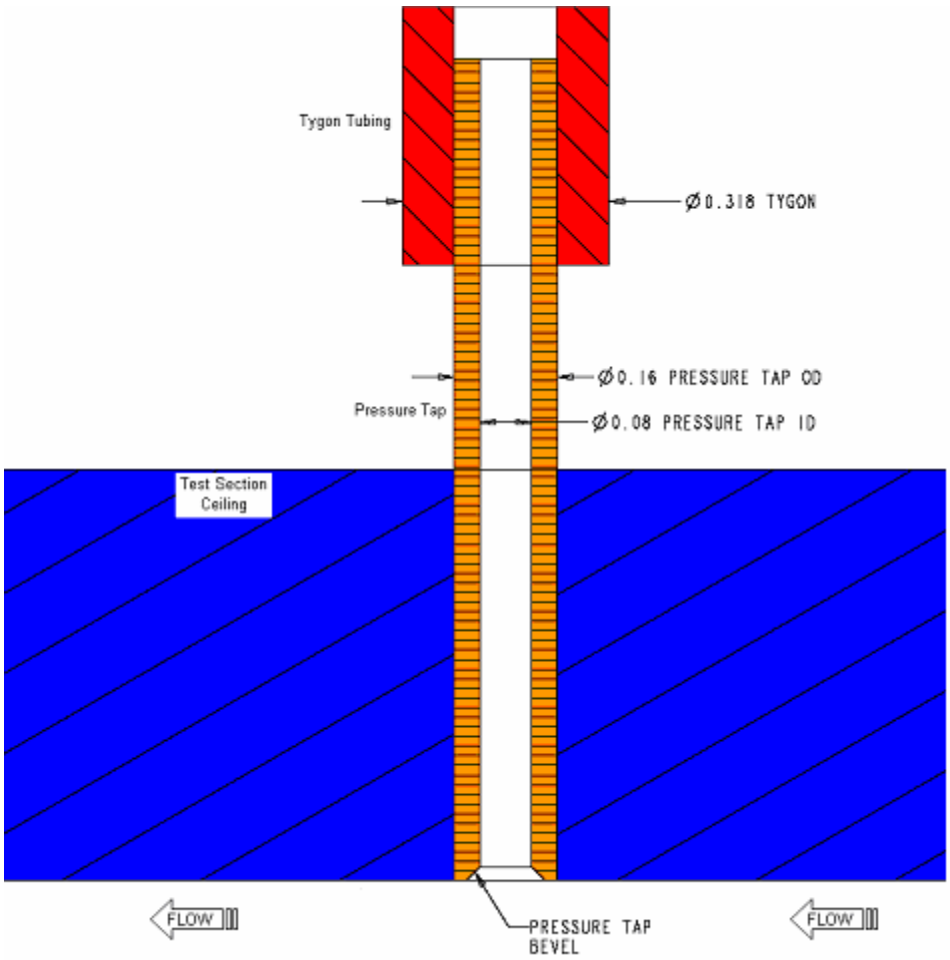

Figure 4.11 Illustration of a static pressure tap installed in the channel ceiling. The pressure tap is beveled on the flow end to ensure the tap does not affect the flow. All dimensions are in cm.

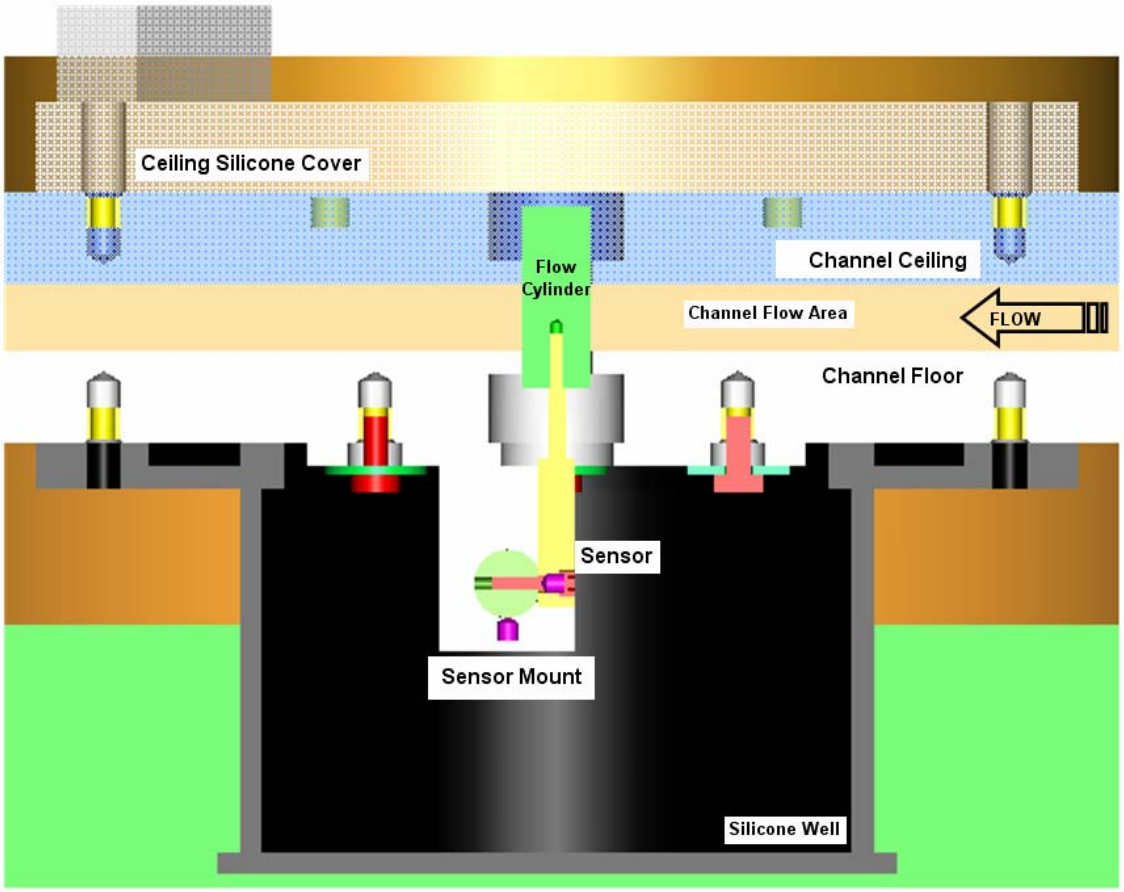

Figure 4.12 Annotated cut-away view of the sensor mounted in the channel.

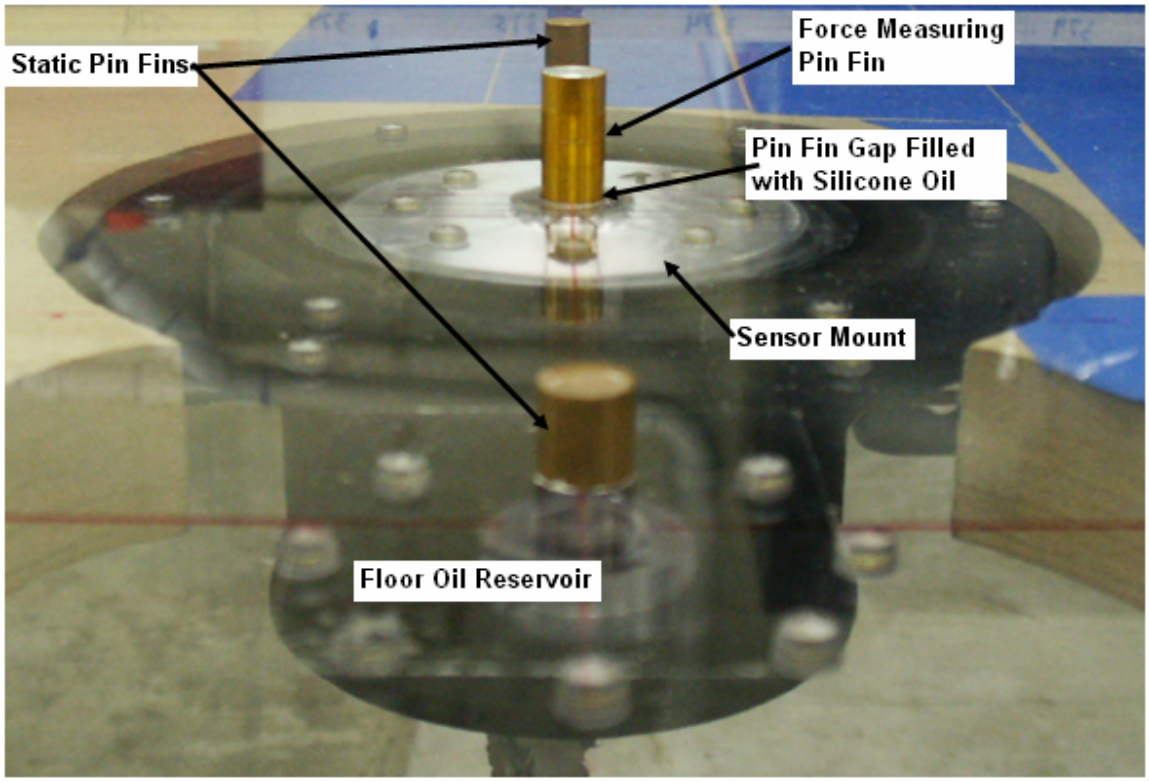

Figure 4.13 Annotated photograph of the DSC-6 sensor and pin fin mounted in the test channel. To permit visualization, the channel ceiling is removed for this photograph.

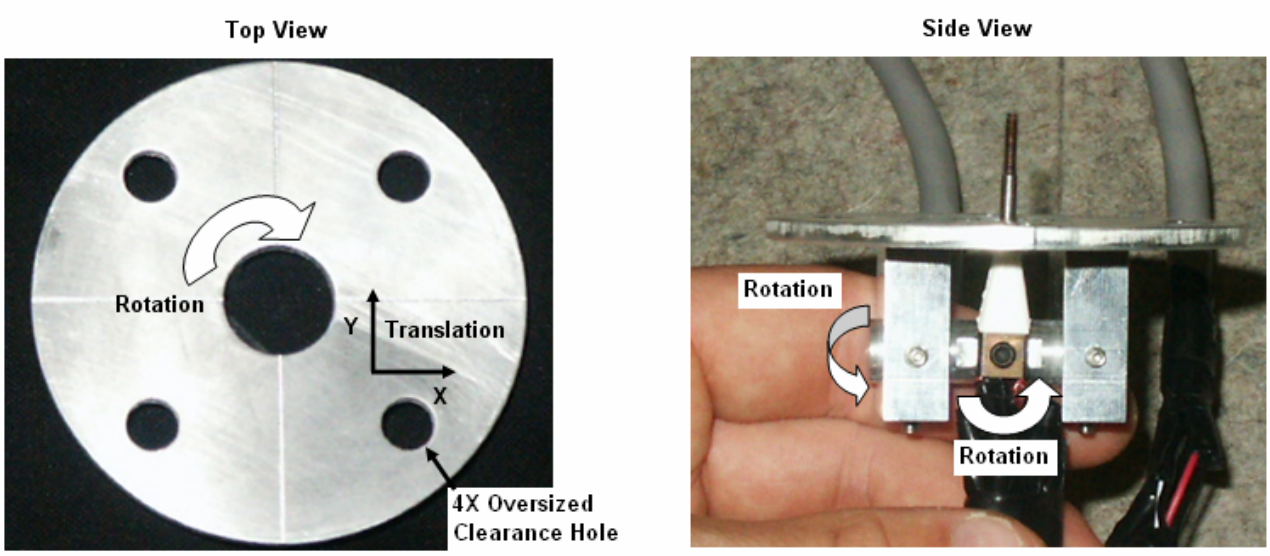

Figure 4.14 Top and side view of sensor mounting bracket. Two degrees of translation and three degrees of rotation are permitted by the mount, allowing the user to align the sensor orthogonal to the channel floor and parallel to the flow. The side view shows the sensor installed in the mount.

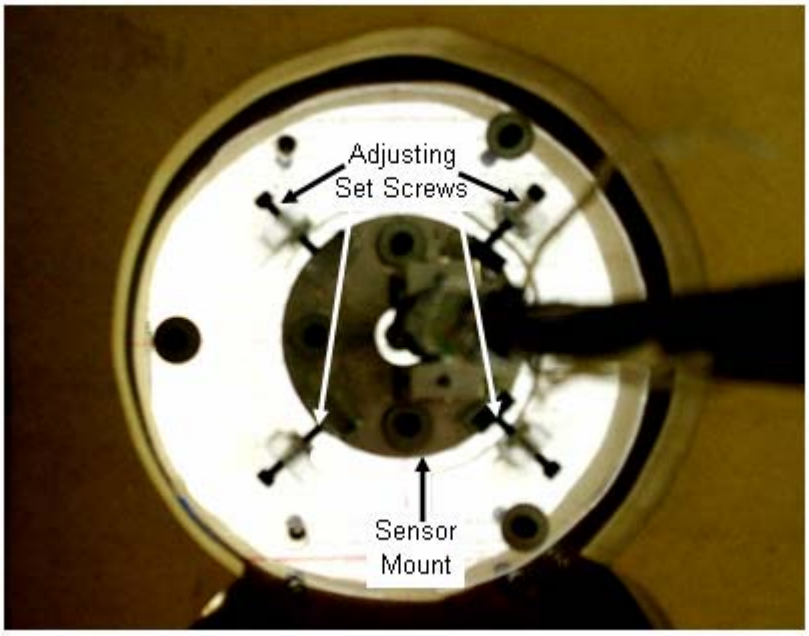

Figure 4.15 Bottom looking up view of the set screw ring installed around the sensor mount on the test channel floor.

Chapter 5

Facility Benchmarking and Experimental Results

This chapter presents the results from the flow benchmarking tests as well as force measurement results from actual cylinder testing. A summary of the data obtained from successful tests is provided, as well as a cursory view of failed tests. The failures are presented so that the reader can understand what parameters are important to achieve a successful test, and the lessons I learned while conducting the tests.

Section 5.1 describes the process used to benchmark the channel flow in the test section. Friction factor measurements are presented to show the channel achieved full hydrodynamic development. Spanwise static pressure measurements are used to show the uniformity of the flow across the test section. The friction factor and spanwise static pressure measurements demonstrate the importance of properly installed inlet guides at the front of the channel.

Section 5.2 provides lift and drag results from force tests conducted on a single row of H/D = 1, S/D = 12 cylindrical pin fins. The results from two different test series are presented to show the sensitivity of the experiment to the gap size and silicone oil viscosity. The poor results from the Large Gap Test Series, which used a pin fin gap size of 0.025 cm in the floor relative to the Small Gap Test Series, which used a pin fin gap size of 0.014 cm, are presented to highlight the need to ensure the gap size is small enough to prevent excessive silicone oil leakage. Data from the Small Gap Test Series are presented as valid results. Best fit trend lines of the experimental drag coefficients calculated from the Small Gap Test Series, although larger in magnitude, appear to approximately follow the trend of an infinite cylinder drag coefficient. The drag coefficient peaks to a value of $C_D = 1.96$ at $Re = 1.4 \times 10^4$ and becomes approximately constant for increasing Reynolds number.

5.1 Facility Benchmarking

Two requirements were imposed upon the flow in the test section. The velocity profile of the channel flow had to be hydrodynamically fully developed before reaching the pin fin array, and the flow needed to be uniform in the spanwise direction. Spanwise uniformity ensured that the streamwise velocity magnitude was consistent from left to right in the test section and that any spanwise component of the velocity was negligible. This section describes the benchmarking process used to show the channel met these two objectives.

Hydrodynamic development in the test channel was proven by calculating the Darcy friction factor in the channel flow. The Darcy friction factor is defined by Munson et al. [1998] to be:

$$f = \frac{\Delta P}{\left(\frac{\Delta x}{D_H}\right)\left(\frac{1}{2}\rho U^2\right)} \tag{5.1}$$

The friction factor represents a non-dimensional static pressure loss for a given channel length (Δx). For hydrodynamically fully developed flow, the friction factor is constant. Alternately stated, the static pressure drop is linear with respect to channel distance in the axial direction. The friction factor is only a function of the flow Reynolds number, relative surface roughness, and the geometric shape of the channel cross section. For turbulent channel flows (all flows in this project are considered to be turbulent), analytical solutions for the friction factor do not exist. As such, empirical correlations are used to predict the friction factor in the channel. Kakac et al. [1987] provide the following correlations for flow in a rectangular duct:

$$f_F = \frac{0.1268}{Re^{0.3}} \quad \text{for } 5.0\,X\,10^3 \le Re \le 3.0\,X\,10^4 \tag{5.2}$$

$$f_F = \frac{0.0868}{Re^{0.25}} \quad \text{for } 1.2\,X\,10^4 \le Re \le 1.2\,X\,10^6 \tag{5.3}$$

Equation 5.2 and Equation 5.3 overlap in the region of $1.2 \text{ X } 10^4 \leq Re \leq 3.0 \text{ X } 10^4$. Kakac et al. [1987] state that Equation 5.2 is preferable to Equation 5.3 for all flows in the overlap region. Note that the Reynolds number is based on the mass averaged velocity and the channel hydraulic diameter for these correlations. Equation 5.2 and 5.2 provide a correlation for the Fanning friction factor, which is a non-dimensional quantification of skin friction. The Fanning friction factor can be related to the Darcy friction factor according to Equation 5.4 [Munson et al., 1998].

$$f = 4 * f_F \tag{5.4}$$

Thus, Equation 5.2 and Equation 5.3 can be transformed into the Darcy friction factor as provided by Equation 5.5 and 5.6 (respectively).

$$f = \frac{0.5072}{Re^{0.3}} \quad \text{for } 5.0 \text{ X } 10^3 \leq Re \leq 3.0 \text{ X } 10^4 \tag{5.5}$$

$$f = \frac{0.3472}{Re^{0.25}} \quad \text{for } 1.2 \text{ X } 10^4 \leq Re \leq 1.2 \text{ X } 10^6 \tag{5.6}$$

For this project, the Darcy friction factor was calculated from static pressure measurements obtained from the pressure taps listed in Table 4.1. The pressure difference (ΔP in Equation 5.1) was found by using the first pressure tap, located 15.7 hydraulic diameters downstream of the inlet, as the reference high pressure and subtracting the pressure at each axial location. In this manner, the static pressure relative to the first pressure tap was plotted on a curve for the entire length of the channel according to Equation 5.7.

$$\Delta P = P_1 - P_i \tag{Equation 5.7}$$

The slope of the linear portion of the curve represented the fully developed friction factor. To prove full hydrodynamic development in the test channel, it was

necessary to show a linear static pressure profile upstream of the pin fin array and match the published friction factor correlations provided in Equations 5.5 and 5.6. The measured friction factor was said to match the correlation if agreement within ± 5% was obtained.

Initially, the test section was constructed with no inlet guides attached to the entrance. The inlet guides were omitted in the original design because they were difficult and time consuming to install. With an entrance length of 37 hydraulic diameters, it was believed that any effects from flow separation at the channel entrance would be dissipated before reaching the pin fin array. Figure 5.1 plots the results from multiple friction factor tests conducted on the channel with no inlet guides. The experimentally measured friction factors are shown relative to the published correlations and the bounding 5% allowances. Although a few friction factor measurements fell within the acceptable limits, most did not. The friction factor measurements that did fall within the acceptable limits, most notably $Re = 1.5 \times 10^4$, were not repeatable. At first, it was believed that the poor friction factor results were caused by variations in the test channel height. Several attempts were made to constrain the channel to the correct height by adding more internal support airfoils and different medium density fiberboard top covers (reference the discussion in Section 4.2). However, these efforts proved fruitless (as reflected in Figure 5.1).

In the end, adding inlet guides to the channel entrance was the correct solution to the friction factor problem. Figure 5.2 plots the calculated friction factor for the test section channel with the inlet guides installed. Obviously, the data matched the published correlations much better with the inlet guides installed. The measured friction factors almost exactly overlaid the published correlations. Figure 5.3 plots the difference between the reference pressure tap (first pressure tap) and the series of downstream pressure taps for a $Re = 1.3 \times 10^4$ flow. Figure 5.3 shows that the slope of the pressure curve increased across the ceiling flange. This phenomenon, found in every friction factor test, can be attributed to an area change under the ceiling flange. Using a wooden block that was the height of the channel, it was observed that the channel height under the ceiling flange was less than the desired height of 0.96 cm. The decreased height reduced the channel flow area and forced the flow to accelerate underneath the ceiling flange.

Referencing Bernoulli's Equation for flow with no elevation change and negligible losses,

$$P_s + \frac{1}{2}\rho U^2 = P_T = C \tag{5.8}$$

one can see that the static pressure must decrease if the velocity increases. In Figure 5.3, this pressure decrease manifests itself as an increase in pressure difference (reference Equation 5.7), leading to the steeper slope. Note that the flow decelerates downstream of the local acceleration when the channel height returns to the nominal 0.96 cm. The downstream area change was confirmed with the wooden feeler block. Reference to Figure 4.9 shows that four airfoils were placed under the ceiling flange to minimize this phenomenon. The acceleration could not be completely eliminated and was instead tolerated because the flow reached a fully developed state upstream of the pin fin array.

Table 5.1 summarizes the friction factor results from each friction factor test conducted with the inlet guides installed. Table 5.1 shows that the R^2 value for every friction factor test exceeded 0.98. This indicated that the static pressure decreased linearly in the channel, and supported the conclusion that the flow was fully developed.

Spanwise uniformity was assessed using static pressure taps 11 – 17. As described in Section 4.2, the pressure taps were placed across the width of the channel, 8.67 D_h (16.6 cm) upstream of the pin fin array. By assuming the total pressure at any given axial location was constant across the channel, the static pressure was related to the flow velocity by Bernoulli's Equation (Equation 5.8). It was decided that the static pressure of any given pressure tap should not vary by more than 2.5% from the average row static pressure, when normalized by the dynamic pressure head. This criterion is algebraically stated in Equation 5.9.

$$\frac{\overline{\Delta P} - \Delta P_i}{\frac{1}{2}\rho U^2} \leq 2.5\% \tag{5.9}$$

Figure 5.4 plots the normalized static pressure difference for three different installations of the inlet guides (Installation A, Installation B, and Installation C). Each installation was a complete installation, not just a readjustment of the guides. As such, each installation was independent of another. All three uniformity tests were conducted at a Reynolds number of 1.3×10^4. Figure 5.4 demonstrates that the spanwise flow uniformity was sensitive to how the inlet guides were installed. Installation B yielded poor flow uniformity, but the previously tested Installation A and subsequently tested Installation C both produced acceptable flow uniformity.

Extreme care must be taken while installing the guides to ensure that the PVC half pipes are installed evenly across the width of the channel. If the guides are installed slightly askew to the channel floor or ceiling, significant spanwise non-uniformities can develop (as evidenced by Figure 5.4). Because the flow uniformity is so sensitive to the inlet installation, it is recommended that the static pressure distribution across the width of the channel is analyzed at least once after every new inlet guide installation. If only one Reynolds number will be checked for spanwise uniformity, it is recommended that the $Re = 7.5 \times 10^3$ flow is checked. It is likely that the flow uniformity will be most sensitive to the inlet guide installation at $Re = 7.5 \times 10^3$, because viscous effects are the most important at the lowest Reynolds number.

Figure 5.5 provides a plot of five different spanwise static pressure distributions for Installation A. The plot shows that all five flow cases fall within the specified 2.5% criterion. The fact that all tests fall within the acceptable limits demonstrates that the fluid-dynamic effect of the upstream airfoil ceiling supports are acceptable at this location.

5.2 Results of Force Measurements

The testing methodology described in Section 3.5 was not fortuitously conceived without several iterations of the experimental process. Several tests were conducted in order to gain the experience necessary to refine and improve the methodology. This section will summarize the results from the two major test series conducted as part of the project. The first test series, appropriately named the Large Gap Test Series, was conducted with a 0.025 cm pin fin gap in the floor. Data from the Large Gap Test Series

is presented to show what does not work. The second test series, the Small Gap Test Series, was conducted with a smaller pin fin gap to minimize silicone oil leakage. The lift and drag results presented from the Small Gap Test Series represent the culmination of knowledge and experience gained from the failures in both test series.

Large Gap Test Series

The Large Gap Test Series was conducted with sensor serial number 5117 (prior to damaging the x-axis). The sensor x-axis was aligned in the flow direction, while the y-axis was aligned perpendicular to the flow. The defining geometric parameters of the hole and pin fin configuration used for this test are provided by Figure 5.6. This test series utilized a 0.953 cm diameter pin fin with a 1.003 cm diameter hole in the channel floor and a 0.980 cm hole diameter in the channel ceiling. The clearance hole in the test section floor was enlarged to aid in the assembly of the sensor to the test section. Considerable difficulty was encountered while assembling the sensor to the test section for this first test. The exacting tolerances required for successful sensor and pin fin installation necessitated several days of effort to achieve an acceptable center in the clearance hole. This process became easier as more experience with the sensor installation was gained.

For the Large Gap Test Series, all data was recorded and analyzed between 90 seconds and 150 seconds (60 second data analysis window) after the start of the test. Although this is contrary to the instructions specified in Section 3.5, I did not yet have the experience and knowledge to conduct the test properly.

The Large Gap Test Series suffered from excessive silicone oil leakage out of the bottom pin fin gap. The first three tests were conducted with $1.0 \text{ X } 10^3$ cSt oil in the top and bottom reservoirs. All three tests were observed to leak significant amounts of silicone oil from the pin fin gap onto the channel floor. To alleviate this problem, the silicone oil in to the floor reservoir was replaced with $1.0 \text{ X } 10^4$ cSt oil for the subsequent tests. The silicone oil in the ceiling reservoir remained $1.0 \text{ X } 10^3$ cSt oil, as the previous tests did not experience silicone leakage from the ceiling reservoir. Increasing the viscosity of the oil in the bottom reservoir did not stop the oil from leaking out of the

bottom pin fin gap. Significant leakage was noted for all tests in the Large Gap Test Series, increasing in severity with flow rate.

The tell-tale sign of oil leakage, and the subsequent gathering behind the pin fin, is a high rate of sensor drift that decreases the magnitude of the signal. As discussed in Section 3.5, it is believed that the silicone oil that gathers behind the pin fin actually retards flow separation from the cylinder and makes it more aerodynamic. This effect on the sensor signal can be seen most dramatically in Figure 5.7, which plots the sensor output for a Re = 7.5 X 10^3 test conducted as part of the Large Gap Test Series. Figure 5.7 shows that the sensor output decreases by nearly 40% over the 60 second data analysis window. It is believed that this results from the silicone leakage that was noted in the test observations.

Although the results from the Large Gap Test Series are considered invalid due to excessive silicone leakage, the calculated drag and lift coefficients for each test are respectively summarized in Figure 5.8 and Figure 5.9. The aerodynamic coefficients are normalized by the mass averaged bulk channel velocity.

$$C_D = \frac{\mathscr{D}}{\frac{1}{2}\rho U^2 A_{FR}} \tag{5.10}$$

$$C_L = \frac{\mathscr{L}}{\frac{1}{2}\rho U^2 A_{FR}} \tag{5.11}$$

Figure 5.8 shows that significant deviation between drag coefficient measurements exists at Re = 7.5 X 10^3. The minimum drag coefficient is 0.83; the maximum drag coefficient is 1.45. The difference between the two results is approximately 50% of the average measured drag coefficient at Re = 7.5 X 10^3. Again, the inconsistent measurements are attributed to the silicone oil leakage noted above.

The magnitude of the drag coefficient is not the only parameter affected by silicone oil leakage. Reference to Figure 5.8 and Figure 5.9 shows that the magnitude of the measured lift coefficient can be as high as 70% the magnitude of the measured drag

coefficient. The fact that the lift coefficient is significant compared to the drag coefficient shows that this test cannot be valid.

Figure 5.10 and Figure 5.11 plot the averaged C_D and C_L results for each Reynolds number. Note that only the Re = 7.5 X 10^3 and Re = 1.3 X 10^4 flows were conducted multiple times.

Small Gap Test Series

The Small Gap Test Series was conducted with sensor serial number 5121. The sensor was installed such that the x-axis was aligned with the streamwise direction and the y-axis was aligned perpendicular to the flow. To remedy the silicone leakage problems experienced in the first test series, this test series utilized a smaller pin fin gap. Figure 5.12 provides a dimensioned schematic of the pertinent geometric parameters. Note that the gap size was made smaller by increasing the diameter of the pin fin to 0.975 cm (relative to the other pins that were 0.953 cm in diameter). The floor hole maintained a diameter of 1.003 cm, and the ceiling hole was increased to 1.003 cm. The diameter of the pin fin was increased by wrapping two layers of 0.005 cm thick Kapton tape around the pin fin. The tape joint, barely detectable by the human touch, was placed at the downstream edge of the cylinder to minimize aerodynamic effects. Increasing the diameter of the pin fin decreased the H/D aspect ratio to 0.98. This small change was assumed to be negligible in light of the expected real world manufacturing tolerances.

The viscosity grade of the silicone oils used in the Small Gap Test Series also changed. A series of qualitative, observational tests were conducted to select an appropriate silicone oil. The first test used 1.0 X 10^4 cSt oil in both the bottom and top reservoirs. This test experienced significant oil leakage from the ceiling reservoir at Re $\geq$ 1.3 X 10^4 and from the floor reservoir at Re $\geq$ 1.8 X 10^4. Thus, the silicone oil was replaced with 1.0 X 10^5 cSt oil in the ceiling and 5.0 X 10^4 cSt oil in the floor. This configuration worked fine for flows less than Re = 1.5 X 10^4. For flows greater than Re = 1.5 X 10^4, the 5.0 X 10^4 cSt silicone oil was again observed to leak excessively out of the bottom pin fin gap. To remedy the problem, 1.0 X 10^5 cSt silicone oil was used in both the ceiling and floor reservoirs. Although oil leakage could not be totally prevented at flow rates greater than Re = 2.5 X 10^4, the 1.0 X 10^5 cSt oil was able to retard the onset

of silicone oil leakage long enough that data could be collected between 90 and 150 seconds (as discussed in Section 3.5) for flow rates up to $Re = 3.5 \times 10^4$. Flow rates higher than $Re = 3.5 \times 10^4$ were attempted with the 1.0×10^5 cSt oil, but resulted in failure due to silicone leakage and bubble formation in the floor reservoir. Coincidentally, $Re = 3.5 \times 10^4$ was the limiting flow rate at which the parallel heat transfer test facility (discussed in Chapter 4) could achieve successful results [Lyall, 2006]. Due to the difficulties in both test rigs, the decision was made to forego testing at flows greater than $Re = 3.5 \times 10^4$.

A multitude of tests were conducted in the Small Gap Test Series. Not every test yielded successful results. Several tests failed due to excessive silicone leakage or bubble formation in the floor reservoir. A successful test was defined to be a test in which only minimal silicone oil leakage was observed, and no bubbles were found in the silicone reservoirs. It was rare that more than three tests in a row could be conducted without forming a bubble in the reservoir. Some Reynolds numbers were tested more than others in effort to quantify testing sensitivities. In particular, $Re = 1.3 \times 10^4$ was the favorite flow rate to use while varying the test conditions.

Figure 5.13 summarizes the drag coefficient results based on the mass averaged channel velocity for the successful tests completed in the Small Gap Test Series. Each test is categorized by the silicone oil used in the floor reservoir. Inspection of Figure 5.13 shows that the largest scatter in the drag data occurred at the lowest Reynolds number, $Re = 7.5 \times 10^3$. This is expected as this is where the forces are the smallest. The ability of the DSC-6 sensor to make precise measurements at the low forces is not as good as at the high forces, due to resolution.

Table 5.2 summarizes the maximum and minimum drag coefficients recorded for each tested Reynolds number, and the date the test occurred. The day to day variation due to repeatability is less than 6% for flows above $Re = 1.03 \times 10^4$. Note that the maximum and minimum drag measurement for $Re = 1.5 \times 10^4$ both occur on November 28th, even though a third test was conducted on December 13th. The day to day variation due to repeatability for flows less than $Re = 1.03 \times 10^4$ is less than 20%. Again, the increased difference between the measured data points is attributed to poor sensor resolution of the small forces.

An interesting observation can be made by looking closely at the tests conducted at Re = 1.3 X 10^4. At this Reynolds number, four tests were conducted with 5.0 X 10^4 cSt silicone oil in the floor reservoir. Two additional tests were conducted with 1.0 X 10^5 cSt silicone oil in the floor reservoir. Figure 5.14 provides a plot of all six data points and the average of those points. The 1.0 X 10^5 cSt silcone tests did not yield significantly different results than the 5.0 X 10^4 cSt tests. In fact, one 1.0 X 10^5 cSt test lies within the scatter of the 5.0 X 10^4 cSt tests. The other (lower) 1.0 X 10^5 cSt test does lie slightly outside the scatter of the 5.0 X 10^4 cSt tests, but not by much. The lower 1.0 X 10^5 cSt test is 3.0% below the mean, while the lowest 5.0 X 10^4 cSt test is 2.4% below the mean. Figure 5.14 suggests that the test results are independent of the silicone oil viscosity, as long as the oil is viscous enough to resist ejection from the pin fin gap. Intuitively, this result makes sense. The silicone oil is Newtonian, regardless of the viscosity, and should only act as a mechanical damper. A pure damping element can only affect the time response of the pin fin, not the magnitude of the response. Thus, the viscosity of the Newtonian silicone oil should not affect the time averaged response of the pin fin. Because only two data points at a single Reynolds number (Re = 1.3 X 10^4) from the 1.0 X 10^5 cSt oil tests are available to compare with the 5.0 X 10^4 cSt oil tests, it is recommended that more tests at different Reynolds numbers are conducted to corroborate this result.

The drag coefficients (C_D) from every test shown in Figure 5.13 were averaged at each Reynolds number (Re), and plotted in Figure 5.15. A minimum of three successful tests were required at each Reynolds number before the average was taken. A cubic polynomial trend line was fit through the averaged drag coefficients. Figure 5.15 also plots two other drag coefficients in addition to the mass averaged drag coefficient. The maximum velocity drag coefficient, C_{Dmax}, is provided by Equation 5.12.

$$C_{Dmax} = \frac{\mathcal{D}}{\frac{1}{2}\rho U_{max}^2 A_{FR}} \tag{5.12}$$

The velocity used to normalize the drag force in Equation 5.12 is the maximum velocity (at the channel centerline) in a fully developed turbulent profile. Kakac et al. [1987]

provide the following correlation for the maximum velocity of a fully developed turbulent profile:

$$\frac{U}{U_{max}} = 1 - \frac{n-s}{3(n-1)} - \frac{s-1}{(n-1)(2n+1)}$$
$$\text{Where}: \quad n = 0.00625Re^{.75} - 2.0625 \qquad (5.13)$$
$$s = 0.004Re^{.75}$$

The second drag coefficient can be defined with the minimum flow area velocity, as in Equation 5.14

$$C_{Dmin} = \frac{\mathcal{D}}{\frac{1}{2}\rho U_{min}^2 A_{FR}} \qquad (5.14)$$

The minimum area velocity, U_{min}, occurs within the pin fin array where the cross sectional area of the channel is reduced due to the pin fins. Equation 5.15 provides the algorithm to calculate U_{min}.

$$U_{min} = \frac{\dot{m}}{\rho[(W*H)-(n*D*H)]} \qquad (5.15)$$

The magnitude of each of the three drag coefficients shown in Figure 5.15 varies with the magnitude of the normalizing velocity. Figure 5.15 shows that C_{Dmax} is the smallest of the experimental drag coefficients, meaning that the turbulent centerline velocity is greater than the mass averaged and minimum area flow velocity. The three curves are also slightly shifted on the x-axis, owing to the different velocity used to calculate the Reynolds number for each drag coefficient species. At this juncture, it is not clear which characteristic velocity is the correct velocity with which to scale the pin fin drag. More tests are needed at different pin diameters to see if the data will collapse to a single curve for any of the given drag coefficient species.

Figure 5.16 plots all three drag coefficients, the infinite cylinder drag coefficient, and the pressure drag integrated from Ames et al. [2005] on the same graph as a function of Re_D (Reynolds number based on the cylinder diameter). Immediately, one notices the difference in magnitude between the experimental and infinite cylinder drag coefficients. But, the experimental drag curves appear to follow the trend of the infinite cylinder drag curve until about $Re_D = 1.3 \text{ X } 10^4$ ($Re = 2.5 \text{ X } 10^4$) At $Re_D = 1.3 \text{ X } 10^4$, the experimental drag coefficients peak and become approximately constant while the infinite cylinder drag coefficient continues to asymptotically increase in magnitude until $Re_D = 1.5 \text{ X } 10^5$. However, the small slope of the infinite cylinder drag coefficient in this range ($Re_D > 1.3 \text{ X } 10^4$) renders this difference nearly negligible.

Figure 5.16 shows that the experimental drag coefficients are significantly larger than the pressure drag that was calculated from the data presented by Ames et al. [2005]. At $Re_D = 1.0 \text{ X } 10^4$ ($Re = 1.9 \text{ X } 10^4$), the difference between the integrated pressure drag and C_{Dmin} is approximately 100% (recall from Section 2.1 that the integrated pressure drag is normalized by the minimum flow area velocity). Geometry differences between the two tests do exist, but the most likely explanation for the difference between the two drag coefficients is viscous drag. Pressure integration cannot account for the viscous drag imposed upon the cylinder. The DSC-6, however, can only measure total drag. Reference to Figure 2.2 shows that at $Re_D = 9.0 \text{ X } 10^3$ ($Re = 1.8 \text{ X } 10^4$), the viscous drag is negligible compared to the pressure drag for an infinite cylinder. The data presented in Figure 5.16 suggests that viscous drag is much more important in channel flows with H/D = 1 than it is for infinite cylinders. One might expect viscous drag to be more important on a cylinder in channel flow, as a fully developed velocity profile represents the convergence of two boundary layers. Recall from boundary layer theory that viscous effects are typically neglected in external flows (such as that experienced by an infinite cylinder), being confined in consideration to only the boundary layer. The interesting results shown in Figure 5.16 demonstrate the need for further investigation and benchmarking of the measurement methodology used in this project. Such verification efforts, however, are outside the scope of this thesis.

Figure 5.17 plots the experimental lift coefficient from each individual test, while Figure 5.18 provides the averaged lift coefficient for each Reynolds number. It is

expected for this geometry that the lift coefficient has a zero magnitude. The measured values indicate lift forces that are near zero. The plotted lift coefficient is normalized by the mass averaged velocity. Using the turbulent centerline velocity or the minimum area velocity will only change the magnitude of the lift coefficient, without adding any insight to this discussion.

Although Figure 5.18 shows that the lift coefficient decreases with increasing velocity (Reynolds number), it is not believed that the lift coefficient is physically a function of the flow rate. Figure 5.19 plots the average lift force measured for each Reynolds number. Note that no general trend in the lift force data exists. The random nature of the lift forces shown in Figure 5.19 suggests that the measurements are dominated by experimental error. The lift coefficients shown in Figure 5.18 decrease with increasing velocity, simply because the velocity is used to normalize the lift force. If the lift force does not significantly change, but the velocity increases, the lift coefficient must decrease.

Table 5.3 repeats the information in Figure 5.15 and Figure 5.18 in tabular format. Note that the lift coefficient (theoretically zero) is approximately one order of magnitude smaller than the drag coefficient for flows less than $Re = 1.3 \times 10^4$. For flows greater than $Re = 1.5 \times 10^4$, the lift coefficient is approximately two orders of magnitude smaller than the drag coefficient.

Table 5.4 summarizes the averaged lift and drag forces measured at each Reynolds number. Additionally, the ratio of the lift force to drag force is shown ($\mathscr{L}/\mathscr{D}$). Figure 5.20 provides a graphical representation of the drag and $\mathscr{L}/\mathscr{D}$ relationship.

Because the true time averaged lift force on the cylinder should be zero, the measured lift force represents the measurement error in the lift direction. Table 5.4 and Figure 5.20 show that the error in the lift force is less than 2% of the measured drag force for drag forces greater than 1.6×10^{-2} N. At a force of 3.4×10^{-3}N (the minimum tested drag force), the error increases to approximately 12% of the applied drag force. Keep in mind that the data presented in Table 5.4 and Figure 5.20 has already been corrected for cross axis effects with ξ and ψ (see section 3.2). Thus, the data presented here represents the cross axis error inherent in the setup and execution of the experiment. This information

will be invaluable for estimating the minimum resolvable lift and drag forces for more complicated pin fin shapes with appreciable lift forces.

This chapter has summarized the channel flow benchmarking activities and experimental results obtained by the project. The friction factor data shows that inlet guides are necessary to achieve a hydrodynamically fully developed velocity profile. Additionally, each inlet guide installation should be checked with a survey of the spanwise static pressures in the channel to ensure that flow uniformity is achieved.

Visual observation of the force tests shows that a gap size of less than 0.02 cm is necessary to prevent excessive silicone oil leakage. It appears that as long as the silicone oil is viscous enough to prevent leakage out of the pin fin gap, it does not matter what viscosity of oil is used in the test. For this reason, it is recommended that $1.0 \text{ X } 10^5$ cSt viscosity oil is used in both the floor and ceiling reservoir.

Testing shows that the trend of the pin fin drag coefficient approximately follows the trend of the infinite cylinder drag coefficient, although the magnitude of the pin fin drag coefficient is higher than the infinite cylinder drag coefficient for all three normalizing velocities. Comparison of the experimental C_{Dmin} to integrated pressure drag coefficients from Ames et al. [2005] indicate that viscous drag is much more important in H/D = 1 channel flows than for infinite cylinders. This hypothesis requires further investigation and benchmarking of the measurement methodology.

Lift force measurements on the cylindrical pin fin indicate that the experimental error in the lift measurement is approximately 2% of the applied drag for drag forces greater than $1.6 \text{ X } 10^{-2}$ N. Although this thesis does not address all of the goals of the overall project, it provides a good starting point to tackle the more complex objectives (such as two-axis force resolution) scheduled for future testing.

Table 5.1 Summary of Friction Factor Linear Curve Fits for Installation A

Date	Re	Measured f	R^2	Predicted f [Kakac, et al., 1987]	%Δ
9/30/2005	7340	0.034	1.000	0.0351	-2.45%
10/14/2005	12526	0.033	1.000	0.0328	-0.46%
9/27/2005	12714	0.030	0.999	0.0298	2.17%
11/4/2005	13440	0.029	0.986	0.0293	0.43%
9/29/2005	20776	0.028	0.999	0.0289	-1.61%
9/29/2005	30286	0.026	0.998	0.0263	-0.38%
9/28/2005	44445	0.024	0.992	0.0239	-0.95%

Table 5.2 Summary of Maximum and Minimum Recorded Drag Coefficients for the Small Gap Test Series

Target Re	Tested Re	Max C_D	Test Date	Min C_D	Test Date	$\%\Delta = \frac{\mathrm{Max}(C_D) - \mathrm{Min}(C_D)}{\mathrm{Min}(C_D)}$
7500	7525	1.65	11/9/2005	1.41	11/10/2005	17.01%
10300	10371	1.76	11/13/2005	1.58	11/13/2005	11.46%
13000	13138	1.83	11/11/2005	1.74	12/7/2005	5.22%
15000	14906	1.84	11/28/2005	1.80	11/28/2005	2.63%
18000	18012	1.85	12/19/2005	1.82	11/19/2005	1.60%
25000	25108	1.96	11/28/2005	1.86	12/2/2005	5.30%
30000	30463	1.89	12/16/2005	1.81	12/14/2005	4.57%
35000	35347	1.88	11/29/2005	1.85	12/2/2005	1.35%

Table 5.3 Summary of Averaged Aerodynamic Coefficient Results from the Small Gap Test Series

Target Re	Tested Re	C_D	C_L	Tested Re_{max}	C_{Dmax}	Tested Re_{min}	C_{Dmin}
7500	7525	1.52	0.19	8551	1.18	8307	1.25
10300	10371	1.66	0.08	11786	1.29	11449	1.37
13000	13138	1.80	0.09	14929	1.39	14503	1.47
15000	14906	1.81	-0.01	16939	1.41	16455	1.49
18000	18012	1.83	0.02	20468	1.42	19883	1.50
25000	25108	1.92	0.00	28532	1.49	27717	1.57
30000	30463	1.85	0.01	34617	1.44	33628	1.52
35000	35347	1.86	0.01	40167	1.44	39020	1.53

Table 5.4 Summary of Averaged Lift and Drag Force Measurements from the Small Gap Test Series

Target Re	Tested Re	$\mathcal{D}$ (N)	$\mathcal{L}$ (N)	$\lvert \mathcal{L} / \mathcal{D} \rvert$ (%)
7500	7525	3.42E-03	4.21E-04	12.30%
10300	10371	7.07E-03	3.53E-04	4.99%
13000	13138	1.22E-02	5.79E-04	4.73%
15000	14906	1.59E-02	-1.15E-04	0.72%
18000	18012	2.34E-02	3.15E-04	1.35%
25000	25108	4.77E-02	8.98E-05	0.19%
30000	30463	6.66E-02	2.19E-04	0.33%
35000	35347	9.17E-02	3.43E-04	0.37%

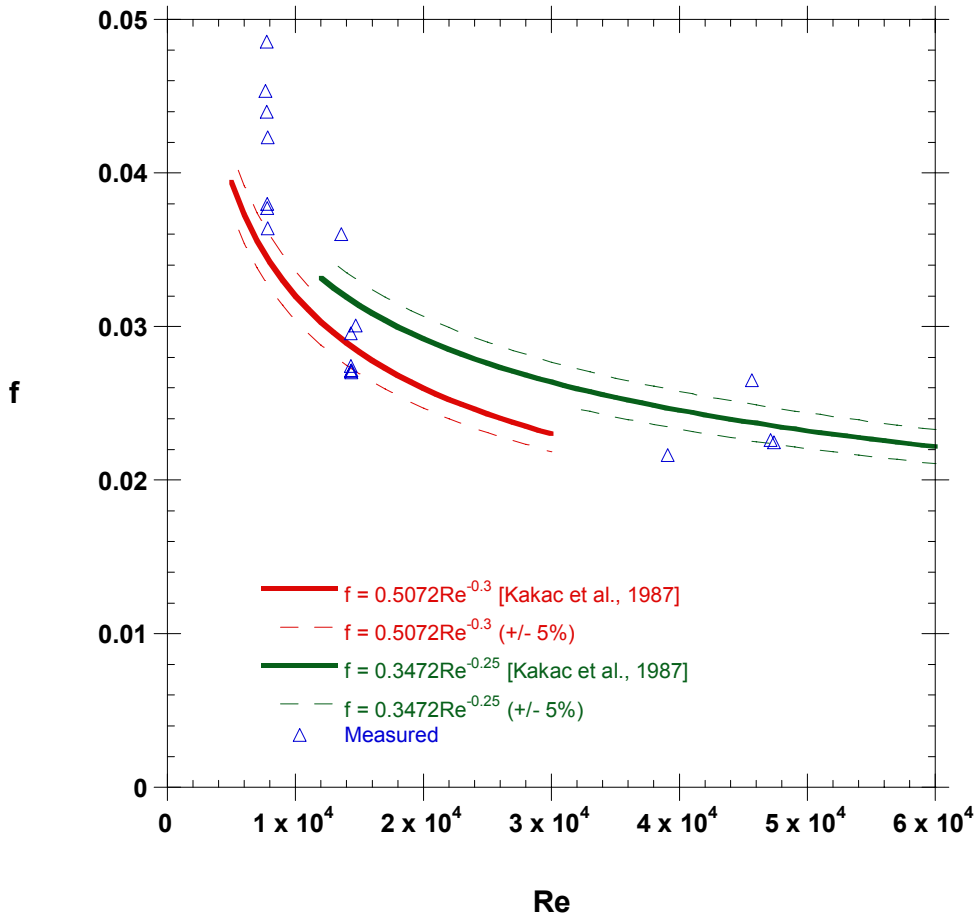

Figure 5.1 Plot of friction factor results with no channel inlet guides. The plot shows that most friction factor measurements were greater than 5% different than the published correlations.

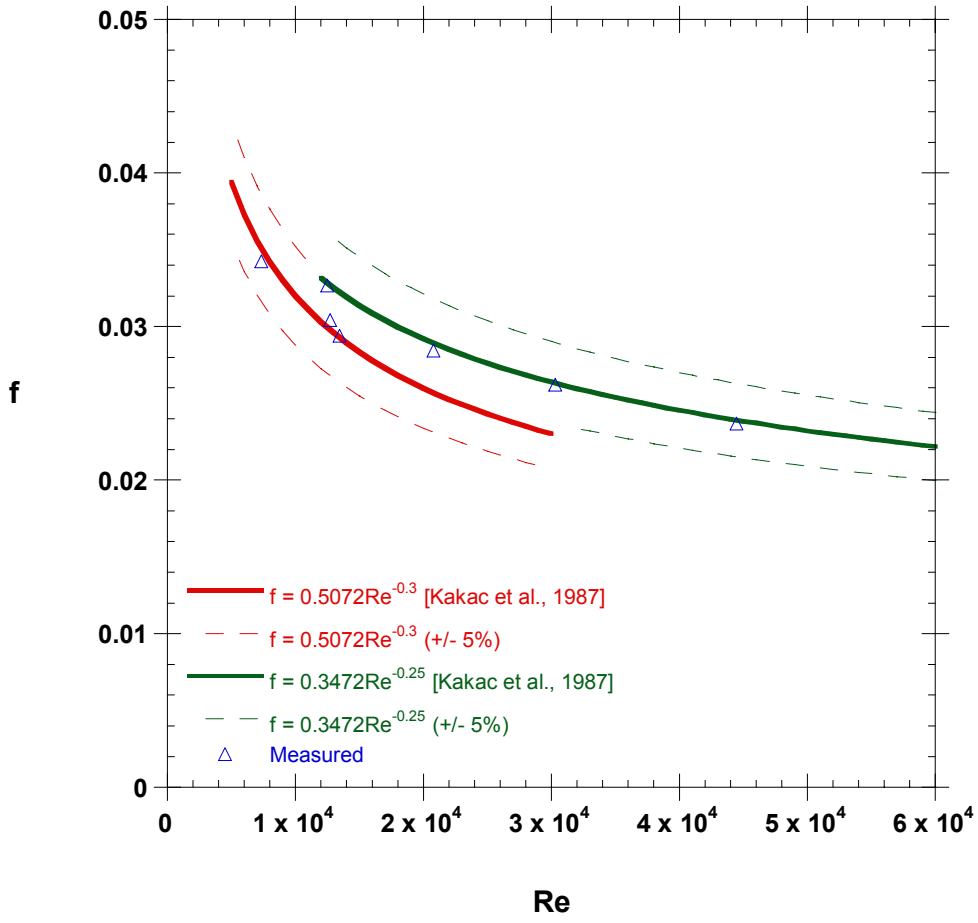

Figure 5.2 Plot of friction factor results with the channel inlet guides installed. The friction factor measurements match the correlation much better than the data taken without the inlet guides installed.

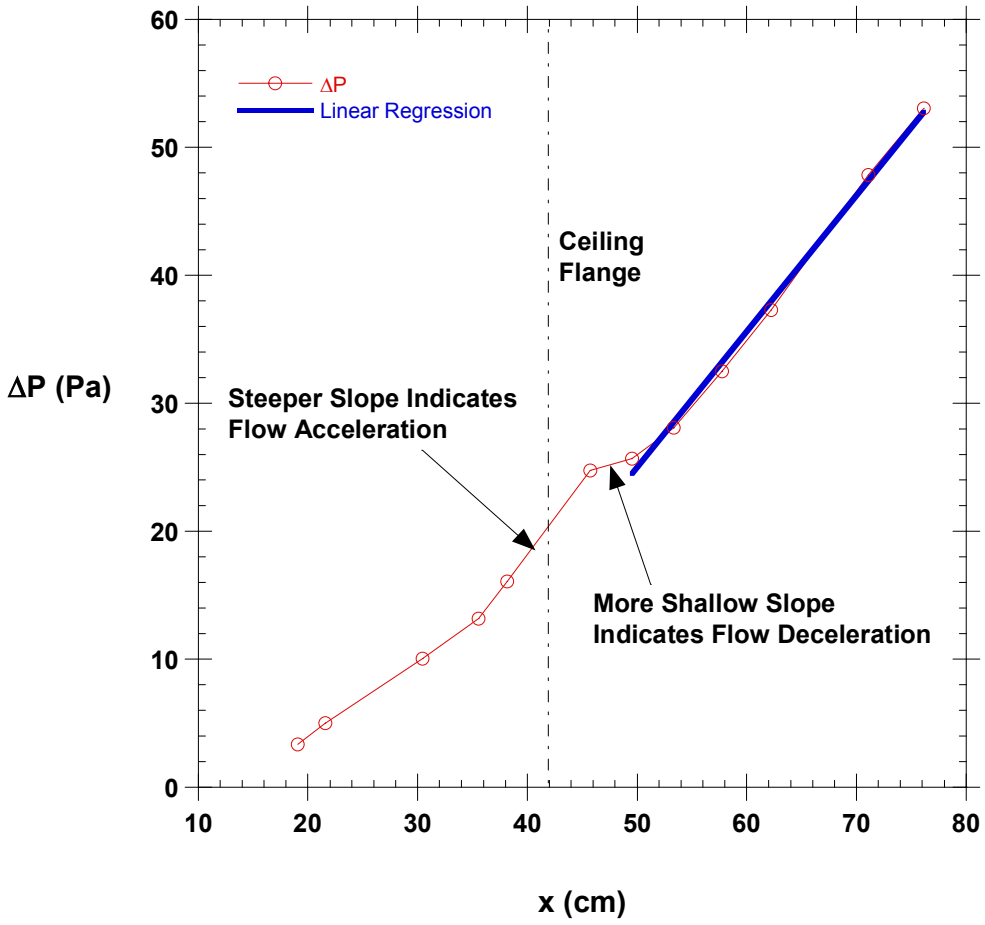

Figure 5.3 Plot of the static pressure difference down the length of the channel for a Re = 1.3 X 10^4 flow. The plot shows the acceleration of the flow immediately behind the ceiling flange, and the subsequent deceleration after the channel returns to the correct height (0.96 cm). The linear regression used to calculate the friction factor is also shown passing through the last six pressure taps upstream of the pin fin array.

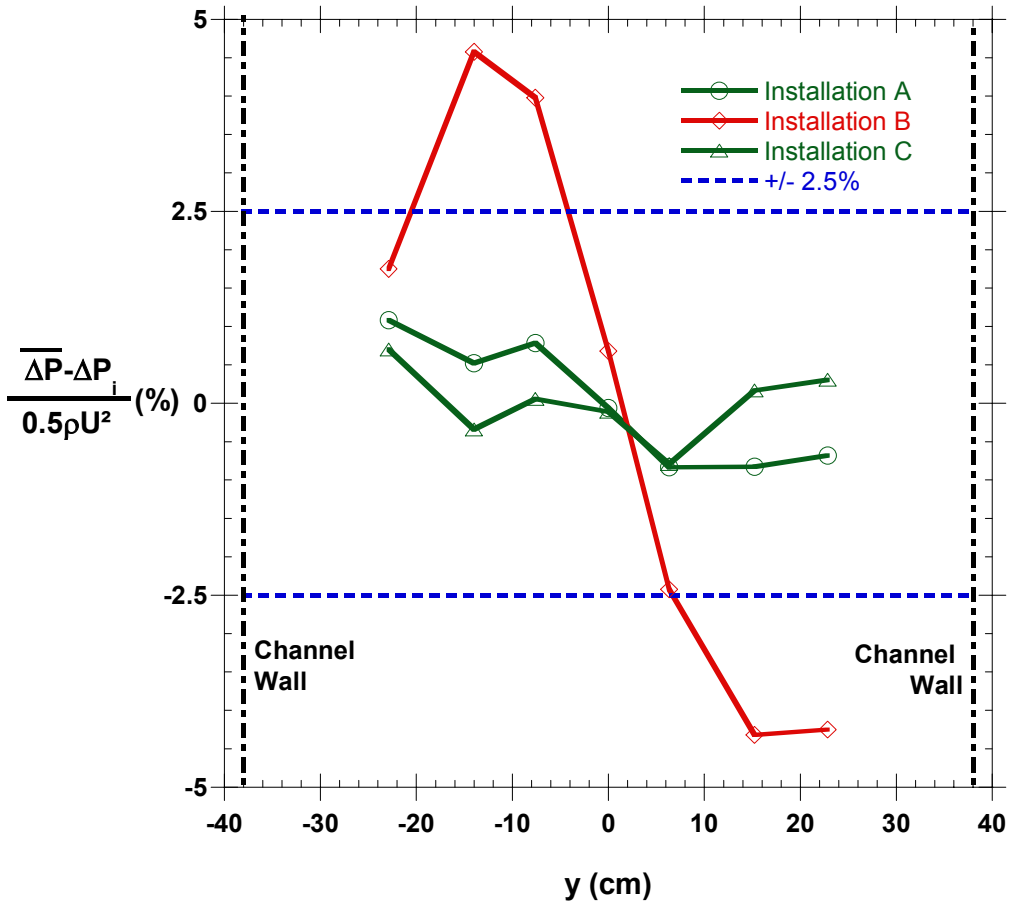

Figure 5.4 Plot of span wise uniformity in the test channel for three different inlet guide installations. The plot demonstrates that the flow uniformity is sensitive to the installation of the inlet guides.

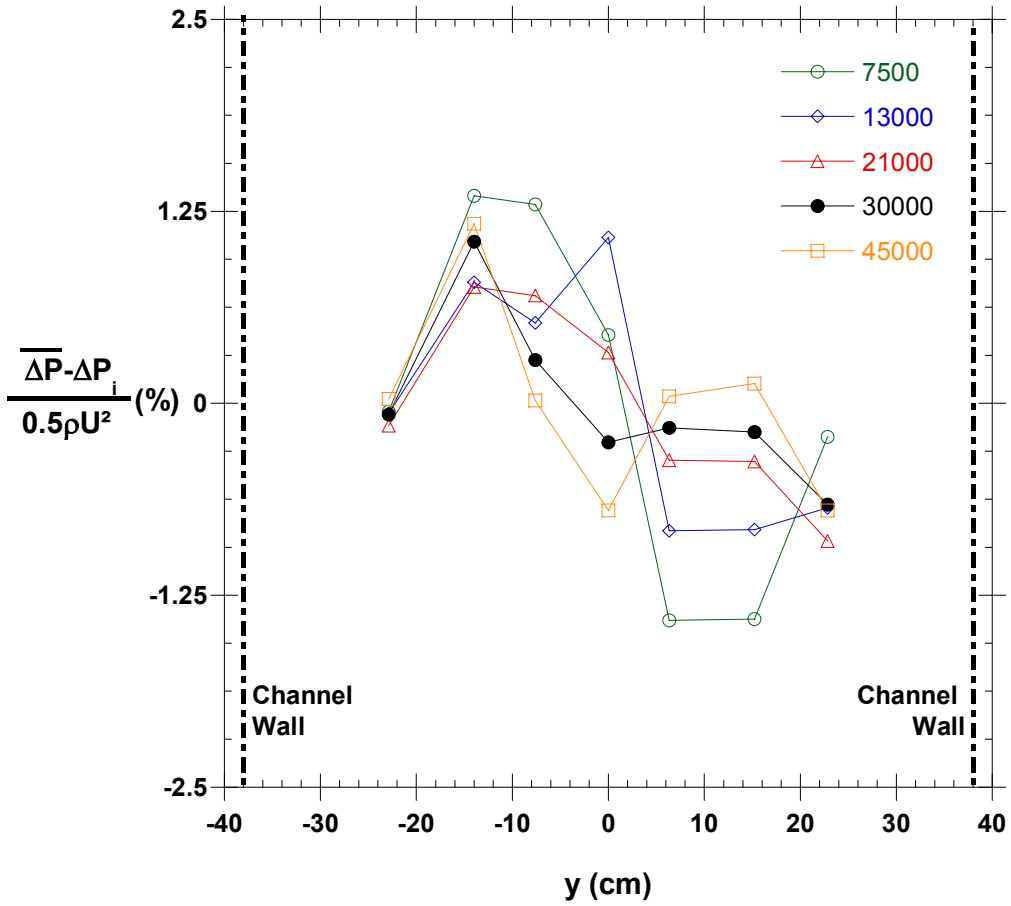

Figure 5.5 Plot of span wise static pressure distributions for Installation A. The plot shows that all normalized pressure differences fall within the 2.5% requirement for all Reynolds numbers.

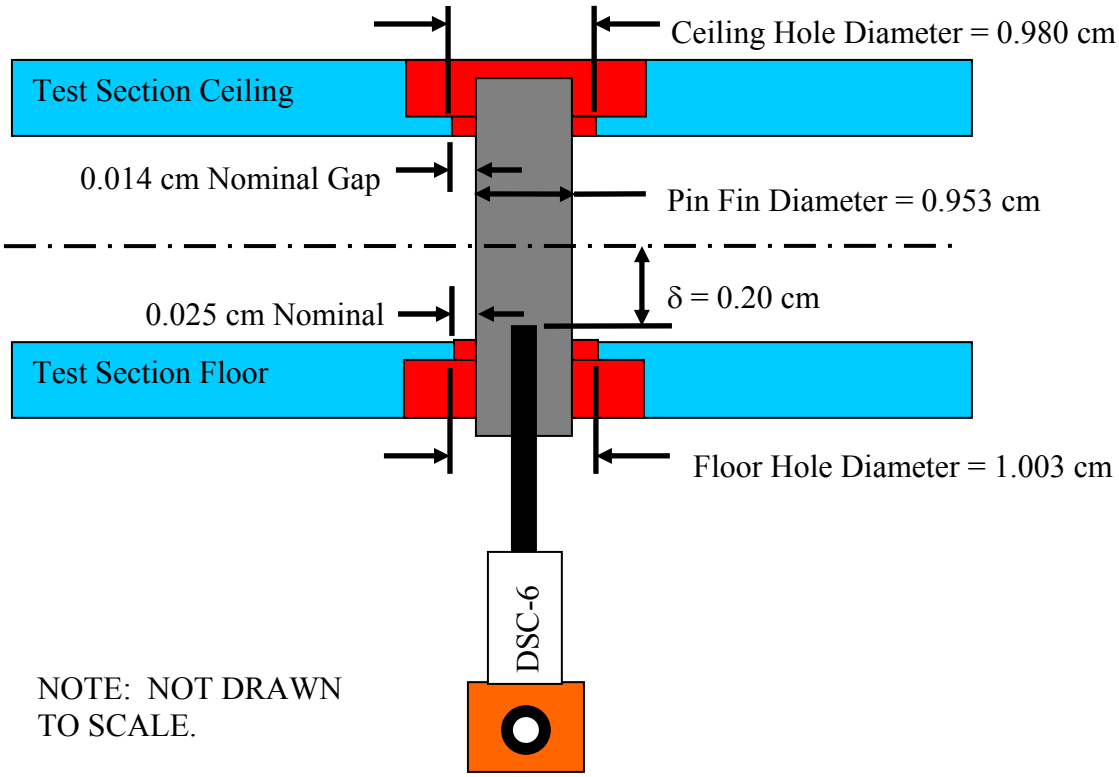

Figure 5.6 Dimensioned schematic of physical setup for the Large Gap Test series. Note that the hole in the test channel floor is larger than the ceiling hole to aid in the installation of the sensor.

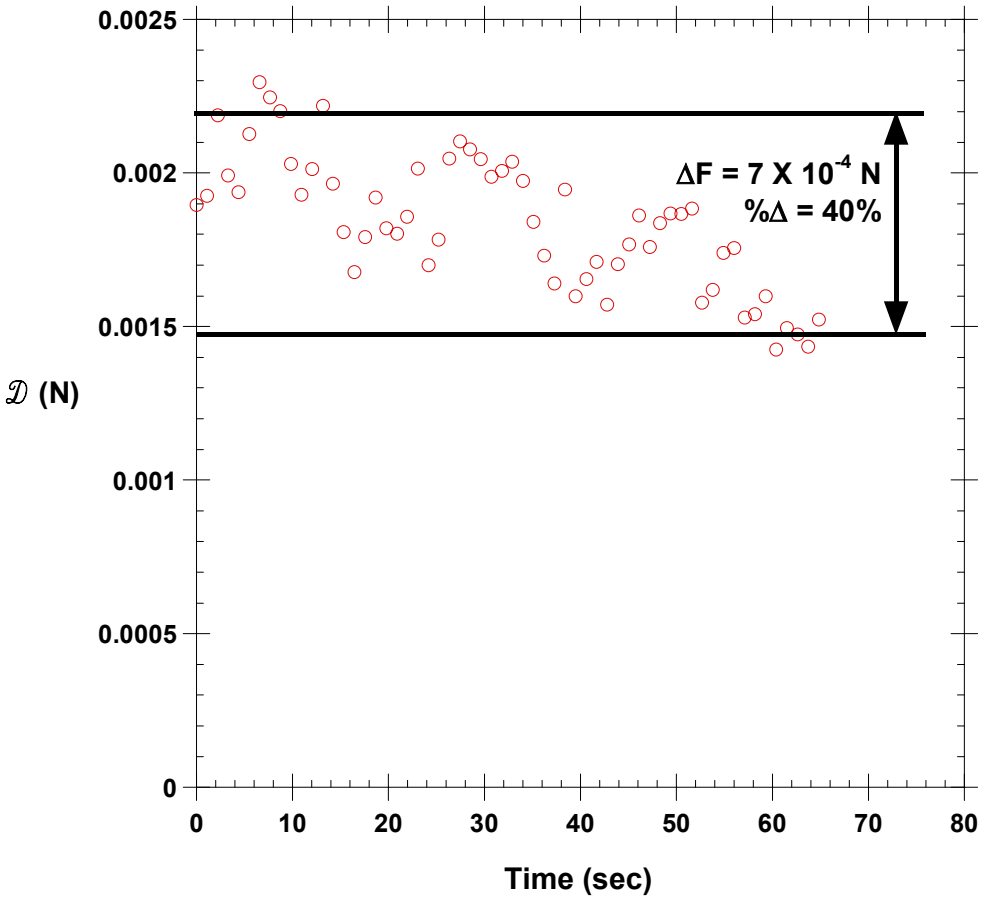

Figure 5.7 Plot illustrating the dramatic decrease in sensor output for the Re = 7.5 X 10^3 test conducted in the Large Gap Test Series. The roll-off of the output is believed to be caused by silicone oil collecting behind the pin fin.

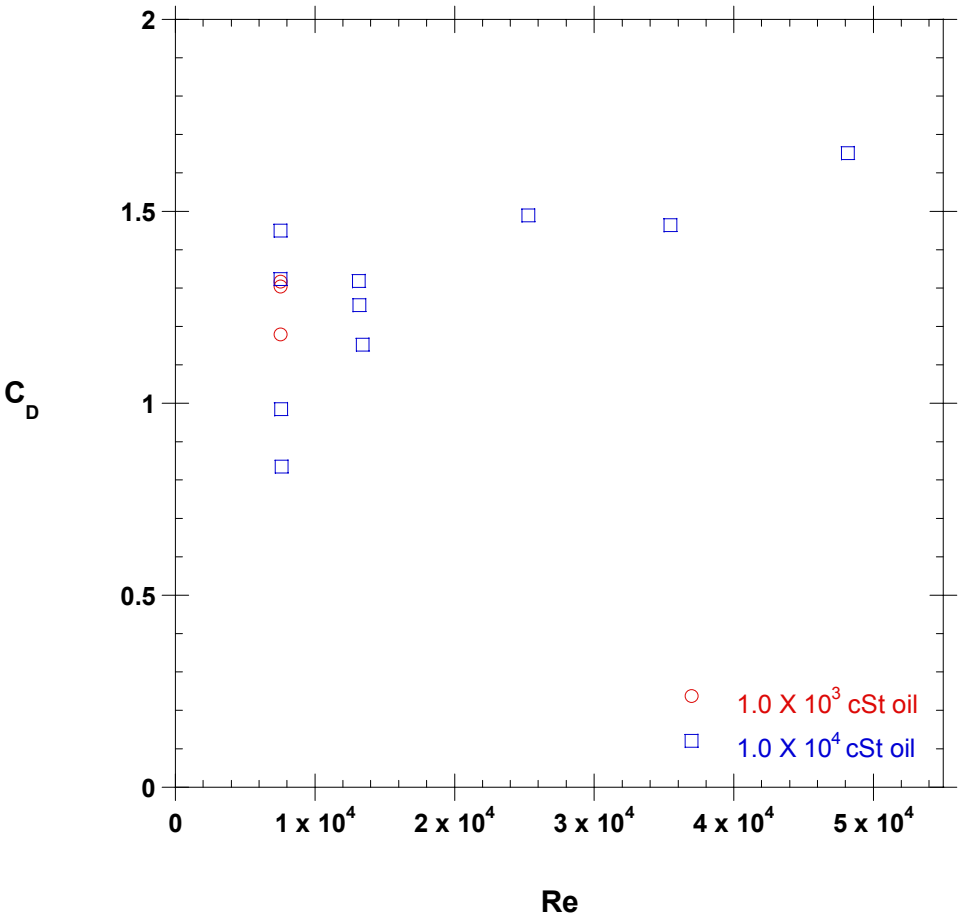

Figure 5.8 Plot of drag coefficient results from the Large Gap Test Series. Note that the legend indicates which silicone oil viscosity was used in the floor oil reservoir. All tests used 1.0 X 10^3 cSt oil in the ceiling reservoir.

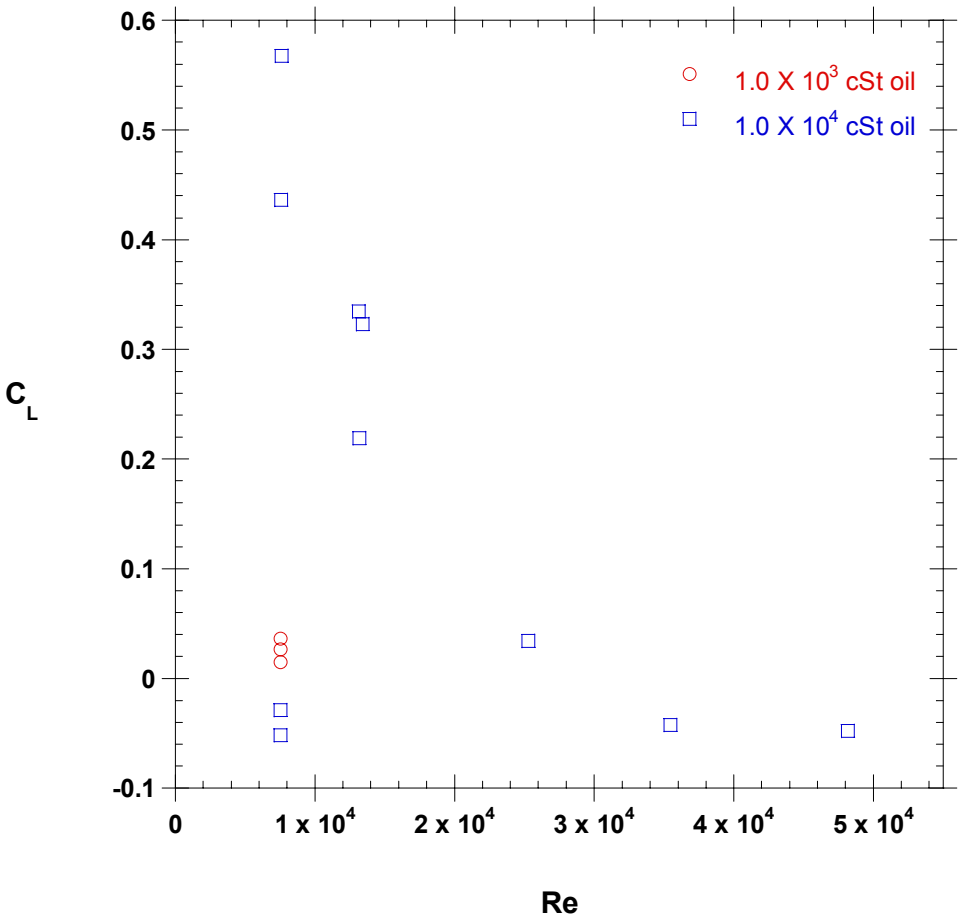

Figure 5.9 Plot of lift coefficient results from the Large Gap Test Series. The legend indicates which silicone oil viscosity was used in the floor oil reservoir. All tests used 1.0 X 10^3 cSt oil in the ceiling reservoir.

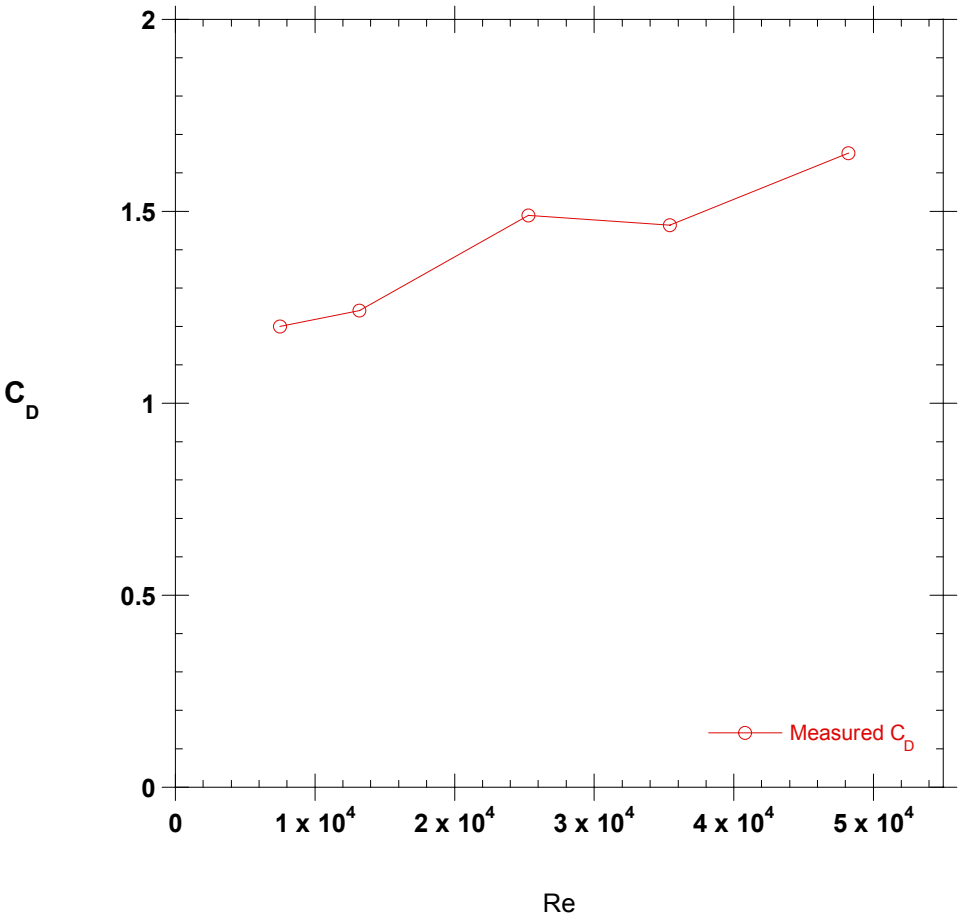

Figure 5.10 Plot of averaged drag coefficients for the Large Gap Test Series. Note that only the Re = 7.5 X 10^3 and Re = 1.3 X 10^4 flows were conducted multiple times. The other points represent a single test.

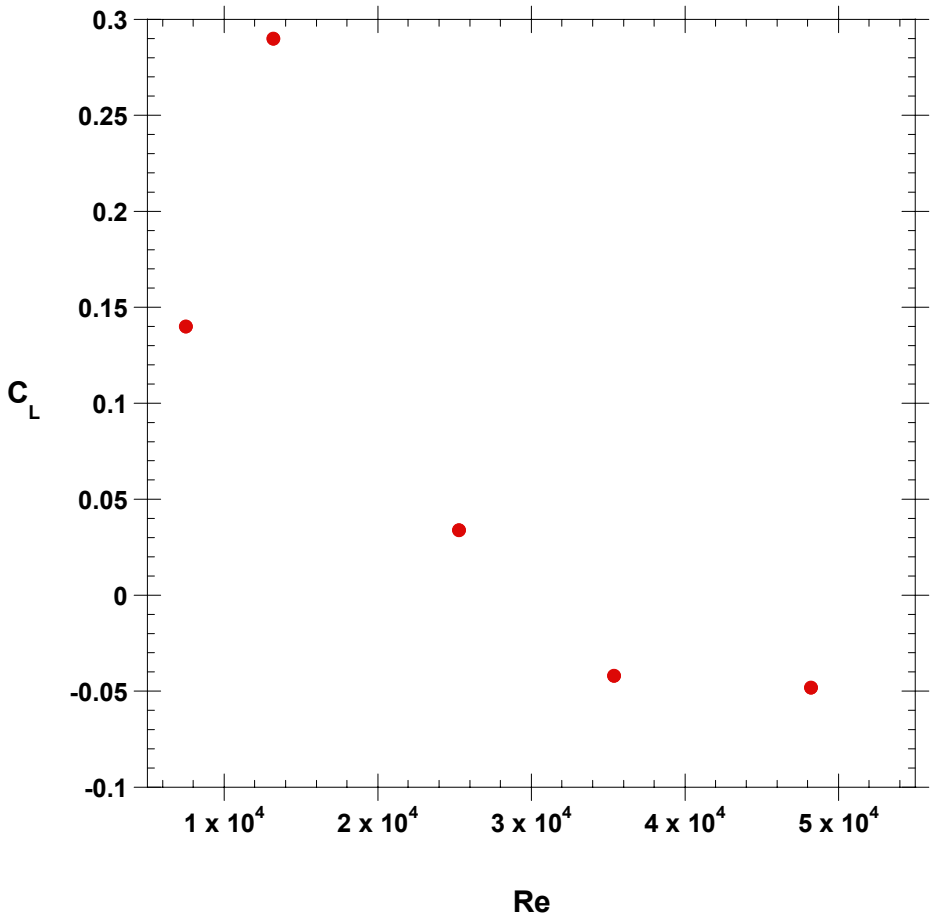

Figure 5.11 Plot of averaged lift coefficients for the Large Gap Test Series. Note that only the Re = 7.5 X 10^3 and Re = 1.3 X 10^4 flows were conducted multiple times. The other points represent a single test.

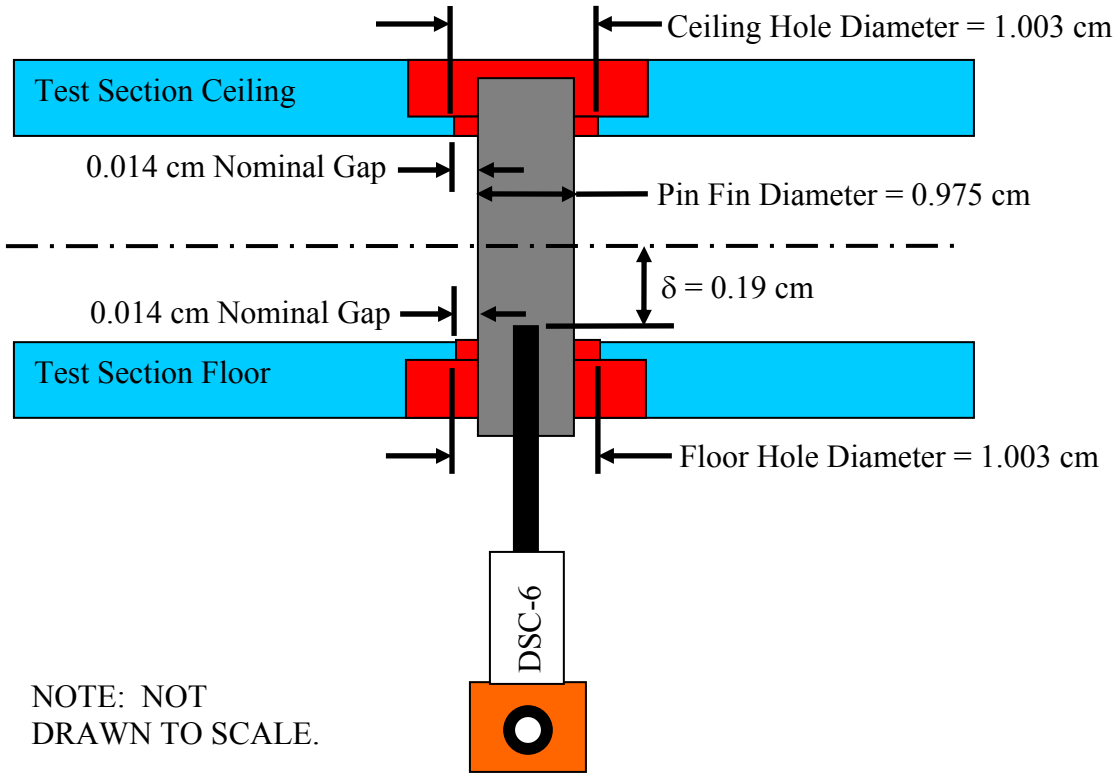

Figure 5.12 Dimensioned schematic of pertinent geometric information for the Small Gap Test Series. Note that the pin fin gap is decreased by increasing the diameter of the pin fin.

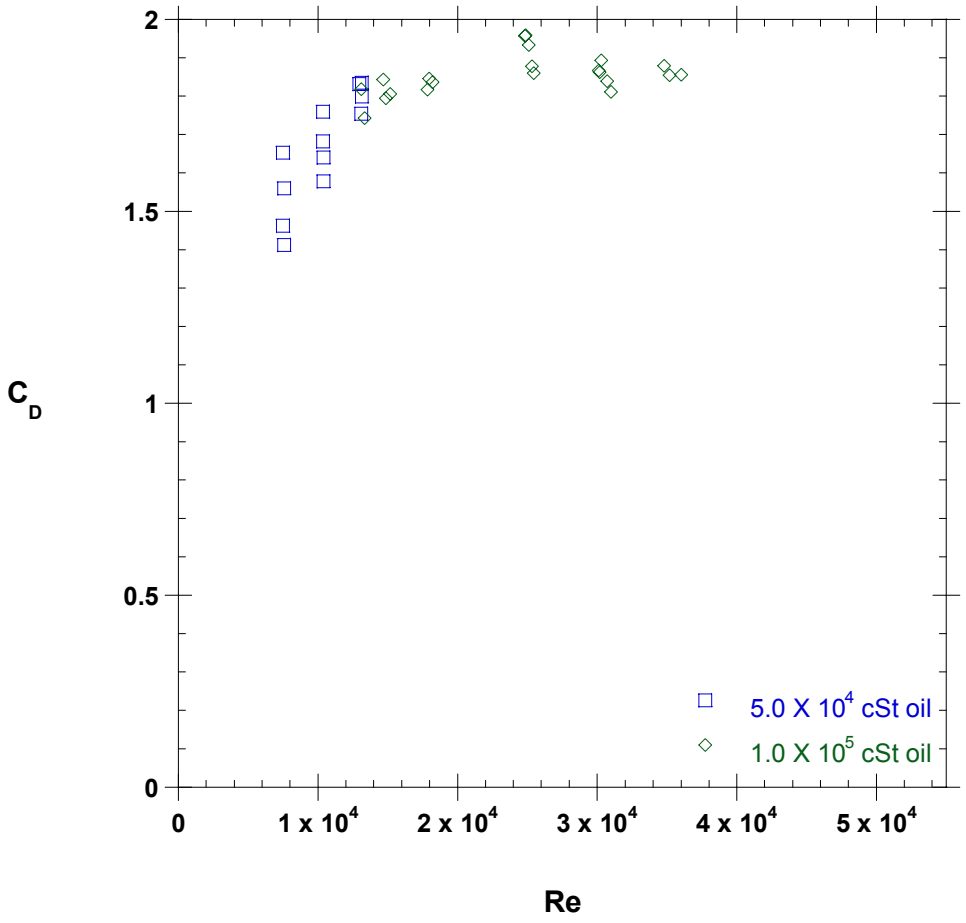

Figure 5.13 Plot of drag coefficient results for successful tests completed in the Small Gap Test Series. The legend indicates the viscosity of the oil in the floor oil reservoir. All tests were conducted with 1.0 X 10^5 cSt silicone oil in the ceiling reservoir. Note that the scatter in the data for a given Reynolds number generally decreases with increasing Reynolds number.

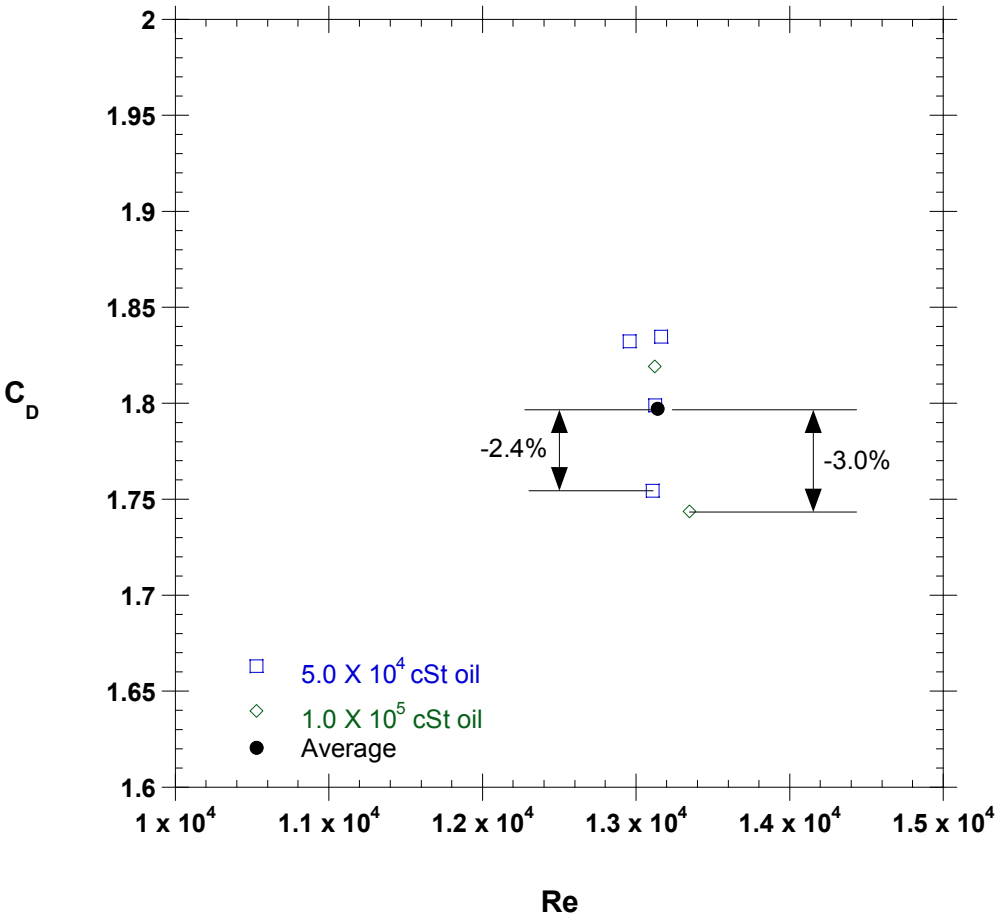

Figure 5.14 Plot of drag coefficient results at Re = 1.3 X 10^4. The legend indicates the viscosity of the oil used in the floor oil reservoir. All tests used 1.0 X 10^5 cSt oil in the ceiling reservoir. The plot suggests that the measured drag coefficient is independent of silicone oil viscosity.

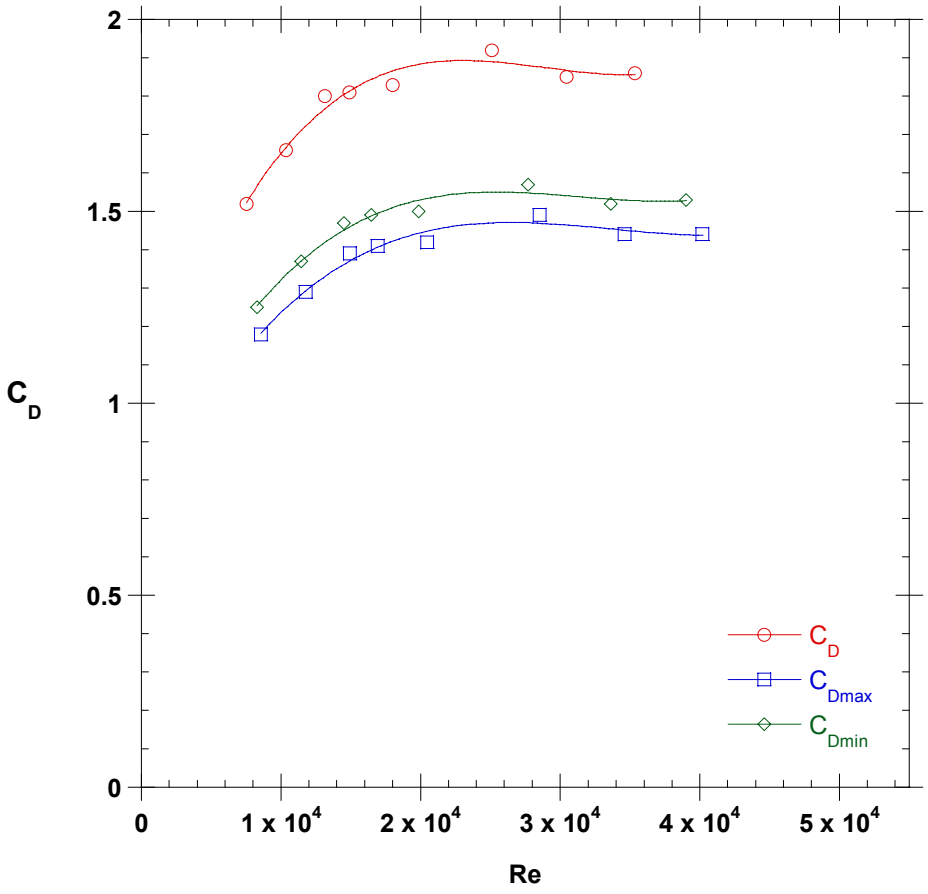

Figure 5.15 Plot of averaged drag coefficients for all three drag coefficients (C_D, C_{Dmax}, C_{Dmin}) as a function of Re. The measured drag coefficients peak at a channel Reynolds number of approximately Re = 2.5 X 10^4.

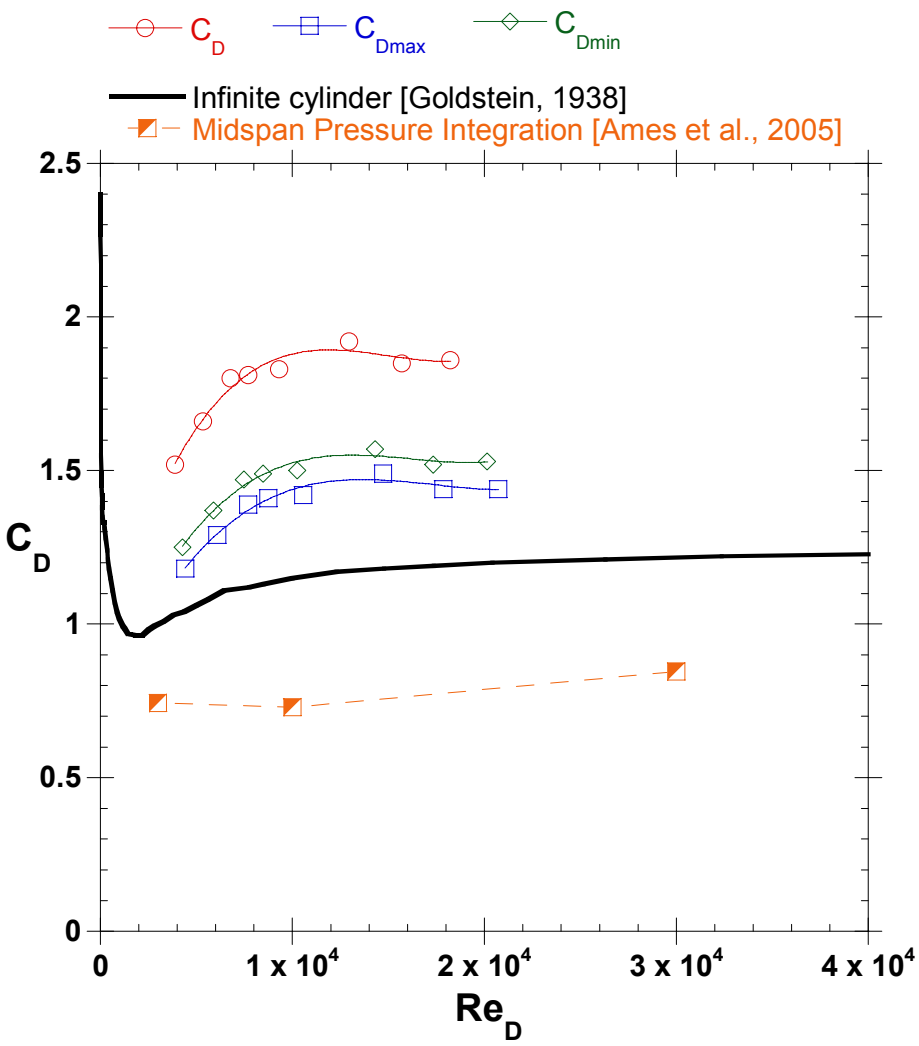

Figure 5.16 Plot of averaged drag coefficients for all three drag coefficients (C_D, C_{Dmax}, C_{Dmin}) compared with an infinite cylinder drag coefficient as a function of Re_D. The pressure drag integrated from Ames et al. [2005] is also shown for comparison.

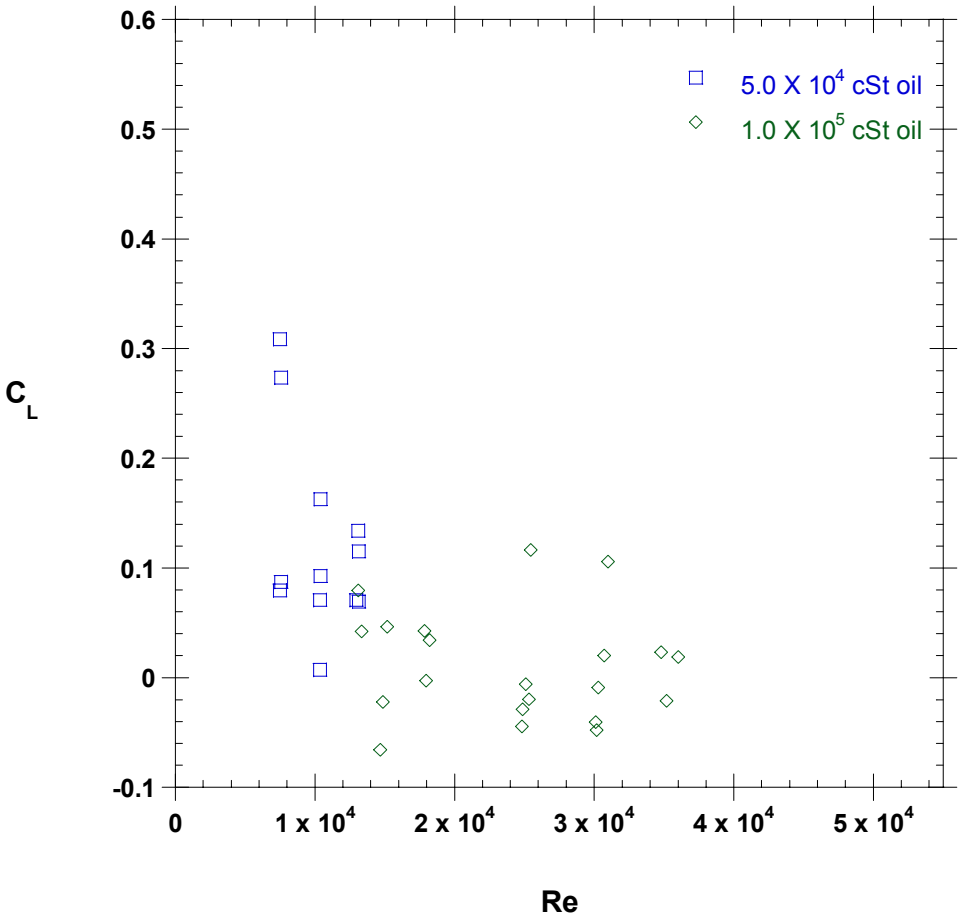

Figure 5.17 Plot of lift coefficient results for successful tests completed in the Small Gap Test Series. The legend indicates the viscosity of oil used in the floor oil reservoir. All tests were conducted with 1.0 X 10^5 cSt silicone oil in the ceiling reservoir.

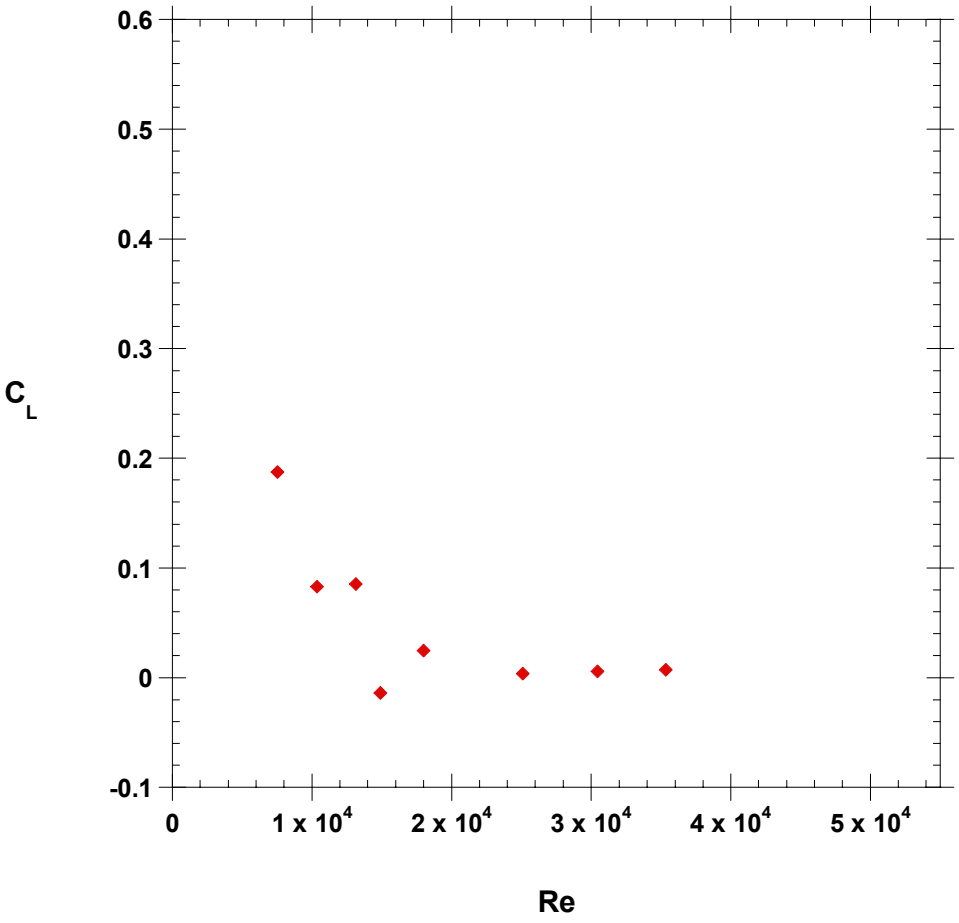

Figure 5.18 Plot of averaged lift coefficients for each tested Reynolds number in the Small Gap Test Series.

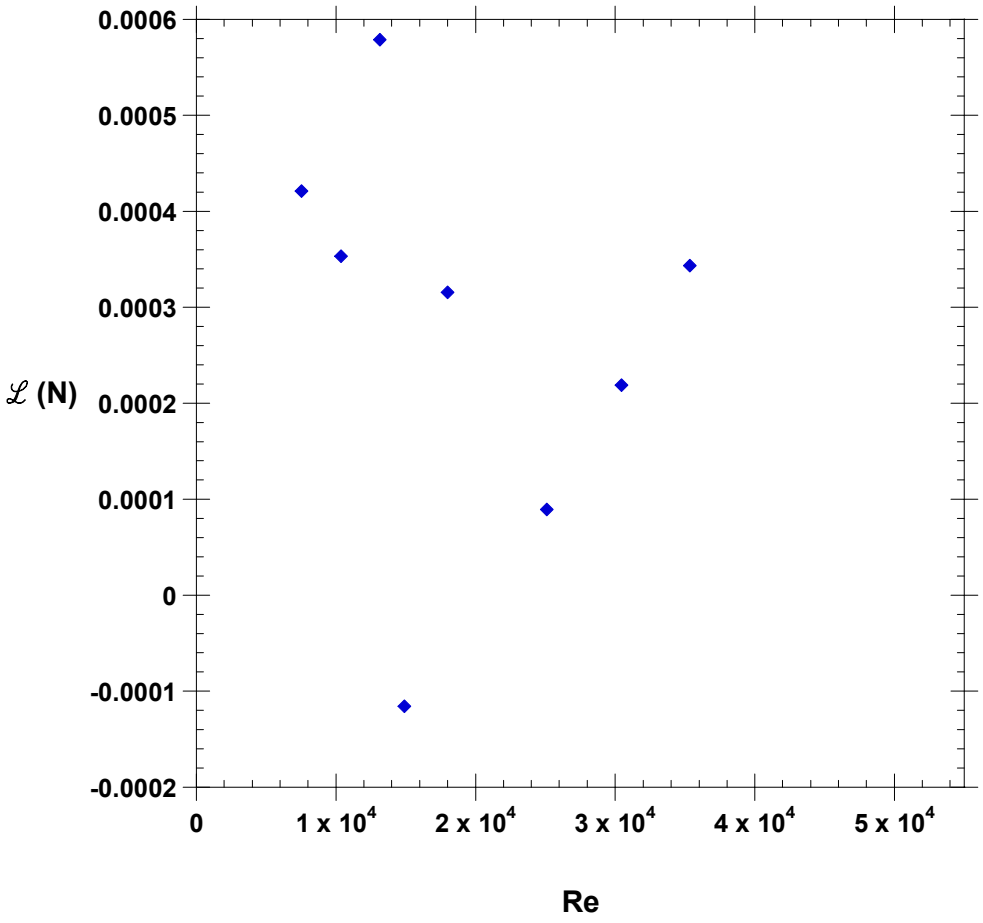

Figure 5.19 Plot of average lift forces for each specifically tested Reynolds number. No general trend exists in the data, reinforcing the statement that the lift measurement is dominated by experimental error.

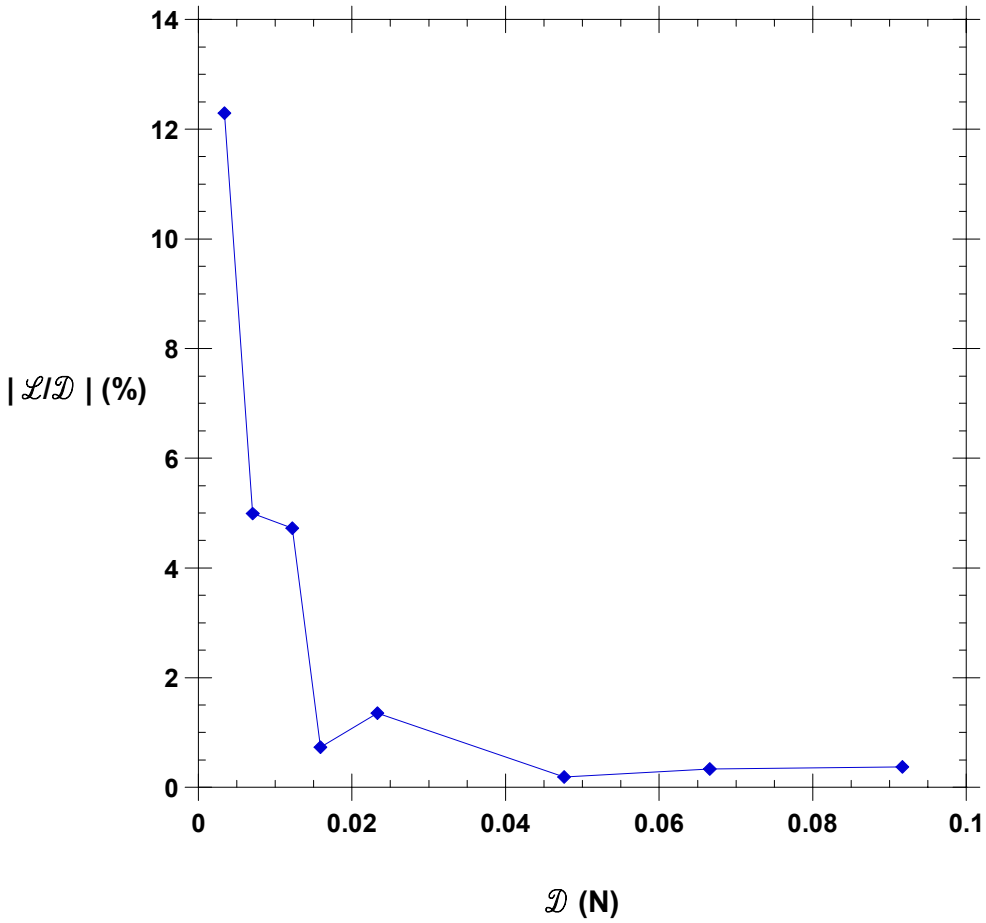

Figure 5.20 Ratio of the measured lift force to the measured drag force. For a cylindrical pin fin, the lift force should be zero. Thus, the $\mathscr{L}$ / $\mathscr{D}$ ratio plotted above represents the error in the measured lift force as a function of the measured drag force. For forces greater than 0.016 N, the lift force error is less than 2% of the measured drag force.

Chapter 6
Conclusions

This thesis summarizes the development of a new force measurement methodology. The methodology is capable of measuring small magnitude, two-axis forces on pin fins in channel flow. To accommodate the needs of this project, a new test facility was designed and constructed. The behavior of the DSC-6 sensor has been characterized both in and out of the flow. It is apparent that different testing procedures are needed to accommodate different flow rates in the test channel.

This final chapter comments on the viability of the developed test method in Section 6.1. The results of the tested pin fin geometry are summarized in Section 6.2. Section 6.3 provides recommendations for future testing and further development of this methodology.

6.1 Viability of Test Facility and Experimental Methodology

The test facility was benchmarked with static pressure taps to demonstrate flow uniformity and full hydrodynamic development. With proper installation of the inlet guides, the test section was shown to achieve flow uniformity within 2.5% from side to side of the test section. Additionally, the channel friction factor was shown to match published correlations within 5%. This indicates that the velocity profile within the channel reached full hydrodynamic development. The facility was able to provide sufficient mass flow rates, with margin to spare, for the entire test range. As such, the test facility was deemed adequate.

The force measurement methodology was used to measure the drag of cylindrical pin fins in flows ranging from $Re = 7.5 \times 10^3$ to $Re = 3.5 \times 10^4$. The tests showed that the force measurements were repeatable within 20% for drag forces as small as 3.0×10^{-3} N and within 5% for forces as small as 1.0×10^{-2} N.

Lift force measurements on the cylindrical pin fin indicate that the experimental error in the lift measurement is approximately 2% of the applied drag for drag forces greater than 1.6×10^{-2} N. Given the successful bench top calibration of the DSC-6 sensor for

two-component forces, and the small error introduced in flow testing, it is reasonable to assume this methodology is fully capable of resolving two-axis forces as well as it measures one-axis forces.

Although the results from the cylindrical pin fin test show that the measurements are repeatable, benchmarking is still required to ensure the force measurements are accurate. Additionally, it is not possible to test at flows greater than 3.5×10^4, as too much silicone oil leaks out of the pin fin gap. The upper limit of the flow rate may be reduced for pin fin cross sections that are less aerodynamic than a cylinder. The stronger pressure differences at the surface of a bluff body are likely to induce more silicone leakage. It may be necessary to use thicker viscous filler fluids or smaller pin fin gaps to prevent excessive leakage for more bluff objects.

In summary, the new test facility met its objectives. The experimental methodology successfully resolved the required minimum force magnitudes. Although the results are repeatable, a benchmarking test is required to validate the methodology.

6.2 Overview of Results

A single row of H/D = 1, S/D = 12 pin fins was tested. The measured drag values were transformed into drag coefficients by using three different normalizing velocities. The mass averaged open flow area velocity (U), the maximum turbulent velocity (U_{max}), and the mass averaged minimum flow area velocity (U_{min}) were considered. In all three cases, the measured drag coefficients were found to be larger in magnitude than the infinite cylinder drag coefficients. However, the trend of the measured drag coefficient curves appeared to approximately follow the trend of the infinite cylinder drag coefficient.

At this time, it is unclear which velocity is the correct drag coefficient scaling velocity. Additional testing at different H/D and S/D values is required to see if the drag coefficient data will collapse to a single curve for any one velocity.

The drag coefficients obtained from this project are approximately 100% higher (based on U_{min}) than the pressure drag coefficients calculated from the midline pressure distribution (based on U_{min}) of Ames et al. [2005]. This result suggests that viscous drag

on the pin fin is significantly more important in channel flow than in freestream flow. However, more work is needed to understand the difference between the two results.

6.3 Recommendations for Future Testing

Several interesting features of this project remain to be explored. First and foremost, is a benchmarking test of the cylindrical pin fin. Because pre-existing drag data for pin fins in channel flow does not exist, it may be necessary to independently quantify the pressure drag and viscous drag on the pin fin. The pressure drag may be obtained by measuring the static pressure distribution over the entire pin fin surface. Quantification of the viscous drag is more difficult, but may be possible via an oil interferometry method. However, the small size of the pin fin makes spatial resolution a problem with oil interferometry. Another (more promising) approach may be use to particle image velocimetry (PIV) measurements to survey the wake behind the pin fin and the boundary layer on the pin fin surface. In doing so, one could respectively calculate the pressure and viscous drag on the cylinder. Regardless, an innovative benchmarking technique is needed to validate the results of this experiment and resolve the discrepancy with the integrated pressure drag coefficient calculated from the data of Ames et al. [2005].

Investigation of the lip force mentioned by DeTurris [1992] and Chapter 2 of this thesis should also be investigated. Due to time constraints and the assembly difficulty of the test section, a taper was not machined into the pin fin below the surface of the floor (or above the ceiling). As noted in Chapter 2, this is the only source of error identified by DeTurris [1992] that is applicable to this project. Although the more viscous silicone oil used in this project (5.0×10^4 cSt and 1.0×10^5 cSt) should better attenuate the pressure distribution within the silicone fluid, the matter should still be investigated. I recommend conducting a test with a taper added to the cylinder above and below the channel walls. If the tapered cylinder achieves the same drag measurements as the straight cylinder, the lip force can obviously be neglected.

If possible, future investigators would be well served to develop an installation technique that automatically centers the pin fin in the channel floor and ceiling holes. I was unable to engineer a successful tooling technique capable of effortless installation.

Additionally, future studies may benefit from installing the DSC-6 with the x and y axes aligned 45° to the flow. In the current installation, with the y-axis aligned perpendicular to the flow, the sensor must attempt to measure a zero force. Measuring a zero quantity is difficult. Better results may be achievable by evenly distributing the drag force to both the x and y axes, and using trigonometry to resolve the components.

Finally, it may be possible increase the sensitivity of the DSC-6 sensor (and increase the accuracy and repeatability of the measurements) by lengthening the cantilever beam. This option was not explored in this thesis, as the undocumented cross axis sensitivity of the DSC-6 sensor artificially made longer beam lengths appear less accurate. Once the cross axis correction factors were identified, longer cantilever beam lengths were found to be effective. However, the discovery was made only after all sensor mounting hardware had been built, and the cantilever beam length could not be increased. It would be interesting to test the DSC-6 sensor with a longer beam length to see if better results are attained.

References

Ames, F.E. and Dvorak, L.A., "Turbulent Transport in Pin Fin Arrays: Experimental Data and Predictions," *ASME Journal of Turbomachinery*, vol. 128, January 2006, pp. 71–81.

Ames, F.E., Dvorak, L.A., and Morrow, M.J., "Turbulent Augmentation of Internal Convection Over Pins in Staggered-Pin Fin Arrays," *ASME Journal of Turbomachinery*, vol. 127, January 2005, pp. 183–190.

Armstrong, J., and Winstanley, D., 1988, ''A Review of Staggered Array Pin Fin Heat Transfer for Turbine Cooling Applications,'' *ASME Journal of Turbomachinery*, vol. 110, January 1988, pp. 94–103.

Chicago Blower Corporation, "Design 53 Single-Stage Pressure Blowers," brochure (Glendale Heights, IL: Chicago Blower Corporation, October 1998).

DeTurris, D., Schetz, D., and Hellbaum, R.F. "Direct Measurements of Skin Friction in a SCRAMjet Combustor," AIAA Paper 90-2342, July 1990.

DeTurris, Diane Joan, 1992, "A Technique for Direct Measurement of Skin Friction in Supersonic Combustion Flow," Doctor of Philosophy Dissertation, Department of Aerospace and Oceanographic Engineering, Virginia Polytechnic Institute and State University.

Dow Corning Corporation, "Product Information: 200 Fluid 10,000 cs, 12,500 cs, 30,000 cs," brochure (Dow Corning Corporation, October 9, 2000).

Goldstein, Sydney, *Modern Developments in Fluid Dynamics: an Account of Theory and Experiment Relating to Boundary Layers, Turbulent Motion and Wakes*, (Oxford: The Clarendon Press, 1938).

Han, Je-Chin, Dutta, Sandip, and Ekkad, Srinath V., *Gas Turbine Heat Transfer and Cooling Technology,* (London, Great Britain: Taylor and Francis, 2000).

Incropera, Frank P., and DeWitt, David P., *Fundamentals of Heat and Mass Transfer*, 4th ed. (New York, NY: John Wiley & Sons, 1996).

Kakac, S, Shah, R.K., and Aung, W., *Handbook of Single Phase Convective Heat Transfer,* (New York, NY: Wiley, 1987).

Kistler Morse, "Displacement Sensor (DS-6) Inspection and Operation Instructions," brochure (Bothell, WA: Kistler Morse, August 1998).

Lang, Robert, "Venturi Quotation #044110," Facsimile from Lambda Square Inc., 24 March 2005.

Lambda Square Inc./LSI, "Installation Instructions for the Oripac (Model 4150-P, 4150, Model 5200)," brochure (Babylon, NY: Lambda Square Inc./LSI, February 3, 1996.).

Lee, Seri, "Electronics Cooling: How to Select a Heat Sink," *http://www.electronics-cooling.com/Resources/EC_Articles/JUN95/jun95_01.htm*, (Laconia, New Hampshire: Aavid Thermal Technologies, Inc., June 1995).

Lyall, M.E., 2006, "An Experimental Investigation of High Resolution Heat Transfer Measurements in a Channelized Pin Fin Array," Master's Thesis, Department of Mechanical Engineering, Virginia Polytechnic Institute and State University.

Moffat, Robert J., "Describing the Uncertainties in Experimental Results," *Experimental Thermal and Fluid Science*, vol. 1, no. 1 (January 1988), pp. 3 – 17.

Munson, Bruce R., Young, Donald F., and Theodore H. Okiishi, *Fundamental of Fluid Mechanics*, 3rd ed. (New York, NY: John Wiley & Sons, 1998).

Prausa, J.N., 2004, "Heat Transfer Coefficient and Adiabatic Effectiveness Measurements for an Internal Turbine Vane Cooling Feature," Master's Thesis, Department of Mechanical Engineering, Virginia Polytechnic Institute and State University.

Schetz, J.A., Fred D. Durham Chair of Aerospace and Ocean Engineering at Virginia Polytechnic Institute and State University (Blacksburg, VA: August 26, 2004), personal interview.

Schetz, J.A., "Direct Measurement of Skin Friction in Complex Flows Using Movable Wall Elements," AIAA Paper 2004-2112, July 2004.

Setra Systems Inc, "Model 264 Very Low Differential Pressure Transducer," brochure (Boxborough, MA: Setra Systems Inc., April 19, 2001).

Spaeth, J., Engineer at Super Radiator Coils (Richmond, VA: March 8, 2005), email.

Standard Practices of Calibration of Force-Measuring Instruments for Verifying the Force Indication of Testing Machines, ASTM E74-02 (West Conshohocken, PA: ASTM International, April 5, 2002).

Thermacore Thermal Management Solutions, "Liquid Cooling System for Microprocessor Thermal Management," *http://www.thermacore.com/lcs_need.htm*, (Lancaster, PA: Thermacore Thermal Management Solutions).

Vlachos, P., Assistant Professor of Mechanical Engineering at Virginia Polytechnic Institute and State University (Blacksburg, VA: November 24, 2004), personal interview.

Appendix A: Analysis of Optical Force Measurement Methodology

This appendix shows how the deflection of the mechanical spring can be related to the applied aerodynamic lift and drag forces. A significant result from this analysis is that the mechanical spring pre-tension must be known in order to calculate the applied aerodynamic forces. Accurately quantifying the spring pre-tension is difficult, as it requires the experimental measurement of a zero deflection.

Geometry / Setup

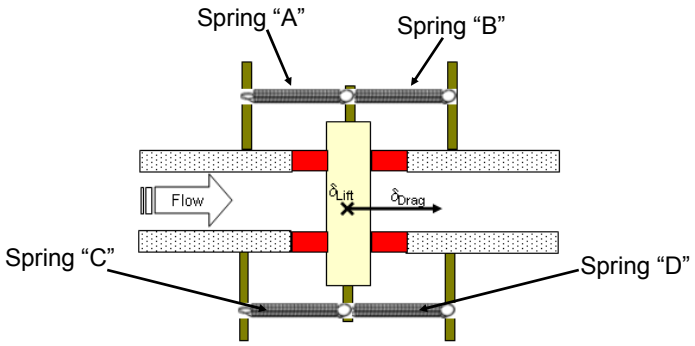

Spring "A" and Spring "B" pull on each other (even with no flow), Inducing an initial extension(δ_1) on each other. (Spring C and Spring D do exactly the same).

ΔF_x = Drag/2 & ΔF_y=Lift/2 because there are springs on the top and bottom of the channel.

Figure A.1 Explanation of mechanical spring setup. Four springs are used to measure the applied lift and drag forces.

Analysis Methodology

- Consider Spring A only: analysis of all springs follows the same methodology
- Determine force vector acting on Spring A before application of aerodynamic forces
- Determine force vector acting on Spring A after application of aerodynamic forces
- Subtract the force vectors to achieve the aerodynamic force vector

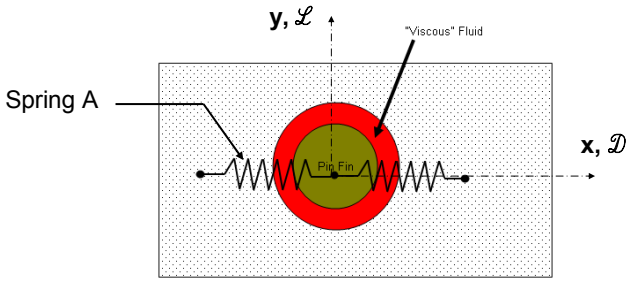

Figure A.2 Explanation of the analysis methodology.

Nomenclature

- Time 1: Time Before Lift and Drag are Applied
- Time 2: Time at Which Lift and Drag are Applied
- k = Spring Constant (Scalar)
- L_i = Initial Length of Spring (Scalar)
- L_t = Extended Length of Spring at Time t (Scalar)
- $\delta_t = L_t - L_i$ (Scalar)
- F_t = Total Applied Force at Time t (Vector)
- F_{it} = Spring Preload Component of F_t (Vector)
- $k\delta_t$ = "Extension" Force Component of F_t (Vector)
- ϕ_t = Angle of F_t at Time t (Scalar)
- ΔF = Total Applied Force $((L^2+D^2)^{\wedge}.5)$ (Vector)
- ΔF_x = X-Component of Applied Force = Drag/2 (Vector)
- ΔF_y = Y-Component of Applied Force = Lift/2 (Vector)

Figure A.3 Review of nomenclature used in this appendix (also provided on the nomenclature page).

Equilibrium state before application of aerodynamic forces (Time 1)

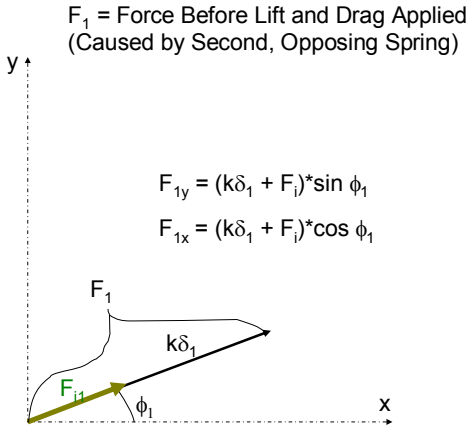

Figure A.4 Illustration of forces acting on the mechanical spring before the aerodynamic forces are applied.

Force Vector With Applied Lift and Drag (Time 2)

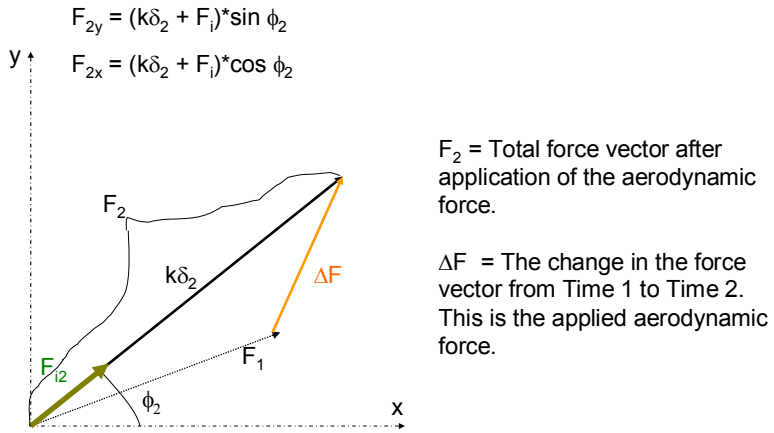

Figure A.5 Illustration of forces acting on the mechanical spring after the aerodynamic forces are applied.

Components of F_2

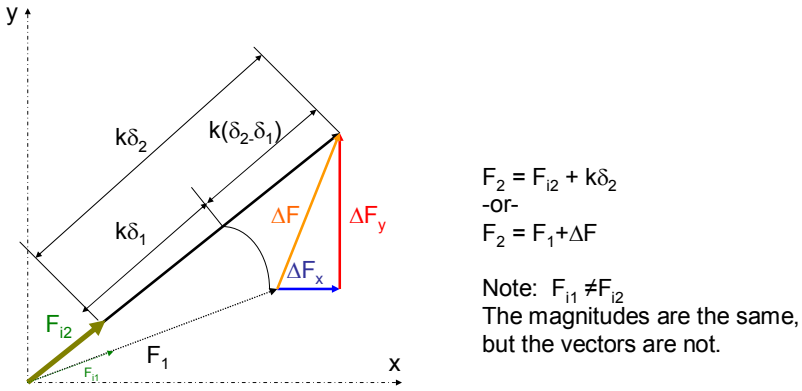

Figure A.6 Component breakdown of applied mechanical spring forces.

"Zoom" of $k(\delta_2-\delta_1)$ component

ΔF is force caused by the aerodynamic lift and drag. Hence, we desire to measure ΔF.

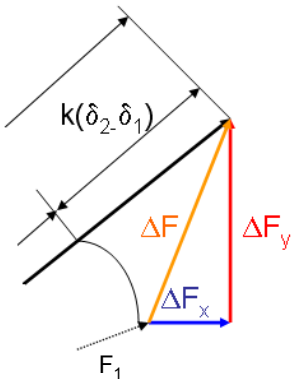

$F_2 = F_1+\Delta F$

$\Delta F = F_2-F_1$

$\Delta F = (F_{i2}+k\delta_2) - (F_{i1}+k\delta_1)$

Components…

Lift:

$\Delta F_y \neq k(\delta_2-\delta_1)*\sin\phi$

$\Delta F_y = \{(k\delta_2 + F_i)*\sin\phi_2\} - \{(k\delta_1 + F_i)*\sin\phi_1\}$

Drag:

$\Delta F_x \neq k(\delta_2-\delta_1)*\cos\phi$

$\Delta F_x = \{(k\delta_2 + F_i)*\cos\phi_2\} - \{(k\delta_1 + F_i)*\cos\phi_1\}$

Figure A.7 Final analysis of applied aerodynamic lift and drag forces. The figure shows that measurement of the applied lift and drag forces requires knowledge of the spring pre-tension.

Appendix B: Status Summary of Two-Axis DSC-6 Sensors

This appendix provides the disposition of all received two-axis DSC-6 sensors.

Table B.1 Summary of Two-Axis DSC-6 Sensors

S/N	X-Axis	Y-Axis	
	Wiring Configuration	Wiring Configuration	Notes
5117	Nominal	Nominal	Damaged x-axis strain gauge
5118	Nominal	Inverse	Erratic output while submerged in silicone oil
5119	Nominal	Nominal	Damaged x-axis, broken wires both axes
5120	Inverse	Inverse	Ready to use, broken wire is fixed
5121	Inverse	Nominal	In-use
5122			Never used; Ready for use
5123	Nominal	?	Electrically leaks to ground, Randy could not fix
5124	Inverse	Nominal	Broken strain gauge

Notes:

"Damaged axis" indicates a strain gauge is out of tolerance (1000 + 100 W), but can still read a force.

"Broken axis" indicates that the strain gauge is totally broken.

Calibration Data Provided by Kistler Morse

S/N	X-Axis			Y-Axis			T/C Val		
	R_1 (Ω)	R_3 (Ω)	GF	R_2 (Ω)	R_4 (Ω)	GF	a	b	c
5117	1046	1076	6.9	1053	1046	6.6	0-100	17.8-37.8	2.6/1.1
5118	1073	1043	6.4	1070	1082	6.7	0-100	17.8-37.8	1/5
5119	1059	1065	6.6	1069	1043	6.3	0-100	17.8-37.8	5.7/8
5120	1057	1042	6.7	1057	1038	6.6	0-100	17.8-37.8	5.4/3
5121	1071	1021	6.6	1087	1055	6.7	0-100	17.8-37.8	.8/1
5122	1091	1057	6.9	1086	1050	6.8	0-100	17.8-37.8	10/5
5123	1092	1075	6.3	1069	1083	6.5	0-100	17.8-37.8	10/22
5124	1099	1082	6.3	1051	1071	7.2	0-100	17.8-37.8	2/9

Appendix C: Experimental Uncertainty Calculations

This appendix presents the uncertainty analysis for C_D, C_L, and Re.

Uncertainty for Drag Coefficient, C_D

$$C_D = \frac{2 * g * H * W^2 * V_x / V_{ex}}{d_x * D * Q^2 * (2.54 - \delta)\rho}$$

$$u_{CD} = \sqrt{\left(\frac{\partial C_D}{\partial\left(\frac{V_x}{V_{ex}}\right)} u_{V_x/V_{ex}}\right)^2 + \left(\frac{\partial C_D}{\partial(d_x)} u_{d_x}\right)^2 + \left(\frac{\partial C_D}{\partial(\delta)} u_{\delta}\right)^2 + \left(\frac{\partial C_D}{\partial(W)} u_W\right)^2 + \left(\frac{\partial C_D}{\partial(H)} u_H\right)^2 + \left(\frac{\partial C_D}{\partial(\rho)} u_{\rho}\right)^2 + \ldots}$$
$$\sqrt{\ldots + \left(\frac{\partial C_D}{\partial(Q)} u_Q\right)^2 + \left(\frac{\partial C_D}{\partial(D)} u_D\right)^2 + u_{Rotation}^2 + u_{Perpendicularity}^2 + u_{Linear\_Regression}^2 + u_{Temperature}^2 + u_{Drift}^2}$$

Volumetric Flow Rate

$$Q = \left(\frac{\rho_{STD}}{\rho}\right) \frac{5.9816 * (d^2) * K * Y \sqrt{dp} * \sqrt{\frac{2.703 * P_L}{460 + T_L}}}{\frac{2.703 * 14.7}{460 + 60}} * \frac{4.71936 * 10^{-4}\ \text{m}^3/\text{sec}}{1\ \text{CFM}}$$

$$u_Q = \sqrt{\left[\frac{\partial Q}{\partial(dp)} * u_{dp}\right]^2 + \left[\frac{\partial Q}{\partial(T_L)} * u_{TL}\right]^2 + \left[\frac{\partial Q}{\partial(P_L)} * u_{PL}\right]^2 + u_{meter}^2}$$

Sensor Voltage Ratio

$$\frac{V_x}{V_{ex}} = \frac{(V_{ox} - V_{zero\_x})}{V_{ex}} - \xi \frac{(V_{oy} - V_{zero\_y})}{V_{ey}}$$

$$u_{\frac{V_x}{V_{ex}}} = \sqrt{\left[\frac{\partial\left(\frac{V_x}{V_{ex}}\right)}{\partial(V_{ox})} * u_{V_{ox}}\right]^2 + \left[\frac{\partial\left(\frac{V_x}{V_{ex}}\right)}{\partial(V_{ex})} * u_{V_{ex}}\right]^2 + \left[\frac{\partial\left(\frac{V_x}{V_{ex}}\right)}{\partial(V_{zero\_x})} * u_{V_{zero\_x}}\right]^2 + \left[\frac{\partial\left(\frac{V_x}{V_{ex}}\right)}{\partial(\xi)} * u_{\xi}\right]^2 + \ldots}$$
$$\sqrt{\left[\frac{\partial\left(\frac{V_x}{V_{ex}}\right)}{\partial(V_{oy})} * u_{V_{oy}}\right]^2 + \left[\frac{\partial\left(\frac{V_x}{V_{ex}}\right)}{\partial(V_{ey})} * u_{V_{ey}}\right]^2 + \left[\frac{\partial\left(\frac{V_x}{V_{ex}}\right)}{\partial(V_{zero\_y})} * u_{V_{zero\_y}}\right]^2}$$

Re = 7.5 X 10^3

Variable	Value	Precision Uncertainty	Bias Uncertainty	Total Uncertainty	u_{CD}	% C_D
C_D	1.56	0.064	0.079	0.102	**0.102**	**6.50%**
V_x/V_{ex}	1.12E-04	1.008E-06	0	1.01E-06	1.40E-02	0.90%
d_x (V/V-kg-cm)	0.11	0	1.16E-03	1.16E-03	1.58E-02	1.01%
δ (cm)	-0.19	0	1.27E-02	1.27E-02	7.27E-03	0.47%
W (cm)	0.61	0	7.94E-04	7.94E-04	4.06E-03	0.26%
H (cm)	9.60E-03	0	3.81E-04	3.81E-04	6.19E-02	3.97%
ρ (kg/m³)	1.12	3.09E-05	1.42E-03	1.42E-03	1.98E-03	0.13%
Q (m³/s)	0.038	1.26E-05	3.68E-04	3.68E-04	2.99E-02	1.92%
D (cm)	0.010	0	5.08E-05	5.08E-05	8.13E-03	0.52%
Rotation (°)	0	0	10	10	2.37E-02	1.52%
Perpendicularity (°)	0	0	5	5	5.94E-03	0.38%
Linear Regression Uncertainty	N/A	6.25E-02	0	6.25E-02	6.25E-02	4.01%
Temperature Uncertainty (g)	N/A	0	1.16E-03	1.16E-03	5.01E-03	0.32%
Sensor Drift (g)	N/A	0	5.03E-03	5.03E-03	2.18E-02	1.40%

Re = 3.5 X 10^4

Variable	Value	Precision Uncertainty	Bias Uncertainty	Total Uncertainty	u_{CD}	%C_D
C_D	1.85	3.54E-03	8.90E-02	**0.089**	**8.90E-02**	**4.80%**
V_x/V_{ex}	2.89E-03	2.663E-06	0	2.66E-06	1.71E-03	0.09%
d_x (V/V-kg-cm)	0.11	0	1.16E-03	1.16E-03	1.88E-02	1.01%
δ (cm)	-0.19	0	1.27E-02	1.27E-02	8.64E-03	0.47%
W (cm)	0.61	0	7.94E-04	7.94E-04	4.83E-03	0.26%
H (cm)	9.60E-03	0	3.81E-04	3.81E-04	7.36E-02	3.97%
ρ (kg/m³)	1.11	8.53E-05	1.41E-03	1.41E-03	2.36E-03	0.13%
Q (m³/s)	0.180	4.41E-05	1.58E-03	1.58E-03	3.27E-02	1.76%
D (cm)	0.010	0	5.08E-05	5.08E-05	9.66E-03	0.52%
Rotation (°)	0	0	10	10	2.82E-02	1.52%
Perpendicularity (°)	0	0	5	5	7.06E-03	0.38%
Linear Regression Uncertainty	N/A	2.96E-03	0	2.96E-03	2.96E-03	0.16%
Temperature Uncertainty (g)	N/A	0	3.33E-02	3.33E-02	6.65E-03	0.36%
Sensor Drift (g)	N/A	0	1.08E-03	1.08E-03	2.15E-04	0.01%

Uncertainty for Drag Coefficient, C_L

$$C_L = \frac{2 * g * H * W^2 * V_y / V_{ey}}{d_y * D * Q^2 * (2.54 - \delta)\rho}$$

$$u_{CL} = \sqrt{\left(\frac{\partial C_L}{\partial\left(\frac{V_T}{V_{ey}}\right)} u_{V_y/V_{ey}}\right)^2 + \left(\frac{\partial C_L}{\partial(d_y)} u_{d_y}\right)^2 + \left(\frac{\partial C_L}{\partial(\delta)} u_{\delta}\right)^2 + \left(\frac{\partial C_L}{\partial(W)} u_W\right)^2 + \left(\frac{\partial C_L}{\partial(H)} u_H\right)^2 + \left(\frac{\partial C_L}{\partial(\rho)} u_{\rho}\right)^2 + \ldots}$$
$$\sqrt{\ldots + \left(\frac{\partial C_L}{\partial(Q)} u_Q\right)^2 + \left(\frac{\partial C_L}{\partial(D)} u_D\right)^2 + u^2_{Rotation} + u^2_{Perpendicularity} + u^2_{Linear\_Regression} + u^2_{Temperature} + u^2_{Drift}}$$

Volumetric Flow Rate

$$Q = \left(\frac{\rho_{STD}}{\rho}\right) \frac{5.9816 * (d^2) * K * Y \sqrt{dp} * \sqrt{\frac{2.703 * P_L}{460 + T_L}}}{\frac{2.703 * 14.7}{460 + 60}} * \frac{4.71936 * 10^{-4}\ \text{m}^3/\text{sec}}{1\ \text{CFM}}$$

$$u_Q = \sqrt{\left[\frac{\partial Q}{\partial(dp)} * u_{dp}\right]^2 + \left[\frac{\partial Q}{\partial(T_L)} * u_{TL}\right]^2 + \left[\frac{\partial Q}{\partial(P_L)} * u_{PL}\right]^2 + u^2_{meter}}$$

Sensor Voltage Ratio

$$\frac{V_y}{V_{ex}} = \frac{(V_{oy} - V_{zero\_y})}{V_{ey}} - \psi \frac{(V_{ox} - V_{zero\_x})}{V_{ex}}$$

$$u_{\frac{V_y}{V_{ey}}} = \sqrt{\left[\frac{\partial\left(\frac{V_y}{V_{ey}}\right)}{\partial(V_{oy})} * u_{V_{ox}}\right]^2 + \left[\frac{\partial\left(\frac{V_y}{V_{ey}}\right)}{\partial(V_{ey})} * u_{V_{ey}}\right]^2 + \left[\frac{\partial\left(\frac{V_y}{V_{ey}}\right)}{\partial(V_{zero\_y})} * u_{V_{zero\_y}}\right]^2 + \left[\frac{\partial\left(\frac{V_y}{V_{ey}}\right)}{\partial(\psi)} * u_{\psi}\right]^2 + \ldots}$$
$$\sqrt{\left[\frac{\partial\left(\frac{V_y}{V_{ey}}\right)}{\partial(V_{ox})} * u_{V_{ox}}\right]^2 + \left[\frac{\partial\left(\frac{V_y}{V_{ey}}\right)}{\partial(V_{ex})} * u_{V_{ex}}\right]^2 + \left[\frac{\partial\left(\frac{V_y}{V_{ey}}\right)}{\partial(V_{zero\_x})} * u_{V_{zero\_x}}\right]^2}$$

Re = 7.5 X 10^3

Variable	Value	Precision Uncertainty	Bias Uncertainty	Total Uncertainty	u_{CL}	% C_L
C_L	8.73E-02	3.48E-02	2.34E-02	4.20E-02	**4.20E-02**	**48.00%**
V_y/V_{ey}	6.08E-06	2.73E-07	0	2.73E-07	3.91E-03	4.48%
d_y (V/V-kg-cm)	0.11	0	1.12E-03	1.12E-03	8.82E-04	1.01%
δ (cm)	-0.19	0	1.27E-02	1.27E-02	4.07E-04	0.47%
W (cm)	0.61	0	7.94E-04	7.94E-04	2.27E-04	0.26%
H (cm)	9.60E-03	0	3.81E-04	3.81E-04	3.46E-03	3.97%
ρ (kg/m³)	1.12	3.09E-05	1.42E-03	1.42E-03	1.10E-04	0.13%
Q (m³/s)	3.85E-02	1.26E-05	3.68E-04	3.68E-04	1.67E-03	1.92%
D (cm)	9.75E-03	0	5.08E-05	5.08E-05	4.54E-04	0.52%
Rotation (°)	0	0	10	10	1.33E-03	1.52%
Perpendicularity (°)	0	0	5	5	3.32E-04	0.38%
Linear Regression Uncertainty	N/A	3.45E-02	0	3.45E-02	3.45E-02	39.58%
Temperature Uncertainty (g)	N/A	0	1.19E-03	1.19E-03	5.16E-03	5.91%
Sensor Drift (g)	N/A	0	5.18E-03	5.18E-03	2.25E-02	25.74%

Re = 3.5 X 10^4

Variable	Value	Precision Uncertainty	Bias Uncertainty	Total Uncertainty	u_{CD}	%C_D
C_L	-2.12E-02	4.05E-03	6.93E-03	0.008	**8.00E-03**	**37.90%**
V_y/V_{ey}	-3.21E-05	5.63E-06	0	5.63E-06	3.73E-03	-17.57%
d_y (V/V-kg-cm)	0.11	0	1.12E-03	1.12E-03	2.15E-04	-1.01%
δ (cm)	-0.19	0	1.27E-02	1.27E-02	9.88E-05	-0.47%
W (cm)	0.61	0	7.94E-04	7.94E-04	5.52E-05	-0.26%
H (cm)	9.60E-03	0	3.81E-04	3.81E-04	8.42E-04	-3.97%
ρ (kg/m³)	1.11	8.53E-05	1.41E-03	1.41E-03	2.70E-05	-0.13%
Q (m³/s)	1.80E-01	4.41E-05	1.58E-03	1.58E-03	3.74E-04	-1.76%
D (cm)	9.75E-03	0	5.08E-05	5.08E-05	1.10E-04	-0.52%
Rotation (°)	0	0	10	10	3.22E-04	-1.52%
Perpendicularity (°)	0	0	5	5	8.07E-05	-0.38%
Linear Regression Uncertainty	N/A	1.59E-03	0	1.59E-03	1.59E-03	-7.51%
Temperature Uncertainty (g)	N/A	0	3.43E-02	3.43E-02	6.85E-03	-32.31%
Sensor Drift (g)	N/A	0	1.11E-03	1.11E-03	2.22E-04	-1.05%

Uncertainty for Channel Reynolds Number, Re

$$\mathrm{Re} = \frac{2\rho Q}{\mu(W+H)}$$

$$u_{\mathrm{Re}} = \sqrt{\left(\frac{\partial \mathrm{Re}}{\partial \rho}u_\rho\right)^2 + \left(\frac{\partial \mathrm{Re}}{\partial Q}u_Q\right)^2 + \left(\frac{\partial \mathrm{Re}}{\partial \mu}u_\mu\right)^2 + \left(\frac{\partial \mathrm{Re}}{\partial W}u_W\right)^2 + \left(\frac{\partial \mathrm{Re}}{\partial H}u_H\right)^2}$$

Volumetric Flow Rate

$$Q = \left(\frac{\rho_{STD}}{\rho}\right)\frac{5.9816*\left(d^2\right)*K*Y\sqrt{dp}*\sqrt{\frac{2.703*P_L}{460+T_L}}}{\frac{2.703*14.7}{460+60}} * \frac{4.71936*10^{-4}\,\mathrm{m^3/sec}}{1\,\mathrm{CFM}}$$

$$u_Q = \sqrt{\left[\frac{\partial Q}{\partial(dp)}*u_{dp}\right]^2 + \left[\frac{\partial Q}{\partial(T_L)}*u_{TL}\right]^2 + \left[\frac{\partial Q}{\partial(P_L)}*u_{PL}\right]^2 + u_{meter}^2}$$

Re = 7.5 X 10^3

Variable	Value	Precision Uncertainty	Bias Uncertainty	Total Uncertainty		u_{Re}	%Re
Re	7568	2.5	73.9	74		**74.0**	**0.98%**
W (cm)	0.61	0	7.94E-04	7.94E-04		9.7	0.13%
H (cm)	9.60E-03	0	3.81E-04	3.81E-04		4.7	0.06%
ρ (kg/m³)	1.12	3.09E-05	1.42E-03	1.42E-03		9.6	0.13%
Q (m³/s)	3.85E-02	1.26E-05	3.68E-04	3.68E-04		72.5	0.96%

Re = 3.5 X 10^4

Variable	Value	Precision Uncertainty	Bias Uncertainty	Total Uncertainty		u_{Re}	%Re
Re	35192	9.1	317.0	317		**317**	**0.90%**
W (cm)	0.61	0	7.94E-04	7.94E-04		45	0.13%
H (cm)	9.60E-03	0	3.81E-04	3.81E-04		22	0.06%
ρ (kg/m³)	1.11	8.53E-05	1.41E-03	1.41E-03		45	0.13%
Q (m³/s)	1.80E-01	4.41E-05	1.58E-03	1.58E-03		310	0.88%

Appendix D: Test Facility Component Datasheets

This appendix presents the available information regarding the heat exchanger, venturi, orifice, and blower used in the test facility.

Customer:	Virginia Tech		Date:	3/8/2005
Job Ref.:	High Flow		By:	Jeff Spaeth
Job Item:			Record:	
Dry Water Coil	Units (SI)			
AirSide:				
Air Flow	m3/hr. (Std.)	1,397		
Required Capacity	kW	13.45		
Entering Air Temp.	°C	54.4		
Required Air Temp.	°C	26.0		
Airside Pressure	kPa	101.329		
Tubeside:				
Fluid ID		WATER		
Fluid Flow Rate	L/Min.	15.14		
Entering Fluid Temp.	°C	21.11		
Coil Selection:				
Model Number		18.75x42-4R-12/120		
Die Surface		1/2 - 1-1/4 x 1.083 Stag.(Sine-#16)		
Die Number & Location		16 (All Plants)		
Face Area	m^2	0.51		
Face Velocity	m/sec.	0.8		
Number of Circuits		3		
Tube Velocity	m/sec.	0.7		
Configuration		Thermal Counterflow		
Tube Material		CU		
Tube Wall Thickness	mm	0.406		
Fin Material		AL		
Fin Thickness	mm	0.1397		
Header Diam.	mm	22.225		
Capacity:				
Rating	kW	13.73		
Leaving Air Temp.	°C	25.4		
Leaving Fluid Temp.	°C	34.1		
Fluid Press. Drop	kPa.	20.9		
Air Friction	kPa.	0.01		

Figure D.1 Heat exchanger performance specifications, as quoted by Jeff Spaeth of Super Radiator Coils [Spaeth, 2004].

Coil Data		Materials & Options	
Fin Height	18.75"	Tube Material	Copper
Finned Length	42.00"	Tube Wall Thickness	0.016"
Rows	4	Fin Material	Aluminum
Fins Per Inch	10	Fin Thickness	0.0055"
Die Surface	1/2 - 1-1/4 x 1.083 Stag.(Sine-#16)	Header Diameter	0.875"
Die & Location	#16 (All Plants)	Casing Material	16G Gal.Steel
Number of Circuits	3	Casing Style	Encased
Tubes High	15	Num.Int.Plates	None
Circuiting Type	Thermal Counterflow	Coil Hand / Airflow	Left Hand

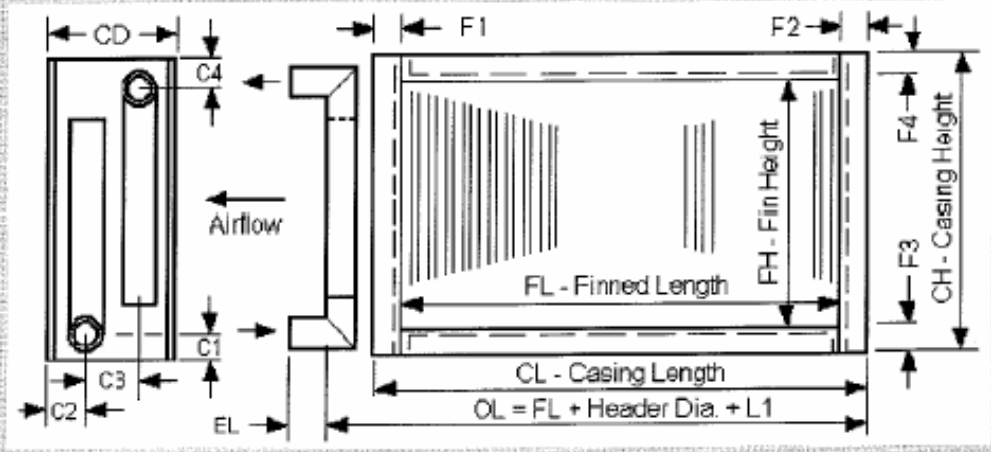

-- Coil Sketch And Dimensions --

Casing Height (CH Dim.)	21.25"	F1 / F2 / F3 / F4 Dims.	1.25"
Overall Length (OL Dim.)	45.75"	L1 Dim.	2.88"
Coil Depth (CD Dim.)	6.50"	C1 / C4 Dim.	1.50"
Casing Length (CL Dim.)	44.50"	C2 / C3 Dims.	1.63 / 3.25"
Ext./Conn. Lgth. (EL Dim.)	2.00"	Approx. Coil Weight	66 Lb.

Figure D.2 Pertinent heat exchanger dimensions, as provided by Jeff Spaeth of Super Radiator Coils [Spaeth, 2004].

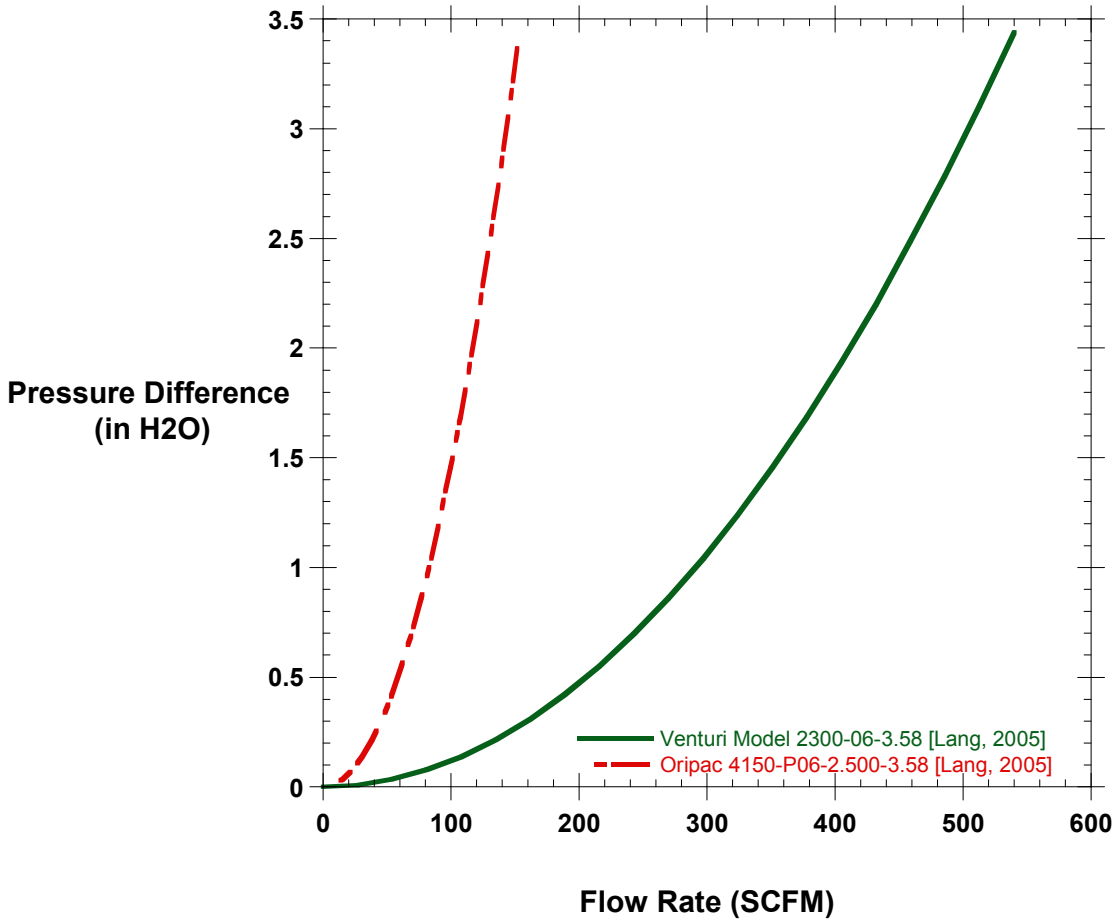

Figure D.3 Plot of flow rate as a function of pressure difference for the orifice and venturi meters [Lang, 2005].

$$Q_{actual}\ (CFM\ ) = (Q_{STD}\ )\frac{\rho_{STD}}{\rho_{actual}}$$

$$Q_{STD}\,(SCFM) = \frac{5.9816 * (d^2) * K * Y * \sqrt{dp} * \sqrt{\frac{2.703 P_L * SG}{460 + T_L}}}{\frac{2.703 * 14.7 * SG}{460 + T_b}}$$

$$Y = 1 - (.41 + .35\beta^4)\frac{.0361 * dp}{1.4 P_L} \qquad K = \frac{C}{\sqrt{1 - \beta^4}} \qquad \rho = \frac{P}{RT}$$

Where:

5.9816=physical constant
d = bore in inches
K = Flow Coefficient
Y = Expansion Factor
dp = Differential Pressure (in H_2O)

P_L = Line pressure (psia)
T_L = Line Temperature (°F)
T_b = Base Temperature (60°F)
β = beta ratio
SG = Specific gravity (air = 1.00)

Flow Meter Parameters		
	Orifice	Venturi
bore, d, (in):	2.5	3.58
discharge coefficient, C:	0.6084	0.995
expansion factor, Y =		0.9971
β:	0.4122	0.5903

Figure D.4 Physical parameters and equations for calculating the mass flow rate through the orifice and venturi [Lang, 2005].

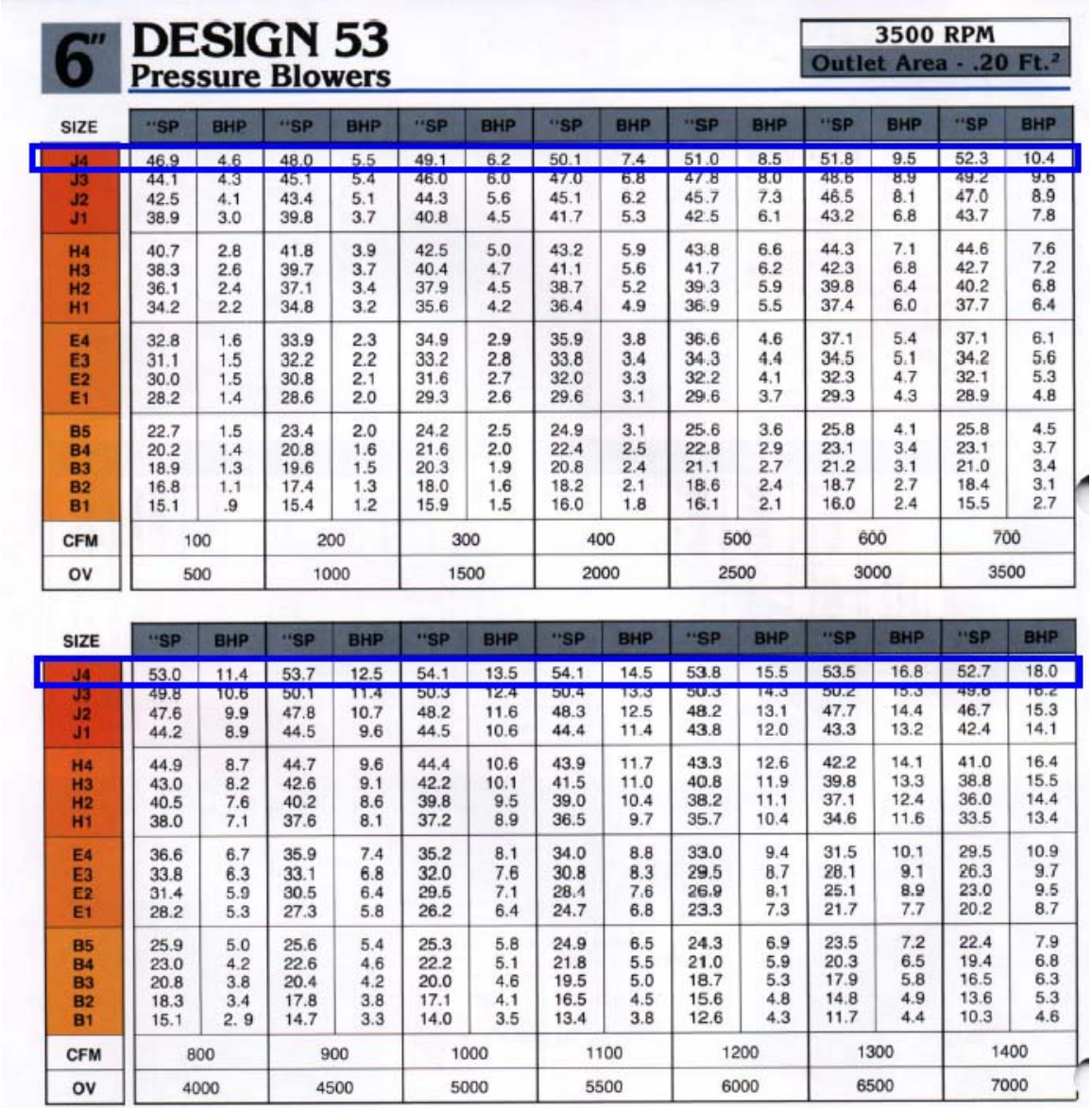

6" DESIGN 53
Pressure Blowers

3500 RPM
Outlet Area - .20 Ft.²

SIZE	"SP	BHP	"SP	BHP	"SP	BHP	"SP	BHP	"SP	BHP	"SP	BHP	"SP	BHP
J4	46.9	4.6	48.0	5.5	49.1	6.2	50.1	7.4	51.0	8.5	51.8	9.5	52.3	10.4
J3	44.1	4.3	45.1	5.4	46.0	6.0	47.0	6.8	47.8	8.0	48.6	8.9	49.2	9.6
J2	42.5	4.1	43.4	5.1	44.3	5.6	45.1	6.2	45.7	7.3	46.5	8.1	47.0	8.9
J1	38.9	3.0	39.8	3.7	40.8	4.5	41.7	5.3	42.5	6.1	43.2	6.8	43.7	7.8
H4	40.7	2.8	41.8	3.9	42.5	5.0	43.2	5.9	43.8	6.6	44.3	7.1	44.6	7.6
H3	38.3	2.6	39.7	3.7	40.4	4.7	41.1	5.6	41.7	6.2	42.3	6.8	42.7	7.2
H2	36.1	2.4	37.1	3.4	37.9	4.5	38.7	5.2	39.3	5.9	39.8	6.4	40.2	6.8
H1	34.2	2.2	34.8	3.2	35.6	4.2	36.4	4.9	36.9	5.5	37.4	6.0	37.7	6.4
E4	32.8	1.6	33.9	2.3	34.9	2.9	35.9	3.8	36.6	4.6	37.1	5.4	37.1	6.1
E3	31.1	1.5	32.2	2.2	33.2	2.8	33.8	3.4	34.3	4.4	34.5	5.1	34.2	5.6
E2	30.0	1.5	30.8	2.1	31.6	2.7	32.0	3.3	32.2	4.1	32.3	4.7	32.1	5.3
E1	28.2	1.4	28.6	2.0	29.3	2.6	29.6	3.1	29.6	3.7	29.3	4.3	28.9	4.8
B5	22.7	1.5	23.4	2.0	24.2	2.5	24.9	3.1	25.6	3.6	25.8	4.1	25.8	4.5
B4	20.2	1.4	20.8	1.6	21.6	2.0	22.4	2.5	22.8	2.9	23.1	3.4	23.1	3.7
B3	18.9	1.3	19.6	1.5	20.3	1.9	20.8	2.4	21.1	2.7	21.2	3.1	21.0	3.4
B2	16.8	1.1	17.4	1.3	18.0	1.6	18.2	2.1	18.6	2.4	18.7	2.7	18.4	3.1
B1	15.1	.9	15.4	1.2	15.9	1.5	16.0	1.8	16.1	2.1	16.0	2.4	15.5	2.7
CFM	100		200		300		400		500		600		700	
OV	500		1000		1500		2000		2500		3000		3500	

SIZE	"SP	BHP	"SP	BHP	"SP	BHP	"SP	BHP	"SP	BHP	"SP	BHP	"SP	BHP
J4	53.0	11.4	53.7	12.5	54.1	13.5	54.1	14.5	53.8	15.5	53.5	16.8	52.7	18.0
J3	49.8	10.6	50.1	11.4	50.3	12.4	50.4	13.3	50.3	14.3	50.2	15.3	49.6	16.2
J2	47.6	9.9	47.8	10.7	48.2	11.6	48.3	12.5	48.2	13.1	47.7	14.4	46.7	15.3
J1	44.2	8.9	44.5	9.6	44.5	10.6	44.4	11.4	43.8	12.0	43.3	13.2	42.4	14.1
H4	44.9	8.7	44.7	9.6	44.4	10.6	43.9	11.7	43.3	12.6	42.2	14.1	41.0	16.4
H3	43.0	8.2	42.6	9.1	42.2	10.1	41.5	11.0	40.8	11.9	39.8	13.3	38.8	15.5
H2	40.5	7.6	40.2	8.6	39.8	9.5	39.0	10.4	38.2	11.1	37.1	12.4	36.0	14.4
H1	38.0	7.1	37.6	8.1	37.2	8.9	36.5	9.7	35.7	10.4	34.6	11.6	33.5	13.4
E4	36.6	6.7	35.9	7.4	35.2	8.1	34.0	8.8	33.0	9.4	31.5	10.1	29.5	10.9
E3	33.8	6.3	33.1	6.8	32.0	7.6	30.8	8.3	29.5	8.7	28.1	9.1	26.3	9.7
E2	31.4	5.9	30.5	6.4	29.5	7.1	28.4	7.6	26.9	8.1	25.1	8.9	23.0	9.5
E1	28.2	5.3	27.3	5.8	26.2	6.4	24.7	6.8	23.3	7.3	21.7	7.7	20.2	8.7
B5	25.9	5.0	25.6	5.4	25.3	5.8	24.9	6.5	24.3	6.9	23.5	7.2	22.4	7.9
B4	23.0	4.2	22.6	4.6	22.2	5.1	21.8	5.5	21.0	5.9	20.3	6.5	19.4	6.8
B3	20.8	3.8	20.4	4.2	20.0	4.6	19.5	5.0	18.7	5.3	17.9	5.8	16.5	6.3
B2	18.3	3.4	17.8	3.8	17.1	4.1	16.5	4.5	15.6	4.8	14.8	4.9	13.6	5.3
B1	15.1	2. 9	14.7	3.3	14.0	3.5	13.4	3.8	12.6	4.3	11.7	4.4	10.3	4.6
CFM	800		900		1000		1100		1200		1300		1400	
OV	4000		4500		5000		5500		6000		6500		7000	

Figure D.5 Performance specifications of J4 high pressure blower [Chicago Blower Corporation, 1998].

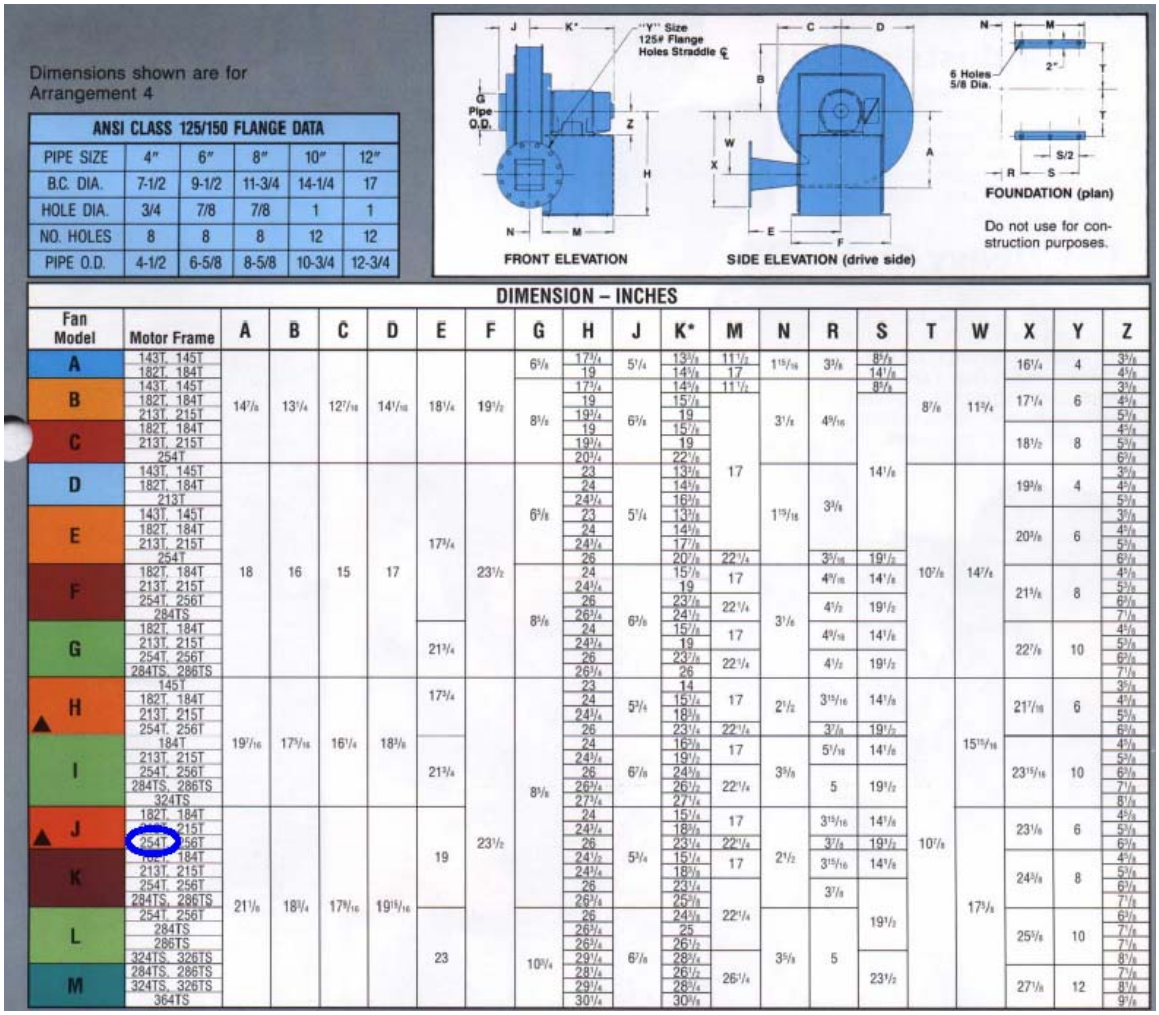

Dimensions shown are for Arrangement 4

ANSI CLASS 125/150 FLANGE DATA

PIPE SIZE	4"	6"	8"	10"	12"
B.C. DIA.	7-1/2	9-1/2	11-3/4	14-1/4	17
HOLE DIA.	3/4	7/8	7/8	1	1
NO. HOLES	8	8	8	12	12
PIPE O.D.	4-1/2	6-5/8	8-5/8	10-3/4	12-3/4

DIMENSION – INCHES

Fan Model	Motor Frame	A	B	C	D	E	F	G	H	J	K*	M	N	R	S	T	W	X	Y	Z
A	143T, 145T	14 7/8	13 1/4	12 7/16	14 1/16	18 1/4	19 1/2	6 5/8	17 3/4	5 1/4	13 3/4	11 1/2	1 15/16	3 3/8	8 3/4	8 7/8	11 3/4	16 1/4	4	3 5/8
	182T, 184T								19		14 5/8	17			14 1/8					4 5/8
B	143T, 145T							8 5/8	17 3/4	6 1/8	14 5/8	11 1/2	3 1/8	4 9/16	8 3/4			17 1/4	6	3 5/8
	182T, 184T								19		15 7/8									4 5/8
	213T, 215T								19 3/4		19									5 5/8
C	182T, 184T								19		15 7/8							18 1/2	8	4 5/8
	213T, 215T								19 3/4		19									5 5/8
	254T								20 3/4		22 1/8									6 5/8
D	143T, 145T	18	16	15	17	17 3/4	23 1/2	6 5/8	23	5 1/4	13 7/8	17	1 15/16	3 3/8	14 1/8	10 7/8	14 7/8	19 3/8	4	3 5/8
	182T, 184T								24		14 5/8									4 5/8
	213T								24 3/4		16 3/8									5 5/8
E	143T, 145T								23		13 7/8							20 5/8	6	3 5/8
	182T, 184T								24		14 5/8									4 5/8
	213T, 215T								24 3/4		17 7/8									5 5/8
	254T								26		20 7/8	22 1/4		3 5/16	19 1/2					6 5/8
F	182T, 184T							8 5/8	24	6 1/8	15 7/8	17	3 1/8	4 9/16	14 1/8			21 3/8	8	4 5/8
	213T, 215T								24 3/4		19									5 5/8
	254T, 256T								26		23 7/8	22 1/4		4 1/2	19 1/2					6 5/8
	284TS								26 3/4		24 1/2									7 1/8
G	182T, 184T					21 3/4			24		15 7/8	17		4 9/16	14 1/8			22 7/8	10	4 5/8
	213T, 215T								24 3/4		19									5 5/8
	254T, 256T								26		23 7/8	22 1/4		4 1/2	19 1/2					6 5/8
	284TS, 286TS								26 3/4		26									7 1/8
H ▲	145T	19 7/16	17 5/16	16 1/4	18 3/8	17 3/4	23 1/2	8 5/8	23	5 3/4	14	17	2 1/2	3 15/16	14 1/8	10 7/8	15 15/16	21 7/16	6	3 5/8
	182T, 184T								24		15 1/4									4 5/8
	213T, 215T								24 3/4		18 3/8									5 5/8
	254T, 256T								26		23 1/4	22 1/4		3 7/8	19 1/2					6 5/8
I	184T					21 3/4			24	6 7/8	16 5/8	17	3 3/8	5 1/16	14 1/8			23 15/16	10	4 5/8
	213T, 215T								24 3/4		19 1/2									5 5/8
	254T, 256T								26		24 3/8	22 1/4		5	19 1/2					6 5/8
	284TS, 286TS								26 3/4		26 1/2									7 1/8
	324TS								27 3/4		27 1/4									8 1/8
J ▲	182T, 184T	21 1/8	18 3/4	17 9/16	19 15/16	19	23 1/2	8 5/8	24	5 3/4	15 1/4	17	2 1/2	3 15/16	14 1/8	10 7/8	17 3/4	23 1/8	6	4 5/8
	213T, 215T								24 3/4		18 3/8									5 5/8
	254T, 256T								26		23 1/4	22 1/4		3 7/8	19 1/2					6 5/8
K	184T								24 1/2		15 1/4	17		3 15/16	14 1/8			24 3/8	8	4 5/8
	213T, 215T								24 3/4		18 3/8									5 5/8
	254T, 256T								26		23 1/4	22 1/4		3 7/8	19 1/2					6 5/8
	284TS, 286TS								26 3/4		25 3/8									7 1/8
L	254T, 256T					23		10 3/4	26	6 7/8	24 3/8	22 1/4	3 5/8	5	19 1/2			25 5/8	10	6 5/8
	284TS								26 3/4		25									7 1/8
	286TS								26 3/4		26 1/2									7 1/8
	324TS, 326TS								29 1/4		28 3/4	26 1/4			23 1/2					8 1/8
M	284TS, 286TS								28 1/4		26 1/2							27 1/8	12	7 1/8
	324TS, 326TS								29 1/4		28 3/4									8 1/8
	364TS								30 1/4		30 5/8									9 1/8

Figure D.6 Pertinent dimensions of the J4 high pressure blower [Chicago Blower Corporation, 1998].

Appendix E: Mechanical Drawings

This appendix provides the mechanical drawings of components specifically designed and machined for the test section.

A total of four Flange pieces are needed to construct the test section. One Flange piece is glued to the top surface of Ceiling Board A at the downstream edge. A second Flange piece is glued to the top surface of Ceiling Board B at the upstream edge. Together, these pieces act as a ceiling flange to join the two ceiling together.

A third Flange piece is glued to the top surface of Ceiling Board B at the downstream edge. The fourth Flange piece is glued to the bottom surface of the Test Floor Board at the downstream edge. These two pieces form a flange with which the sheet metal diffuser can mate.

Two Floor Stop pieces are required. One Floor Stop piece is bolted to the Test Floor Board and the downstream plenum wall, while the second Floor Stop piece is bolted to the downstream plenum wall and only rests on Ceiling Board A.

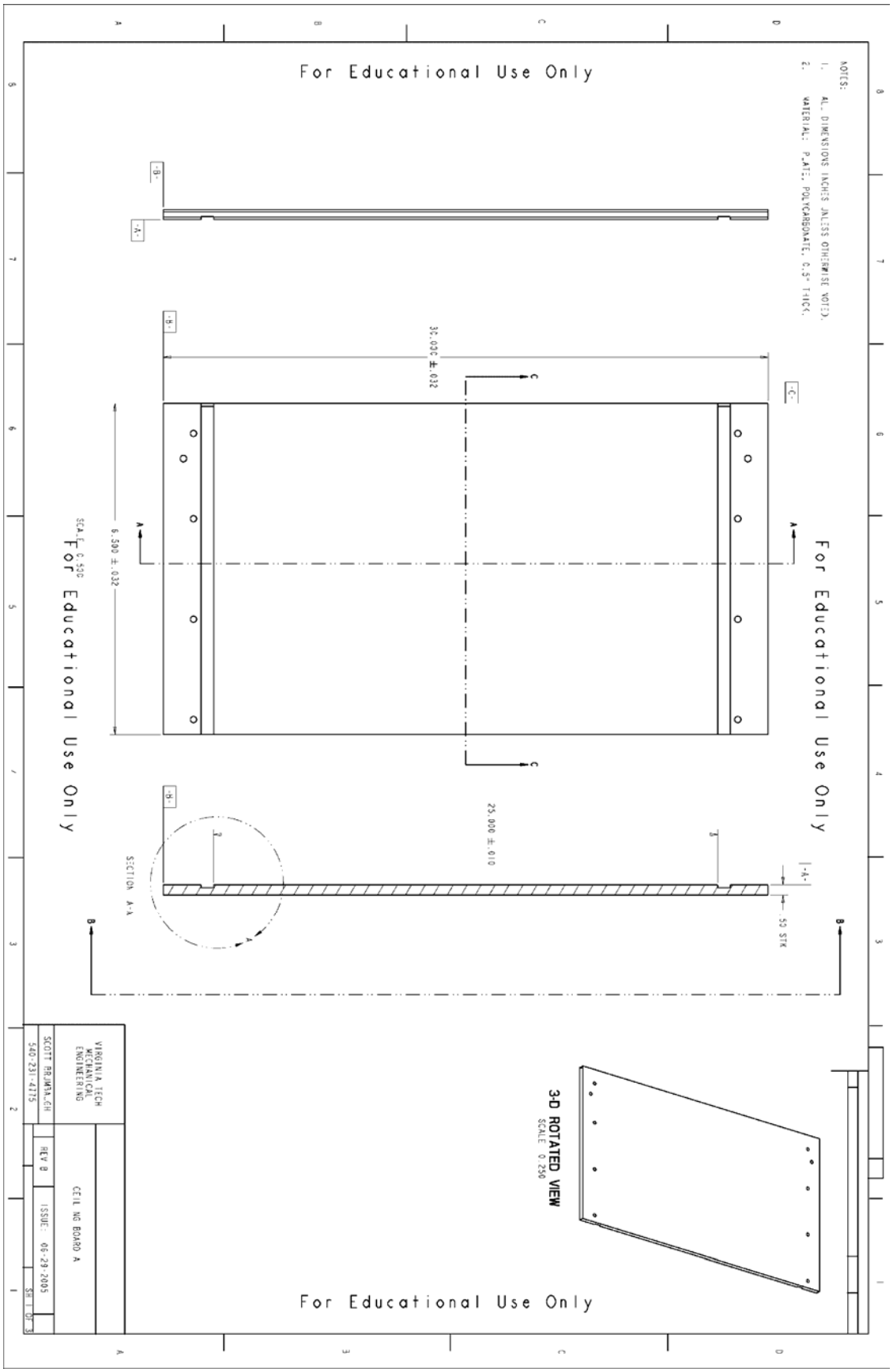
For Educational Use Only
NOTES:
1. ALL DIMENSIONS INCHES UNLESS OTHERWISE NOTED.
2. MATERIAL: PLASTIC POLYCARBONATE, 0.5" THICK.
35.000 ± .032
6.500 ± .032
25.000 ± .010
SECTION A-A
.50 STK
3-D ROTATED VIEW
SCALE 0.250
VIRGINIA TECH
MECHANICAL
ENGINEERING
SCOTT BRAMAN
540-231-4715
REV B
CEILING BOARD A
ISSUE: 06-29-2005
SHT 1 OF 3

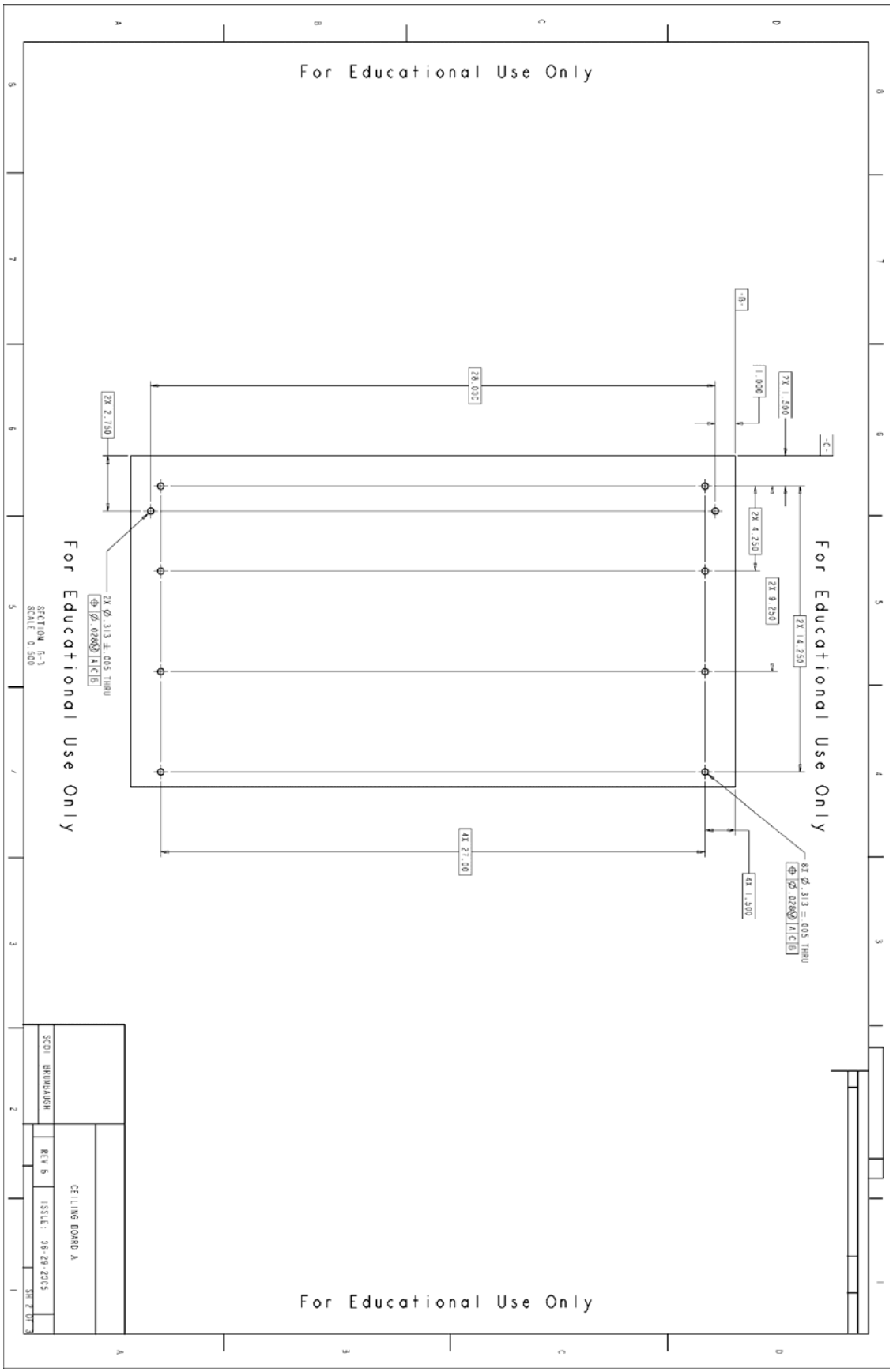
For Educational Use Only
For Educational Use Only
For Educational Use Only
For Educational Use Only
28.000
2X 2.750
1.000
2X 1.500
-B-
-C-
2X 4.250
2X 9.250
2X 14.250
4X 27.00
4X 1.500
2X Ø.313±.005 THRU
Ø.028Ⓜ A C B
8X Ø.313 ±.005 THRU
Ø.028Ⓜ A C B
SECTION B-B
SCALE 0.500
CEILING BOARD A
REV: B
ISSUE: 06-02-2006
SHEET 2 OF 3

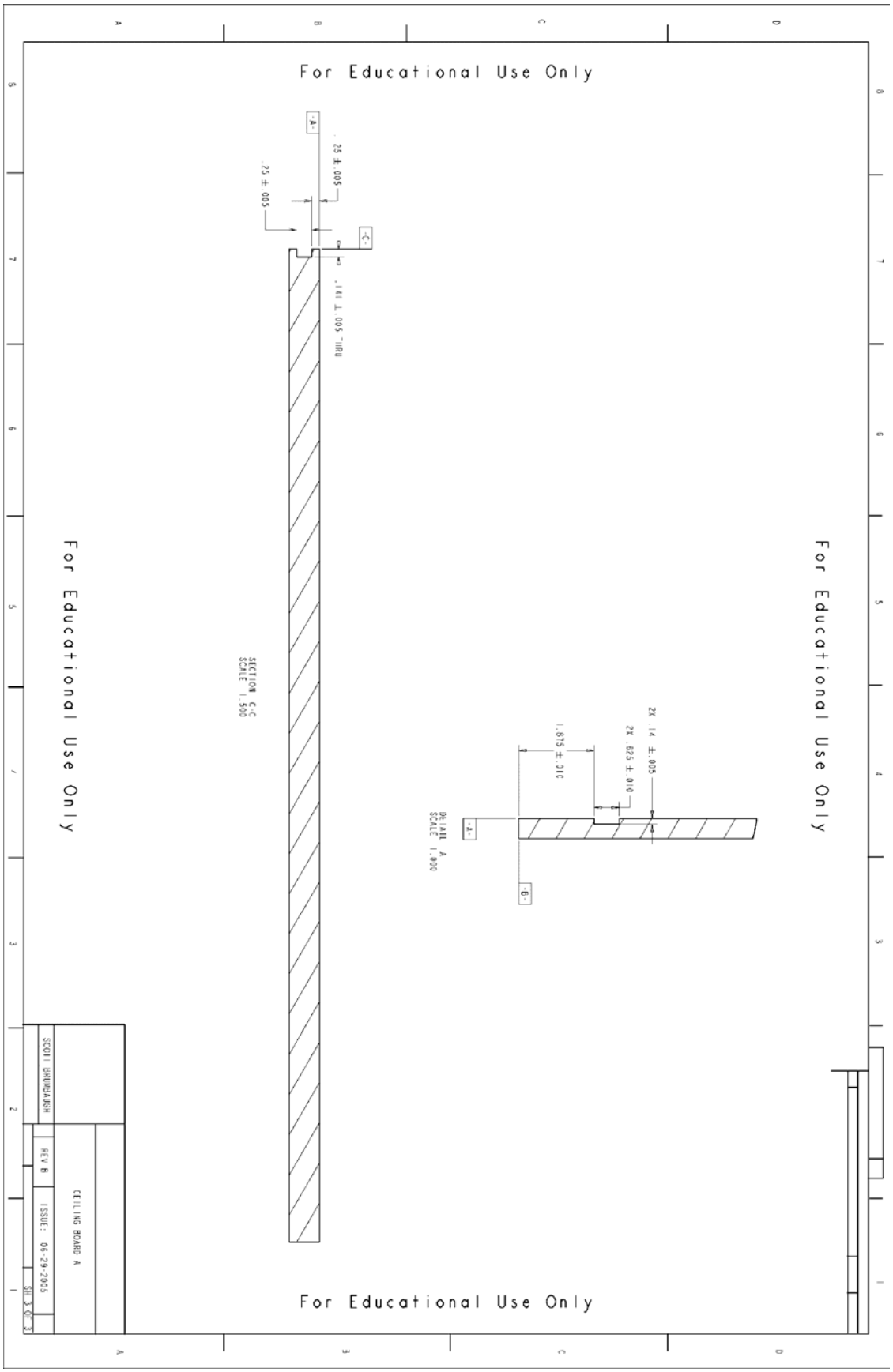
For Educational Use Only
For Educational Use Only
For Educational Use Only
For Educational Use Only
.25 ±.005
.25 ±.005
.141 ±.005 THRU
SECTION C-C
SCALE 1.500
2X .14 ±.005
2X .625 ±.010
1.875 ±.010
DETAIL A
SCALE 1.000
SCOTT BRUNDARSH
CEILING BOARD A
REV B
ISSUE: 06-29-2005
SH 3 OF 3

NOTES:

1. ALL DIMENSIONS INCHES UNLESS OTHERWISE NOTED.

2. ITEM 2 IS #6-32 INTERNAL THREAD, NON-LOCKING INSERT.

3. INSTALL ITEM 2 PER MANUFACTURER'S DIRECTIONS. INSERTS ARE TO BE INSTALLED INTO THE PLANE SHOWN (OPPOSITE DTM -A-). DIMENSIONS AND TOLERANCES APPLY TO ASSEMBLED INSERT (INTERNAL THREAD). DO NOT DRILL THROUGH OTHER SIDE.

4. MATCH DRILL HOLES WITH CORRESPONDING HOLES IN "TEST FLOOR BOARD" SUCH AS TO CREATE PERFECTLY ALIGNED "POSITION LOCATING" HOLES. ENSURE ALIGNMENT OF DATUM -B- IN BOTH PIECES BEFORE MATCH DRILLING.

5. MATCH DRILL HOLES WITH CORRESPONDING HOLES IN "TEST FLOOR BOARD" SUCH AS TO CREATE PERFECTLY ALIGNED "POSITION LOCATING" HOLES. ENSURE ALIGNMENT OF DATUM -E- IN BOTH PIECES BEFORE MATCH DRILLING.

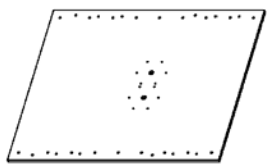

3-D ROTATED VIEW
SCALE 0.125

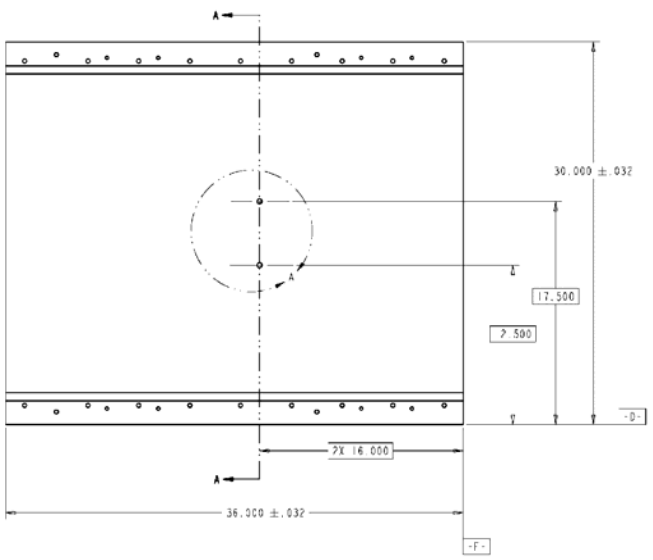

SCALE 0.250

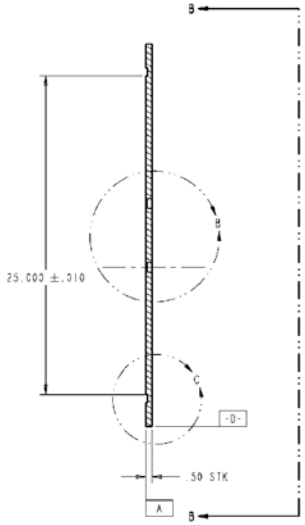

SECTION A-A

ITEM	QTY	DESCRIPTION
1	1	PLATE, POLYCARBONATE, 0.5" THICK
2	12	INSERT, NON-LOCKING, 6-32 INTERNAL THD

VIRGINIA TECH MECHANICAL ENGINEERING

CEILING BOARD B

SCOTT BRUMBAUGH
540-231-4775

REV B | ISSUE: 06 29 2005

SH 1 OF 6

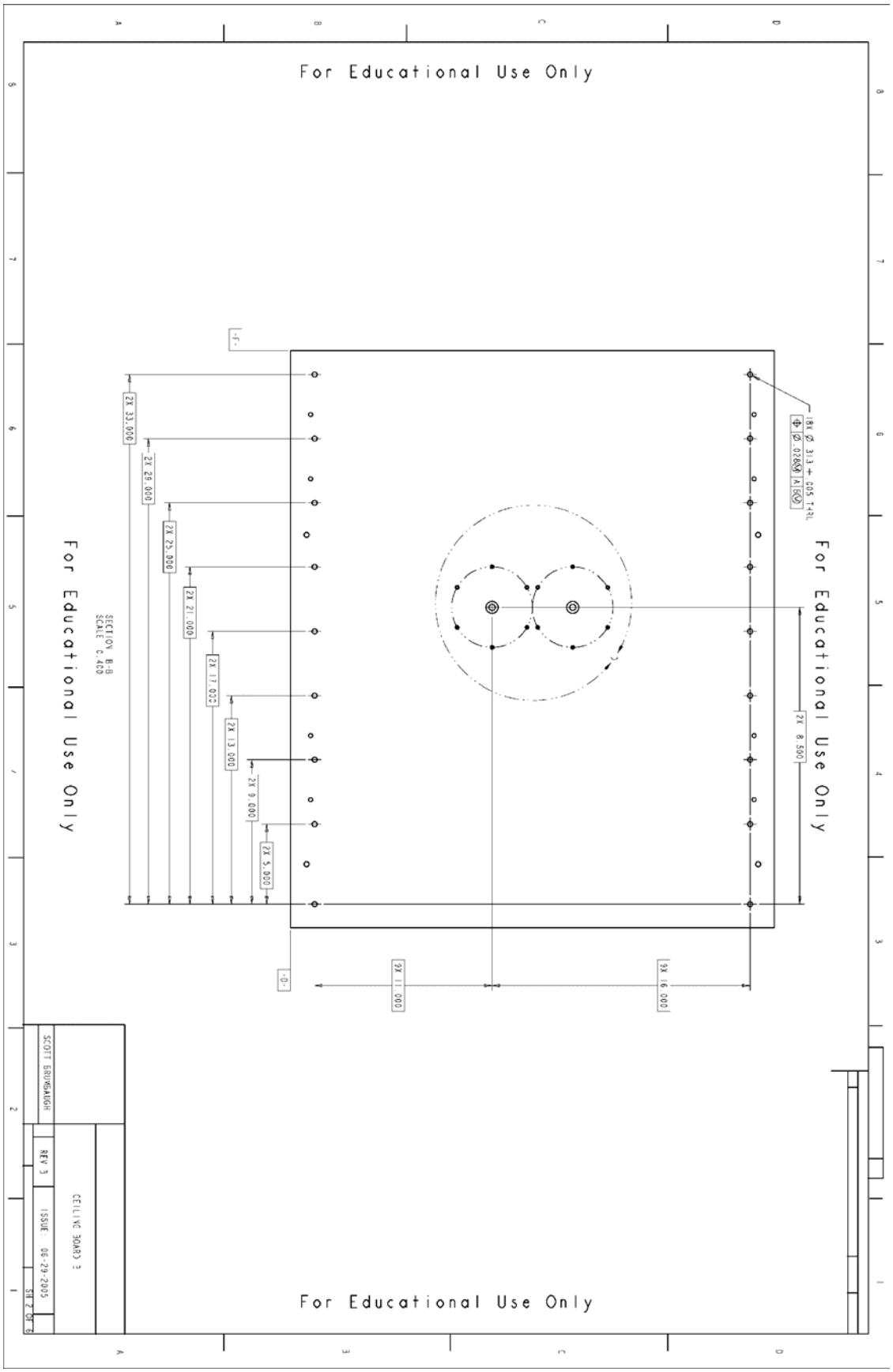
For Educational Use Only
For Educational Use Only
For Educational Use Only
For Educational Use Only
SECTION B-B
SCALE: 0.400
2X 33.000
2X 29.000
2X 25.000
2X 21.000
2X 17.000
2X 13.000
2X 9.000
2X 5.000
2X 8.500
2X 11.000
2X 16.000
SCOTT BRUMBAUGH
REV 3
ISSUE: 06-29-2005
CEILING BOARD 3

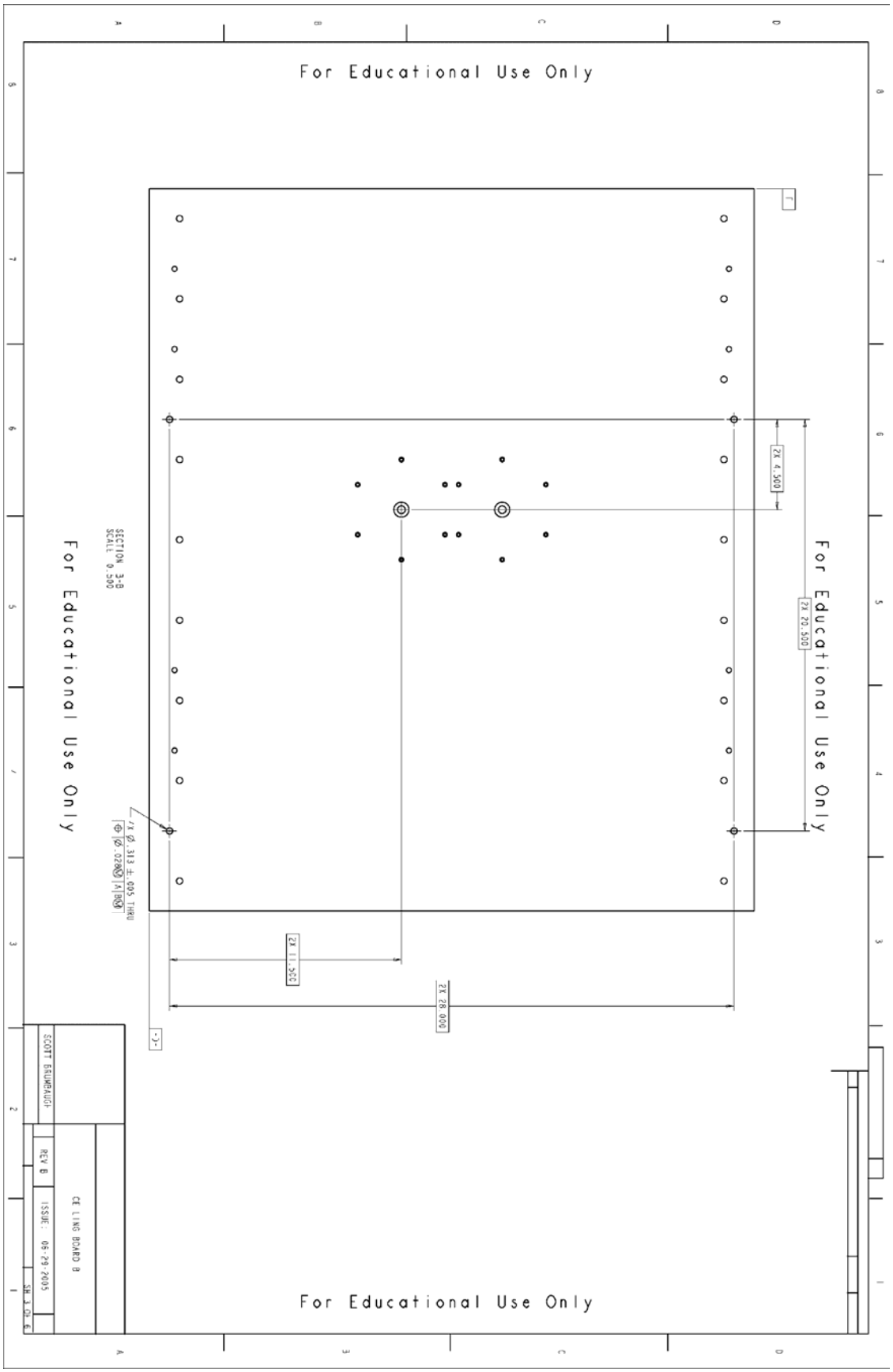
For Educational Use Only
For Educational Use Only
For Educational Use Only
For Educational Use Only
SECTION 3-B
SCALE 0.500
2X 4.500
2X 20.500
2X 11.250
2X 28.000
SCOTT BAUMBAUGH
REV B
ISSUE: 05-29-2005
CE LINK BOARD B

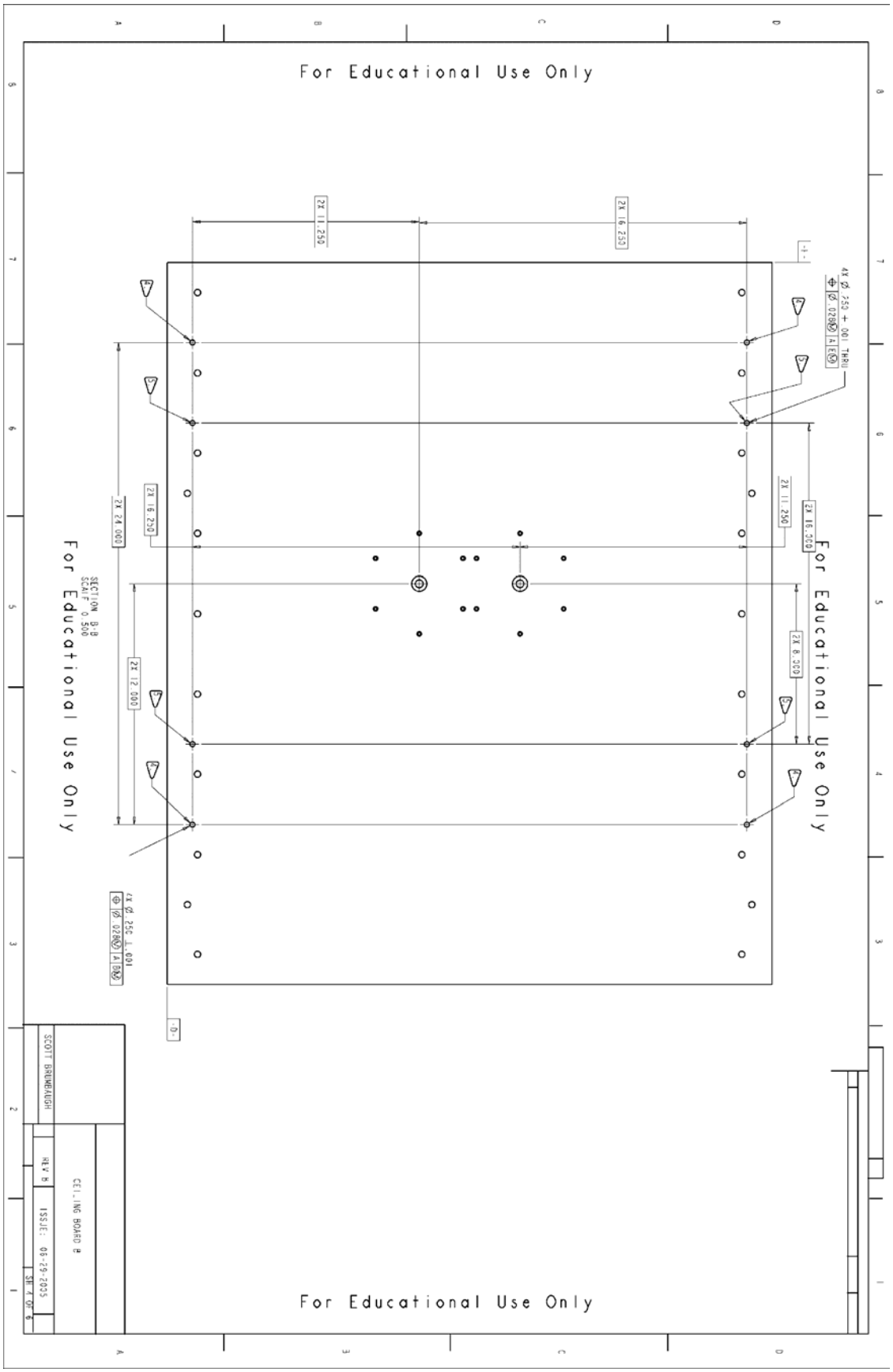
For Educational Use Only
2X 11.250
2X 16.250
4X Ø .250 +.001 -.000 THRU
Ø.020 M B S
2X 16.220
2X 24.000
2X 12.000
2X 11.250
2X 16.500
2X 8.000
SECTION B-B
SCALE 0.500
4X Ø .250 +.001 -.000
Ø.020 M B S
SCOTT BRUMBAUGH
REV: B
CEILING BOARD B
ISSUE: 08-29-2025
SHEET 1 OF 1

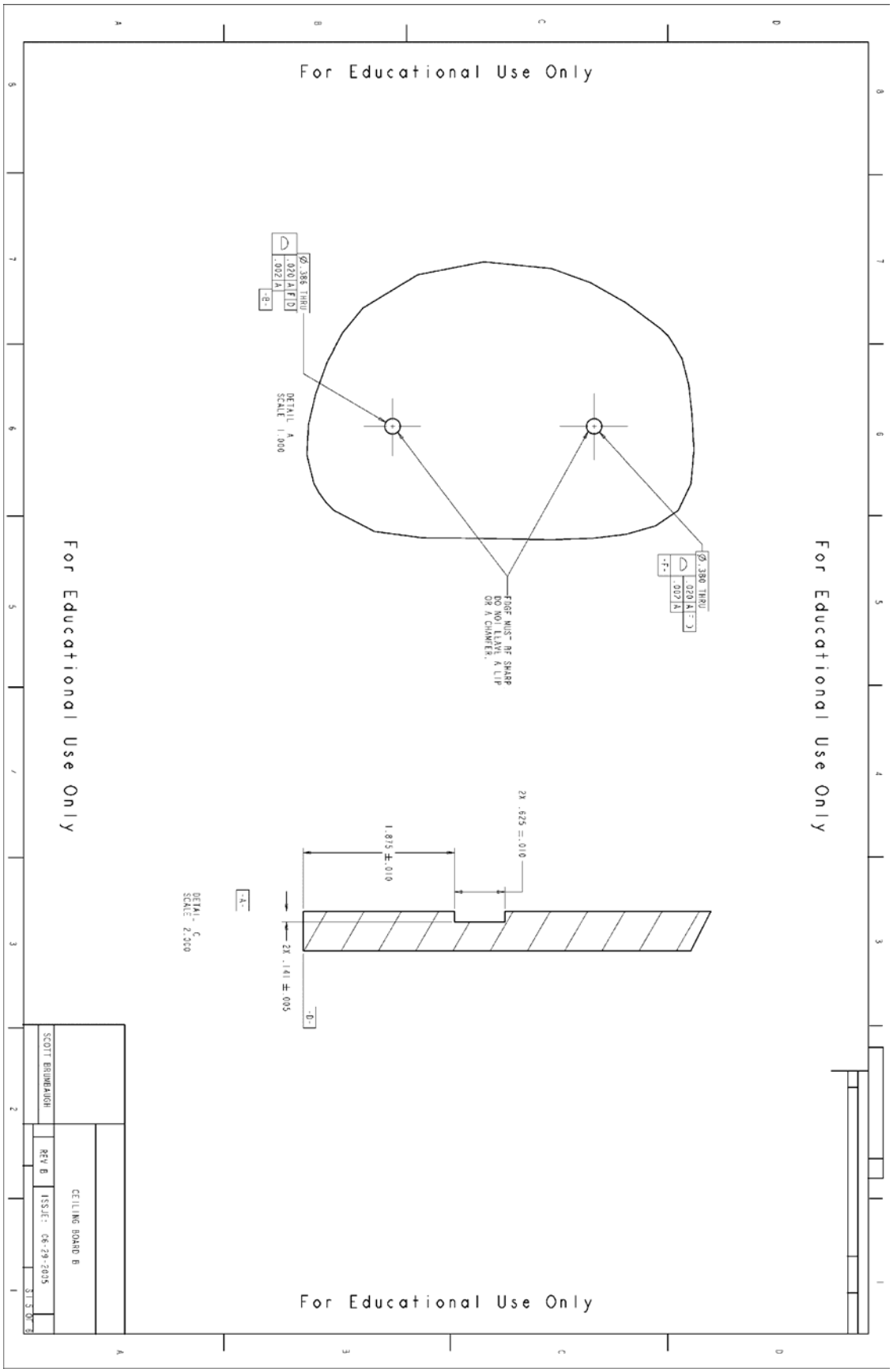
For Educational Use Only
For Educational Use Only
For Educational Use Only
For Educational Use Only
DETAIL A
SCALE 1.000
EDGE MUST BE SHARP
DO NOT ELAYE A LIP
OR A CHAMFER.
DETAIL C
SCALE 2.300
1.875 ±.010
2X .625 ±.010
2X .141 ±.005
SCOTT BRUNBAUGH
CEILING BOARD B
REV B
ISSUE: 06-29-2005
SIZE
B

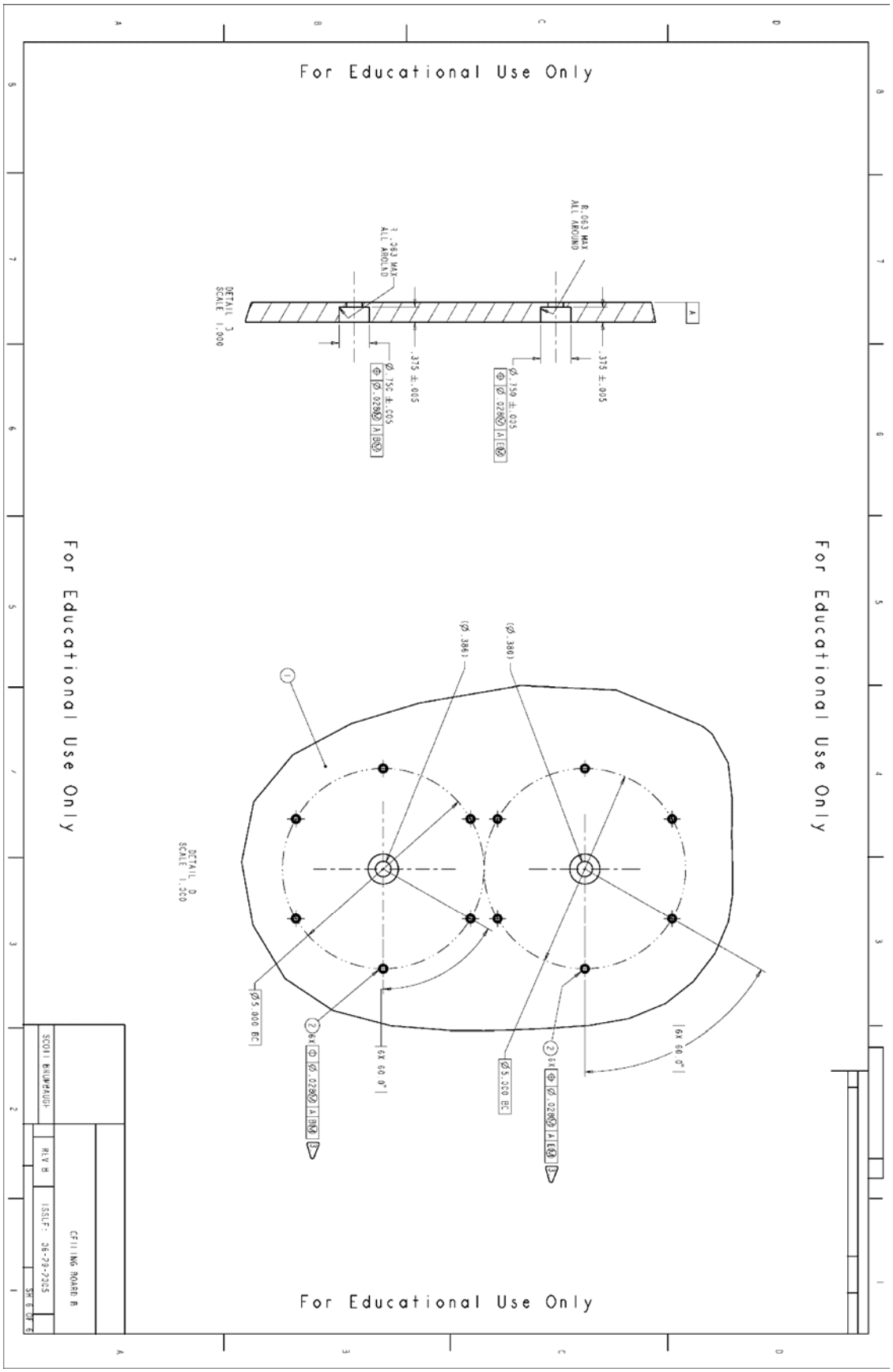
For Educational Use Only
For Educational Use Only
For Educational Use Only
For Educational Use Only
DETAIL C
SCALE 1.000
.375 ± .005
DETAIL D
SCALE 1.000
6X 60.0°
6X 60.0°
SCOTT NEUMEKOUGH
REV B
CF111NG BOARD B

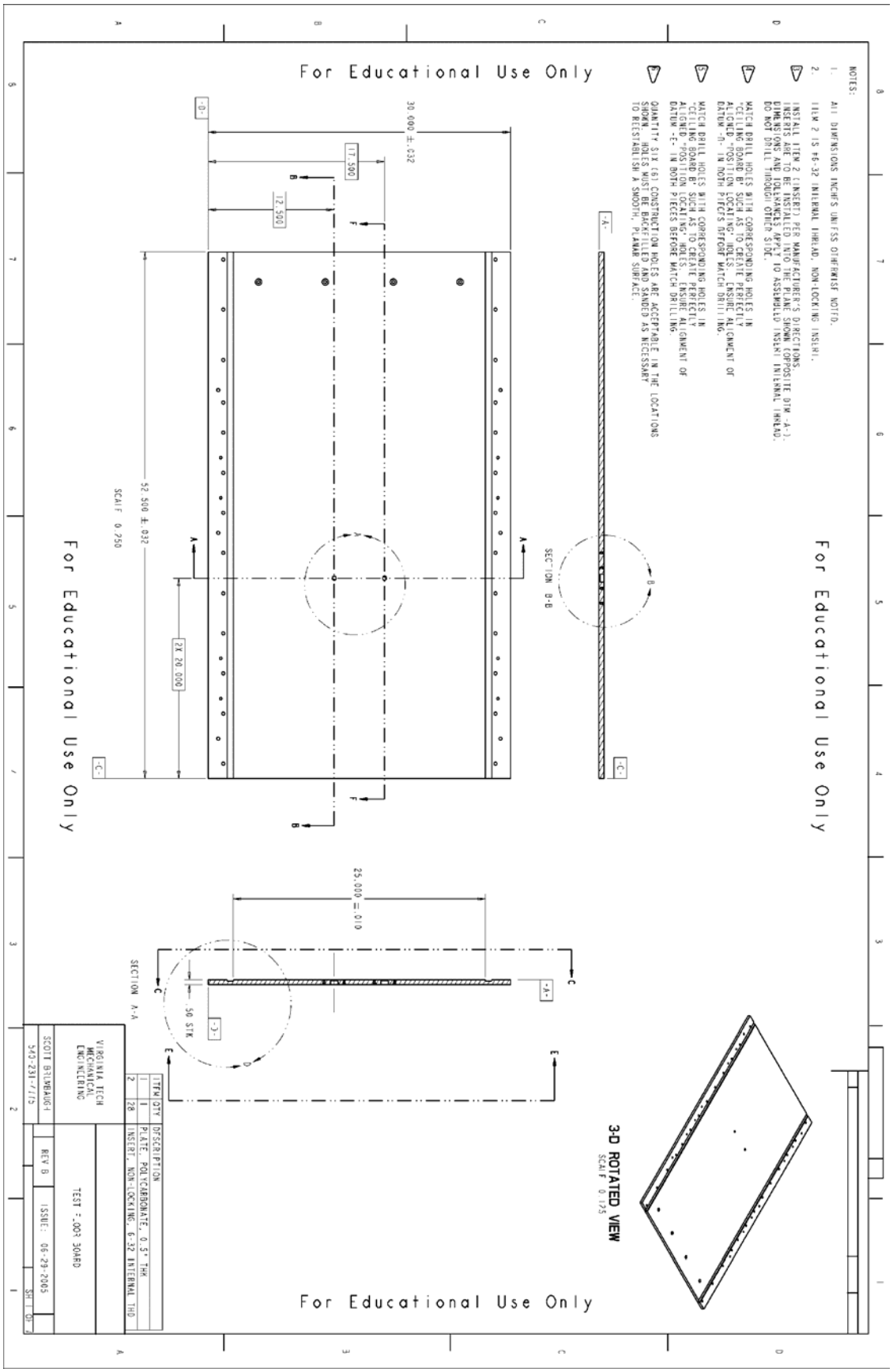
For Educational Use Only
NOTES:
1. ALL DIMENSIONS INCHES UNLESS OTHERWISE NOTED.
2. ITEM 2 IS #6-32 UNIFORM THREAD, NON-LOCKING INSERT.
INSTALL ITEM 2 (INSERTS) PER MANUFACTURER'S DIRECTIONS.
INSERTS ARE TO BE INSTALLED FROM OPPOSITE DTM -A-.
DIMENSIONS AND TOLERANCES APPLY TO ASSEMBLY WITH INSERTS INSTALLED.
DO NOT DRILL THROUGH OTHER SIDE.
MATCH DRILL HOLES WITH CORRESPONDING HOLES IN "CEILING BOARD B" SUCH AS TO CREATE PERFECTLY ALIGNED "POSITION LOCATING" HOLES. ENSURE ALIGNMENT OF DATUM -A- IN BOTH PIECES BEFORE MATCH DRILLING.
MATCH DRILL HOLES WITH CORRESPONDING HOLES IN "CEILING BOARD B" SUCH AS TO CREATE PERFECTLY ALIGNED "POSITION LOCATING" HOLES. ENSURE ALIGNMENT OF DATUM -E- IN BOTH PIECES BEFORE MATCH DRILLING.
QUANTITY SIX (6) CONSTRUCTION HOLES ARE ACCEPTABLE IN THE LOCATIONS SHOWN. HOLES MUST BE BACKFILLED AND SANDED AS NECESSARY TO REESTABLISH A SMOOTH, PLANAR SURFACE.
30.000 ±.032
17.500
12.500
52.500 ±.032
2X 20.000
SCALE 0.750
SECTION B-B
SECTION A-A
25.000 ±.010
.50 STK
3-D ROTATED VIEW
SCALE 0.125
ITEM QTY DESCRIPTION
1 1 PLATE, POLYCARBONATE, 0.5" THK
2 28 INSERT, NON-LOCKING, 6-32 INTERNAL THD
VIRGINIA TECH MECHANICAL ENGINEERING
TEST JIG BOARD
SCOTT BAUMBAUGH
540-231-7175
REV B
ISSUE: 06-29-2005
SHT 1 OF 1

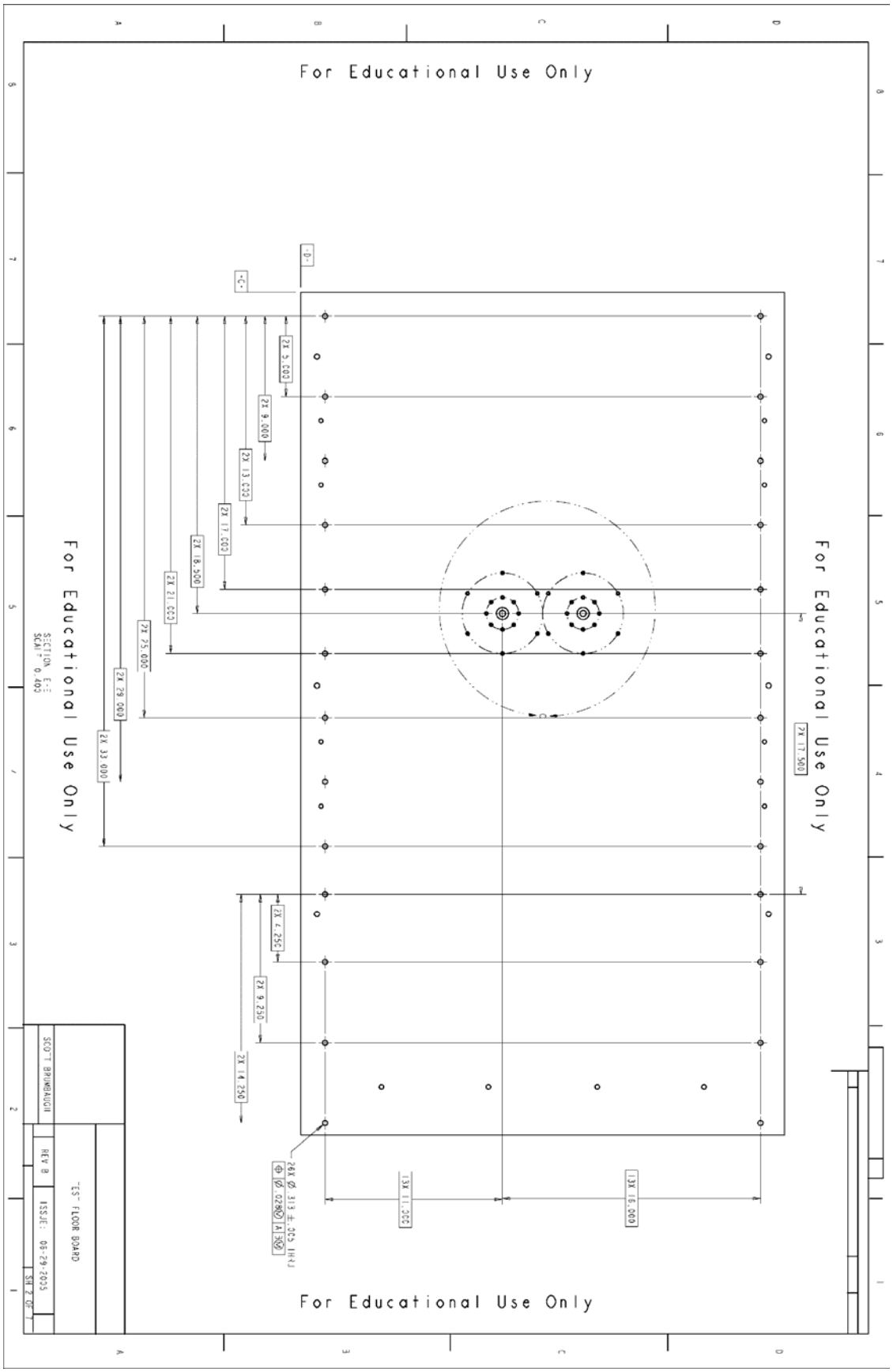
For Educational Use Only
For Educational Use Only
For Educational Use Only
For Educational Use Only
SCOTT BRANNAUGH
REV: B
ISSUE: 06-02-2005
"ES" FLOOR BOARD
SH 2 OF 2

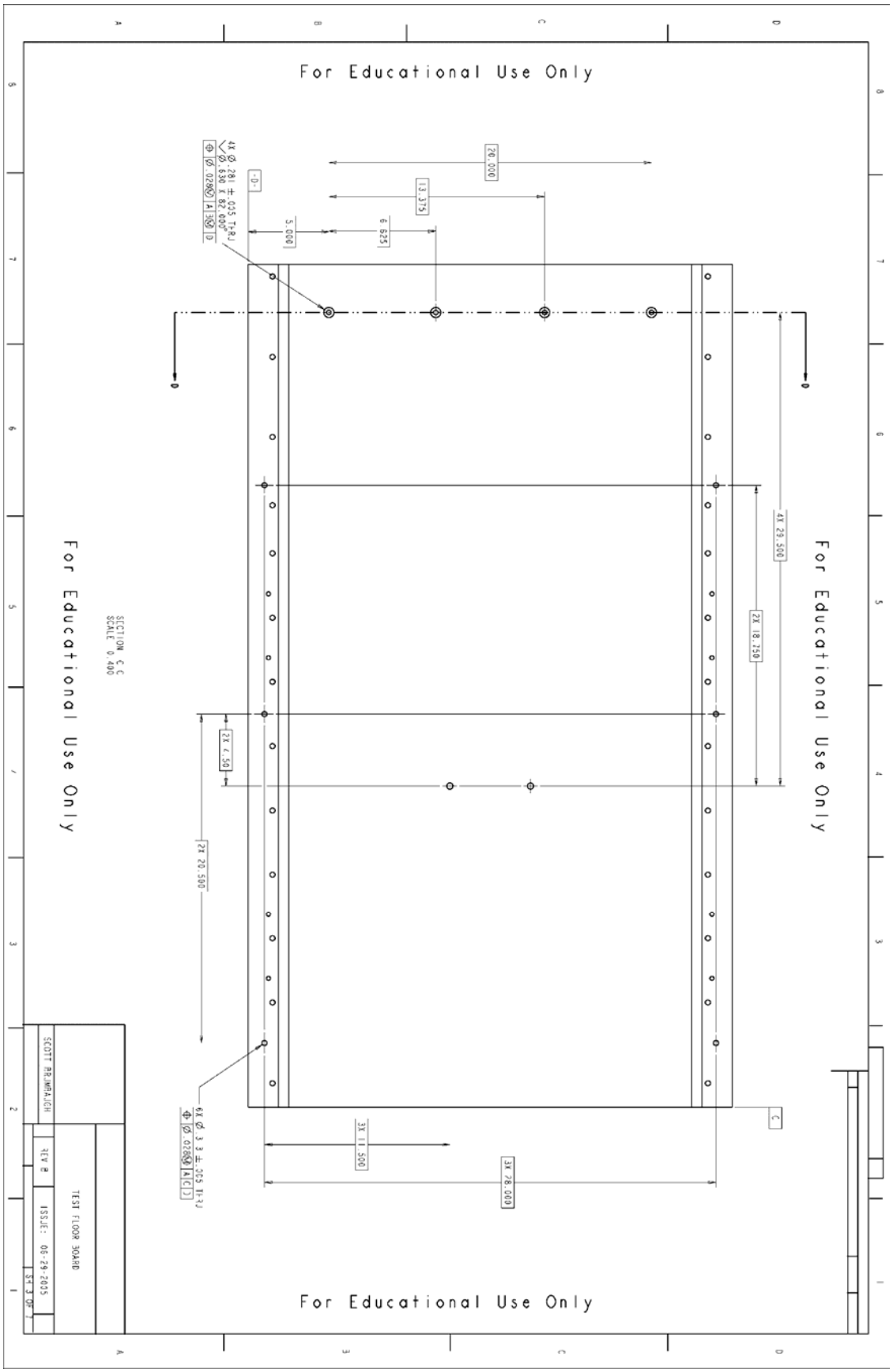
For Educational Use Only
For Educational Use Only
For Educational Use Only
For Educational Use Only
SECTION C-C
SCALE 0.400
20.000
13.375
6.625
5.000
4X 29.500
2X 18.250
2X 4.50
2X 20.500
3X 11.500
3X 78.000
TEST FLOOR BOARD
REV B
ISSUE: 08-29-2005
SHEET 3 OF 7

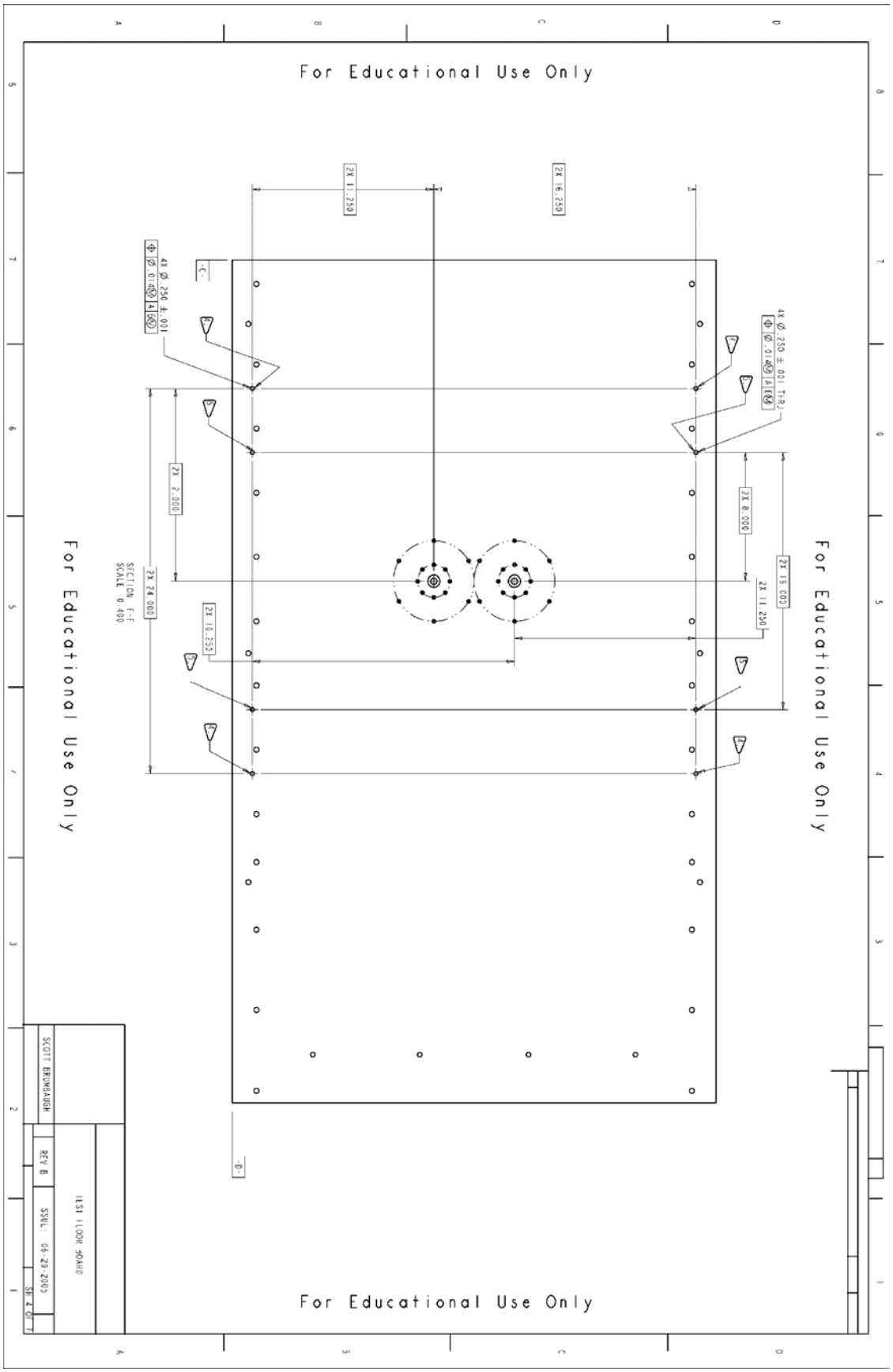
For Educational Use Only
For Educational Use Only
For Educational Use Only
For Educational Use Only
2X 1.250
2X 16.250
4X Ø.250 ±.001
4X Ø.250 ±.001 T-R-J
2X 2.000
2X 8.000
2X 24.000
2X 15.000
2X 11.250
2X 10.252
SECTION F-F
SCALE 0.400
SCOTT BRENNAUGH
REV: B
SSGL: 06-29-2005
TEST FLOOR BOARD
SH 1 OF 1

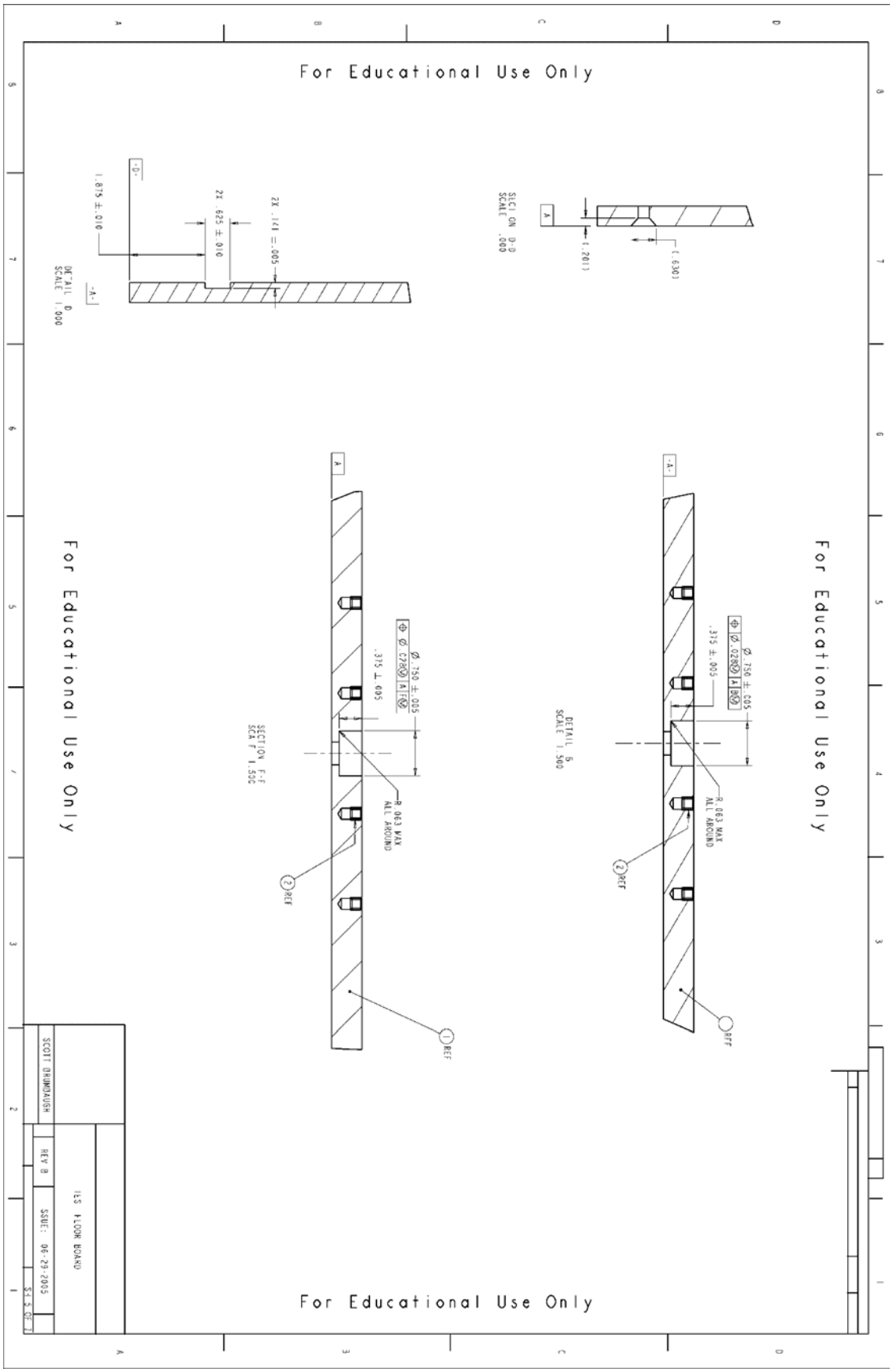
For Educational Use Only
For Educational Use Only
For Educational Use Only
For Educational Use Only
SCOTT DRUMMOND
REV B
SDUE: 06-29-2005
SHEET 5 OF 7

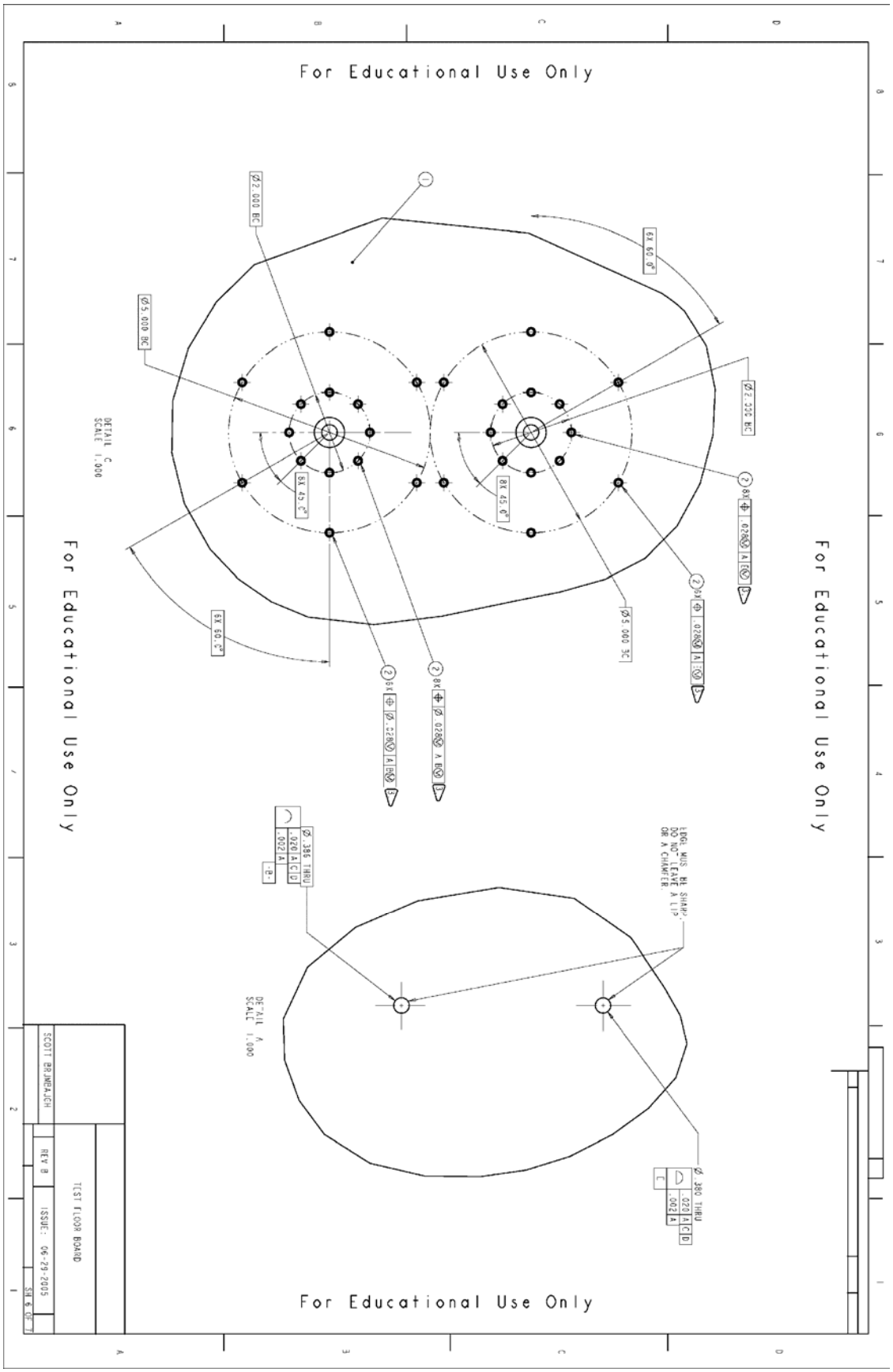
For Educational Use Only
For Educational Use Only
For Educational Use Only
For Educational Use Only
Ø2.000 BC
Ø5.000 BC
6X 60.0°
8X 45.0°
8X 45.0°
6X 60.0°
Ø5.000 BC
Ø2.000 BC
DETAIL C
SCALE 1.000
DETAIL A
SCALE 1.000
EDGE MUST BE SHARP, DO NOT LEAVE A LIP OR A CHAMFER
Ø.386 THRU
.002 A
-B-
Ø.380 THRU
.002 A
SCOTT BRUNBAUGH
TEST FLOOR BOARD
REV: B
ISSUE: 06-26-2005
SH 6 OF 7

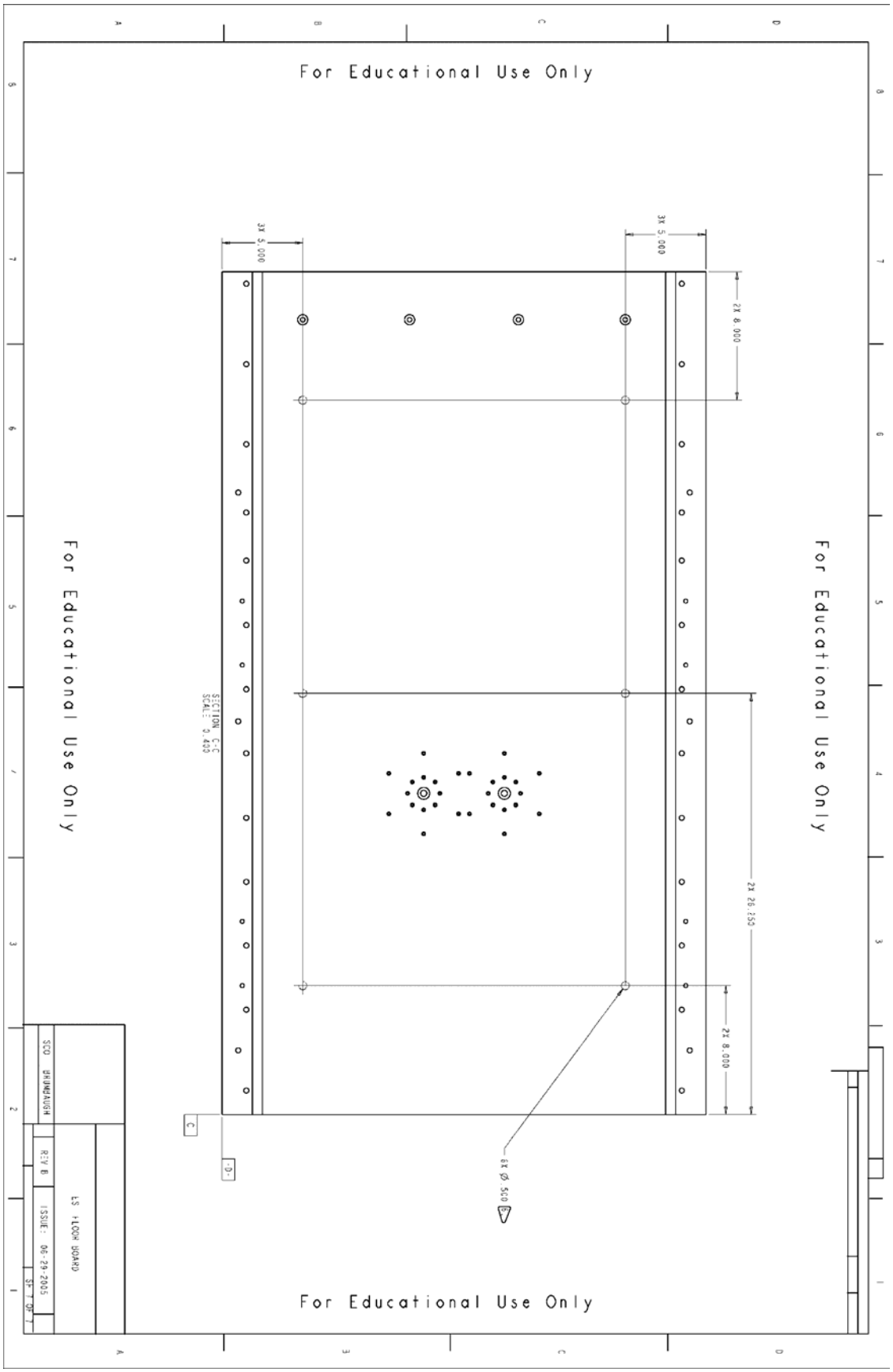
For Educational Use Only
For Educational Use Only
For Educational Use Only
For Educational Use Only
3X 5.000
3X 5.000
2X 8.000
2X 26.250
2X 8.000
SECTION C-C
SCALE: 0.400
8X Ø.500
C
D
SCO UNMANNED
ES FLOOR BOARD
REV B
ISSUE: 06-29-2005
SHT 1 OF 1

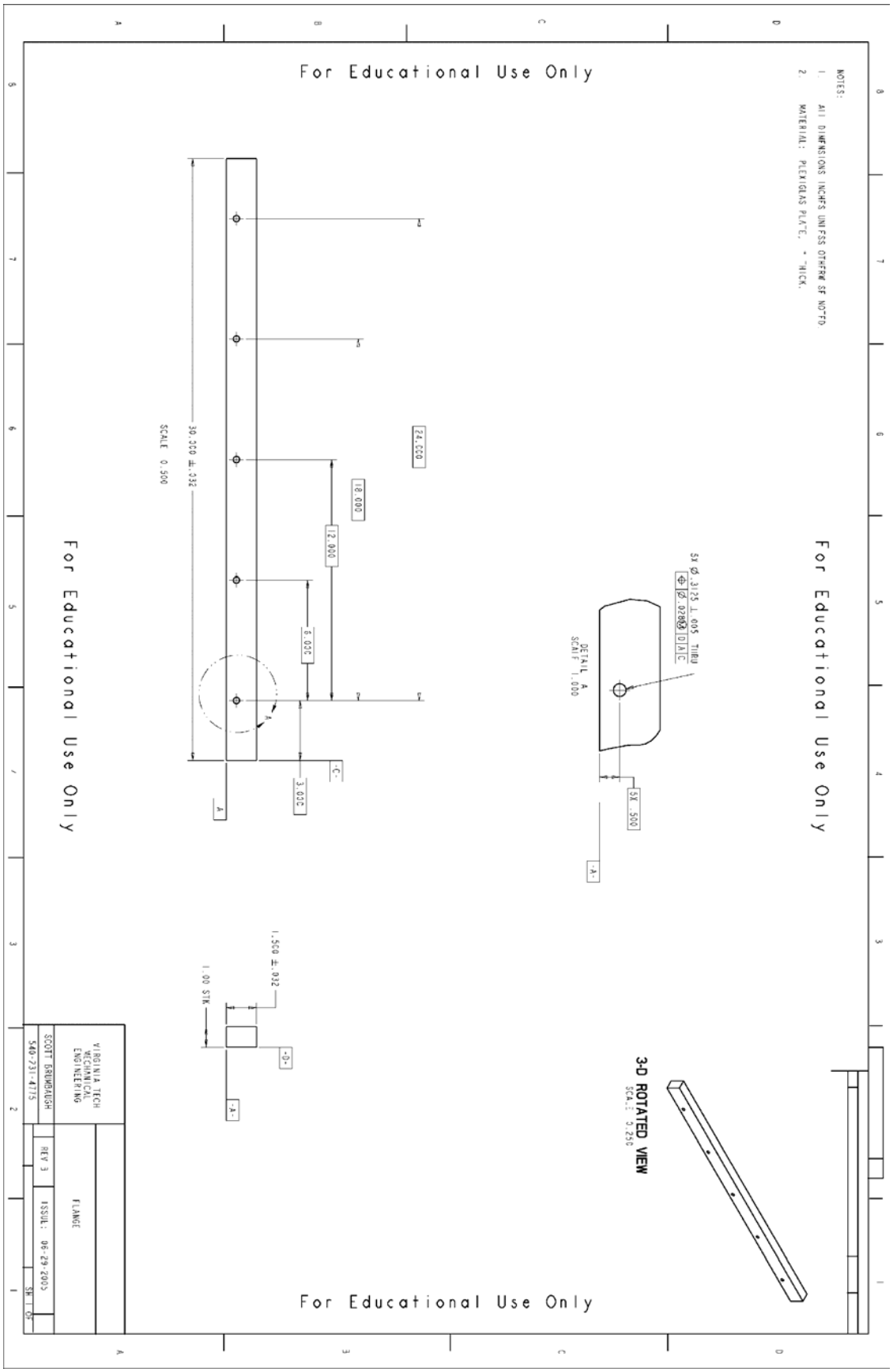
For Educational Use Only
NOTES:
1. ALL DIMENSIONS INCHES UNLESS OTHERWISE NOTED.
2. MATERIAL: PLEXIGLAS PLATE, " THICK.
24.000
18.000
12.000
6.000
3.000
30.000 ±.032
SCALE 0.500
5X Ø.3125 ±.005 THRU
Ø.020M A C
DETAIL A
SCALE 1.000
5X .500
1.500 ±.032
1.00 STK
3-D ROTATED VIEW
SCALE 0.250
VIRGINIA TECH
MECHANICAL
ENGINEERING
SCOTT GRUMBAUGH
540-731-4775
FLANGE
REV 3
ISSUE: 06-29-2005
SIZE
QTY

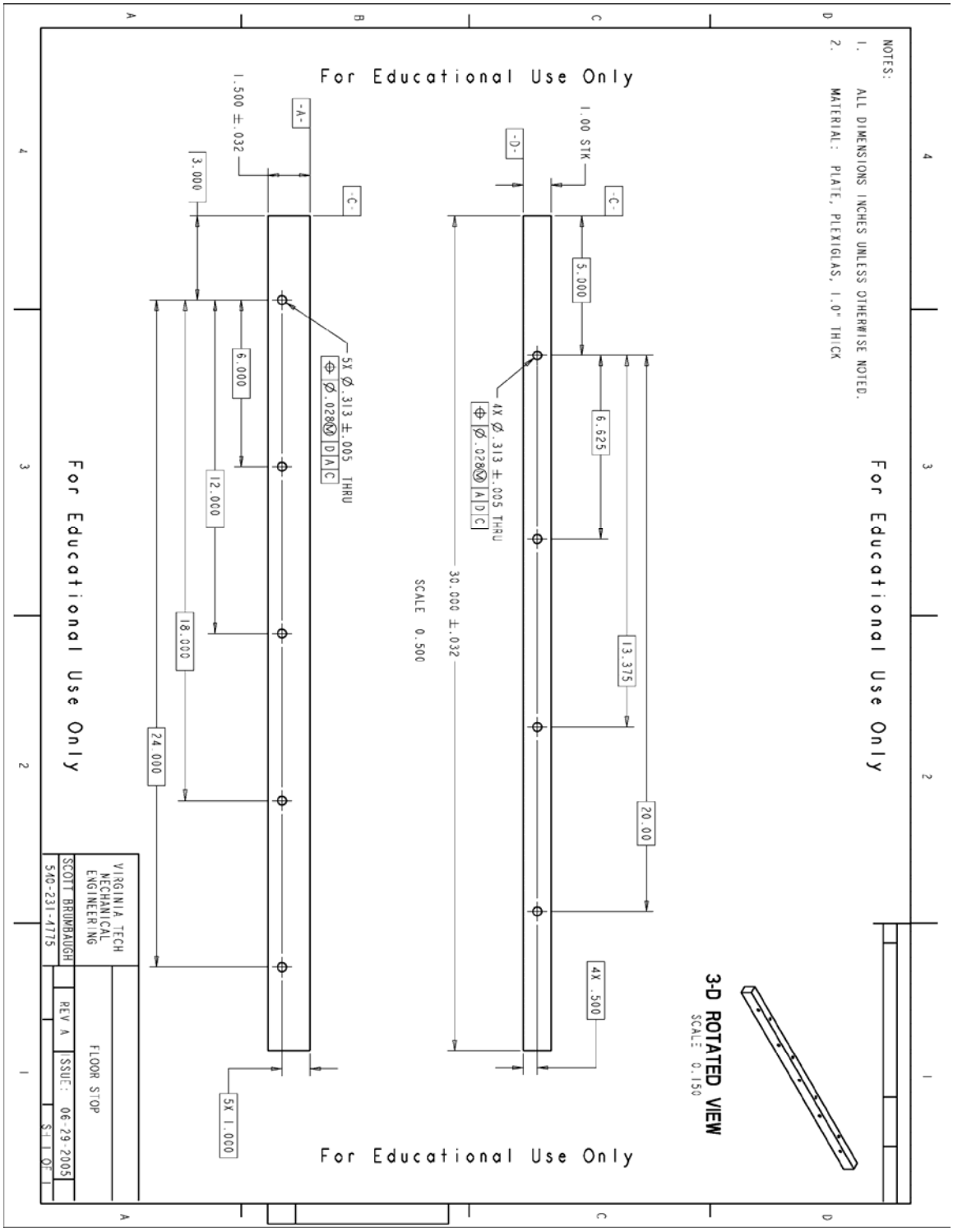
NOTES:
1. ALL DIMENSIONS INCHES UNLESS OTHERWISE NOTED.
2. MATERIAL: PLATE, PLEXIGLAS, 1.0" THICK
For Educational Use Only
1.00 STK
-D-
-C-
5.000
6.625
13.375
20.00
4X .500
4X Ø.313 ±.005 THRU
Ø.028Ⓜ D A C
30.000 ±.032
SCALE 0.500
1.500 ±.032
-A-
3.000
6.000
12.000
18.000
24.000
5X Ø.313 ±.005 THRU
Ø.028Ⓜ D A C
5X 1.000
3-D ROTATED VIEW
SCALE 0.150
VIRGINIA TECH
MECHANICAL
ENGINEERING
SCOTT BRUMBAUGH
540-231-4775
FLOOR STOP
REV A
ISSUE: 06-29-2005
SHEET 1 OF 1

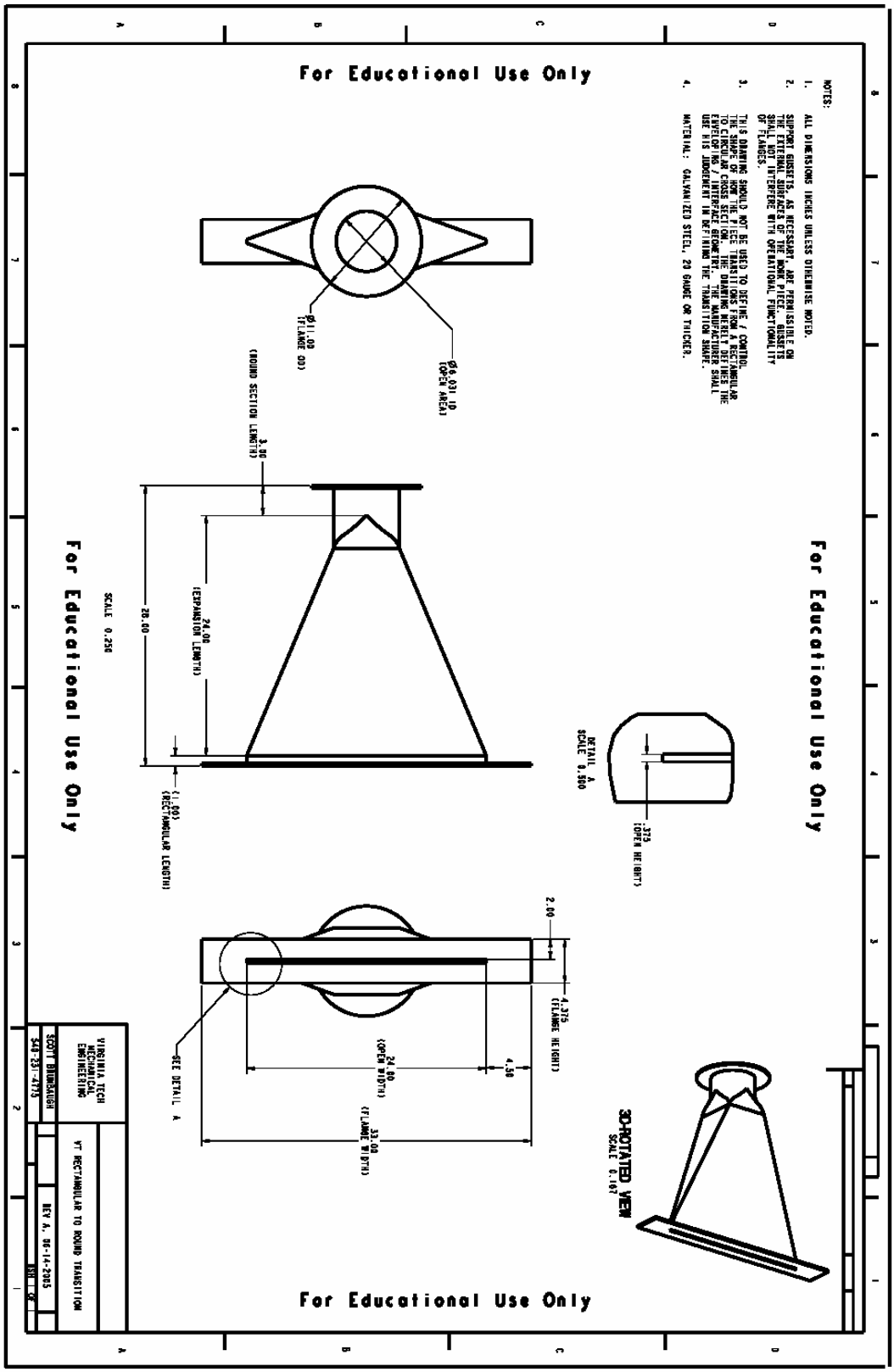
For Educational Use Only
NOTES:
1. ALL DIMENSIONS INCHES UNLESS OTHERWISE NOTED.
2. SUPPORT GUSSETS, AS NECESSARY, ARE PERMISSIBLE ON THE EXTERIOR OF THE TRANSITION, BUT SHALL NOT INTERFERE WITH OPERATIONAL FUNCTIONALITY OF FLANGES.
3. THIS DRAWING SHOULD NOT BE USED TO DEFINE / CONTROL THE SHAPE ON SOME INTERMEDIATE CROSS SECTION BETWEEN TO CIRCULAR CROSS SECTION. THE DRAWING MERELY DEFINES THE ENVELOPING / INTERFACE GEOMETRY. THE MANUFACTURER SHALL USE HIS JUDGEMENT IN DEFINING THE TRANSITION SHAPE.
4. MATERIAL: GALVANIZED STEEL, 20 GAUGE OR THICKER.
Ø11.00 (FLANGE OD)
Ø6.031 ID (OPEN AREA)
3.00 (ROUND SECTION LENGTH)
24.00 (EXPANSION LENGTH)
20.00
1.00 (RECTANGULAR LENGTH)
SCALE 0.250
DETAIL A SCALE 0.500
.375 (OPEN HEIGHT)
2.00
4.375 (FLANGE HEIGHT)
SEE DETAIL A
24.00 (OPEN WIDTH)
4.50
33.00 (FLANGE WIDTH)
3D-ROTATED VIEW SCALE 0.167
VIRGINIA TECH MECHANICAL ENGINEERING
SCOTT BRUMBAUGH
540-231-4773
VT RECTANGULAR TO ROUND TRANSITION
REV A, 05-14-2005

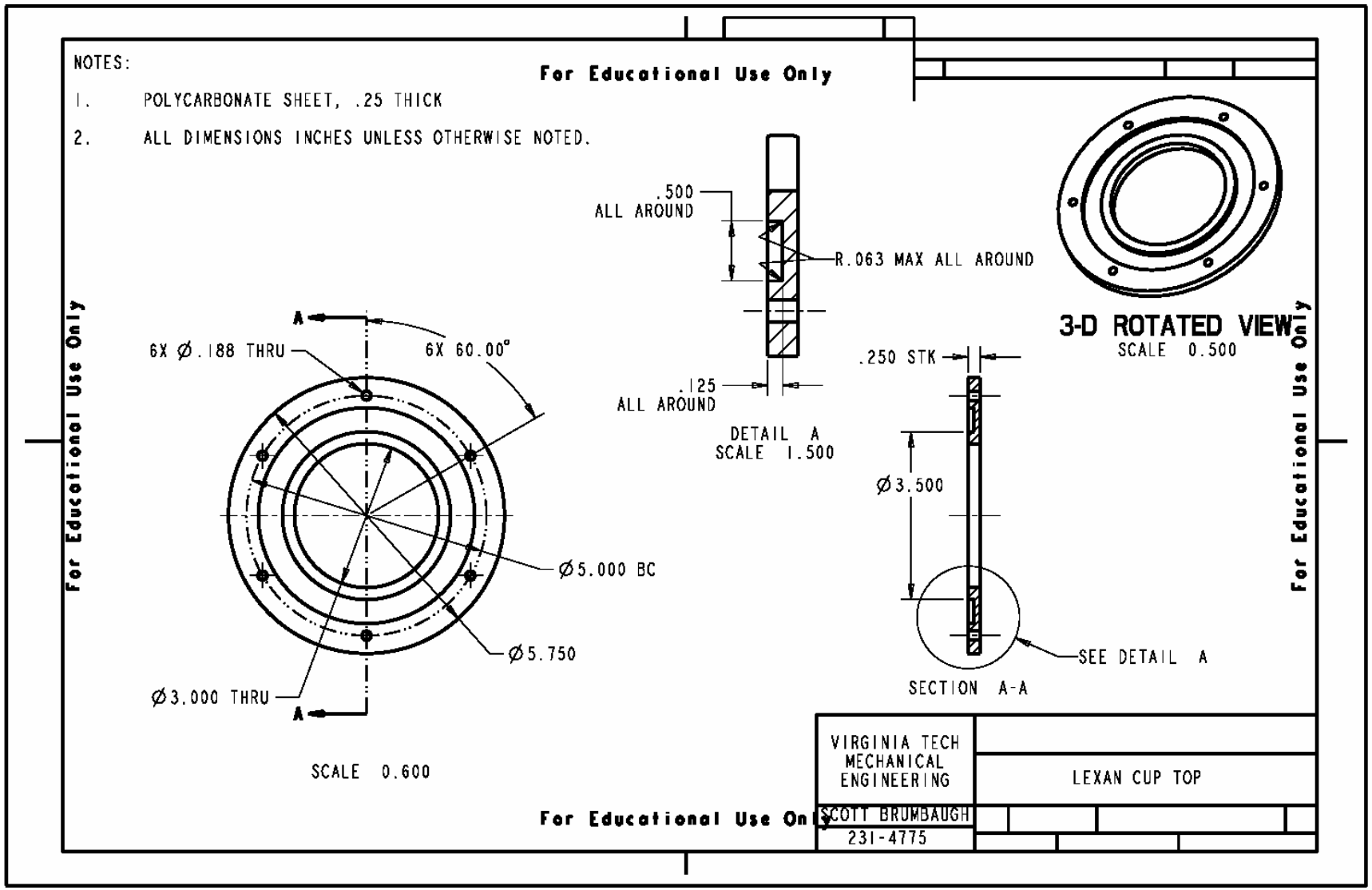
NOTES:
For Educational Use Only
1. POLYCARBONATE SHEET, .25 THICK
2. ALL DIMENSIONS INCHES UNLESS OTHERWISE NOTED.
.500
ALL AROUND
R.063 MAX ALL AROUND
.125
ALL AROUND
DETAIL A
SCALE 1.500
3-D ROTATED VIEW
SCALE 0.500
6X Ø.188 THRU
6X 60.00°
Ø5.000 BC
Ø5.750
Ø3.000 THRU
A
A
SCALE 0.600
.250 STK
Ø3.500
SEE DETAIL A
SECTION A-A
For Educational Use Only
For Educational Use Only
For Educational Use Only
VIRGINIA TECH
MECHANICAL
ENGINEERING
LEXAN CUP TOP
SCOTT BRUMBAUGH
231-4775

NOTES:

1. MATERIAL: POLYCARBONATE SHEET, .125 THICK
2. ALL DIMENSIONS INCHES UNLESS OTHERWISE NOTED

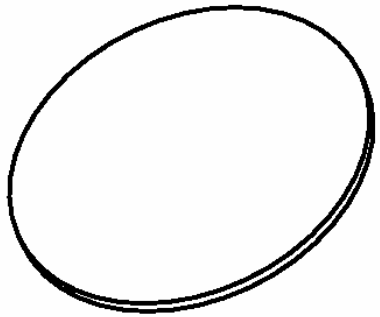

3-D ROTATED VIEW
SCALE 1.000

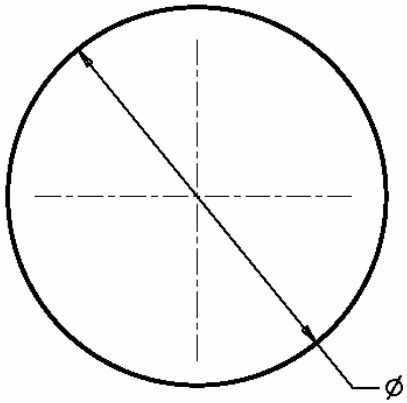

SCALE 1.000

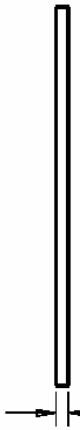

VIRGINIA TECH MECHANICAL ENGINEERING	LEXAN CUP BOTTOM
SCOTT BRUMBAUGH	
231-4775	

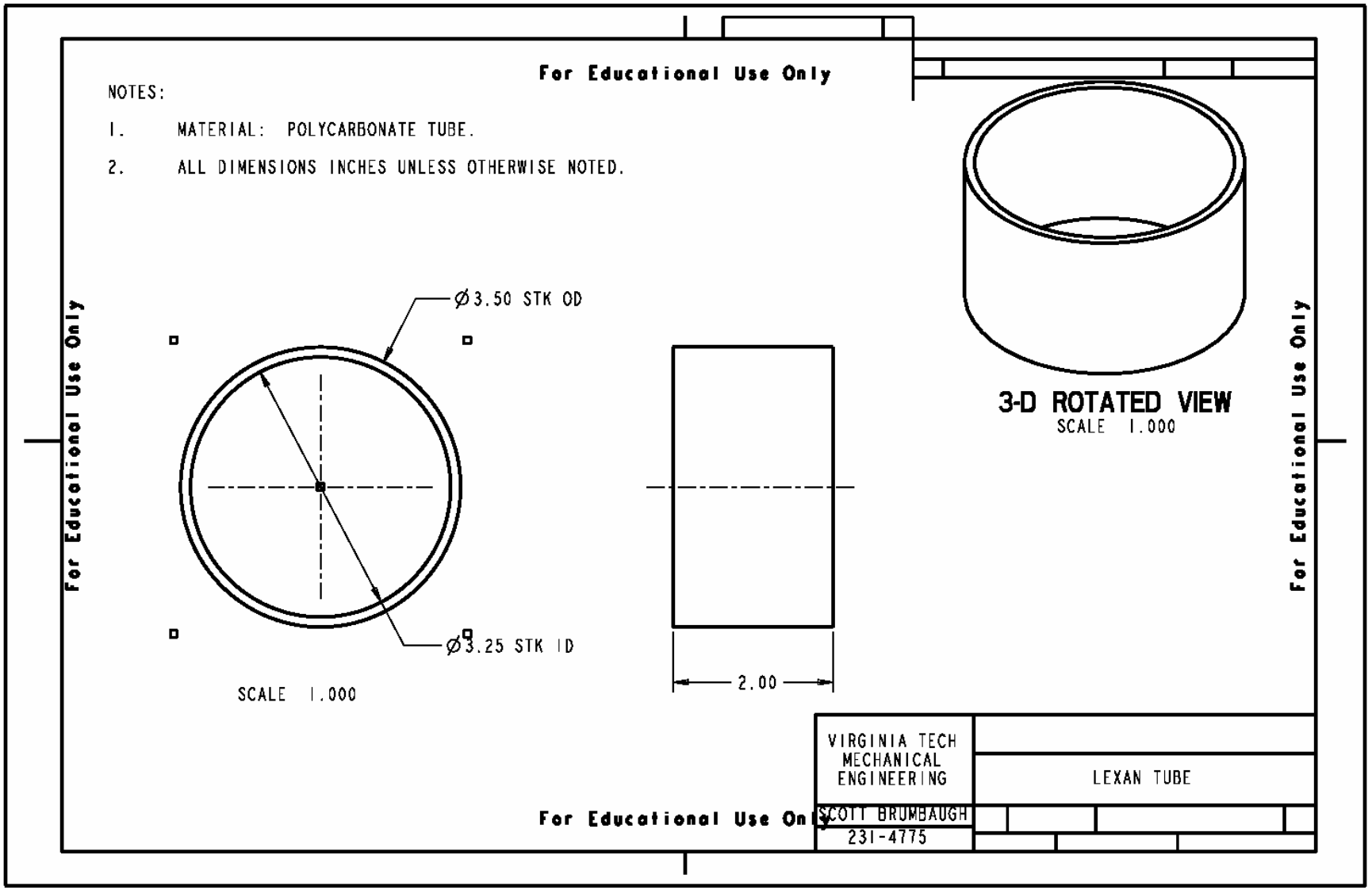
For Educational Use Only
NOTES:
1. MATERIAL: POLYCARBONATE TUBE.
2. ALL DIMENSIONS INCHES UNLESS OTHERWISE NOTED.
Ø3.50 STK OD
Ø3.25 STK ID
SCALE 1.000
2.00
3-D ROTATED VIEW
SCALE 1.000
For Educational Use Only
For Educational Use Only
For Educational Use Only
VIRGINIA TECH
MECHANICAL
ENGINEERING
SCOTT BRUMBAUGH
231-4775
LEXAN TUBE

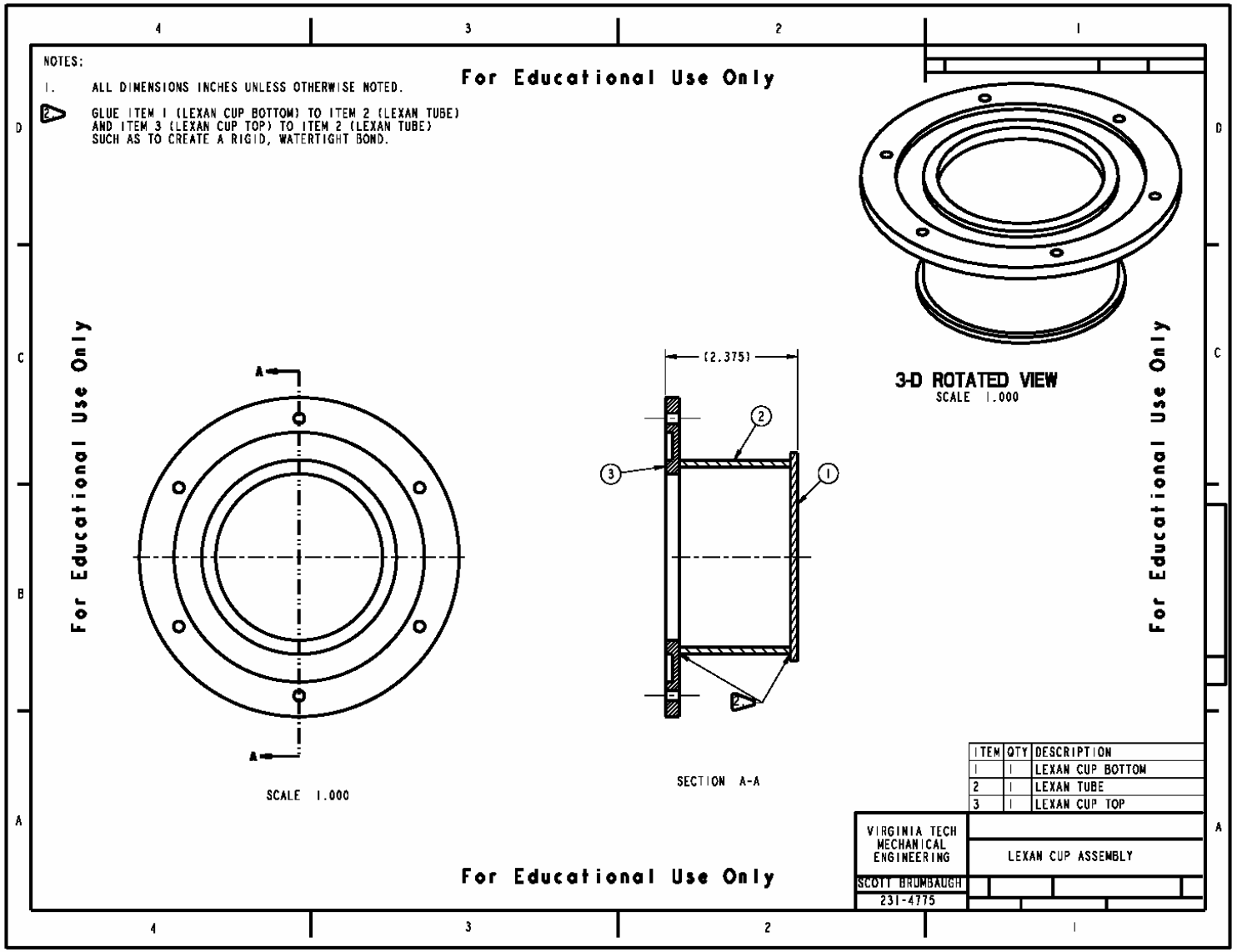
NOTES:
1. ALL DIMENSIONS INCHES UNLESS OTHERWISE NOTED.
2 GLUE ITEM 1 (LEXAN CUP BOTTOM) TO ITEM 2 (LEXAN TUBE) AND ITEM 3 (LEXAN CUP TOP) TO ITEM 2 (LEXAN TUBE) SUCH AS TO CREATE A RIGID, WATERTIGHT BOND.
For Educational Use Only
For Educational Use Only
For Educational Use Only
For Educational Use Only
3-D ROTATED VIEW
SCALE 1.000
SCALE 1.000
(2.375)
SECTION A-A
ITEM QTY DESCRIPTION
1 1 LEXAN CUP BOTTOM
2 1 LEXAN TUBE
3 1 LEXAN CUP TOP
VIRGINIA TECH MECHANICAL ENGINEERING
LEXAN CUP ASSEMBLY
SCOTT BRUMBAUGH
231-4775

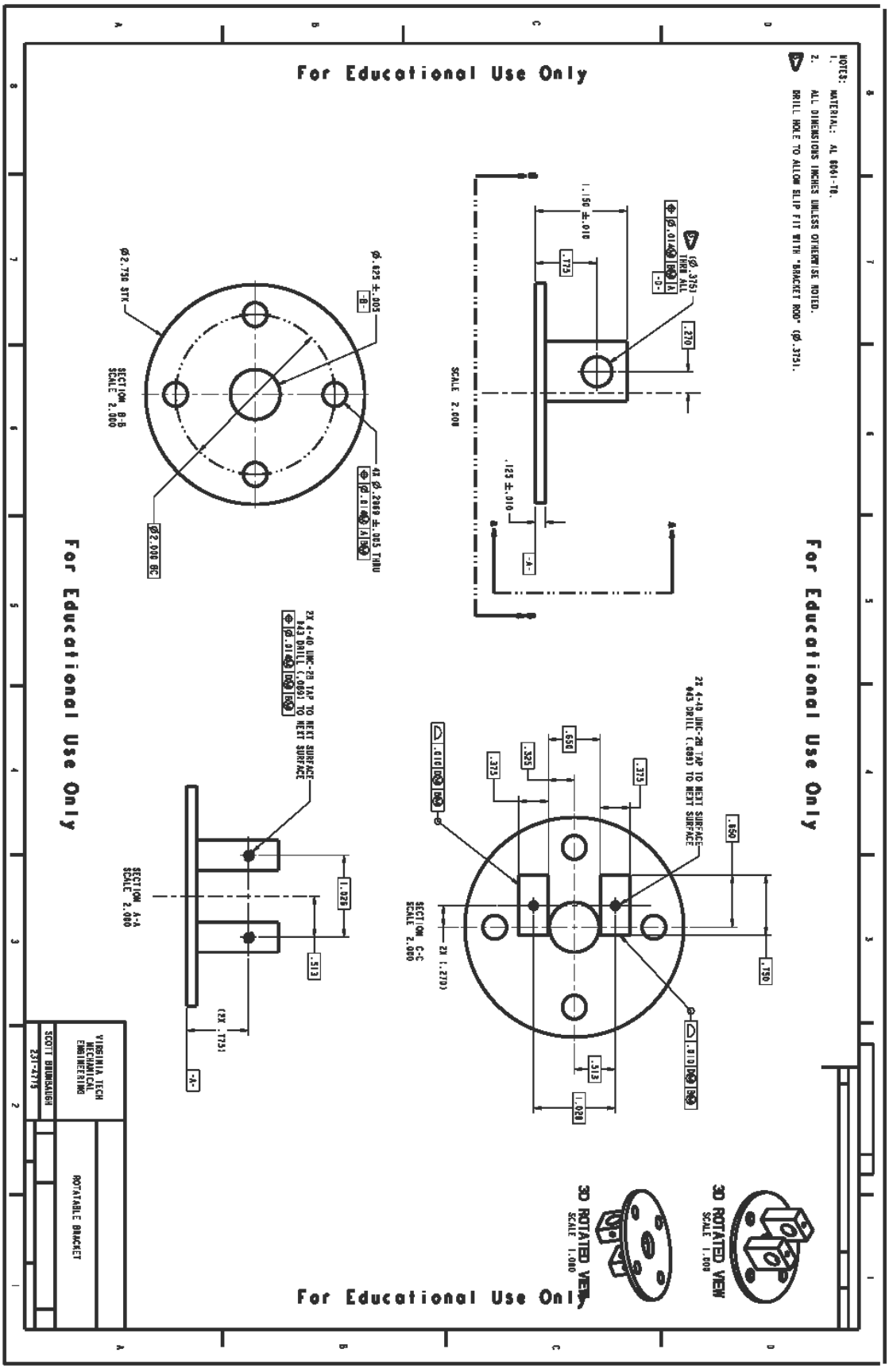
For Educational Use Only
NOTES:
1. MATERIAL: AL 6061-T6.
2. ALL DIMENSIONS INCHES UNLESS OTHERWISE NOTED.
DRILL HOLE TO ALLOW SLIP FIT WITH "BRACKET ROD" (Ø.375).
SECTION B-B
SCALE 2.000
SECTION A-A
SCALE 2.000
SECTION C-C
SCALE 2.000
SCALE 2.000
3D ROTATED VIEW
SCALE 1.000
3D ROTATED VIEW
SCALE 1.000
VIRGINIA TECH
MECHANICAL
ENGINEERING
SCOTT BRUMBAUGH
231-2475
ROTATABLE BRACKET

NOTES:

1. MATERIAL: ALUMINUM 7075 PRECISION GROUND ROD.
2. ALL DIMENSIONS INCHES UNLESS OTHERWISE NOTED.

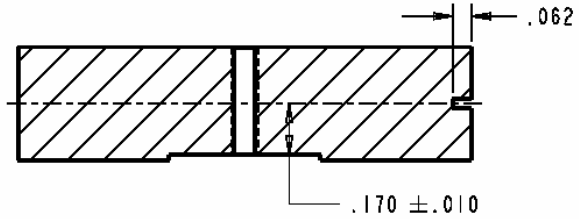

SECTION A-A

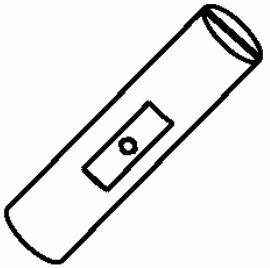

3-D ROTATED VIEW
SCALE 2.000

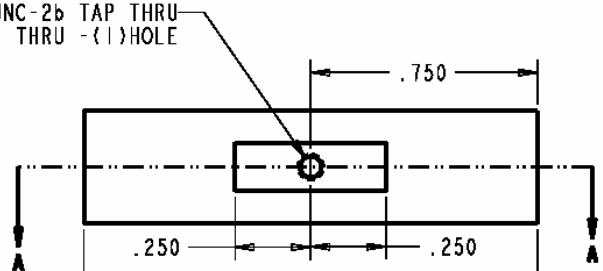

SCALE 3.000

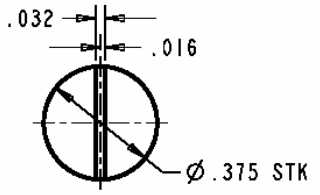

VIRGINIA TECH MECHANICAL ENGINEERING	BRACKET ROD
SCOTT BRUMBAUGH 231-4775	

NOTE:

1. ALUMINUM, 7075, PRECISION GROUND ROD.
2. ALL DIMENSIONS INCHES UNLESS OTHERWISE NOTED.

3-D ROTATED VIEW
SCALE 2.000

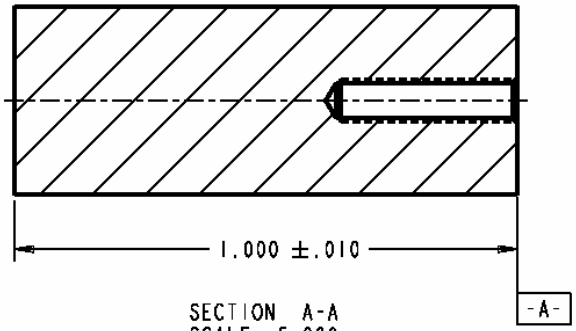

SECTION A-A
SCALE 5.000

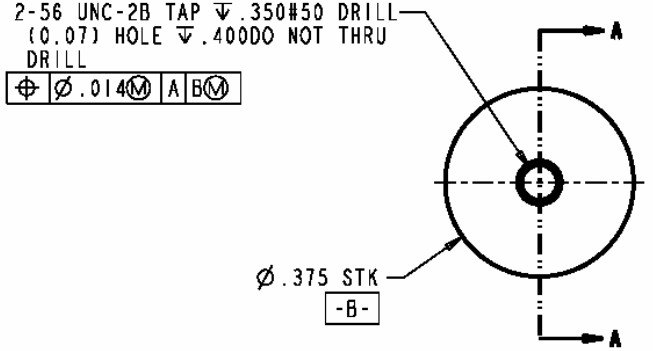

VIRGINIA TECH MECHANICAL ENGINEERING		FLOW ELEMENT CYLINDER	
SCOTT BRUMBAUGH 231-4775	REV A	ISSUE: 06-20-2005	

NOTES:

1. MATERIAL: ALUMINUM 7075 ROD.
2. ALL DIMENSIONS INCHES UNLESS OTHERWISE NOTED.
3. THIS PIECE IS INTENDED TO BE A GAGE. CREATE HOLE SUCH THAT THE .375 CYLINDER (FLOW ELEMENT CYLINDER) SNUGLY SLIDES THROUGH THE HOLE.
4. INDICATE WHICH SURFACE IS DTM -A- BY MARKING THE SURFACE WITH INK APPROXIMATELY AS SHOWN.

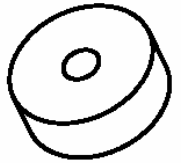

3-D ROTATED VIEW
SCALE 1.000

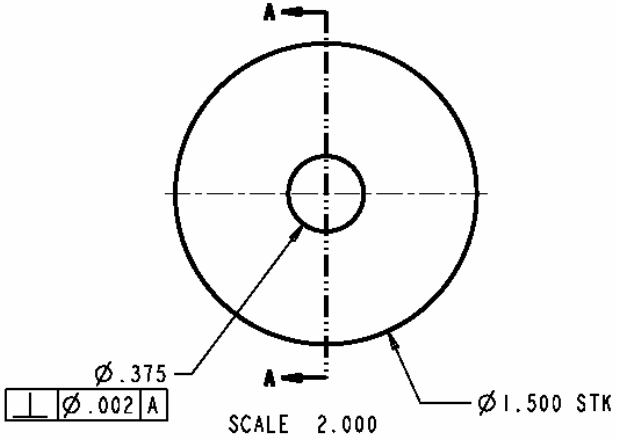

SCALE 2.000

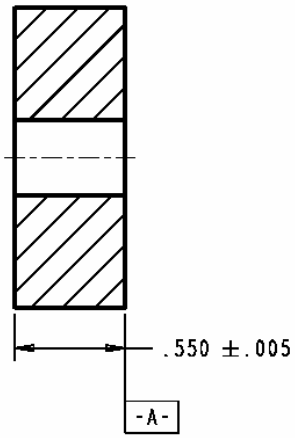

SECTION A-A

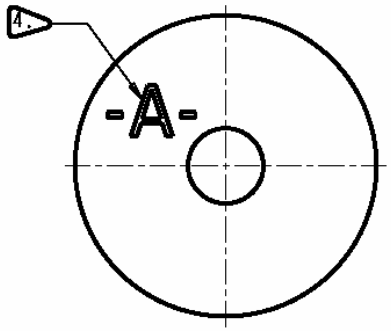

VIRGINIA TECH MECHANICAL ENGINEERING	GAGE CYLINDER
SCOTT BRUMBAUGH 231-4775	

NOTE:

1. ALUMINUM, 2024-T3, PRECISION GROUND ROD.
2. ALL DIMENSIONS INCHES UNLESS OTHERWISE NOTED.

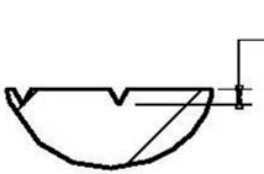

DETAIL A
SCALE 15.000

3-D ROTATED VIEW
SCALE 2.000

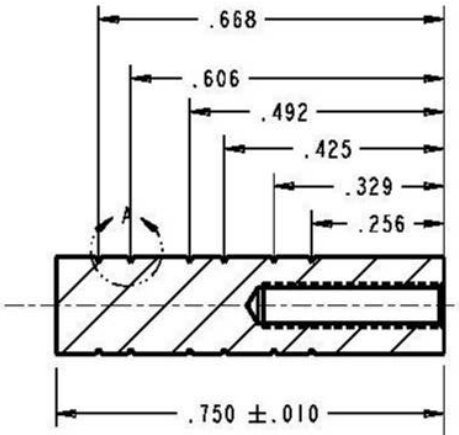

SECTION A-A
SCALE 5.000

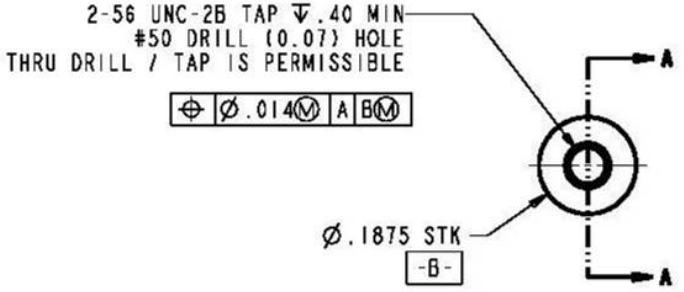

VIRGINIA TECH MECHANICAL ENGINEERING	Calibration Extension Beam
SCOTT BRUMBAUGH 231-4775	REV A ISSUE: 08-30-2005

Appendix F: Summary of Dow Corning 200 Silicone Fluid Properties

This appendix provides a summary of properties for the Dow Corning 200 Silicone Fluid.

Table F.1 Typical Properties of Dow Corning 200 Silicone Fluid [Dow Corning Corporation, 2000]

Dow Corning Fluid	Viscosity[1] at 25 C, centistokes	Flash Point[2]	Pour Point[3]	Specific Gravity at 77 F	Visc-Temp Coefficient[4]	Coefficient of Expansion cc/cc/°C	Refractive Index at 77 F	Surface Tension at 77 F dyne/cm	Thermal Conductivity[5] at 77F	Boiling Point
200	0.65	30 F	-90 F*	0.761	0.31	0.00134	1.375	15.9	0.00024	211 F at 760 mm
	1.0	100 F	-123 F*	0.818	0.37	0.00134	1.382	17.4	0.00024	305 F at 760 mm
	1.5	145 F	-105 F*	0.853	0.46	0.00134	1.387	18.0	0.00025	377 F at 760 mm
	2.0	175 F	-119 F*	0.873	0.48	0.00117	1.390	18.7	0.00026	446 F at 760 mm
	3.0	215 F	-85 F	0.900	0.51	0.00106	1.394	19.2	0.00027	158-212 F at 0.5 mm
	5.0	275 F	-85 F	0.920	0.55	0.00105	1.397	19.7	0.00028	248-320 F at 0.5 mm
	10	325 F	-85 F	0.940	0.57	0.00108	1.399	20.1	0.00032	>392 F at 0.5 mm
	20	450 F	-76 F	0.955	0.59	0.00107	1.400	20.6	0.00034	>392 F at 0.5 mm
	50	535 F	-67 F	0.960	0.59	0.00104	1.402	20.8	0.00036	>482 F at 0.5 mm
										VOLATILITY Weight Loss after 48 hours at temp.
	100	575 F	-67 F	0.968	0.60	0.00096	1.4030	20.9	0.00037	at 392 F, <2%
	200	600 F	-63 F	0971	0.60	0.00096	1.4031	21.0	0.00037	at 392 F, <2%
	350	600 F	-58 F	0.972	0.60	0.00096	1.4032	21.1	0.00038	at 392 F, <2%
	500	600 F	-58 F	0.972	0.60	0.00096	1.4033	21.1	0.00038	at 392 F, <2%
	1,000	600 F	-58 F	0.972	0.61	0.00096	1.4035	21.2	0.00038	at 392 F, <2%
	12,500	600 F	-51 F	0.973	0.61	0.00096	1.4035	21.5	0.00038	at 392 F, <2%
	30,000	600 F	-47 F	0.973	0.61	0.00096	1.4035	21.5	0.00038	at 392 F, <2%
	60,000	600 F	-42 F	0.973	0.61	0.00096	1.4035	21.5	0.00038	at 392 F, <2%

[1] Standard Viscosity Grades [2] Open Cup ASTM D92-33 [3] ASTM D97-39 Sect. 5-7 * Freeze Point

[4] 1 - Viscosity at 210 F / Viscosity at 100 F

Appendix G: Sensor Deflection Derivation and Sample Calculation

A sample calculation for a 0.95 cm diameter pin fin is provided to demonstrate the calculation of sensor deflection.

Engr: SjB
Date: 5/5/2005
Case:

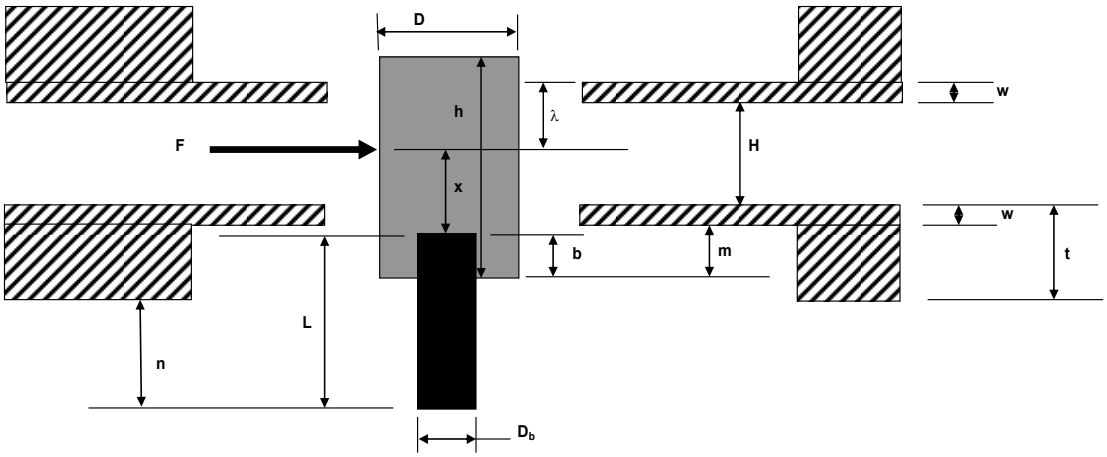

Sensor Dims			
Beam height, L (in):	1.25	l (m) =	0.03175
Beam diameter, D_b (in):	0.062	d (m) =	0.001575
Base of cylinder to top of threads, b (in):	0.3	b (m) =	0.00762
Beam Material:	17-4 PH		
Beam Modulus, E (psi):	28600000		

Deflection Estimates	Deflection @ top cylinder/Lexan Interface		
	in	cm	m
Strength of materials / Beam Theory:	0.001132	0.002876	2.88E-05
Kistler Morse Eq:	0.000665	0.001689	1.69E-05

Channel / Setup Geometry			
x (in) =	-0.075	x (m) =	-0.001905
Floor/Ceiling thickness, t (in):	0.5	t (m) =	0.0127
Apparent Floor/Ceiling thickness, w (in):	0.125	w (m) =	0.003175
Channel Height, H (in):	0.378	z (m) =	0.009601
Cylinder Diameter, d (in):	0.378	p (m) =	0.009601
**Applied Force, F (N):	0.103	F (kg) =	0.010503
Cylinder Material:	Al 6061		
Cylinder Density (kg/m³):	2700		
Misalignment Tipping of Sensor / Cylinder (°):	0		

**Applied force provided by drag_calc_7. xls, D/H = 2 (D=0.75) in air

Conclusion

A force of 0.103 N corresponds to Re=50000 for a 0.375"D cylinder (CD = 1.1). We see that @ Re=50000, the expected deflection is .0012" - 0.0007". I will round this up to 0.005" for conservativism. The size tolerance on the hole is +/- .001 on diameter

Calculated Values			
m = (-x+b)-(z/2+w) = Cyl Dist. BELOW Apparent Ledge (in) =	0.061	m (m) =	0.001549
n = (w+m-b+l)-t = (Sensor Dist BELOW Full Lexan) (in) =	0.636	n (m) =	0.016154
λ = z/2 + w (in) =	0.314	λ (m) =	0.007976
Cylinder height, h (in) =	0.689	h (m) =	0.017501

Figure G.1 Definition of geometric parameters and summary of deflection results.

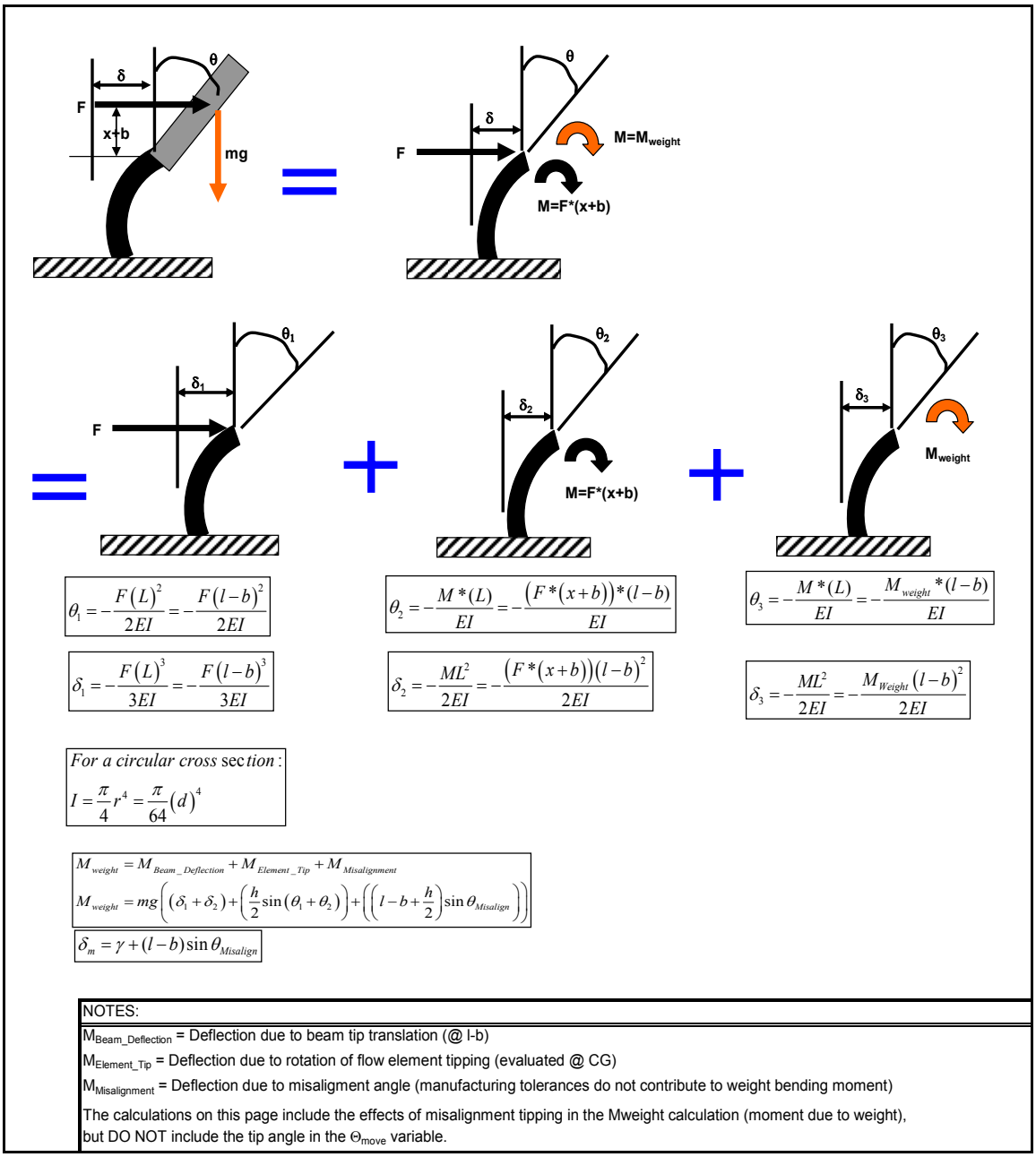

NOTES:

$M_{Beam\_Deflection}$ = Deflection due to beam tip translation (@ l-b)

$M_{Element\_Tip}$ = Deflection due to rotation of flow element tipping (evaluated @ CG)

$M_{Misalignment}$ = Deflection due to misaligment angle (manufacturing tolerances do not contribute to weight bending moment)

The calculations on this page include the effects of misalignment tipping in the Mweight calculation (moment due to weight), but DO NOT include the tip angle in the Θ_{move} variable.

Figure G.2 Explanation of superposition method used to calculate sensor deflection.

Engr: SjB
Date: 5/5/2005

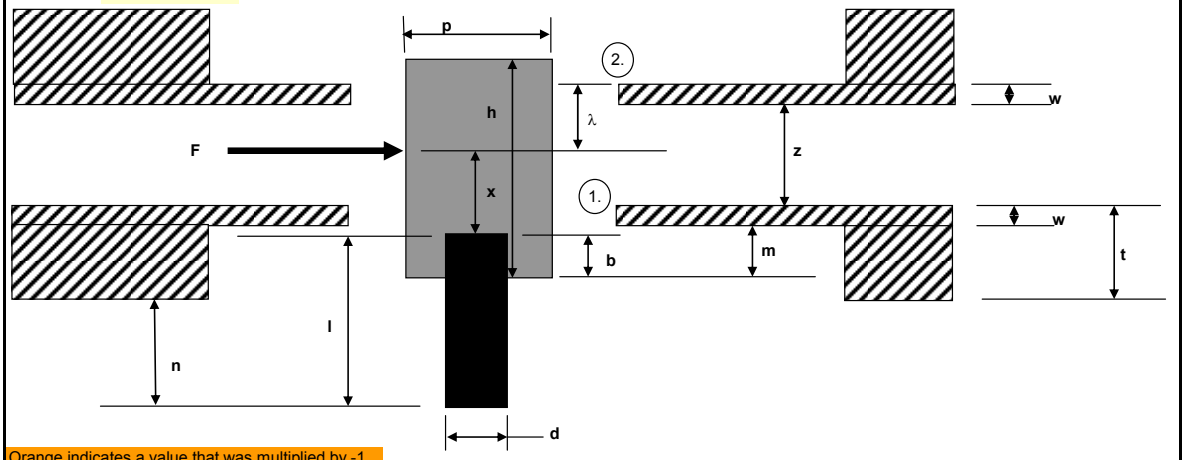

Orange indicates a value that was multiplied by -1.

Beam			
x (in):	0.075	**x (m) =**	**0.001905**
h (in):	0.689	**h (m) =**	**0.0175006**
b (in):	0.3	**b (m) =**	**0.00762**
L (in):	1.25	**l (m) =**	**0.03175**
D_b (in):	0.062	**d (m) =**	**0.0015748**
D (in):	0.378	**p (m) =**	**0.0096012**
Misalign. (°):	0	**Misalign. (rad):**	**0**
E (psi):	28600000	**E (N/m²) =**	**1.9719E+11**
$Mass_{Ext}$ (g):	33.54890057	**$Mass_{Ext}$ (kg) =**	**0.033548901**

Tunnel			
H (in):	0.378	**z (m) =**	**0.0096012**
w (in):	0.125	**w (m) =**	**0.003175**
m(in):	0.061	**m (m) =**	**0.0015494**

Flow			
F (N):	**0.103**		

Calculations			
I (m^4) =	3.01906E-13		
EI (Nm²) =	0.059532829		
M_{weight} (Nm) =	-6.83911E-06		

Deflection Summary at DSC / Flow Element Interface

1		2		3	
θ_1 (rad) =	-0.000503692	θ_2 (rad) =	-0.000397652	θ_3 (rad) =	-2.77205E-06
θ_1 (°) =	-0.028859446	θ_2 (°) =	-0.022783773	θ_3 (°) =	-0.000158827
δ_1 (m) =	-8.10273E-06	δ_2 (m) =	-4.79767E-06	δ_3 (m) =	-3.34447E-08
δ_1 (in) =	-0.000319005	δ_2 (in) =	-0.000188885	δ_3 (in) =	-1.31672E-06

Movement Σ @ (l-b) = 1+2+3	
θ_{Move} (rad) =	-0.000904116
θ_{Move} (°) =	-0.051802045
δ_{Move} (m) =	-1.29338E-05
δ_{Move} (in) =	-0.000509207

1. Deflection Summary at Top of Wind Tunnel Floor

Vertical Rise Above (l-b) tip = m+w = ζ_1
ζ_1 (m) = 0.0047244

Movement Only	
θ_{Move} (rad) =	-0.000904116
θ_{Move} (°) =	-0.051802045
δ_{Move} (m) =	-1.72053E-05
δ_{Move} (in) =	-0.000677372

2. Deflection Summary at Top of Wind Tunnel Ceiling

Vertical Rise Above (l-b) tip = m+w+z+w = ζ_2
ζ_2 (m) = 0.0175006

Movement Only	
θ_{Move} (rad) =	-0.000904116
θ_{Move} (°) =	-0.051802045
δ_{Move} (m) =	-2.87564E-05
δ_{Move} (in) =	-0.001132143

Figure G.3 Sample calculation of sensor deflection.

Appendix H: Test Section Installation Instructions

This appendix provides detailed instructions of how to assemble the test section. For a completely new installation, the instructions should be followed in order. Partial assemblies may begin at the appropriate step, and then follow the instructions in sequential order. Parts are referred to by the drawing name provided on their respective mechanical drawings.

1.) Using a straight edge, check the flatness of the test section MDF table top. Apply 0.01 cm thick masking tape as necessary to ensure the table is flat.

2.) Install the Floor Stop onto the bottom of the Test Floor Board using QTY four machine head ¼“ – 20 bolts, 7.62 cm long. Cover the countersunk screw heads with clear packing tape to provide a smooth flow surface.

3.) Install QTY one 0.80 cm shoulder bolts in the aft shoulder bolt hole on each side of the Test Floor Board (reference the Test Floor Board mechanical drawing). The shoulder bolts should fit snugly in the holes. The shoulder bolts are used to constrain the location of the MDF spacers.

4.) Place the Test Floor Board on the MDF table top, and align the Test Floor Board such that the black lines on the datum side of the Test Floor Board align with the black lines on the datum side of the MDF table top (red lines are used to align aluminum I-beams). The Floor Stop end of the Test Floor Board should face the plenum.

5.) Install a 0.635 cm thick by 1.27 cm wide Poron gasket strip in each gasket gland in the Test Floor Board.

6.) With a micrometer, check the thickness of each MDF spacer every 5 cm. The MDF spacer should uniformly be 0.96 cm thick. Where necessary, apply 0.01 cm thick masking tape to increase the thickness of the MDF spacers. Remove tape or sand the MDF spacers as necessary to reduce the thickness of the MDF spacers.

7.) Install both MDF spacers on top of the Floor Test Board and the Poron gaskets. Install QTY two (one each side) 0.80 cm shoulder bolts in the forward shoulder bolt holes (reference the Test Floor Board mechanical drawing) to secure the MDF spacers in place.

Reference the markings on the MDF spacers to determine the correct test channel side for each MDF spacer.

8.) Install QTY five internal ceiling support airfoils according to Figure 4.9. Use 0.005 cm thick double sided carpenter's tape to adhere the airfoils to the Test Floor Board.

9.) Install QTY three copper pin fins at the aft end of the Test Floor Board according to Figure 4.9. Use 0.005 cm thick double sided carpenter's tape to adhere the pin fins to the Test Floor Board.

10.) Mark the streamwise and spanwise reference axes at the Test Floor Board sensor hole. These axes will be used to properly align the DSC-6 sensor during installation.

11.) Install the DSC-6 sensor onto the Rotatable Bracket (sensor mount). Loosely secure the DSC-6 sensor to the Rotatable Bracket.

12.) Install the Rotatable Bracket and DSC-6 sensor assembly onto the sensor gauging Lexan plate.

13.) Install the Flow Element Cylinder (0.95 cm diameter aluminum pin) onto the DSC-6 sensor.

14.) Slide the Gage Cylinder over the Flow Element Cylinder such that the Gage Cylinder rests squarely on the Lexan plate. This will ensure the Flow Element Cylinder is perpendicular to the Lexan plate. Ensure that the DSC-6 lead wires (Alpha cable) are not twisted or trying to push the DSC-6 sensor in any direction. The Alpha cable is fairly stiff, and may push the DSC-6 sensor out of alignment if not properly adjusted.

15.) Snugly tighten the DSC-6 sensor to the Rotatable Bracket with the #2-56 bolt while ensuring the Gage Cylinder continues to rest squarely on the Lexan plate.

16.) Tighten the QTY four set screws on the Rotatable Bracket to secure the rotating pin on which the sensor is bolted. Again, ensure the Gage Cylinder continues to rest squarely on the Lexan plate.

17.) Re-tighten the #2-56 bolt holding the DSC-6 sensor to the Rotatable Bracket.

18.) Remove the Gage Cylinder, and double check the perpendicularity of the Flow Element with a triangle square.

19.) Remove the DSC-6 and Rotatable Bracket assembly from the sensor gauging Lexan plate, and install the assembly onto the bottom of the Test Floor Board with QTY four 1.59 cm long #6-32 bolts and QTY four #6 fender washers. Loosely tighten the

Rotatable Bracket to the Test Floor Board, ensuring the Rotatable Bracket axis scribes align with the marked reference axes on Test Floor Board. Be careful not to excessively deflect the DSC-6 sensor during the installation process.

20.) Install a 24 AWG grounding wire underneath one of the #6 fender washers. Connect the other end of the grounding wire to the SCXI chassis.

21.) Recheck axis alignment between the Rotatable Bracket and the Test Floor Board, and tighten the Rotatable Bracket to the Test Floor Board.

22.) Install the Set Screw Ring to the bottom of the Test Floor Board.

23.) Iteratively use the set screws on the Set Screw Ring to center the Flow Element Cylinder (pin fin) in the channel floor hole. Use the VI "ni_vi_9_2axis_center.vi" to check the center of the pin fin. The pin fin should be centered to within 0.005 V in each direction. Ensure the Rotatable Bracket axes are aligned with the Test Floor Board reference axes before tightening the sensor mount down for the last time.

24.) Install the Poron foam gasket to the flange of the Lexan Cup Assembly (floor silicone reservoir). Clean any debris out of the cup.

25.) Slide the Lexan Cup Assembly (floor silicone reservoir) over the DSC-6 lead wires (Alpha cable), and install the cup over the DSC-6. Use QTY six, 1.59 cm long #6-32 bolts and QTY six #6 fender washers to secure the Lexan Cup Assembly to the Test Floor Board. Use a diametrically opposed pattern to evenly torque the bolts down. Do not over tighten the bolts, as this may crack the Lexan Cup Assembly.

26.) Recheck the center of the DSC-6 sensor in the channel floor hole using "ni_vi_9_2axis_center.vi" From experience, installation of the Lexan Cup Assembly has occasionally deflected the DSC-6 sensor such that it is no longer center in the floor hole.

27.) Secure the DSC-6 lead wires (Alpha cable) to the Unistrut table frame with electrical tape. This will prevent accidental damage to the DSC-6 by pulling on the wires.

28.) Install the other pin fins around the force sensing pin fin (Flow Element) as desired. Use 0.005 cm thick double sided carpenter's tape to secure the pin fins to the Test Floor Board.

29.) Install a 0.635 cm thick by 1.27 cm wide Poron gasket strip in each gasket gland in Ceiling Board B.

30.) Install Ceiling Board B over the Test Floor Board and force sensing pin fin. Use extreme caution while installing Ceiling Board B that the sensing pin fin is not excessively pushed or deflected. It is possible to push the DSC-6 sensor out of center while installing Ceiling Board B. Check the center of the DSC-6 center with "ni_vi_9_2axis_center.vi" to ensure sensor center is still acceptable.

31.) Install the MDF Cover over Ceiling Board B (as shown in Figure 4.10).

32.) Adjust Ceiling B such that the gap behind the force sensing pin is 0.011 – 0.015 V larger than the gap upstream of the pin fin (as measured by deflecting the Flow Element pin fin and observing the sensor output with "ni_vi_9_2axis_center.vi"). The gap bias will be removed during installation of the sheet metal diffusers. Installation of the diffuser tends to push Ceiling Board B upstream. Ensure that the spanwise gap is even on both sides of the sensor.

33.) Insert QTY nine ¼"– 20 bolts in each side of the test section. Starting on the left side of the test section, finger tighten the middle bolt (5^{th} from the front or back). Continue to finger tight the ¼" – 20 bolts working away from the center bolt, alternating test section sides each time. In this manner, the test section will be tightened down as evenly as possible.

34.) Periodically check the alignment of the force sensing pin. Ensure that the downstream gap is 0.011 – 0.015 V larger than the upstream gap. Use a wooden block and hammer to knock Ceiling Board B into position as necessary to achieve the desired gap on each side of the Flow Element.

35.) Use a wrench to tighten the ¼"– 20 bolts down in the alternating pattern described in Step 33. Only tighten each bolt by two revolutions each time. Continuously check the alignment of the force sensing pin and adjust Ceiling B to the correct position using the hammer and wooden block.

36.) Once Ceiling Board B is completely tightened down, again check the alignment of the force sensing pin with "ni_vi_9_2axis_center.vi".

37.) Use the wooden gauge block to check the height of the test section under Ceiling Board B.

38.) Install a 0.635 cm thick by 1.27 cm wide Poron gasket strip in each gasket gland in Ceiling Board A. Install a 0.635 cm thick by 0.32 cm wide Poron gasket in the gland located on the downstream face of Ceiling Board A.

39.) Install Ceiling Board A at the front of the test section. Apply pressure on Ceiling Board A to compress the Poron gasket and push downstream snugly against the ceiling flange. Bolt Ceiling Board A to Ceiling Board B with QTY four ¼"– 20 bolts (finger tight only).

40.) Continue to push downwards and downstream on Ceiling Board A while installing QTY two ¼"– 20 bolts on each side of Ceiling Board A. Leave the 2nd hole upstream from the ceiling flange on each side empty (to leave room for the aluminum I-beam). Also leave the furthest upstream holes empty (so that the test section can be slid into the plenum). Finger tighten each bolt in an alternating manner starting with the left downstream bolt working upstream and side to side in the channel.

41.) Use a wrench to tighten the QTY four ¼"– 20 bolts in the ceiling flange. Do not over tighten the bolts, as the ceiling flange may crack.

42.) Use a wrench to tighten the ¼"– 20 bolts in the alternating pattern described in Step 40. Only tighten each bolt by two revolutions each time.

43.) Install the aluminum I-beam over Ceiling Board A. Use the red marks on the MDF table to align the aluminum I-beam. Tighten the QTY four ½"– 12 bolts to the MDT table in an alternating pattern.

44.) Slide the test section into the plenum slot until the Floor Stop rests squarely against the aft plenum wall. Be careful not to bump the test section or plenum too hard.

45.) Secure the DSC-6 lead wires to the wooden post with electrical tape, as shown in Figure 4.7. Ensure that the lead wires do not twist or push the sensor in any direction. Taping the DSC-6 lead wires to the wooden post minimizes swaying in the lead wires that could lead to spurious noise in the sensor output.

46.) Use QTY one, ¼"– 20 bolt on each side of the test section in the plenum to tighten the final upstream bolt hole.

47.) Use QTY five ¼"– 20 bolts to secure the Floor Stop to the aft plenum wall.

48.) Use QTY five ¼"– 20 bolts to secure the ceiling Floor Stop to the aft plenum wall.

49.) Leaning into the plenum, use the wooden gauge block to check the height of the test section under Ceiling Board A. Pay special attention to the areas where Ceiling Board A and Ceiling Board B join together, and where the test section penetrates the downstream plenum wall. These are locations where the channel cross sectional area has been problematic in the past.

50.) Apply AT – 200Y around the test channel inside the plenum. This will prevent air from escaping the plenum to open atmosphere. If additional leaks persist during operation, AT - 200Y may be applied to the external gap between the test section and aft plenum wall.

51.) Install the bottom PVC inlet guide with QTY two 17.8 cm long ¼"– 20 bolts. Ensure that the inlet guide is flush with the test section floor. Apply clear packing tape over the test section floor / inlet guide joint to smooth the joint.

52.) Install the top PVC inlet guide with QTY two 17.8 cm long ¼"– 20 bolts. Ensure that the inlet guide is flush with the test section floor. Apply clear packing tape over the test section ceiling / inlet guide joint to smooth the joint.

53.) Install the sheet metal diffuser to the outlet of the test section. Slide the rubber flex fitting over the flow measurement PVC pipe while mating the diffuser to the test section outlet. Do not yet tighten the clamp on the rubber flex fitting. Be sure to align the black tick marks on top of the diffuser with the black tick marks on top of the Ceiling Board B flange. Use QTY ten 6.35 cm long ¼"– 20 bolts to secure the diffuser to the test section. Place a wooden spreader bar between the bolt head and the sheet metal diffuser flange in order to spread the load. Because the diffuser flange is relatively thin, high intensity localized forces deform the diffuser.

54.) Tighten the clamp on the rubber flex fitting at the joint between the diffuser PVC pipe and the flow measurement PVC pipe.

55.) Check the sensor alignment with "ni_vi_9_2axis_center.vi." The gap between the pin fin and channel walls should now be even for both the streamwise and spanwise directions.

56.) Apply AT – 200Y sealant tape around the DSC-6 lead wires where they exit the bottom of the silicone cup. Apply silicone caulking over the AT-200Y such as to seal the bottom of the Lexan Cup. The purpose of the AT-200Y is to prevent silicone caulking

from entering the Lexan Cup. Silicone caulking releases acetic acid as it dries. The acetic acid could damage the DSC-6 sensor. The AT-200Y tape is meant to prevent the acetic acid from diffusing into the silicone reservoir.

57.) Fill the silicone fill bottle (modified soda bottle) with the desired silicone viscosity. Note that it may take up to 48 hours for all bubbles to rise out of the silicone oil.

58.) Once the bubbles have risen out of the silicone fill bottle, connect the silicone fill bottle to the Lexan Cup Assembly (floor silicone oil reservoir) with a 1 meter long section of 0.635 cm diameter Tygon tubing.

59.) Once the silicone caulking on the Lexan Cup Assembly has dried, fill the floor silicone reservoir with silicone oil by squeezing the modified soda bottle. A clamp may be used to apply continuous pressure to the bottle. Do not fill the Lexan Cup Assembly with silicone oil while the caulking is still wet, as this may result in acetic acid mixing with the silicone oil. Fill the silicone reservoir until silicone oil seeps out of the pin fin gap in the Test Floor Board.

60.) Pour the desired viscosity silicone oil into the ceiling silicone reservoir (a counterbore hole in Ceiling B). To minimize bubbles in the ceiling reservoir, pour the oil onto a stick and allow it to slide down the stick into the ceiling reservoir.

61.) Remove the sheet metal diffuser and wipe away excess silicone oil as necessary. Remove excess silicone oil at a rate of once every 2 hours until the silicone oil stops leaking out of the pin fin gap. The test section is ready to conduct a test when the silicone oil does not seep out of the pin fin gap in a 30 minute period.

62.) Connect a 24 AWG grounding wire between the Unistrut frame and the SXCI chassis.

63.) Reinstall the plenum ceiling with X ¼“– 20 bolts.

64.) Reinstall the sheet metal diffuser according to Step 53.